AD-A154 117 A STUDY OF THE TURBULENT LAYER IN THE WATER AT AN AIR-WATER INTERFACE(U) STANFORD UNIV CALIF DEPT OF CIVIL ENGINEERING T K CHEUNG JAN 85 TR-287 1/3

UNCLASSIFIED N00014-84-K-0242 F/G 8/3 NL

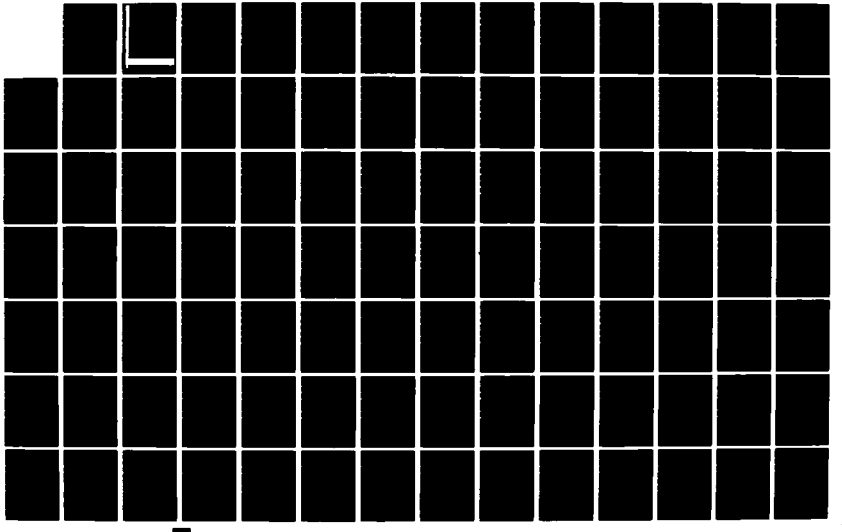

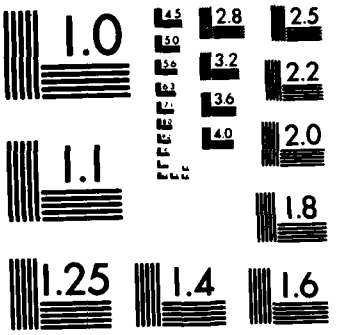

MICROCOPY RESOLUTION TEST CHART
NATIONAL BUREAU OF STANDARDS-1963-A

January 1985

Technical Report No. 287

A STUDY OF THE TURBULENT LAYER IN THE WATER AT AN AIR-WATER INTERFACE

by

Tak Kee Cheung

This research was sponsored by
Office of Naval Research
Contract N00014-84-K-0242
NR - 661-003/11-18-83 (430)

This document is unclassified and its distribution is unlimited

Department of CIVIL ENGINEERING
STANFORD UNIVERSITY

Environmental Fluid Mechanics Laboratory
Department of Civil Engineering
Stanford University
Stanford, California 94305

A STUDY OF THE TURBULENT LAYER IN THE WATER AT AN AIR-WATER INTERFACE

by

Tak Kee Cheung

Technical Report No. 287

January 1985

This research was sponsored by
Office of Naval Research
Contract N00014-84-K-0242
NR - 661-003/11-18-83 (430)

This report is unclassified and its distribution is unlimited

ACKNOWLEDGMENTS

This report is an unchanged reproduction of the dissertation submitted by me in partial fulfillment of the requirements for the degree of Doctor of Philosophy at Stanford University. Initial research on this project was supported by the National Science Foundation through Grant ENG-79-01176. The work reported here is currently supported by the Fluid Mechanics Division, Office of Naval Research, under Contract N00014-84-K-0242, NR - 661-003/11-18-83 (430). The content of this report does not necessarily reflect the position or policy of the U.S. Government and no official endorsement should be inferred.

I wish to express my sincere thanks to Professor Robert L. Street for his unconditional support, patience, and advice throughout the course of this project. I also wish to thank Professor En Yun Hsu for his ideas, comments, and for reviewing this manuscript. Special thanks are due to Professors John K. Eaton and Helen L. Reed for reading the manuscript and making valuable suggestions.

The discussions and comments of Dr. Stephen P. Klotz and Mr. Bruce M. Howe, who first introduced me to the research, are appreciated. Professor Jeffrey R. Koseff provided much help in my learning to use the laser Doppler anemometer. I am also indebted to Dr. Chin-Tsau Hsu of TRW for pointing out the errors during the initial development of the governing equations.

Mr. John Hessler and Mr. Marion Burzinski were responsible for much of the instrument design and fabrication. Typing of the manuscript by Ms. Ditter Peschcke-Koedt and Ms. Jane Burks and the excellent drafting done by Ms. Lynn Pohl are gratefully acknowledged.

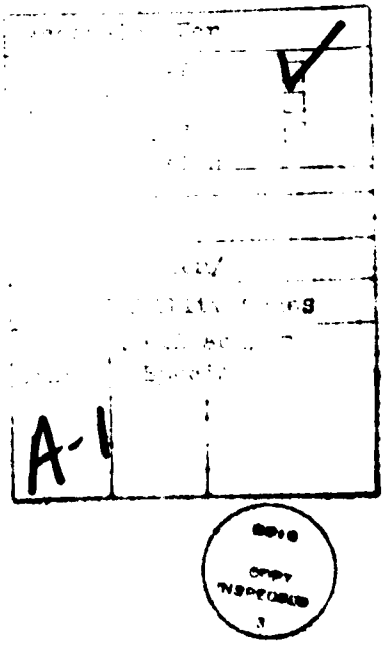

Errata

p. 12 Equation (2-1) should be

$$\overline{f(x)} = \lim_{T \to \infty} \frac{1}{T} \int_0^T f(\underline{x}, t)\, dt$$

p. 16 1st line, τ should be $1/\tau$

p. 127 8th line "In is clear ..." should be "It is clear..."

p. 258 Lin, J. and M. Gad-et-Hale,..., J. Phys. Ocean should be ... J. Geo. Res.

ABSTRACT

Because the global weather and ocean circulations are driven by transfers across the atmosphere-ocean interface, studies of it remain at the forefront of research efforts in atmospheric sciences and oceanography. Many questions concerning the momentum and energy transfers in the water surface layer beneath the air-water interface remain unanswered. The present experimental program was undertaken with the goal of learning how the energy, which is transferred from the wind, is distributed among the mean, wave, and turbulent flow fields in the water. The interactions between these three flow fields were also examined.

The experiments were performed in the Stanford Wind, Water-Wave Research Facility. A two-component, frequency-shifted, laser Doppler anemometer system was used with frequency trackers to measure the water velocity. Three major sets of experiments were done: i) wind-generated waves in Eulerian coordinates with wind speeds ranging from 1.5 m/s to 13.1 m/s, ii) wind-ruffled mechanically generated waves (22 mm in amplitude and at a frequency of 1 Hz) in Eulerian coordinates with wind speeds ranging from 0.0 to 6.2 m/s, and iii) wind-ruffled mechanically generated waves in wave-following Eulerian coordinates with wind speeds ranging from 0.0 to 6.1 m/s. A novel optical wave-follower, which allowed velocity measurements very close to the mobile surface, was constructed and deployed in the wave-following measurements. The mean, wave, and turbulent fields were isolated, and from them, other quantities of interest were computed.

The results show that the waves affect the mean flow, but the mean velocity profiles show logarithmic behavior. The wave field generally

agrees with the prediction of a linear water-wave theory. In the wind-wave experiments, the turbulent quantities behave similar to those in flows over flat plates. In the mechanical-wave experiments, the turbulent quantities have different trends from those of the wind-wave cases, which suggests possible weak wave-related turbulence. The mean wave-induced shear stress is negative, which implies that the waves augment the mean flow. Thus, the waves can also transfer energy indirectly to turbulence via the mean flow. The turbulent field draws its energy from the mean flow through the mean turbulent shear stress and from the wave field via the wave-induced turbulent stresses. Experimental observations agree with simple analysis of the momentum and energy equations. This study contributes to the basic understanding of the fundamental principles which govern transfers at an air-water interface.

TABLE OF CONTENTS

CHAPTER

CHAPTER

APPENDIX

LIST OF ILLUSTRATIONS

ABBREVIATIONS:

WW - wind-wave Eulerian frame experiments

MW-EF - mechanical-wave Eulerian frame experiments

MW-WF-EF - mechanical-wave wave-following Eulerian frame experiments

LIST OF TABLES

NOMENCLATURE

a	wave amplitude of water wave.
c	phase speed of water wave (wave celerity).
D	wave-follower vertical scan amplitude.
f	frequency in Hz; decay factor of the wave-following coordinates; arbitrary quantities of interest.
f_D	frequency of dominant wave; Doppler frequency in Hz.
F_i	$i = 1,2,3$; body forces in the direction of x, y, and z, respectively.
g	acceleration due to gravity; arbitrary quantities of interest.
h	depth (-y).
H	depth of water in the test channel.
k	wave number of water wave.
L	measuring fetch; linear operator.
p	pressure.
$\underline{r}$	surface vector (x,y).
r_{ij}	turbulent Reynolds stresses.
$S_{\eta\eta}$	surface displacement spectrum.
t	time.
t^*	time in wave-following coordinates.
T	total sampling time.
T_∞	mean air free-stream temperature.
T_{bulk}	mean bulk water temperature.
u	instantaneous streamwise velocity component.
u_i	$i = 1,2,3$; velocity components in subscript notation; (u,v,w).
u_*	friction velocity.
u_S	Eulerian surface drift velocity.

u_{SL} Lagrangian surface drift velocity.

u_{Stokes} Stokes surface drift velocity

u_∞ mean air free-stream velocity.

u^+ $(\overline{u_S}-\overline{u})/u_*$; mean horizontal velocity defect in law-of-the-wall coordinates.

v instantaneous vertical velocity component.

V_{in} input voltage to optical wave-follower.

V_{pot} position output voltage of the optical wave-follower.

w instantaneous spanwise velocity component.

x streamwise distance or fetch measured with respect to the air inlet.

$\underline{x}$ position vector in three-dimensional space; (x_1,x_2,x_3) or (x,y,z).

x_i same as $\underline{x}$.

x^* streamwise distance or fetch in wave-following coordinates measured with respect to the air inlet.

y vertical distance (positive upwards) measured with respect to the still water level.

y_η wave decay depth.

y^+ yu_*/ν; vertical distance in law-of-the-wall coordinates.

y^* vertical distance in wave-following coordinates.

$(y^*)^+$ y^*u_*/ν; vertical distance in wave-following law-of-the-wall coordinates.

z spanwise distance measured with respect to the centerline of the channel.

z^* spanwise distance in wave-following coordinates measured with respect to the centerline of the channel.

Greek Symbols

α $a\omega/u_S$; ratio of velocity amplitude of the wave motion to the surface drift velocity.

δ turbulent boundary-layer thickness.

Δ denotes a change when used as a prefix.

ϵ^2 multiplicative constant used in order-of-magnitude analysis.

η surface displacement with respect to the still water level.

$\hat{\eta}_S$ amplitude of the 1 Hz component of $\tilde{\eta}$.

θ_g phase lag of g with respect to the wave height signal $\tilde{\eta}$.

κ von Karman constant.

ν kinematic viscosity.

ρ density.

τ wave period.

ω $2\pi f$; circular frequency.

Superscripts

$'$ turbulent component.

$\tilde{}$ wave or periodic component.

$\bar{}$ mean component.

$\hat{}$ amplitude.

Special Symbols and Usage

$\sim$ when used after a variable denotes its typical value in an order-of-magnitude estimate.

$\langle\ \rangle$ phase average.

CHAPTER 1

INTRODUCTION

1.1 BACKGROUND AND MOTIVATION

Gas-liquid boundary-layer flows occur in many situations of practical importance. Many industrial and geophysical, as well as meteorological, processes involve such flows; in particular, the air-water interaction problem seems to be the most common. The transfers of momentum, mass, and energy across an air-water interface have been the subject of study for decades. However, because turbulence plays a major role in both the air and water surface layers about the interface, progress in developing a deep understanding of the processes governing the transfers has been slow. Many questions remain, especially about transfers in the water surface layer beneath the interface.

For example, when wind blows over water waves, how is the energy which is transferred from the wind distributed in the water near the interface, say, among the mean drift current, turbulence, and wave motion? How does this distribution change with depth and by what mechanism? How do the turbulent and wave quantities behave near the interface? Questions such as these are perhaps best answered by performing a series of well-planned laboratory experiments.

The work described here is part of an ongoing program at Stanford to study and gain a better understanding of the air-water interaction problem. The focus of this particular effort is on the water surface layer beneath the interface. A brief review of previous research (at Stanford and elsewhere) which is believed to be most relevant is given in the next section.

1.2 PREVIOUS RELATED STUDIES

1.2.1 Laboratory and Field Studies

Shemdin (1972) obtained mean velocity profiles in the wind-driven water surface layer inside a wind-wave facility. Neutrally buoyant particles were used as velocity tracers under reference wind speeds of 3.1, 5.7, and 9.6 m/s. He showed that the drift profiles were logarithmic. Similar studies were made by Wu (1975), who used floats to measure surface and near-surface drift current and a pitot-static tube to measure the subsurface drift current. The reference wind speeds used by Wu were from 2.8 to 13.3 m/s. He found that the current immediately below the water surface varied linearly with depth and the current near, but not immediately below, the water surface followed a logarithmic velocity distribution. McLeish and Putland (1975) measured wind-driven flow profiles in the top millimeter of water in both laminar and turbulent laboratory flow using microscopic bubble traces. They confirmed the existence of a viscous sublayer (linear profile), but it was considerably thinner than that at a solid boundary. Deeper in the water layer, they found that the mean profile became logarithmic.

Dobroklonsky and Lesnikov (1975) obtained kinematic characteristics of wind-wave flow by taking motion pictures of near-neutrally buoyant polystyrene indicator balls at various depths in the water. They reported logarithmic mean drift velocity profiles and that the total Reynolds stress originated from two sources: a wave source and a turbulent source. Later, Anisimova et al. (1978) measured drift velocity profiles over various sectors of wind-generated waves using the same wind-wave tank and measurement technique.

Howe et al. (1982) reported laboratory measurements of velocity and temperature fields on both sides of a wind-driven air-water interface for wind speeds of 1.6 to 13.1 m/s. Mean velocities and turbulent intensities in water were obtained using a two-component laser Doppler anemometer. Their mean velocity profiles when plotted in law-of-the-wall coordinates showed that, both in the air and in the water, the profiles were logarithmic. In addition, the mechanism of momentum transfer was affected by surface roughness changes. In the water surface layer the velocity fluctuations due to the wave-related motion were of the same order as the purely turbulent motions. Goossens et al. (1982) used a LDA to measure turbulent intensities and Reynolds stresses in air-driven water flows. More recently, similar experiments were performed by Lin and Gad-el-Hak (1984). However, they (Goossens et al., Lin and Gad-el-Hak) did not separate out the wave effect as Howe et al. (1982) did.

Bliven et al. (1984) conducted a series of laboratory experiments to measure the velocity field below surface gravity waves. The series consisted of cases in which waves were generated by a paddle actuated with an analog record of wind-wave surface elevation but without wind stress, and cases with the paddle-generated waves and wind stress. Their technique permits wave-generated turbulence to be investigated with minimal turbulence from other sources, such as shear currents and direct wind stress. Their study showed the existence of a Reynolds stress which increased as the wave steepness increased and decayed exponentially with depth. Turbulent energy increased as wave steepness increased and can be modeled by an exponential decay. The ratio of the exponential decay rate for turbulent energy to wave particle velocity decay rate was less than one, which indicates that the turbulent energy

penetration depth is on the order of the wave length rather than the wave height as suggested by Donelan (1978).

Field measurements of water velocity under wind waves were made by Bowden and White (1966), Shonting (1964, 1967, 1968, 1970), Simpson (1969), Yefimov and Khristoforov (1969, 1971), Taira (1971), Thornton and Krapohl (1974), and Cavaleri et al. (1978). Bowden and White, and Simpson found that the horizontal velocities were generally greater than those predicted by linear theory. According to Thornton and Krapohl, the measured wave-induced velocities were 2-4% greater than those calculated by using linear wave theory. Furthermore, the phase relationships among the vertical velocity, horizontal velocity and the surface elevation were in good agreement with linear wave theory. Cavaleri et al. observed that the amplitudes of the vertical and horizontal velocities were about 10% less than expected on the basis of linear wave theory. However, Shonting, Yefimov and Kristoforov, and Cavaleri et al. showed that the vertical and horizontal velocities were not in quadrature, thus indicating the existence of a vertically downward momentum flux.

1.2.2 Theoretical and Empirical Development

Kondo (1976) proposed a hypothesis of hydrodynamic similarity for both the air and water boundary layers adjoining an air-water interface. Using the high frequency components of the surface wave spectrum as a measure of roughness, he treated the interface as though it were a solid boundary for both the air and the water surface-layer flows. Although he did not assert that the instantaneous orbital motion of significant waves had no effect on turbulent transport, he proposed that such a wave effect would make a secondary contribution to the current.

Jones and Kenney (1977) examined a number of one-dimensional velocity spectra obtained in aquatic mixed layers (all field wind-wave data). They scaled the spectra with the surface stress and the distance from the free surface and compared with turbulent boundary-layer measurements (Bradshaw, 1967). The good agreement between the spectra of the aquatic mixed layer and a turbulent boundary layer suggests that the surface wave orbital velocities act merely as "inactive" motions and do not interfere with the lower-frequency stress-carrying eddies.

Csanady (1978) extended the law of the wall of turbulent boundary-layer theory to turbulent flow along a sharp density interface which he termed the "law of the interface." He further modified this law and made it applicable to an air-sea interface. One important difference between the law of the wall and the law of the interface, according to Csanady, was that the velocity gradient at an interface was typically much less than the stress divided by the molecular viscosity. He explained this finding in terms of the presence of viscous wavelets on the interface which contributed to momentum transfer through a combination of "sheltering" and the generation of an interfacial viscous boundary layer. He postulated a simple model for the effective viscosity for miscible fluids which he found to be related to the Keulegan parameter and a wave constant. A modified model was also postulated for the effective viscosity at an air-sea interface due to the influence of capillary waves. However, for flows with high friction velocity, these two models were shown to be equivalent.

According to classical wave theory, wave-induced orbital motions beneath the interface cannot support a shear stress. However, various experiments, such as those of Shonting (1967) and Howe et al. (1981)

indicate the existence of wave-induced shear stress. Yefimov and Grishin (1972) examined the two-dimensional nonlinear problem of wave perturbation in the surface layer of the ocean. They introduced an eddy viscosity coefficient to take into account the generation of turbulence by wave motion and computed Reynolds wave stresses by the method of matched asymptotic expansions. They found that the wave stresses led to a stationary Eulerian velocity and a mass-transport velocity. This interaction of the wave field with the turbulence field and the concept of the wave eddy viscosity were also discussed by, for instance, Navrotskii (1967), Kitaigorodskii and Miropolskii (1968), and Phillips (1977). A recent review on the subject of wave turbulence was given by Katsaros (1976).

Liu et al. (1979) developed a model for the marine atmospheric layer including the interfacial sublayers on both sides of the air-water interface where molecular constraints on transport are important. Flux-profile relations which were based on the postulation of intermittent renewal of the surface fluid were matched to the logarithmic profiles and compared with both field and laboratory measurements. By using these relations, one can make numerical determinations of air-water exchanges of momentum, heat, and water vapor by employing the bulk parameters of mean wind speed, temperature, and humidity at a certain height in the atmospheric surface layer and the water temperature.

Street (1979) presented a simple theory for turbulent heat and mass transfers across a rough, air-water interface. The theoretical predictions and results obtained from laboratory data were in quantitative agreement; however, the assumptions and data needed to allow a prediction were somewhat restrictive (cf., Liu et al., 1979). Klotz and

Street (1981a) presented a solution for the coupled laminar boundary-layer equations of heat, mass, and momentum at a smooth interface; the numerical solution applies to flows with and without pressure gradient and uses the Keller box method. Klotz and Street (1981b) described the numerical simulation of the turbulent boundary layer at a rough, air-water interface. A key problem lies in the parameterization of the roughness effects at the interface and their influence on the eddy coefficients in the near-interface regions (see, for example, their Fig. 4 where it is clear that the heat transfer has been successfully handled, but the momentum transfer has not).

Donelan (1978) measured velocity spectra beneath wind waves on Lake Ontario using a miniature drag sphere. Linear statistical methods were used to separate the velocity into wave and turbulent parts (cf., Benilov et al., 1974). The most prominent feature of these spectra is the enhancement about the dominant wave frequency. Sufficiently far from the peak, the frequency dependence tends to $f^{-5/3}$, with the high frequencies showing an increase in spectral density. Lumley and Terray (1983) proposed a new model to explain the shape of these velocity spectra. Their model shows that these features can be understood without recourse to dynamics, but arise instead from an essentially kinematic process in which frozen, isotropic turbulence is convected bodily by the orbital velocity field associated with the surface wave motion.

1.2.3 Conclusions

It is widely accepted that a viscous sublayer and a layer in which there is a logarithmic variation of the mean velocity profile exist in the water layer at an air-water interface (Shemdin, 1972; McLeish and Putland, 1975; Wu, 1975; Howe et al., 1980). However, there seems to be

some dispute about the viscous sublayer thickness as compared to that at a solid boundary. McLeish and Putland concluded from their experiment that the viscous sublayer at a free surface was considerably thinner than that at a solid boundary. However, according to Csanady (1978), the presence of viscous wavelets on the interface implies a thicker viscous sublayer due to higher energy dissipation, and an augmented eddy viscosity is needed to model the experimental results.

It has been suggested also that the orbital motion of waves in the water layer has little effect on turbulent transport (Kondo, 1976; Jones and Kenney, 1977). However, the experiments of Shonting (1967) and Yefimov and Kristoforov (1969) showed otherwise. Howe et al. (1982) reported that near, but not immediately below, the interface the wave-related motions were of the same order as the purely turbulent motions, and deviation of mean velocity profiles from a $1/\kappa$ slope ($\kappa = 0.4$) was apparent when waves were present compared to the wave-absent case. It is quite possible that right below the interface there exists a zone where the organized wave motion dominates, hence becoming important in transport.

It is difficult to control conditions in field experiments. Laboratory studies such as those of Howe were done using fixed probes, but led to significant results. Experiments with a progressive, mechanically generated wave train under the shearing action of a turbulent wind may also prove to be interesting as shown by Hsu et al. (1981). However, the interface cannot be approached as closely as one desires due to the larger amplitude of the mechanically generated waves. Furthermore, Hsu et al. (1981) showed that a wave-following coordinate system, which allowed measurements in the air between the wave crests when

mechanically generated waves were present, was crucial for understanding the physical processes of energy and momentum transfer to the waves. In view of all the aforementioned questions and arguments, it is only natural to conclude that further experimental investigations are necessary.

1.3 OBJECTIVES OF THE STUDY

As a first attempt to answer some of the questions stated in the previous section, a series of experiments were undertaken with the following objectives:

1. Obtain velocity data (mean and turbulent) in the water layer under wind-generated waves in Eulerian coordinates.
2. Obtain velocity data (mean and turbulent) in the water layer under wind-ruffled mechanically generated waves in Eulerian coordinates.
3. Design, construct, and qualify an optical wave-following mechanism which enables the velocity probe to sample very close to the mobile interface.
4. Obtain velocity data (mean and turbulent) in the water layer under wind-ruffled mechanically generated waves in wave-following Eulerian coordinates.
5. Identify similarities and differences between results obtained in Eulerian coordinates and wave-following Eulerian coordinates.
6. Compare measured quantities with existing data and theoretical models.
7. Develop a qualitative model of the flow which explains its observed characteristics.

1.4 SELECTION OF EXPERIMENTAL CONDITIONS

The range of variables for the experimental program is summarized in Table 1. Two specific surface conditions were considered: 1) wind-generated waves only, and 2) wind-ruffled mechanically generated waves. Also, two reference frames were used for the second flow condition.

The air free-stream velocity ranged from 1.5 m/s to 13.1 m/s for wind-generated wave runs. For the wind-ruffled mechanically generated wave condition, the air velocity ranged from 0.0 m/s to 6.0 m/s. The mechanically generated waves had an amplitude of 22 mm and a frequency of 1.00 Hz. These values were chosen so that the waves were of deep water type and the small amplitude wave theory was applicable. For almost all the cases, the temperature of the air was slightly warmer than that of the water.

Table 1

Summary of Range of Variables for the Experimental Program

Case	u_∞ (m/s)	Mechanically Generated Wave	Wave Following	Amplitude of 1 Hz Component of the Wave (mm)
1	1.5	no	no	-
2	2.6	no	no	-
3	3.2	no	no	-
4	4.7	no	no	-
5	6.7	no	no	-
6	9.9	no	no	-
7	13.1	no	no	-
8	0.0	yes	no	21.9
9	1.7	yes	no	21.1
10	2.5	yes	no	21.9
11	4.1	yes	no	22.1
12	6.2	yes	no	20.9
13	0.0	yes	yes	21.3
14	1.7	yes	yes	20.9
15	2.5	yes	yes	21.9
16	4.1	yes	yes	21.5
17	6.1	yes	yes	20.5

CHAPTER 2

THEORETICAL FOUNDATIONS

2.1 OVERVIEW

The present study consists of three sets of distinct, but closely related experiments. Each set of experiments has its own theoretical framework. In the following sections, the theoretical background for each set is outlined; then a comparison of the similarities and differences among them is given.

2.2 CASE I: WIND WAVE IN EULERIAN FRAME

2.2.1 Triple Decomposition

Following Benilov et al. (1974), one can decompose any flow variable $f(\underline{x},t)$, such as velocity, into three components:

$$f(\underline{x},t) = \overline{f}(\underline{x}) + \tilde{f}(\underline{x},t) + f'(\underline{x},t)$$

where

$\overline{f}(\underline{x})$ = the mean value of $f(\underline{x},t)$

$\tilde{f}(\underline{x},t)$ = the wave-induced component

$f'(\underline{x},t)$ = the fluctuating component

$\underline{x}$ = the Cartesian coordinate vector (x_1, x_2, x_3, or x, y, z),

x_1 or x = the streamwise distance measured with respect to the air inlet

x_2 or y = the vertical distance (positive upwards) measured with respect to the still-water level, and

x_3 or z = the spanwise distance measured with respect to the centerline of the test facility.

The time average is defined as:

$$\overline{f}(\underline{x}) = \lim_{T\to\infty} \int_{o}^{T} f(\underline{x},t)\, dt \qquad (2\text{-}1)$$

For a sampled data system, the time average takes the form:

$$\overline{f}(\underline{x}) = \lim_{N\to\infty} \frac{1}{N} \sum_{i=1}^{N} f(\underline{x},t_i)$$

It is also assumed that both $\tilde{f}$ and f' have zero means, i.e., $\overline{\tilde{f}} = 0$ and $\overline{f'} = 0$. The statistical properties of $\tilde{f}$ and f' can be found by the wave-separation method outlined in the next section.

2.2.2 Wave-Separation Method

In order to isolate the wave component of a flow variable, a coherent relationship is assumed between the wave-induced component and the wave motion at the interface. That is, the wave-induced component $\tilde{f}(\underline{x},t)$ is assumed to be statistically coherent with the surface displacement $\eta(\underline{r},t)$:

$$\tilde{f}(\underline{x},t) = L\eta(\underline{r},t)$$

where L is some linear operator and $\underline{r}$ is a horizontal vector at the interface. A necessary second assumption is mutual orthogonality of the three components:

$$\overline{\tilde{f}\bar{f}} = 0, \quad \overline{\tilde{f}f'} = 0, \quad \overline{\bar{f}f'} = 0$$

Naturally, η is composed of wave components only, i.e., $\eta = \tilde{\eta}$ and $\overline{\eta} \equiv \eta' \equiv 0$. In Appendix A, it is shown that information about all second moments of $\tilde{f}$ and f' can be obtained without reconstructing realizations of $\tilde{f}$ and f'. For this study, only second moments are of interest; hence, no reconstruction of $\tilde{f}$ or f' is required.

2.2.3 Governing Equations

The governing equations in this case are those for an incompressible Newtonian fluid, viz.,

continuity:
$$\frac{\partial u_i}{\partial x_i} = 0 \tag{2-2}$$

momentum:
$$\frac{\partial u_i}{\partial t} + u_j \frac{\partial u_i}{\partial x_j} = -\frac{1}{\rho}\frac{\partial p}{\partial x_i} + \nu \frac{\partial^2 u_i}{\partial x_j \partial x_j} + F_i \tag{2-3}$$

where $F_1 = F_3 = 0$, $F_2 = -g$. Let

$$u_i = \bar{u}_i + \tilde{u}_i + u_i' \tag{2-4a}$$

$$p = \bar{p} + \tilde{p} + p' \tag{2-4b}$$

Substituting Eqs. 2-4a and 2-4b into Eq. 2-2 and then taking the time average gives:

$$\frac{\partial \bar{u}_i}{\partial x_i} = 0 \tag{2-5a}$$

$$\frac{\partial}{\partial x_i}(\tilde{u}_i + u_i') = 0 \tag{2-5b}$$

Substituting Eqs. 2-4a and 2-4b into Eq. 2-3 and using the continuity equation yields:

$$\frac{\partial}{\partial t}(\bar{u}_i + \tilde{u}_i + u_i') + \frac{\partial}{\partial x_j}[(\bar{u}_j + \tilde{u}_j + u_j')(\bar{u}_i + \tilde{u}_i + u_i')]$$

$$= -\frac{1}{\rho}\frac{\partial}{\partial x_i}(\bar{p} + \tilde{p} + p') + \nu \frac{\partial^2}{\partial x_j \partial x_j}(\bar{u}_i + \tilde{u}_i + u_i') + F_i \tag{2-6}$$

or

$$\frac{\partial}{\partial t}(\bar{u}_i + \tilde{u}_i + u_i') + \frac{\partial}{\partial x_j}(\bar{u}_i\bar{u}_j + \bar{u}_i\tilde{u}_j + \bar{u}_i u_j'$$

$$+ \tilde{u}_i\bar{u}_j + \tilde{u}_i\tilde{u}_j + \tilde{u}_i u_j' + u_i'\bar{u}_j + u_i'\tilde{u}_j + u_i'u_j')$$

$$= -\frac{1}{\rho}\frac{\partial}{\partial x_i}(\bar{p} + \tilde{p} + p') + \nu \frac{\partial^2}{\partial x_j \partial x_j}(\bar{u}_i + \tilde{u}_i + u_i') + F_i \tag{2-7}$$

Time averaging Eq. 2-7 produces:

$$\frac{\partial}{\partial x_j}\left(\bar{u}_i\bar{u}_j + \overline{\tilde{u}_i\tilde{u}_j} + \overline{u_i'u_j'}\right) = -\frac{1}{\rho}\frac{\partial \bar{p}}{\partial x_i} + \nu\frac{\partial^2 \bar{u}_i}{\partial x_j \partial x_j} + F_i$$

or

$$\frac{\partial}{\partial x_j}\left(\bar{u}_i\bar{u}_j\right) = -\frac{1}{\rho}\frac{\partial \bar{p}}{\partial x_i} + \nu\frac{\partial^2 \bar{u}_i}{\partial x_j \partial x_j} - \frac{\partial}{\partial x_j}\left(\overline{u_i'u_j'} + \overline{\tilde{u}_i\tilde{u}_j}\right) + F_i \qquad (2\text{-}8)$$

Since no simple averaging process is available for the random wave-induced components, further simplification of equations is not possible. A different decomposition was given by Benilov and Zaslavskii (1974), but such decomposition complicates the equations and makes comparison with phase-averaging results (see Sec. 2.3.1) impossible.

If it is assumed that the mean flow and the wave-induced motion are two-dimensional, then the time-averaged equations (2-5a, 2-8) become:

continuity:

$$\frac{\partial \bar{u}}{\partial x} + \frac{\partial \bar{v}}{\partial y} = 0 \qquad (2\text{-}9)$$

momentum:

$$\frac{\partial}{\partial x}\left(\bar{u}\,\bar{u}\right) + \frac{\partial}{\partial y}\left(\bar{u}\,\bar{v}\right) = -\frac{1}{\rho}\frac{\partial \bar{p}}{\partial x} + \nu\left(\frac{\partial^2 \bar{u}}{\partial x^2} + \frac{\partial^2 \bar{u}}{\partial y^2}\right) - \frac{\partial}{\partial x}\left(\overline{u'u'}\right)$$

$$- \frac{\partial}{\partial y}\left(\overline{u'v'}\right) - \frac{\partial}{\partial x}\left(\overline{\tilde{u}\,\tilde{u}}\right) - \frac{\partial}{\partial y}\left(\overline{\tilde{u}\,\tilde{v}}\right) \qquad (2\text{-}10)$$

$$\frac{\partial}{\partial x}\left(\bar{v}\,\bar{u}\right) + \frac{\partial}{\partial y}\left(\bar{v}\,\bar{v}\right) = -\frac{1}{\rho}\frac{\partial \bar{p}}{\partial y} + \nu\left(\frac{\partial^2 \bar{v}}{\partial x^2} + \frac{\partial^2 \bar{v}}{\partial y^2}\right) - \frac{\partial}{\partial x}\left(\overline{v'u'}\right)$$

$$- \frac{\partial}{\partial y}\left(\overline{v'v'}\right) - \frac{\partial}{\partial x}\left(\overline{\tilde{v}\,\tilde{u}}\right) - \frac{\partial}{\partial y}\left(\overline{\tilde{v}\,\tilde{v}}\right) - g \qquad (2\text{-}11)$$

2.2.4 Boundary Conditions

The no-slip boundary condition applies at the channel floor:

$$u_i = 0 \quad \text{at} \quad y = -H$$

where H is the water depth. A similar condition also applies at the

air-water interface provided no (or negligible) wave breaking occurs:

$$u_{i_{air}} = u_{i_{water}} \qquad \text{at} \qquad y = \eta$$

The labels "air" and "water" refer to the respective velocity components on each side of the interface. The no-wave-breaking assumption is valid for this study with the possible exception of some of the high wind-speed cases. Other dynamical conditions to be satisfied at an interface for the general case of a viscous fluid with surface tension are:

1. continuity of the tangential stress as one passes through the interface.
2. discontinuity in the normal stress proportional to the mean curvature of the boundary surface due to surface tension as one passes through the interface.

Mathematical formulation of these conditions can be found in Wehausen and Laitone (1960).

2.3 CASE II: WIND-RUFFLED MECHANICALLY GENERATED WAVE IN EULERIAN FRAME

2.3.1 Phase Average

One can decompose each flow variable into three components in a manner similar to that used for the wind-wave case:

$$f(\underline{x},t) = \overline{f}(\underline{x}) + \tilde{f}(\underline{x},t) + f'(\underline{x},t)$$

Again, the time average of f is as defined in Eq. 2-1.

In order to separate out the periodic component $\tilde{f}$, we define a phase average:

$$\langle f(\underline{x},t)\rangle = \lim_{N\to\infty} \frac{1}{N} \sum_{n=0}^{N-1} f(\underline{x},t+n\tau) \qquad (2\text{-}12)$$

where τ is the time period of the imposed periodic excitation. The periodic excitation in this case is the mechanically generated wave,

and τ is the frequency of the wave. Of course, in practice, N is always finite but large.

Because f' is uncorrelated to the periodic excitation over time, the phase average of f contains only the mean and the periodic components, i.e.,

$$\langle f(\underline{x},t)\rangle = \bar{f}(\underline{x}) + \tilde{f}(\underline{x},t)$$

The time average of the phase average is, therefore, equal to the mean, viz.,

$$\overline{\langle f(\underline{x},t)\rangle} = \bar{f}(\underline{x})$$

Thus,

$$\tilde{f}(\underline{x},t) = \langle f(\underline{x},t)\rangle - \bar{f}(\underline{x})$$

$$f'(\underline{x},t) = f(\underline{x},t) - \langle f(\underline{x},t)\rangle$$

The following relations can be developed from the above definitions:

$$\langle f'\rangle = 0 \qquad \langle \tilde{f}g\rangle = \tilde{f}\langle g\rangle$$

$$\overline{\bar{f}g} = \bar{f}\bar{g} \qquad \langle \bar{f}\rangle = \bar{f}$$

$$\tilde{\bar{f}} = 0 \qquad \langle \bar{f}g\rangle = \bar{f}\langle g\rangle$$

$$\bar{f}' = 0 \qquad \overline{\tilde{f}g'} = 0$$

$$\langle \tilde{f}g'\rangle = 0$$

2.3.2 Governing Equations

Equations 2-5a and 2-8 still hold for this case. By use of the definition of phase average, further decomposition of the equations is possible. Taking the phase average of Eq. 2-2 and then substracting Eq. 2-5a gives:

$$\frac{\partial \tilde{u}_i}{\partial x_i} = 0 \quad , \quad \frac{\partial u_i'}{\partial x_i} = 0 \qquad (2\text{-}13a,b)$$

Again, phase averaging Eq. 2-6 produces:

$$\frac{\partial \tilde{u}_i}{\partial t} + \frac{\partial}{\partial x_j}\left(\bar{u}_i\bar{u}_j + \bar{u}_i\tilde{u}_j + \tilde{u}_i\bar{u}_j + \tilde{u}_i\tilde{u}_j + \langle u_i'u_j'\rangle\right)$$

$$= -\frac{1}{\rho}\frac{\partial}{\partial x_i}\left(\bar{p} + \tilde{p}\right) + \nu\frac{\partial^2}{\partial x_j \partial x_j}\left(\bar{u}_i + \tilde{u}_i\right) + F_i \qquad (2\text{-}14)$$

Subtracting Eq. 2-8 from Eq. 2-14 yields:

$$\frac{\partial \tilde{u}_i}{\partial t} + \frac{\partial}{\partial x_j}\left(\bar{u}_i\tilde{u}_j + \tilde{u}_i\bar{u}_j + \widetilde{\tilde{u}_i\tilde{u}_j} + \widetilde{u_i'u_j'}\right) = -\frac{1}{\rho}\frac{\partial \tilde{p}}{\partial x_i} + \nu\frac{\partial^2 \tilde{u}_i}{\partial x_j \partial x_j}$$

or, upon rearrangement,

$$\frac{\partial \tilde{u}_i}{\partial t} + \frac{\partial}{\partial x_j}\left(\bar{u}_i\tilde{u}_j + \tilde{u}_i\bar{u}_j\right) = -\frac{1}{\rho}\frac{\partial \tilde{p}}{\partial x_i} + \nu\frac{\partial^2 \tilde{u}_i}{\partial x_j \partial x_j} - \frac{\partial}{\partial x_j}\left(\widetilde{\tilde{u}_i\tilde{u}_j} + \widetilde{u_i'u_j'}\right) \qquad (2\text{-}15)$$

It is again assumed that the mean and the periodic flow fields are two-dimensional, that is:

$$u_i = (u, v, w) \qquad (2\text{-}16a)$$

$$\bar{u}_i = (\bar{u}, \bar{v}, 0) \qquad (2\text{-}16b)$$

$$\tilde{u}_i = (\tilde{u}, \tilde{v}, 0) \qquad (2\text{-}16c)$$

$$x_i = (x, y, z) \qquad (2\text{-}16d)$$

Using Eq. 2-16, one finds that the time- and phase-averaged continuity and momentum equations become:

$$\frac{\partial \bar{u}}{\partial x} + \frac{\partial \bar{v}}{\partial y} = 0 \qquad (2\text{-}17a)$$

$$\frac{\partial \tilde{u}}{\partial x} + \frac{\partial \tilde{v}}{\partial y} = 0 \qquad (2\text{-}17b)$$

$$\frac{\partial}{\partial x}(\bar{u}\,\bar{u}) + \frac{\partial}{\partial y}(\bar{u}\,\bar{v}) = -\frac{1}{\rho}\frac{\partial \bar{p}}{\partial x} + \nu\left(\frac{\partial^2 \bar{u}}{\partial x^2} + \frac{\partial^2 \bar{u}}{\partial y^2}\right) - \frac{\partial}{\partial x}(\overline{u'u'})$$

$$- \frac{\partial}{\partial y}(\overline{u'v'}) - \frac{\partial}{\partial x}(\overline{\tilde{u}\,\tilde{u}}) - \frac{\partial}{\partial y}(\overline{\tilde{u}\,\tilde{v}}) \qquad (2\text{-}18)$$

$$\frac{\partial}{\partial x}(\bar{v}\,\bar{u}) + \frac{\partial}{\partial y}(\bar{v}\,\bar{v}) = -\frac{1}{\rho}\frac{\partial \bar{p}}{\partial y} + \nu\left(\frac{\partial^2 \bar{v}}{\partial x^2} + \frac{\partial^2 \bar{v}}{\partial y^2}\right) - \frac{\partial}{\partial x}(\overline{v'u'})$$

$$- \frac{\partial}{\partial y}(\overline{v'v'}) - \frac{\partial}{\partial x}(\overline{\tilde{v}\,\tilde{u}}) - \frac{\partial}{\partial y}(\overline{\tilde{v}\,\tilde{v}}) - g \qquad (2\text{-}19)$$

$$\frac{\partial \tilde{u}}{\partial t} + 2\frac{\partial}{\partial x}(\tilde{u}\,\bar{u}) + \frac{\partial}{\partial y}(\bar{u}\,\tilde{v} + \tilde{u}\,\bar{v})$$

$$= -\frac{1}{\rho}\frac{\partial \tilde{p}}{\partial x} + \nu\left(\frac{\partial^2 \tilde{u}}{\partial x^2} + \frac{\partial^2 \tilde{u}}{\partial y^2}\right) - \frac{\partial}{\partial x}(\widetilde{\tilde{u}\,\tilde{u}} + \widetilde{u'u'}) - \frac{\partial}{\partial y}(\widetilde{\tilde{u}\,\tilde{v}} + \widetilde{u'v'}) \qquad (2\text{-}20)$$

$$\frac{\partial \tilde{v}}{\partial t} + \frac{\partial}{\partial x}(\bar{v}\,\tilde{u} + \tilde{v}\,\bar{u}) + 2\frac{\partial}{\partial y}(\bar{v}\,\tilde{v})$$

$$= -\frac{1}{\rho}\frac{\partial \tilde{p}}{\partial y} + \nu\left(\frac{\partial^2 \tilde{v}}{\partial x^2} + \frac{\partial^2 \tilde{v}}{\partial y^2}\right) - \frac{\partial}{\partial x}(\widetilde{\tilde{u}\,\tilde{v}} + \widetilde{u'v'}) - \frac{\partial}{\partial y}(\widetilde{\tilde{v}\,\tilde{v}} + \widetilde{v'v'}) \qquad (2\text{-}21)$$

2.3.3 Boundary Conditions

The boundary conditions stated in 2.2.4 also hold for this case.

2.4 CASE III: WIND-RUFFLED MECHANICALLY GENERATED WAVE IN EULERIAN WAVE-FOLLOWING FRAME

2.4.1 Transformed Coordinate System

The mobile interface poses the biggest challenge to a satisfactory theoretical as well as experimental treatment of the problem. In particular, the random nature of the interface in the wind-wave case makes the problem virtually impossible to solve. However, for the mechanically generated wave cases, some further theoretical development is feasible due to the well-defined periodicity of the main wave. One way

to resolve the interface problem for mechanical-wave cases is to transform the entire problem to a new coordinate system such that both the interface and the lower boundary of the flow are fixed in the new coordinates.

One can transform the Cartesian coordinate system and the flow variables into a new coordinate system such that the velocity components are aligned with the axes of the new curvilinear orthogonal system (Benjamin, 1959; Miles, 1959; Gent and Taylor, 1976). In addition, a pair of constant spatial values in this new coordinate coincide with the channel floor and the interface. This transformation simplifies theoretical analysis, but leads to great difficulties in experimental realization because one needs to constantly align the probe direction with the axes in order to measure the correct velocity components, while at the same time maintaining the probe at a constant spatial location in the transformed system. Therefore, many theoretical works using this type of transformation remain experimentally untested. Another approach is to transform only the coordinate system, but not the flow. That is, the Cartesian flow field is interpreted in a curvilinear coordinate system (Norris and Reynolds, 1975; Hsu et al., 1981). Experimental realizations can be achieved quite easily in this system.

One form of such a coordinate system is given as follows:

$$t = t^* \; ; \qquad x = x^*$$

$$y = y^* + f(y^*)\tilde{\eta} \; ; \qquad z = z^*$$

$$\tilde{\eta} = a \cos(kx^* - \omega t^*)$$

$$f(y^*) = \frac{\sinh(kH + ky^*)}{\sinh(kH)} \tag{2-22}$$

where (x, y, z) denotes spatial points in the Cartesian coordinate system and (x*, y*, z*) denotes spatial points in the new coordinate system. The amplitude of the imposed mechanical wave is a. The transformation between (x, y, z) and (x*, y*, z*) is one-to-one, but non-orthogonal; however, it has the following desirable properties:

$$y^* = 0 \quad \langle = \rangle \quad y = \tilde{\eta}$$

$$y^* = -H \quad \langle = \rangle \quad y = -H$$

Experimental realization of this coordinate system can be achieved by oscillating the probe vertically at a fixed fetch so the probe lies at selected (x*, y*, z*) = constant points. The particular function (Eq. 2-22) is chosen because y* = constant surfaces are streamlines of an inviscid flow below a monochromatic, progressive wavy surface.

2.4.2 Governing Equations in the Transformed Coordinate System

The governing equations in (x, y, z, t) coordinates can be transformed into (x*, y*, z*, t*) coordinates using the chain rule for partial derivatives. This transformation is similar to that of Hsu et al. (1981), but all the higher order terms are retained. Then substituting the decomposition (Eq. 2-4) into the transformed equations and taking time averages, we obtain the two-dimensional mean flow equations in the (x*, y*, z*, t*) coordinates, for example,

continuity:

$$\frac{\partial \bar{u}}{\partial x^*} + \frac{\partial \bar{v}}{\partial y^*}\left[\overline{1\Big/\left(1 + \frac{\partial f}{\partial y^*}\tilde{\eta}\right)}\right] - f\,\overline{\frac{\partial \tilde{\eta}}{\partial x^*}\frac{\partial \tilde{u}}{\partial y^*}} + \overline{\frac{\partial \tilde{v}}{\partial y^*}\Big/\left(1 + \frac{\partial f}{\partial y^*}\tilde{\eta}\right)} = 0 \qquad (2\text{-}23)$$

If the phase averages are taken before the time averages, the difference between the phase- and time-averaged equations yields the wave-

perturbation equations, for example,

continuity:

$$\frac{\partial \tilde{u}}{\partial x^*} - f\frac{\partial \tilde{\eta}}{\partial x^*}\frac{\partial \bar{u}}{\partial y^*} - f\widetilde{\frac{\partial \tilde{\eta}}{\partial x^*}\frac{\partial \tilde{u}}{\partial y^*}} + \widetilde{\left[\frac{\partial(\bar{v} + \tilde{v})}{\partial y^*}\Big/\left(1 + \frac{\partial f}{\partial y^*}\tilde{\eta}\right)\right]} = 0 \qquad (2\text{-}24)$$

Because $y^* = 0$ corresponds to $y = \tilde{\eta}$, so provided $\eta' \ll \tilde{\eta}$, any position (x^*, y^*, z^*) with $y^* < 0$ is always beneath the interface. Thus, these equations are valid for the entire water regime.

2.4.3 Boundary Conditions in the Transformed Coordinate System

In the transformed coordinates, the no-slip boundary conditions become:

$$u_i = 0 \qquad \text{at} \quad y^* = -H$$

and

$$u_{i_{air}} = u_{i_{water}} \qquad \text{at} \quad y^* = 0 \quad \text{provided } \eta' \ll \tilde{\eta}$$

The conditions for the stresses at the interface given in Sec. 2.2.4 are also valid for this case.

2.5 COMPARISON OF THE THEORIES

According to the wave-separation method (Sec. 2.2.2), the surface elevation η is defined to be composed entirely from wave motions and the fluctuating component $\eta' \equiv 0$. For the other two cases (II and III), the deviation of the water surface from the periodic part $\tilde{\eta}$ is the fluctuating component η'. This is the fundamental difference in the definition of wave and fluctuating components for the surface elevation between Case I and Cases II and III. It is possible to use both the phase-averaging and wave-separation methods in Case II. For no wind and low wind-speed cases, $\eta' \ll \tilde{\eta}$, so the results given by the wave-separation method should be good approximations to those obtained by phase averaging.

We believe that the phase-averaging results are more accurate because linearity is not assumed in the separation process. Hence, an error estimate can be made on the wave-separation method by comparing the results given by these two different schemes (see Sec. 3.5.4). Although it can be shown that the theoretical error is small for the linear wave-separation method (see Benilov et al., 1974; Benilov, 1978), an error higher than the theoretical limit is likely due to finite resolution of spectra and numerical integration of the spectra in the wave-separation method.

The main difference between Cases II and III is the coordinate system. In the (x, y, z, t) system, $\tilde{u}(x, y, t)$ and $\tilde{v}(x, y, t)$ are Cartesian velocities that describe actual water motion about the mean velocities $\bar{u}(x, y)$ and $\bar{v}(x, y)$ at fixed x and elevation y. On the other hand, $\tilde{u}(x^*, y^*, t^*)$ and $\tilde{v}(x^*, y^*, t^*)$ are also Cartesian velocities which represent the periodic flow field about the mean velocities $\bar{u}(x^*, y^*)$ and $\bar{v}(x^*, y^*)$ at constant x^* and y^*. Also in Cases I and II, quantities such as $\bar{u}$, $\tilde{u}$, etc., are not well defined in the domain $|y| < |\eta|$. In this region, a given Eulerian space point is sometimes in the air and sometimes beneath the water. However, all statistical quantities are well defined in the transformed coordinate system in Case III for $y^* < 0$, provided $\eta' \ll \tilde{\eta}$.

The time-averaged governing equations are the same for Cases I and II. Then, using the phase average, the periodic flow field can be separated from the mean and turbulent fields in Cases II and III. However, the time-averaged and phase-averaged equations in Case III are quite different from those of Case II. Although many of the terms in the fixed-frame equations can readily be identified in the wave-following

frame equations--this can be seen by comparing Eqs. 2-17a,b with Eqs. 2-23 and 2-24--there are many extra inhomogeneous terms added to the equations in Case III. Hsu et al. (1981) discarded many of these inhomogeneous terms because they are higher-order wave-perturbation quantities and are small compared to the air velocity. In this study, the wave-perturbation quantities are large compared to the mean flow, so the higher-order terms cannot be neglected without further justifications.

CHAPTER 3

EXPERIMENTAL FACILITIES AND INSTRUMENTATION

The experimental facilities and some of the specially designed instruments are described in this section. The results of the qualifying procedures for the instruments are also included here. Special methods or techniques used during data acquisition and reduction are outlined in Secs. 3.4 and 3.5.

3.1 THE WIND, WATER-WAVE CHANNEL

The channel used for the experiments was described in detail by Hsu (1965). This facility has cross-sectional dimensions of 1.93 m high by 0.91 m wide. The overall length is 35 m with a 22-m long glass test section. The cross-sectional area varies by about 1% along the test section. For the current set of experiments, the water depth in the channel was 0.965 m leaving 0.965 m for the vertical depth of the air flow. A schematic view of the facility is shown in Fig. 1.

Situated at the upstream end of the channel is a horizontal-displacement-type mechanical wave-generating plate which is actuated by a hydraulic cylinder. The motion of the hydraulic cylinder is controlled by a closed-loop servo-system. The signal from a function generator, with a frequency resolution of ± 0.05%, forms the input to the servo-system for the generation of a progressive wave train. At the downstream end of the channel is a beach which consists of stainless steel turnings packed in expanded-metal baskets mounted upon a 1 on 5 sloping frame. The reflection coefficient for waves at a frequency of 1 Hz is found to be less than 5% for all the test cases. The reflection

coefficient was expected to be less for wind waves because of smaller amplitude and higher frequency.

Just above and downstream of the beach is a centrifugal, airfoil-bladed fan which draws air through the test section. An air-straightening vane consisting of a 100-mm thick stainless steel honeycomb section prevents the vortex motion created by the fan from extending upstream into the channel test section.

The air inlet is located 4.92 m downstream of the mean position of the wave generating plate, thus allowing the mechanically generated water waves to develop before being acted on by wind. Fiberglass furnace filters are mounted at the entrance to the air inlet to prevent large particles of dust from getting into the channel; a 100-mm thick honeycomb section and fine-meshed screens are also installed at the exit of the air inlet to produce a uniform turbulent velocity profile in the test section. However, there was no transition plate and the basic air inlet conditions were similar to those employed by Hsu (1977) and Chen (1981), except for small differences in the water depth.

3.2 PROBE SUPPORT MECHANISM

A motorized traversing and position indicator (hereafter called the traverse) permitted control of probe location in the vertical and spanwise planes within the wind-wave facility. A detailed description of the traverse is given in a report by Chambers et al. (1970).

The traverse supports an air free-stream temperature probe, a bulk water temperature probe, a pitot-static tube and wave-height gauge(s) (WHG). A typical configuration of the probe setup is shown in Fig. 2.

For the wind-wave experiments, the wave-height gauge was mounted right next to the laser Doppler anemometer (LDA) probe volume. However,

for the mechanically generated wave experiments, the plane of the two wave-height gauges was offset 0.21 m to one side of the channel center line (about midway between the side wall and the center line of the channel), but the sensing wire of the first wave-height gauge remained at the same fetch as the LDA probe volume. The LDA probe volume, the wave-height gauge sensing wire, the pitot-static tube, and the air free-stream temperature probe were at a fetch of 13.0 m from the air-inlet. The bulk water temperature probe was mounted 0.34 m behind the LDA probe volume and 0.35 m below the mean water level surface.

The pitot-static tube was mounted 0.70 m ahead of the main support of the traverse. This distance was the shortest distance ahead of the traverse at which the probes could be mounted and still experience minimal interference effects due to the traverse (Chambers, 1970). For wind-wave experiments, the flow interference effect of the sensing wire and support of the WHG on the water velocity was tested by measuring velocity with and without the gauge next to the LDA probe volume. No noticeable differences were found for the mean and fluctuating velocity components. Indeed, the wire diameter was only 0.15 mm which was much smaller than the length of the LDA probe volume (~ 3 mm), and the support was 150 mm behind the measuring point. However, for mechanically generated waves, the lower support of the WHG frame was found to produce some interference effect on velocity measurements due to the slower decay with depth of the longer wave. Hence, the wave-height gauges were moved off the center line for all the mechanically generated wave cases. The bulk water temperature probe was found to have no influence on velocity measurement for it was quite a distance behind and below the LDA probe volume.

3.3 INSTRUMENTATION AND QUALIFICATION PROCEDURES

3.3.1 Wave Height

Capacitance wave-height gauges were used to measure the water surface elevation. Two gauges were used for all mechanically generated wave cases in order to resolve various components of the water-wave train. However, only one gauge was used for wind-wave runs. Each gauge is constructed with #36 Nylclad insulated copper conductor which is stretched between two ends of a U-shaped frame and connected in parallel to one arm of a Sanborn 958-1100 capacitance bridge amplifier. The gauge (or gauges) was aligned with the wire normal to the mean water level and with half its length immersed in the water. A thorough discussion of the characteristics of the capacitance-wire gauge and its associated electronics was given by Colonell (1966).

The capacitance gauge was calibrated before and after each experiment for the wind wave runs because different gain settings were used for the various flow cases. For the mechanically generated wave cases, the gauges were calibrated before and after a series of experiments. When the probes were cleaned periodically, the change in calibration was found to be less than 0.5% over a period of 2 months.

Static calibration was performed by lowering and raising the probe support mechanism so as to change the immersion depth of the wire. The immersion depths were read off the probe support mechanism (readable to ± 0.25 mm) with the corresponding voltages recorded by the data acquisition system (Sec. 3.3.9).

3.3.2 Air Free-Stream Velocity

The mean air free-stream velocity or the reference wind speed was obtained from the pressure differential of a pitot-static tube. The

pitot-static tube, which has a 3.0 mm diameter, is a Model PAC-12-KL manufactured by United Sensors and Control Corporation.

A Pace differential-pressure transducer (Model P90D) with a full range of ± 21.2 mm of water was used to measure the pressure differential from the pitot-static tube. The Pace transducer was connected as one leg of an inductive bridge of a Sanborn 656-1100 carrier amplifier. The transducer amplifier system was calibrated for several attenuation scales using a Combust Institute micromanometer (with resolution of ± 0.006 mm of fluid of specific gravity 0.82). The calibration curves were checked from time to time during experimental runs and the maximum deviation was 2%.

3.3.3 Temperature

Mean air free-stream temperature and mean bulk water temperature were measured using Victory Engineering 43A38105 bead in glass thermistor probes in conjunction with bridges. Calibration was performed in a Rosemont constant temperature bath; the temperature standard was a Hewlett Packard 2801A quartz thermometer. Parabolas were least-squares fitted to the calibration points with typical standard deviations of ± 0.1°C over a temperature range of 8°C-28°C and a time span of 10 months.

3.3.4 Surface Drift Velocity

The Lagrangian surface drift was determined by measuring the time required for paper punchings to travel a fixed distance (usually 0.5 m or 1.0 m) immediately upstream of the measuring station. To obtain a single value of Lagrangian surface drift for one day's experiment, approximately five measurements were made before the experiment was started and five during the experiment. The mean time of travel for all the trials was computed to obtain the surface drift velocity for the experiment.

For wind-wave experiments, the standard deviations for the mean Lagrangian surface drifts were about 10% for wind speed less than 5 m/s. At higher wind speeds, standard deviations were as large as 13%. This was due mainly to actual fluctuations and timing errors (travel times at the high wind speeds were on the order of two to three seconds).

For mechanically generated wave cases, the main wave-induced periodic motion to the floats and timing errors could possibly be on the order of one second (the period of the main wave). Fortunately, the range of wind speeds used for mechanical wave experiments was low and the percentage error introduced in the float transit timing would not be too high. The standard deviations of the mean Lagrangian surface velocity were found to be about 7% of the mean values.

3.3.5 Distance from the Interface

The LDA probe volume position was read from a dial height gauge (readable to ± 0.01 mm) or from a reference voltage, which is linearly related to the displacement, on the LDA support table. The gauge was zeroed at still-water level by moving the table so that the plane of the blue and the green laser beams of the LDA coincide with the still-water level surface. Some water level change over the course of an experiment was unavoidable. A linear trend with time was assumed and taken into account in establishing the actual probe volume location. In addition, the water set-up due to wind was monitored by four manometers along the channel. The set-up at the measuring location was negligible for wind speeds lower than 6 m/s. For higher wind speeds, depth corrections were necessary due to set-up. The overall accuracy of the corrections was estimated to within ± 0.5 mm.

3.3.6 Water Velocity

Instantaneous values of the horizontal (u) and vertical (v) velocity components were measured with a two-component DISA 55X modular optical laser Doppler anemometer (LDA) system. The system is equipped with Bragg cell frequency shift and is capable of operating in both forward-scatter and backward-scatter modes. Forward-scatter mode was used for all fixed-frame experiments, while backward-scatter mode was used in wave-following experiments.

The laser used for the LDA was a Spectra Physics Model 164-06 argon-ion type. A 600 mm focal length achromatic focusing lens was used, giving half-intersection angles of 2.47° and 2.53° for the LDA beams (see Fig. 3). The beams were oriented such that the plane containing the green and the blue beams was always parallel to the still-water level with the optical axis of the lens perpendicular to the channel sidewall. The forward-scatter optics were normally placed at a 10° angle to the optical axis of the system on the opposite side of the channel. The probe volume in the forward-scatter mode was about 0.15 mm in diameter and 3.0 mm long. The probe volume in the backward-scatter mode was about 0.15 mm in diameter and 3.5 mm long.

Signal processing was accomplished using DISA type 55N20 frequency trackers and DISA type 55L72 range translators. The down shifted Doppler signals from the range translators were band-pass filtered using Krohn-Hite 3100 filters. The signal fed into the trackers was thus enhanced as the level of extraneous noise was reduced. However, care was taken so as not to filter out relevant frequencies. For wind-wave experiments, the filter bandwidth ranged from 40 kHz (centered at the zero velocity frequency) for the lowest wind speed to 140 kHz for the

highest wind speed. During mechanical-wave experiments, the filters were set at bandwidths of 120 kHz.

The linear frequency to voltage relationships of the frequency trackers were found by two point calibrations. This was done periodically during each experiment by using the range translators for known frequencies and recording the output voltages (after the signal conditioning electronics) on the data acquisition system (see Sec. 3.3.9). Hence, we accounted for all the electronic components (filters, amplifiers) in the calibrations. The relationships were linear and drifts were less than ± 0.5 mm/s in each experiment.

Given the frequency, one can compute the velocity from the well-known relationship:

$$u_i = \frac{f_{D_i} \lambda_i}{2 \sin(\theta_i/2)}$$

where

i = blue or green LDA system

f_{D_i} = Doppler frequency of the i-th system

λ_i = laser wavelength of the i-th system

$\theta_i/2$ = half-intersection angle of the i-th system

u_i = velocity component of the i-th system.

The velocity components in the Cartesian coordinate system can be found by combining vectorially the velocity components of the blue and green systems.

In addition to the qualification tests for the scanner-LDA system mentioned in the following section, another qualification test was run to estimate the noise level when the LDA was operated in a simultaneous forward-scatter and backward-scatter mode with the optical scanner

(Sec. 3.3.7). The set-up for the test was similar to that of Cheung and Koseff (1983), except that the scanner was mounted in place and the test flow was generated by the wind-wave facility. The scanning mirror was not moving during this test because the forward-scatter optics was always operated in the fixed-frame mode. However, the back-scattered light was collected through the mirror system. Two wind speeds were used for the test: 0.0 m/s and 4.1 m/s.

The results for the test are listed in Tables 2 and 3. In the cases of the mean and of the peak amplitude of the phase-averaged velocities, the forward-scatter and backward-scatter results differed by about 1 mm/s. This difference is most likely due to small errors in the calibration curves of the trackers. The root-mean-squared (RMS) values were higher for the backward-scatter mode due to a larger probe volume and higher background noise level (see Cheung and Koseff, 1983). If the true RMS values were obtained by cross-correlating the two simultaneous signals, then the noise equivalent RMS velocities are 2-3 mm/s for the backward-scatter mode and 1 mm/s for the forward-scatter mode. A bonus result of this test was the establishment of the stability of the scanner when there was a constant input voltage. The forward-scatter signal did not deteriorate during each run (10 min), indicating that the probe volume stayed within the field of view of the forward-scatter receiving optics (about 0.5 mm at the focal point). Therefore, the scanner is able to hold the probe volume at a fixed point to at least ± 0.5 mm.

3.3.7 Wave Follower

A sketch of the LDA beams steering mechanism is shown in Fig. 4. It consists mainly of a fixed front-surfaced mirror, an optical scanner (General Scanning G-300 PDT) with a front-surfaced mirror, and an

electronic control unit for the scanner (General Scanning CCX-101-T). A close-up picture of the scanner and a perspective view of the LDA-scanner system in relation to the water channel are shown in Figs. 5 and 6.

The angle of rotation of the scanner mirror, and hence the actual position of the LDA probe volume, can be found from the position transducer of the scanner. The probe volume actually traces out an arc rather than a vertical line; however, the maximum scan angle remains small (6.2°). Thus, the arc is an excellent approximation to the assumed vertical motion. Deviation of the scan trajectory from the vertical was 1.5 mm at the most. This distance is of the order of, but less than, the length of the LDA probe volume.

The input to the scanner control unit was a narrowly band-pass-filtered signal from a wave-height gauge situated at the same fetch as the LDA probe volume. The band-pass filter was set at 1.00 Hz with 24 db/octave attenuation slope and the phase lag was zero at 1.00 Hz. A variable attenuator was used to adjust the overall gain of the WHG-scanner system so that the LDA probe volume moved in synchronism with the mechanically generated waves.

Because the laser beams were transmitted through a series of media (air, glass, water), a computer program was written to simulate the actual motion of the beams and to compute the change in intersecting angles among the beams. The effects on the intersecting angles were found to be minimal, and the moving mirror did not induce any Doppler shift to the outgoing or incoming light. A detailed account of the analysis can be found in Appendix B.

Two qualification tests were run to verify the analysis given in Appendix B and to establish the relationship between the position transducer voltage output and the actual distance scanned by the probe volume. In the qualification tests, the wave follower and LDA system were made operational as if they were being used in an actual experiment. However, the driving signal was a 1.00 Hz sine wave from a frequency generator.

In the first qualification test, the probe volume was first made to scan on a piece of graph paper (graduated in mm). The LDA measured the velocities sensed by the probe volume scanning on the graph paper. The LDA laser beams were in the air for this solid-surface scan test. The approximate scan distance was also read from the graph paper (± 0.5 mm). Suppose the position transducer output voltage was $V_{pot} = V_o \cdot \sin 2\pi ft$ which corresponded to some distance $D = kV_o \cdot \sin 2\pi ft = D_o \cdot \sin 2\pi ft$ scanned by the LDA probe volume. Then the LDA measured $\dot{D} = kV_o(2\pi f) \cdot \cos 2\pi ft = 2\pi fD_o \cdot \cos 2\pi ft$. From a data analysis program, $\max\dot{D}$ $(= 2\pi fD_o)$ and V_o were calculated via a cosine fitting procedure (see Appendix C). Since $kV_o = \max\dot{D}/2\pi f$, k can be found.

The second qualification test was done with the probe volume inside the channel and with the laser beams going through the air-glass-water interfaces to test the equations of the model given in Appendix B. Here, the water was assumed to be still as the probe volume oscillated. The constant k established in the first test was 4.269 mm/V and 4.254 mm/V in the second test, the difference being well within experimental uncertainties.

In actual experimental runs, the measured velocity ($\underline{v}_M$) is the velocity of the fluid ($\underline{v}$) relative to the <u>moving</u> probe volume, i.e., $\underline{v}_M = \underline{v} - \underline{\tilde{v}}_{WF}$ where $\underline{\tilde{v}}_{WF}$ represents the wave-follower scan velocity. The

scan velocity $\tilde{y}_{WF}$ can be found by differentiating the scanner position voltage and then multiplying the result by the constant k. Next, the scanning test data were reanalyzed with velocity correction so that the actual Eulerian velocity (y) could be found. Obviously in these tests, the Eulerian velocity was identically zero and all the averages should vanish. Thus, this exercise told us how good the velocity compensation scheme was; furthermore, any non-zero averages would indicate the noise level and the limits of the wave-following LDA system in measuring turbulent quantities.

For the solid surface scan test, the mean u and v were at most 1 mm/s (see Table 4). The mean velocities were slightly larger for the scan test inside the channel (Table 5); this probably was due to some small non-zero mean velocities in such a large body of water, i.e., the water was not truly "still." The phase-average results for u and v, after compensation of the vertical velocity, were found to be at most ± 1 mm/s for $\tilde{u}$ and ± 2 mm/s for $\tilde{v}$; typical figures were about ± 0.5 mm/s or less for both tests. Other "turbulent" quantities are also shown in Tables 4 and 5. Note that the "turbulent" quantities have the same numerical values either with or without vertical correction because of the sinusoidal driving signal. In the second test (Table 5), the noise equivalent values for the mean velocities and the phase-averaged velocities were of the order of 1 to 2 mm/s, about 2 to 5 mm/s for the root-mean-square turbulent quantities, and about 2 to 20 $(mm/s)^2$ for the turbulent stresses. The noise level was higher when the wave-follower scan amplitude (max D) exceeded 22 mm (see Table 5) because the laser beams were near the point where they failed to intersect inside the channel. In actual experiments, the scan amplitude was always less than 22 mm.

Therefore, the wave-following LDA system was shown to be capable of measuring mean and turbulent quantities in the test facility.

The system transfer function of the optical scanner and its control electronics was found by monitoring the input and output voltages. The phase lag of the optical scanner system at 1.00 Hz was found to be essentially zero (less than 0.5°).

In the light of the above, the two constants used in reducing data from the experiments reported in Sec. 4.3 were:

1) scan distance versus position output voltage: 4.254 mm/V; and

2) scan distance versus input voltage: 129.7 mm/V at 1.00 Hz.

3.3.8 Signal Conditioning Electronics

The low-level analog outputs of the wave-height gauge(s) and Pace crystal transducer for the pitot-static tube were amplified by Hewlett Packard 2470B data amplifiers at gains of twenty. This was done to minimize quantization errors inherent to any analog-to-digital data acquisition system.

The LDA tracker outputs, the wave-height gauge output(s), the Pace crystal transducer output, and the position output of the optical scanner were low-pass filtered at 40 Hz (-3db point) by third-order Butterworth anti-aliasing active filters. The maximum phase difference among different channels of the filters was found to be less than one degree over the 0 to 40 Hz frequency range. Therefore, the phase characteristics were virtually identical among all the filter channels. This property is crucial in comparing phases among different signals from the filters. Small adjustments in the gains of the filters were made to allow use of the full dynamic range of the data acquisition system.

3.3.9 Data Acquisition/Reduction System

The data acquisition system consists of four major components: a minicomputer (Hewlett Packard 2100A), a digital magnetic tape drive (Hewlett Packard 7970B), a hard disc drive (Hewlett Packard 7900), and an analog-to-digital subsystem (a modified Hewlett Packard 2313 with simultaneous sample-and-hold capability on 32 analog input channels). The analog voltages from the instruments were sampled and digitized by the analog-to-digital subsystem, and then recorded on digital magnetic tapes for future analysis. Each analog input has a dynamic range of ± 10.230 V and a resolution of ± 5 mV. This system was documented by Takeuchi and Mogel (1975).

Data reduction was performed on a Hewlett Packard 1000 Model 45 computer system. In addition to the fast F-series computer, the system has full graphics capability and a library of data reduction programs tailored to the experiments.

3.4 DATA ACQUISITION PROCEDURES AND TECHNIQUES

A flow chart depicting signal paths is shown in Fig. 7. The chart is for the case of wind-ruffled mechanically generated waves with Eulerian wave-following. The second wave-height gauge, the wave-follower, and the sine wave reference signal were not present for the wind-wave case. Also, the wave-follower was not used for the mechanical-wave fixed-frame experiments.

The sampling frequency was 100 Hz for the wind-wave case and 200 Hz for the others. A higher sampling rate was used for mechanical-wave runs to give better resolution of the main wave in phase averages. The sampling period for each data point was kept at 10.24 minutes despite the difference in sampling rate. For mechanical-wave cases, this record

length was sufficient to resolve the anticipated lowest frequency component and accommodate more than 614 periods of the 1 Hz generated wave. A longer time record would be desirable for a few experiments as indicated by Howe et al. (1978). However, the 10.24-minute record length was chosen as a compromise which allowed a vertical profile to be completed in a reasonable time, thereby minimizing the effects of changes in ambient and bulk-water conditions.

The channel was filled with tap water at least three days before each set of experiments to allow time for de-aeration. Chemical treatment of the water to prevent algae growth was unnecessary. Little or no seeding of the water was needed for the LDA in fixed-frame experiments where forward-scatter mode was used. However, it was essential to seed the water with titanium dioxide to obtain sufficient numbers of good Doppler bursts in wave-following runs where the backward-scatter mode was used.

There are 17 experiments which comprise the three main cases in this study. The general experimental conditions for each experiment are tabulated in Table 1. The typical sequence of steps taken for each experiment is as follows:

1. The LDA probe volume was adjusted to coincide with the initial still water level; this was the initial depth reference level. Manometer levels were also recorded under the no-wind condition.
2. The fan was turned on and the desired wind speed set. After the wind speed reached a steady state, the manometer levels were recorded to note the water set-up. The fan was left on overnight (about 16 hr between successive experiments) to assure that the air and water flow were in equilibrium.

3.* The wave plate was turned on at least an hour before the first data run to ensure full development of the water and air wave fields. The wave generator was set to produce a wave amplitude of about 22 mm and a frequency of 1.00 Hz.

4. The manometer levels were recorded just prior to the first run to find the initial water loss.

5. The LDA table was lowered for the first data point. The LDA probe volume was brought as close to the interface as possible, without letting it leave the water.

6. The data acquisition program was activated and all necessary in line calibrations were made, such as for the trackers and the pressure transducer.

7.† The scanning amplitude was adjusted by varying the calibrated attenuator of the scanner control unit so that the LDA probe volume followed the transformed coordinate system ($y^* = \text{constant}$).

8. The computer was instructed to commence the data taking routine.

9. The LDA table was lowered for the next point and Steps 7 through 9 were repeated until sufficient number of data points (at about 20 depths) were obtained.

10. Once again, the manometer levels were recorded to estimate the final water loss.

11. The fan was turned off and when quiescence was reached, the manometer levels were recorded to give a second estimate of the total water loss.

---

*For mechanically generated wave cases only.

†For Eulerian wave-following case only.

12. Water was added to the channel if necessary and the whole procedure was repeated for the next wind speed.

3.5 DATA REDUCTION PROCEDURES

In this section, the data reduction procedures for each of the three sets of experiments in this study are discussed. Then in Sec. 3.5.4, a comparison between the wave-separation and phase-averaging methods is given.

3.5.1 Wind-Generated Wave Case

The wave-separation method (Sec. 2.2.2) was used to deduce the means and second moments of all quantities of interest. Three major steps were necessary in analyzing the data, viz.,

1. The time mean for each channel of data in an experiment was calculated and the results stored in a disc file.
2. The wave-separation program was run to find the wave-induced and turbulent quantities. The results were stored in a disc file.
3. The mean, wave, and turbulence data files were combined to form a summary file for an experiment.

The autospectra and cross-spectra among the velocity components (u, v) and the water surface elevation (η) were tabulated as well as plotted in Step 2. However, the spectra were not stored on disc due to the large amount of disc space needed.

3.5.2 Mechanical-Wave Eulerian Frame Case

As indicated in Sec. 2.5, it is possible to analyze this case using the wave-separation method and the phase-averaging scheme. The wave-separation method used was identical to that of the wind-wave case. The steps involved for the phase-averaging data analysis procedure are as follows:

1. The time mean for each channel of data was calculated.
2. The wave period of the reference wave-height signal was found by counting the number of sampled points between two successive zero crossings with positive slope.
3. The phase averages were calculated as defined by Eq. 2-12.
4. The mean turbulent stresses ($\overline{u_i' u_j'}$), mean wave-induced stresses ($\overline{\tilde{u}_i \tilde{u}_j}$), and other wave related quantities ($\widetilde{u_i' u_j'}$) were calculated.
5. The amplitude and phase of $\tilde{u}$, $\tilde{v}$, $\widetilde{u_i' u_j'}$, and $\tilde{\eta}$ were found by the cross-spectral method and by the cosine-fitting techniques (see Appendices A and C).
6. The mean, phase-averaged, and turbulence data were stored in a disc data file.

3.5.3 Mechanical-Wave Wave-Following Eulerian Frame Case

The time- and phase-averaging data reduction procedures in Sec. 3.5.2 were also used for this case. However, the vertical velocity measured has to be corrected because of the motion of the wave-follower. The time derivative of the wave-follower position output voltage is related to the vertical velocity component measured by the LDA. A central differencing scheme was used to differentiate this voltage. The result was converted into a velocity by use of the constants given in Sec. 3.3.7. Therefore, the actual vertical velocity is given by

$$v = v_M + \tilde{v}_{WF}$$

where v_M and $\tilde{v}_{WF}$ are the measured and the wave-follower scan velocities, respectively. Because the driving signal of the wave-follower was band-pass filtered and periodic with zero mean, $v'_{WF} = \bar{v}_{WF} = 0$.

Other quantities of interest were found using the same procedures as used for the fixed-frame case (Sec. 3.5.2).

3.5.4 A Quantitative Comparison Between the Wave-Separation and Phase-Averaging Methods

As noted earlier in Sec. 2.5, it is possible to use both the wave-separation and phase-averaging methods in analyzing mechanical-wave fixed-frame measurements. Because for no-wind and low-wind-speed cases, $\eta' << \tilde{\eta}$, the results obtained by the wave-separation method should be good approximations to those given via the phase-averaging process.

Two experiments were run with the following objectives:

1. to show that phase averaging is a better method in analyzing mechanical wave data, and
2. to infer from (1) the errors made by the wave-separation method in reducing wind-wave data.

The experiments were performed at zero wind speed and under mechanically generated waves. A short vertical velocity profile was taken in each experiment. The sampling rate was 200 Hz for the first experiment and 100 Hz (i.e. the same as that used in wind-wave experiments) for the second one. Because there was no wind and the waves were essentially irrotational, except for the very thin Stokes boundary layers along the channel sides and at the interface due to viscous effects, all the turbulent quantities should be very small for both test cases.

The results of the experiments are presented in Table 6. For the first experiment, it is clear that the turbulent quantities obtained by the phase-averaging method are more credible than those given by the wave-separation scheme. The turbulent quantities are very small, which is representative for the test flow, and are within the uncertainty intervals of the LDA. The wave-separation method gives a much higher

turbulence level; however, the separation-method wave quantities are in excellent agreement with the phase-averaging results.

The high turbulence level given by the wave-separation method can be explained as follows. The mean square wave quantities, such as $\overline{\tilde{u}^2}$, are computed by integrating the spectra (Appendix A). Next, the mean square turbulent component is obtained by subtracting the mean square wave component from the total mean square value, i.e. $\overline{u'^2} = \overline{u^2} - \overline{\tilde{u}^2}$. Because the total mean square value is the sum of the wave and turbulent parts, errors introduced in computing $\overline{\tilde{u}^2}$, say by numerical integration, lead to errors in $\overline{u'^2}$. If we assume the "true" results are those given by the phase-averaging method, for example the first data point in Table 6, we have for phase averaging: $\overline{\tilde{u}^2}/\overline{u^2} \simeq 0.99$, $\overline{u'^2}/\overline{u^2} \simeq 0.01$ and for wave separation: $\overline{\tilde{u}^2}/\overline{u^2} \simeq 0.96$, $\overline{u'^2}/\overline{u^2} \simeq 0.04$. This means that the wave-separation method has a 4% error in computing $\overline{\tilde{u}^2}$, hence in $\overline{u'^2}$ also. Although this is a very small <u>percentage</u> error in terms of mean square values, the percentage error in root mean square values is much larger: $(\overline{u'^2})^{1/2}/(\overline{u^2})^{1/2} \simeq 20\%$! This is the reason for the seemingly high turbulence level in the wave-separation scheme. So, based on the results of this test, the phase-averaging process is shown to be the better method.

As pointed out earlier, the phase-averaging scheme cannot be used for wind-wave experiments. However, as shown above, the wave-separation method can introduce seemingly large errors in the calculation of turbulent quantities. Therefore, it is necessary to establish some error bounds on the data obtained by this method.

A second experiment was run and analyzed with all the sampling parameters identical to those for the wind-wave experiments. The

following results are obtained, i) phase-averaging: $\max(\overline{\tilde{u}^2}/\overline{u^2}) \approx 0.99$, $\max(\overline{u'^2}/\overline{u^2}) \approx 0.01$ and ii) wave separation: $\max(\overline{\tilde{u}^2}/\overline{u^2}) \approx 0.98$, $\max(\overline{u'^2}/\overline{u^2}) \approx 0.02$. So the error is reduced for the wave-separation method; furthermore, the percentage error in terms of the root mean square value is at most 13%. The improvement is due mainly to a lower sampling rate that results in a narrower signal bandwidth. Also note that the turbulent quantities given by the phase-averaging method are slightly higher than those in the first experiment. This is due to a coarser resolution of the main wave when it is sampled at a lower frequency. The result is a larger phase jitter which leads to a higher turbulence level. Although the test was for mechanically generated waves, we believe that the percentage error in root mean square values (about 13%) is also applicable for wind-wave experiments. This error bound is assumed and used in subsequent sections for wind-wave data.

3.6 UNCERTAINTY ESTIMATES

The N^{th}-order uncertainty intervals as defined by Moffat (1981) were estimated for all important variables. The N^{th}-order uncertainty of a measured quantity is an estimate of its absolute accuracy and includes instrument calibration uncertainty as well as the effects of unsteadiness and interpolation. The use of such uncertainty estimates is essential for reporting results and assessing the significance of differences among results from different experiments.

Table 7 contains the estimated uncertainties. They were calculated by using the procedure described by Kline and McClintock (1953). As indicated, many of the estimates are dependent upon actual flow conditions.

Table 2

Simultaneous Forward-Scatter Backward-Scatter Runs
(Tracker Range 333 kHz, u_∞ = 0.0 m/s)

$\hat{u}_B$ (BS) (mm/s)	$\hat{u}_B$ (FS) (mm/s)	$\overline{u}_B$ (BS) (mm/s)	$\overline{u}_B$ (FS) (mm/s)	$\sqrt{\overline{u'^2_B}}$ (BS) (mm/s)	$\sqrt{\overline{u'^2_B}}$ (FS) (mm/s)	$\sqrt{\overline{u'^2_B}}$ (CC) (mm/s)
92.0	93.3	-1.31	-2.27	5.78	3.63	3.12
83.2	84.9	-1.62	-2.85	6.02	2.60	1.73
75.3	76.5	-2.05	-3.20	5.16	2.72	1.91
68.2	69.1	-1.90	-2.79	3.92	2.52	1.68
56.4	57.7	-0.89	-2.24	5.07	2.24	1.11
50.5	51.3	-0.75	-1.80	4.04	2.32	1.31
43.7	44.6	-0.38	-1.46	4.08	2.08	0.81
35.3	36.0	0.69	-1.12	3.72	2.11	0.86

Notation: BS, backward-scatter mode; FS, forward-scatter mode; CC, cross-correlated. The subscript "B" denotes the LDA blue channel.

Table 3

Simultaneous Forward-Scatter Backward-Scatter Runs
(Tracker Range 333 kHz, u_∞ = 4.1 m/s)

$\hat{u}_B$ (BS) (mm/s)	$\hat{u}_B$ (FS) (mm/s)	$\overline{u}_B$ (BS) (mm/s)	$\overline{u}_B$ (FS) (mm/s)	$\sqrt{\overline{u'^2_B}}$ (BS) (mm/s)	$\sqrt{\overline{u'^2_B}}$ (FS) (mm/s)	$\sqrt{\overline{u'^2_B}}$ (CC) (mm/s)
89.6	90.6	3.23	2.70	6.30	5.57	5.21
81.1	81.9	1.86	1.02	5.86	4.75	4.37
74.5	75.1	-0.48	-1.29	5.16	4.14	3.72
67.1	68.3	1.52	-1.02	6.39	4.08	3.58
57.4	59.8	0.66	-1.46	8.38	3.74	3.21
52.1	52.9	-0.68	-1.65	4.83	3.29	2.68
44.5	45.5	0.02	-1.15	5.49	3.18	3.17
36.6	37.1	-0.69	-1.50	4.50	3.01	2.40

Notation: BS, backward-scatter mode; FS, forward-scatter mode; CC, cross-correlated. The subscript "B" denotes the LDA blue channel.

Table 4

Scanner Test on Solid Surface
(Tracker Range 100 kHz, Without Vertical Velocity Correction)

$\hat{u}$ (mm/s)	$\hat{v}$ (mm/s)	$\overline{u}$ (mm/s)	$\overline{v}$ (mm/s)	max D (mm)	$\frac{\text{max D}}{\text{max } V_{pot}}$ (mm/V)	$\overline{(u'^2)}^{1/2}$ (mm/s)	$\overline{(v'^2)}^{1/2}$ (mm/s)	$\overline{u'v'}$ $(mm/s)^2$	$\frac{\text{max D}}{\text{max } V_{in}}$ (mm/V)
0.4	136.8	-0.50	-0.34	21.61	4.266	1.01	6.76	0.437	130.10
0.3	137.2	-0.47	-1.07	21.68	4.271	0.96	1.82	0.765	130.29
0.4	137.2	-0.44	-0.91	21.68	4.272	1.01	2.31	0.789	130.29
0.3	137.2	-0.41	-0.34	21.67	4.270	1.01	1.96	0.873	130.23
0.2	137.1	-0.41	-0.77	21.66	4.269	1.10	3.59	0.968	130.25
0.1	137.1	-0.42	-0.96	21.66	4.268	0.98	1.89	0.803	130.17
0.0	137.1	-0.38	-0.70	21.66	4.270	1.03	3.62	0.852	130.25

Note: f is equal to 1.000 ± 0.005 Hz.

Table 5

Scanner Test Inside Channel
(Tracker Range 100 kHz, u_∞ = 0.0, Without Vertical Velocity Correction)

$\hat{u}$ (mm/s)	$\hat{v}$ (mm/s)	$\overline{u}$ (mm/s)	$\overline{v}$ (mm/s)	max D (mm)	$\frac{\text{max D}}{\text{max } V_{pot}}$ (mm/V)	$\overline{(u'^2)}^{1/2}$ (mm/s)	$\overline{(v'^2)}^{1/2}$ (mm/s)	$\overline{u'v'}$ $(mm/s)^2$	$\frac{\text{max D}}{\text{max } V_{in}}$ (mm/V)
0.6	133.6	1.69	-1.02	21.41	4.258	1.86	2.36	1.987	129.84
0.5	133.6	1.62	-0.78	21.41	4.258	1.57	2.16	1.476	129.76
0.5	133.6	1.33	-0.80	21.41	4.257	2.02	2.43	2.594	129.76
1.2	147.2	0.59	-1.41	23.59	4.253	3.71	4.88	12.450	129.76
0.9	147.1	0.90	-1.10	23.57	4.254	3.43	6.53	8.858	129.72
1.6	146.9	0.46	-1.30	23.54	4.243	4.48	4.98	18.020	129.41
0.9	137.7	0.67	-0.52	22.06	4.254	2.84	5.55	6.276	129.76

Table 6

Comparison of Wave-Separation (Method 1) and Phase-Averaging (Method 2) Methods

(mm/s)	Method 1		Method 2		(mm/s)	Method 1		Method 2	
$\sqrt{u^2}$	$\sqrt{\tilde{u}^2}$	$\sqrt{u'^2}$	$\sqrt{\tilde{u}^2}$	$\sqrt{u'^2}$	$\sqrt{v^2}$	$\sqrt{\tilde{v}^2}$	$\sqrt{v'^2}$	$\sqrt{\tilde{v}^2}$	$\sqrt{v'^2}$
Experiment 1 (f_{sample} = 200 Hz)									
73.3	72.0	13.4	73.3	1.7	77.8	76.2	15.7	77.7	1.7
68.2	67.2	11.6	68.0	2.6	72.3	70.8	14.6	72.3	2.6
64.3	63.4	10.8	64.5	1.4	68.1	66.7	13.6	67.9	1.6
60.0	59.2	9.9	59.8	1.8	63.5	62.3	12.7	63.6	1.9
56.4	55.6	9.1	56.4	1.4	59.8	58.6	11.8	59.7	1.5
52.2	51.6	8.2	52.3	1.6	55.3	54.2	10.9	55.1	1.6
47.9	47.4	7.4	47.9	1.4	50.7	49.7	10.0	50.7	1.6
44.0	43.5	6.6	44.0	1.3	46.4	45.5	9.2	46.4	1.4
40.1	39.6	5.9	40.0	1.6	42.3	41.5	8.3	42.4	1.8
35.6	35.3	5.2	35.5	1.0	37.5	36.7	7.3	37.5	1.1
32.1	31.8	4.6	32.0	1.0	33.6	33.0	6.6	33.6	1.1
29.0	28.7	4.2	29.0	1.0	30.2	29.6	5.9	30.2	1.1
26.3	26.0	3.8	26.2	1.2	27.4	26.9	5.4	27.4	1.2
23.4	23.1	3.4	23.3	1.1	24.2	23.8	4.8	24.2	1.1
Experiment 2 (f_{sample} = 100 Hz)									
73.7	73.0	9.9	73.5	3.4	77.7	77.2	8.9	77.8	3.3
69.3	68.8	8.1	69.2	6.3	73.8	73.3	8.7	73.5	6.6
66.5	66.0	7.4	66.6	2.9	70.3	69.8	8.4	70.0	3.1
63.2	62.8	6.9	63.2	2.9	65.0	64.5	7.9	64.8	3.3
59.8	59.4	6.6	59.5	3.2	61.0	60.6	7.5	61.1	3.5
55.6	55.3	5.9	55.4	2.5	58.6	58.2	7.2	58.7	2.6
52.2	51.9	5.3	52.3	3.0	55.2	54.8	6.9	54.9	3.3
48.4	48.4	4.6	48.3	2.5	51.3	51.0	6.1	51.2	2.8
47.6	47.3	5.6	47.4	3.4	54.0	53.5	7.1	54.0	3.9
35.5	35.4	3.1	35.4	2.0	37.0	36.7	4.8	37.0	2.1
33.3	33.2	2.7	33.2	1.4	34.7	34.4	4.4	34.7	1.6
30.7	30.6	2.5	30.7	1.1	32.1	31.8	4.1	32.1	1.2
28.3	28.2	2.3	28.3	1.6	29.4	29.2	3.7	29.4	1.7
26.0	25.9	2.2	26.1	1.0	27.1	36.8	3.4	26.9	1.2
24.2	24.1	2.1	24.2	2.0	25.0	24.8	3.2	24.8	2.2
22.3	22.2	1.9	22.1	1.1	23.0	22.8	3.0	23.1	1.3
20.7	20.6	1.7	20.6	0.9	21.3	21.1	3.0	21.3	1.3
19.0	19.0	1.7	19.1	1.0	19.6	19.4	2.6	19.4	1.1
17.9	17.8	2.0	17.8	1.5	18.3	18.2	2.5	18.4	1.4

Table 7

N^{th}-Order Uncertainty Estimates at 20:1 Odds

Quantity	Typical Uncertainty
$\bar{u}_S$	10%
$\bar{u}$, $\bar{v}$	2% or ± 0.6 mm/s 100 kHz Tracking Range ± 2.0 mm/s 333 kHz Tracking Range
$(\overline{u'^2})^{1/2}$, $(\overline{v'^2})^{1/2}$	13% of total RMS value
$(\overline{\tilde{u}^2})^{1/2}$, $(\overline{\tilde{v}^2})^{1/2}$	2% of total RMS value
$-\overline{u'v'}$	20% in fixed-frame experiments 30% in wave-following frame experiments
$-\overline{\tilde{u}\,\tilde{v}}$	10% in fixed-frame experiments 20% in wave-following frame experiments
$\hat{u}$, $\hat{v}$	2%
$\theta_{\tilde{u}}$, $\theta_{\tilde{v}}$	1°
$\hat{r}_{ij}$	20%
$\theta_{\tilde{r}_{ij}}$	20°
η, $\tilde{\eta}$	2% or ± 0.3 mm
T_∞	0.5% or ± 0.1°C
T_{Bulk}	0.5% or ± 0.1°C
u_∞	2-6%, 3% at 6 m/s
y	± 0.5 mm
δ	10%
u_*	10%

CHAPTER 4

EXPERIMENTAL RESULTS

As stated in Chap. 2, the present study consists of three sets of experiments:

1. wind-wave in Eulerian frame;
2. wind-ruffled mechanically generated wave in Eulerian frame; and
3. wind-ruffled mechanically generated wave in wave-following Eulerian frame.

The results for all three cases are given in the following sections. These results include the mean, wave-induced, and turbulent velocity quantities presented in terms of various dimensional and non-dimensional parameters. The general trends and special behaviors that follow naturally from the data are indicated as they occur. However, a discussion of the implications of these results is withheld and presented in Chap. 5 after all the results are shown here.

4.1 WIND WAVE IN EULERIAN FRAME

4.1.1 Water Surface Conditions

The water surface varied from smooth to rough in the literal sense for the range of reference wind speeds used in this set of experiments. Time traces of typical water surface conditions are shown in Fig. 8. Each trace is four seconds in duration. These time traces represent the water surface elevation at a point as the waves pass by the wave-height gauge.

For the lowest wind-speed case (1.5 m/s), no visible gravity wave was present; however, small capillary-type perturbations were observed during the runs. The wave-height gauge is unable to detect such small

disturbances (< 0.2 mm). Tiny wavelets were present for the 2.6 m/s case, but the water surface remained relatively smooth. At higher wind speeds, the waves were clearly visible. The wave amplitude and the wave slope increase with increasing wind speed. Small wave breaking was observed when the wind speed was greater than 6.7 m/s as indicated by the pointedness of the wave crests and small discontinuities in the wave-height-gauge signal.

Another parameter which is often used in describing the surface conditions is the root-mean-square (RMS) wave amplitude $(\overline{\eta^2})^{1/2}$. This quantity is plotted versus wind speed in Fig. 9. The RMS η is less than 0.2 mm for the two lowest wind speeds, but increases almost linearly at higher wind speeds.

The dominant frequency of the wind-generated waves decreases with increasing wind speed. This gradual shift of dominant wave frequency with wind speed can be seen from the time traces. All the measured wave-height power spectra (not shown here) showed a local maximum at a frequency close to twice the peak frequency. These results are consistent with the findings of Sutherland (1968), Plate et al. (1969), and Chambers et al. (1970).

4.1.2 Surface Drift Velocity

The surface drift velocity measured by timing the paper punchings is a Lagrangian velocity. It is necessary to convert this Lagrangian velocity to a Eulerian velocity in order to use it with the LDA measurements, which are Eulerian. A relation between the Lagrangian velocity $\underline{u}_L(\underline{x}, t)$ and the Eulerian velocity $\underline{u}(\underline{x}, t)$ induced by water waves, correct to the second order of inviscid water-wave theory, is given by (see Phillips, 1977):

$$\underline{u}_L(\underline{x}, t) = \underline{u}(\underline{x}, t) + \left(\int_o^t \underline{u}(\underline{x}, t')dt'\right)\cdot\nabla\underline{u}(\underline{x}, t)$$

$$= \underline{u}(\underline{x}, t) + \underline{u}_{Stokes}(\underline{x}, t)$$

The second term on the right-hand side of the above equation is equivalent to the Stokes mass transport velocity. Assuming a linear theory, this term can be approximated from a one-dimensional surface elevation spectrum ($S_{\eta\eta}(f)$) and is (see Bye, 1967):

$$\bar{u}_{Stokes} = \int_o^{f_c} \frac{2(2\pi f)^3}{g} S_{\eta\eta}(f)df \qquad (4\text{-}1)$$

where f_c, taken to be 10 Hz here, is the upper frequency limit of gravity waves. Therefore, the mean Eulerian surface drift velocity ($\bar{u}_S$) at the location of the wave-height gauge is:

$$\bar{u}_S = \bar{u}_{SL} - \bar{u}_{Stokes}$$

where $\bar{u}_{SL}$ is the mean Lagrangian surface drift velocity.

The variation in the mean Eulerian and Lagrangian surface drift velocities with wind speed is shown in Fig. 10. The Eulerian surface drift velocity is found to be about 2% of the free stream velocity. If no correction to the Lagrangian velocity is made, then the Lagrangian surface drift velocity is about 3% of the free-stream wind speed. These results are consistent with the findings of other investigators (Wu, 1968; Phillips and Banner, 1974).

4.1.3 Mean Velocity Profiles

Mean velocity profiles are shown in Fig 11. The velocity defect $\bar{u}_S - \bar{u}$ is plotted instead of the mean velocity $\bar{u}$ so that the profiles may resemble those for flows over a solid surface. This allows comparison with other well-established data sets, such as those for flows over smooth or rough plates. Full profiles were not taken because the main

goal of this study is to investigate the surface and near-surface flow phenomena. The maximum depth for velocity measurements is in the vicinity of 300 mm or roughly one third of the total water depth.

It is evident that presence of the moving waveforms makes it difficult to approach close enough to the surface with the LDA to observe the behavior of mean velocity profiles near the interface. For high wind-speed cases, the measuring point closest to the surface is of the order of 10 to 20 mm from the mean water level. The general trend of the profiles is similar to flows over solid surfaces. However, there are differences especially when the profiles are plotted in law-of-the-wall coordinates.

In Fig. 12, mean velocity profiles are shown in wall coordinates, where $u^+ = (\overline{u}_S - \overline{u})/u_*$ and $y^+ = yu_*/\nu_w$. The flow was turbulent, as defined by Tennekes and Lumley (1972), even at the lowest wind speed. The friction velocity u_* is determined by a linear least-squares fit (with depth) of the direct measurements of the turbulent shear stress ($-\overline{u'v'}$) and extrapolation of the trend line to the interface. A detailed account of the turbulent shear stresses is given in Sec. 4.1.4. Also plotted in the figure are the universal law of the wall (Schlichting, 1979) for a turbulent flow with zero pressure gradient over smooth walls:

$$u^+ = \frac{1}{\kappa} \ln(-y^+) + 5.5 \qquad (4\text{-}2)$$

and that for the rough walls:

$$u^+ = \frac{1}{\kappa} \ln(-y^+) - 2.1 \qquad (4\text{-}3)$$

where κ (= 0.4) is the von Karman constant. In wall coordinates, the velocity profile for the lowest wind speed clusters around the smooth

wall relationship and as wind speed increases, the usual shift associated with the apparent increase in surface roughness occurs. For wind speeds higher than 3.2 m/s, all the profiles lie below the relationship representing the start of the fully rough flow regime. All the profiles exhibit logarithmic behavior. The profiles for wind speeds less than 3.3 m/s have slopes close to 2.5 (= $1/\kappa$). However, for higher wind speeds, the profiles have a slope smaller than 2.5. Such seemingly anomalous behavior is also reported by Howe et al. (1982).

The mean vertical velocity profiles are shown in Fig. 13. The scales of this plot are the same as those used for the horizontal velocity defect profiles for easy comparison. The actual data are tabulated in Appendix D. For all wind speeds, with the exception of the highest, the mean vertical velocity profiles fall within a band of ± 3 mm/s about zero. At the highest wind speed, the mean vertical velocity is about zero near the surface and increases with depth. However, the mean vertical velocity is very much smaller than the mean horizontal velocity defect for all runs. Furthermore, the mean vertical velocity gradient (with depth) is very close to zero near and away from the interface.

4.1.4 Mean Turbulent Quantities

The turbulent shear stress ($-\overline{u'v'}$) profiles for all the wind-wave experiments are shown in non-dimensional forms in Fig. 14. The u_*^2 values are obtained by a linear least-squares fit with depth of the direct measurements of the shear stress and extrapolation of the trend line to the interface. The depth is normalized by the depth [Delta(δ)] at which the turbulent shear stress vanishes. The Deltas are determined from the same least-squares-fit lines used in deducing u_*^2; that is, Delta is the depth at which the line meets the y-axis. This definition

of Delta has the equivalent physical meaning of a boundary-layer thickness for the turbulent boundary layer (Goossens et al., 1982).

Relatively large amounts of data scatter are present for low speed runs or at depths where the turbulent shear stress is expected to be very small. This is due to the small magnitude of the shear stress (of the order of 10^{-6} m^2/s^2) which approaches the resolution limit of the LDA system ($\simeq 10^{-6}$ m^2/s^2). However, data scatter is very much reduced for higher wind-speed runs where the linear behavior of the turbulent shear stress profiles is obvious.

A decrease of the shear stress near the surface can be seen for the two low speed runs as well as some higher wind-speed flows. However, the measurements were made in a fixed frame. Thus, the shear stress values obtained near the interface were averaged over points which were very close to the surface (near the wave trough) and points which were some distance away from the instantaneous water surface (under the wave peak). Accordingly, it is unwise to conclude that such a decrease in the turbulent shear stress is physical and not due to kinematics of the waves.

On the other hand, the two low wind-speed experiments are fairly close to the smooth flow regime as indicated by the mean profiles in wall coordinates. Then, the decrease of turbulent shear stress near the surface is due to the existence of a viscous sublayer. Another piece of evidence for the existence of the viscous sublayer is that the velocity profiles adhere close to the $u^+ = -y^+$ line for these two low wind-speed cases.

The friction velocities (u_*) are plotted versus wind speed (u_∞) in Fig. 15. The friction velocity grows almost linearly with wind speed

for $u_\infty < 5$ m/s and more rapidly at higher wind speeds. This result agrees with that of Howe et al. (1981, 1982). The corresponding turbulent boundary-layer thickness δ can be found in Appendix D. Delta is about 140 mm for the lowest wind speed and stays relatively constant around 300 mm for higher wind speeds where waves are present.

The root-mean-square (RMS) velocity fluctuation $[\overline{(u'^2)}^{1/2}, \overline{(v'^2)}^{1/2}]$ profiles are plotted in non-dimensional forms in Figs. 16 and 17. The RMS u' profiles for <u>all</u> wind speeds collapse within a narrow band when normalized by u_* and δ. The RMS v' profiles for wind speeds higher than 3 m/s also coalesce into a band when normalized by the same parameters. Clearly, u_* and δ are the appropriate velocity and length scales relating turbulent velocity fluctuations and turbulence decay with depth.

Also plotted in the same figures are the data of Klebanoff (1955) for a turbulent boundary layer with zero pressure gradient. The RMS u' profiles follow this reference data reasonably well, but generally lie above it. The RMS v' profiles also group around the reference data except for the lower wind-speed experiments. It is clear that there is anisotropy between RMS u' and v' within the boundary layer. In addition, the degree of anisotropy increases towards the interface. However, it is unclear whether this trend continues into the inner part of the boundary layer due to extreme difficulty in obtaining data above the wave trough in a fixed frame. On the other hand, turbulent fluctuations decrease and become more isotropic near the edge of the boundary layer.

The RMS v' in normalized units for wind speeds between 1.5-3.2 m/s does not seem to fall into the general trend of the data. In this wind speed range, the non-dimensional RMS v' increases with increasing wind speed, but lies below the main sequence of the rest of the data.

4.1.5 Mean Wave-Induced Quantities

Figure 18 shows the mean wave-induced shear stress ($-\overline{\tilde{u}\,\tilde{v}}$) profiles. The normalization parameters are the same as those used for the turbulent shear stress profiles, thus allowing direct comparison between the two components of the total shear stress. The wave-induced shear stress is negative very close to the interface and decays very rapidly with depth. One can define a penetration depth for the wave-induced shear stress as the depth at which the wave-induced shear stress vanishes. Then, the penetration depth of the wave-induced shear stress increases with wind speed but is at most equal to 0.2δ for the highest wind speed and is considerably less for lower wind-speed experiments. The wave-induced shear stress is of the order of u_*^2 near the surface and is a larger percentage of the total shear stress within that region. However, the turbulent shear stress seems to be the dominant component over most parts of the boundary layer.

The RMS wave-induced velocity profiles [$(\overline{\tilde{u}^2})^{1/2}$, $(\overline{\tilde{v}^2})^{1/2}$] are shown in Figs. 19 and 20. The normalizing parameters are the RMS surface orbital velocity $(\overline{\tilde{u}_o^2})^{1/2}$ computed from the wave-height signal and the wave-decay depth y_η. First, $\overline{\tilde{u}_o^2}$ is given by:

$$\overline{\tilde{u}_o^2} = \int_0^{f_c} (2\pi f)^2 S_{\eta\eta}(f)\,df \qquad (4\text{-}4)$$

where $S_{\eta\eta}(f)$ is the one-sided power spectrum of the wave-height signal and f_c (= 10 Hz) is the upper frequency limit for gravity waves. Next, y_η is the depth at which the integrated-surface orbital amplitude decays by a factor of e^{-1} (Howe et al., 1982); hence, y_η satisfies the following relationship:

$$\frac{\int_0^{f_c} S_{\eta\eta}(f)\, \exp[-2(2\pi f)^2 y_\eta/g]\,df}{\int_0^{f_c} S_{\eta\eta}(f)\,df} = e^{-2} \qquad (4\text{-}5)$$

Here, y_η is used instead of some other length scale, such as the dominant wavelength, because y_η takes into account the amplitude and frequency distribution of the entire wind-generated surface spectrum. In fact, the definition of y_η is equivalent to the reciprocal of an integrated wave number.

The data collapse is excellent using these parameters. Some of the data scatter is partly due to the logarithmic scale which accentuates the distance for $y/y_\eta < 1$. The normalized $(\overline{\tilde{u}^2})^{1/2}$ and $(\overline{\tilde{v}^2})^{1/2}$ decrease only slightly with increasing wind speed but exponentially with depth. However, the vertical component is always larger than the horizontal component at the same depth. The profiles for the two lowest wind-speed cases are not plotted because waves were not present or were insignificant. Therefore, neither $\overline{\tilde{u}_o^2}$ nor y_η could be computed.

When the RMS wave-induced velocity profiles are normalized by the u_* and δ as shown in Figs. 21 and 22, the profiles do not collapse into a band. However, the figures enable us to make a direct comparison between the RMS wave-induced velocity components and the RMS turbulent velocity components. At the lowest wind speed there are essentially no wave-induced fluctuations, so RMS $\tilde{u}$ < RMS u' and RMS $\tilde{v}$ < RMS v'. At u_∞ = 2.6 m/s, the RMS $\tilde{u}$ is smaller than the RMS u', but in the region $-y/\delta < 0.03$, the RMS $\tilde{v}$ is larger than the RMS v'.

At u_∞ = 3.2 m/s, the RMS $\tilde{u}$ is of the same order of magnitude as the RMS u'. For $-y/\delta > 0.02$, the RMS u' becomes the dominant component as the RMS $\tilde{u}$ decays rapidly with depth. Furthermore, the ratio of RMS $\tilde{v}$

to RMS v' is about five-to-one at $-y/\delta \approx 0.01$ and the ratio decreases to unity at $-y/\delta \approx 0.06$, then the RMS v' starts to dominate.

For u_∞ values greater than 3.2 m/s, the maximum RMS $\tilde{u}$ exceeds the maximum RMS u' by a factor of approximately 2, while the maximum RMS $\tilde{v}$ exceeds the maximum RMS v' by a factor of about 3. Of course, as $-y/\delta$ increases, the wave-induced quantities decrease more rapidly than the turbulent quantities.

4.2 MECHANICAL WAVE IN EULERIAN FRAME

4.2.1 Water Surface Conditions

A one-hertz, sinusoidal, mechanically generated motion was used as the basic propagating wave train. The actual measured amplitude of the one-hertz wave component is tabulated in Table 1; the amplitude is about 22 mm for the mechanical-wave experiments. Time traces of the wave-height-gauge signal for the five different wind speeds are shown in Fig. 23; each trace is of a two-second duration.

At zero wind speed, there are no ripples on the water surface, and the wave has a slightly longer trough than the peak. This is due to a slight nonlinearity of the small, but finite, amplitude mechanically generated waves ($ka \lesssim 0.09$). At $u_\infty = 1.7$ m/s, the waveform is slightly distorted from a pure sinusoid, but the water surface is still relatively smooth. The slightly clipped wave peak is due to meniscus effect of the wave-height-gauge wire and is not indicative of the actual wave shape. Small wavelets or ripples can be seen riding on the dominant wave at $u_\infty = 2.5$ m/s. The ripples grow in size and steepness with increasing u_∞ as can be seen from the time traces for higher wind-speed runs.

Since phase averaging is used in analyzing this set of data, the surface elevation η can be decomposed as:

$$\eta = \tilde{\eta} + \eta' \quad \text{and} \quad \overline{\eta} \equiv 0$$

The random component or the ripple η' is the deviation of the instantaneous water surface from the imposed periodic wave field $\tilde{\eta}$. An indicator of the surface "roughness" on the periodic wave surface is given by $(\overline{\eta'^2})^{1/2}$. The variation of $(\overline{\eta'^2})^{1/2}$ with wind speed u_∞ is plotted in Fig. 24. It is evident that $(\overline{\eta'^2})^{1/2}$ grows directly with u_∞ in this wind speed range. The non-zero value of $(\overline{\eta'^2})^{1/2}$ at $u_\infty = 0.0$ m/s represents the noise level of the wave-height gauge.

The reflection coefficient of the traveling wave train was evaluated from the signals of the two wave-height gauges. The details of the method can be found in Papadimitrakis (1982). The reflection coefficient varies slightly with wind speed, but is always less than 5%, which agrees with the results of Bole and Hsu (1967).

4.2.2 Surface Drift Velocity

The mean Lagrangian and Eulerian surface drift velocities versus wind speed are plotted in Fig. 25. The mean drift velocities, both Lagrangian and Eulerian, for this set of experiments are consistently lower than those for wind-wave runs at equivalent wind speeds. As mentioned in Sec. 3.3.4, the timing error can be as much as one second in this case, but this alone cannot account for such consistent results. It is believed that the mechanical wave provides some sheltering effects from the wind along the wave trough, thus leading to a lower mean drift velocity.

4.2.3 Mean Velocity Profiles

The mean velocity defect $(\overline{u}_s - \overline{u})$ profiles are shown in Fig. 26. Since the mechanically generated wave has an amplitude of about 22 mm, the closest measuring point is at least 22 mm from the mean water level. The velocity defect increases with wind speed. At each wind speed, the

defect increases with depth, except for the zero wind-speed case. The mean Lagrangian surface drift velocity measured for the zero wind-speed case is very close to zero, but the computed mean Stokes surface drift is not. Therefore, the mean Eulerian surface drift velocity is negative. It follows, for this case, that the mean velocity $\bar{u}$ is negative near the surface and goes to zero deeper down. Thus, the velocity defect decreases with depth.

The velocity defect profiles in wall coordinates are plotted in Fig. 27. The definitions for u^+ and y^+ are given in Sec. 4.1.3 and the same technique was used to deduce u_*. All the profiles are logarithmic and cluster very close to each other. There is a slight downward shift of the profile with increasing wind speed. Near the interface (small $-y^+$), there is substantial deviation from the logarithmic trend for the two lowest wind-speed experiments.

The well-known relationships for smooth and rough wall flows are also shown in Fig. 27 for comparison. The profiles lie across the rough wall flow regime and have gentler slopes than the reference lines. Furthermore, the slopes of the profiles are about the same as those in the high-wind-speed wind-wave experiments.

The mean vertical velocity profiles are plotted in Fig. 28. For the two low wind-speed experiments, the mean v are within ± 2 mm/s about zero, this increases to ± 6 mm/s at higher wind speeds. Therefore, the mean vertical velocity gradient with depth is very much smaller than the mean horizontal velocity gradient.

4.2.4 Mean Turbulent Quantities

The mean turbulent shear stress ($-\overline{u'v'}$) profiles for all wind speeds other than zero are shown in Fig. 29. The friction velocity u_* and the

turbulent boundary-layer thickness δ are found using the same procedure outlined in Sec. 4.1.4. Since u_* and δ cannot be defined for the zero wind-speed case, this data is not plotted, but is tabulated in Appendix D. The LDA frequency trackers were set at a wider tracking range for higher wind-speed experiments (2.5-6.2 m/s) resulting in a three-fold increase in the uncertainty interval for the mean turbulent shear stress. In addition, there is about -5.0×10^{-6} m^2/s^2 bias in the mean turbulent shear stress values. This small bias is insignificant for wind speeds at 4.1 and 6.2 m/s. However, it is significant for the intermediate wind speed at 2.5 m/s. The u_* for this particular case was found by two different methods. The first method was a direct interpolation of the least-squares-fit line through the origin from Fig. 30. The second method was by taking out the bias from the measured values before using the usual linear least-squares procedure. The u_* values obtained by these two methods agree. Accordingly, δ was found from the second method. No correction was necessary for any other data; the actual measured values are summarized in Appendix D for reference.

When $u_\infty = 0.0$, the measured mean turbulent shear stress is at the noise level and is essentially zero throughout. At higher wind speeds, the linear distribution of the mean turbulent shear stress with depth is apparent. Contrary to the wind-wave results, there is more data scatter for higher wind-speed runs. The increase in data scatter at higher wind speed is partially due to a wider tracking range. Also, at high wind speeds, the distortion of the instantaneous wave shape from the periodic component such as $\tilde{u}$, $\tilde{v}$, and $\tilde{\eta}$ is greater. Given the large amplitude of the periodic component, a very small error in the phase-averaging process can lead to a relatively large error in the mean turbulent shear

stress. All in all, the mean turbulent shear stress profiles are believed to be representative for such flow fields.

The RMS u' and RMS v' profiles are presented in Figs. 31 and 32 using the same scales as those for wind-wave runs. These quantities behave very differently from the wind-wave case. The normalized RMS u' and v' have a value of unity for $-y/\delta > 1$, then increase rapidly toward the interface. Also shown in the figures are the data of Klebanoff (1955). The RMS u' and v' deviate radically from these reference data. In addition, there is no anisotropy between RMS u' and v'. The data collapse for various wind speeds is good. Therefore, in this set of experiments, u_* and δ remain the prominent parameters for the turbulent part of the flow field.

4.2.5 Mean Wave-Induced Quantities

The mean wave-induced shear stress ($-\overline{\tilde{u}\,\tilde{v}}$) profiles are shown in Fig. 33. Similar to the wind-wave experiments, the mean wave-induced shear stress is negative. At $u_\infty = 1.7$ m/s, the magnitude of the mean induced shear stress is about 30 times that of the mean turbulent shear stress ($-\overline{u'v'}$) near the interface, then decreases to about 15 times that value at the edge of the turbulent boundary layer ($-y = \delta$). For $u_\infty = 2.5$ m/s, this ratio is about 15 near the surface and decreases to about 10 at a depth of δ. When the wind speed was 4.1 m/s, the ratio is about 9 near the interface and decays to 3 at δ. At the highest wind speed, this ratio is 7 near the surface and diminishes to almost zero at $-y = \delta$. Therefore, even at the highest wind speed, the mean wave-induced shear stress remains the dominant component in the total mean shear stress within the region δ where turbulence is active.

Let k be the wave number of a 1-Hz monochromatic deep-water wave. If 1/k is used as the normalizing depth, then the mean wave-induced stress decays to about zero at $-ky = 1$ as shown in Fig. 34. In physical units (mm^2/s^2), as tabulated in Appendix D, the mean wave-induced shear stress profiles remain relatively unchanged for $u_\infty = 0.0$ and 1.7 m/s. There is a slight increase in the shear stress value at 2.5 m/s and it has a slightly slower rate of decay. Then at $u_\infty = 4.1$ m/s, there is a significant increase in the mean wave-induced shear stress deeper in the water than the lower wind-speed runs. At the highest wind speed, the mean wave-induced shear stress values are almost twice as those at $u_\infty = 4.1$ m/s. So in physical units, there is a definite increase in mean wave-induced shear stress with wind speed.

The RMS wave-induced or periodic velocity components $[(\overline{\tilde{u}^2})^{1/2}, (\overline{\tilde{v}^2})^{1/2}]$ are plotted in Figs. 35 and 36 with depth normalized on 1/k. The normalizing velocity scale is the theoretical RMS orbital velocity given by the 1-Hz component of the water wave train, namely, $2\pi f_D \hat{\eta}_S/\sqrt{2}$, where $f_D = 1$ Hz and $\hat{\eta}_S$ is the mean amplitude of the 1-Hz component of the water wave spectra. The $1/\sqrt{2}$ factor converts the peak velocity into an RMS velocity. Then, using this velocity scale and 1/k as the length scale, the normalized RMS $\tilde{u}$ and $\tilde{v}$ profiles collapse into a very narrow band. The data collapse is excellent for -ky greater than 0.3. At lower -ky values, i.e., closer to the surface, both the normalized RMS $\tilde{u}$ and $\tilde{v}$ seem to decrease slightly with increasing wind speed. In addition, the RMS $\tilde{u}$ is always less than the RMS $\tilde{v}$ at each wind speed.

The velocity scale used here is different from that used in the wind-wave case $[(\overline{\tilde{u}_o^2})^{1/2}]$. If $(\overline{\tilde{u}_o^2})^{1/2}$ is used as the normalizing parameter, the RMS $\tilde{u}$ and $\tilde{v}$ profiles do not collapse into a band, because the

definition of the wave or periodic velocity component is different for each case. In the phase-averaging process, only the 1-Hz component and its bound harmonics of the signal for u, v, η, etc. are included in the wave or periodic part. On the other hand, the random ripples riding on the main wave are included in the calculation of $(\overline{\tilde{u}_o^2})^{1/2}$, which, therefore, has a larger value than $2\pi f_D \hat{\eta}_S/\sqrt{2}$. The difference between these two velocity scales increases with wind speed because more ripples are generated at high wind speeds which lead to a higher $(\overline{\tilde{u}_o^2})^{1/2}$ while $\hat{\eta}_S$ remains relatively constant for all wind speeds. Since the random ripples are effectively filtered out by phase averaging, $(\overline{\tilde{u}_o^2})^{1/2}$ is not the proper velocity scale for normalizing quantities obtained via phase averaging, viz. RMS $\tilde{u}$ and $\tilde{v}$.

Once again, when the RMS $\tilde{u}$ and $\tilde{v}$ profiles are normalized by u_* and δ, the profiles do not coalesce into a band as presented in Figs. 37 and 38. In the figures, the data bands representing the normalized RMS u' and v' profiles are indicated by the dashed lines. The RMS $\tilde{u}$ is almost an order of magnitude bigger than RMS u' at u_∞ = 1.7 m/s. At u_∞ = 2.5 m/s, the ratio of RMS $\tilde{u}$ to RMS u' decreases to about 6. Then at u_∞ = 4.1 m/s and 6.2 m/s, the ratios become 4 and 2, respectively. The ratios of RMS $\tilde{v}$ to RMS v' are slightly higher than those for the horizontal component because RMS $\tilde{v}$ is always bigger than RMS $\tilde{u}$. It is quite apparent that the RMS $\tilde{u}$ and $\tilde{v}$ dominate over the whole region even though the RMS u' and v' become more significant at high wind speeds.

4.2.6 Wave Perturbation Velocities

The wave perturbation velocities $\tilde{u}$ and $\tilde{v}$ were found by the phase-averaging technique. A typical result for $\tilde{u}$ and $\tilde{v}$ is shown in Fig. 39. Also shown in the figure is the phase average for the water surface

elevation in the same run. It is clear that the periodic velocities are nearly sinusoidal with the same frequency as that of the progressive water waves. The amplitudes ($\hat{u}$, $\hat{v}$) and the phase angles ($\theta_{\tilde{u}}$, $\theta_{\tilde{v}}$), with respect to $\tilde{\eta}$, of the first harmonic of the periodic velocities were obtained by spectral analysis. This technique is fully documented in Hsu et al. (1977). The total harmonic content of the phase average velocity, in terms of energy is given by:

$$\text{mean square total harmonic content} = \left(\overline{\tilde{u}_i^2} - \frac{|\hat{u}_i|^2}{2}\right) \Big/ \overline{\tilde{u}_i^2}$$

$$= 1 - \frac{|\hat{u}_i|^2}{2\overline{\tilde{u}_i^2}}$$

where $i = 1$ or 2. The total harmonic energy content for $\tilde{u}$ and $\tilde{v}$ at each depth in an experiment are tabulated in Appendix D. The $\tilde{u}$ usually has more harmonic components than $\tilde{v}$ near the surface but the difference decreases with depth until the harmonic content becomes almost identical for both $\tilde{u}$ and $\tilde{v}$. For the worst case, the total harmonic energy content for $\tilde{u}$ or $\tilde{v}$ is at most 2.6%. Therefore, it is sufficient to present the amplitude and the phase of the periodic velocity at the excitation frequency. Although the full results for $\tilde{u}$ and $\tilde{v}$ at each data point were graphed, they are too numerous to present here. Readers are referred to a separate report and files on 800 BPI magnetic tapes available at the Stanford University Environmental Fluid Mechanics Laboratory.

The plots of the amplitudes ($\hat{u}$, $\hat{v}$) and the phase lags ($\theta_{\tilde{u}}$, $\theta_{\tilde{v}}$), relative to $\tilde{\eta}$, versus -ky are given in Fig. 40. The amplitudes are normalized by the theoretical peak orbital velocity given by the 1-Hz component of the water wave train, namely $2\pi f_D \hat{\eta}_S$. Both the $\hat{u}$ and $\hat{v}$ profiles show exponential decay with depth. Also, the $\hat{u}$ is always

smaller than $\hat{v}$ for this set of experiments. In the proximity of the interface, there is a slight decrease in $\hat{u}$ and $\hat{v}$ with increasing wind speed. This decrease is most prominent by comparing profiles for u_∞ = 1.7 m/s and u_∞ = 2.5 m/s. Some of these trends are also found in plots of $(\overline{\tilde{u}^2})^{1/2}$ and $(\overline{\tilde{v}^2})^{1/2}$ versus -ky, but they do not give any phase relationships. The numerical values for the phase lags ($\theta_{\tilde{u}}$, $\theta_{\tilde{v}}$) can be found in Appendix D. The following observations on the phase lags can be made irrespective of wind speeds and depth:

1. The phase lag of $\hat{u}$ with respect to the phase of $\hat{\eta}_S$ is very close to 0 but not exactly so. The phase lag varies most between -3° and +2° about 0 for all data points.
2. The phase difference, $\theta_{\tilde{u}} - \theta_{\tilde{v}}$, is always slightly less than 90°. Specifically, the phase difference remains relatively constant at about 89° except at u_∞ = 6.2 m/s where the phase difference decreases to about 86°.

The velocity amplitudes and their respective phases were also found by the cosine curve-fitting techniques (see Appendix C). The spectral and cosine-fitting methods gave virtually identical results: the amplitude values agreed to within ± 0.5% and ± 0.1° for the phase angles. So the cosine-fitting technique verified the results of the spectral method.

4.2.7 Wave-Induced Stresses

The wave-induced turbulent stresses are defined as $\tilde{r}_{ij} = \widetilde{u_i' u_j'}$ and were obtained by the phase-averaging method. In general, the magnitudes of $\tilde{r}_{ij}$ are very small, so the signal-to-noise ratio is much lower than that of $\tilde{u}$ or $\tilde{v}$. The phase-averaged results were used to calculate the amplitudes $\hat{r}_{ij}$ and the phase angles $\theta_{\tilde{r}_{ij}}$ at the excitation frequency. There could be substantial harmonic content in $\tilde{r}_{ij}$, but only $\hat{r}_{ij}$ and

$\theta_{\tilde{r}_{ij}}$ are considered here. The numerical values for $\tilde{r}_{ij}$ are stored on 800 BPI magnetic tapes and all the plots are collected in a separate report.

The $\hat{r}_{ij}$ and $\theta_{\tilde{r}_{ij}}$ values are given in Appendix D. They are also plotted in Fig. 41. The amplitudes are normalized by the square of the friction velocity in these plots. Because the friction velocity is not defined in the zero wind-speed experiment, its results are not shown. At each depth, the $\hat{r}_{11}$ and $\hat{r}_{22}$ are approximately equal in magnitude regardless of wind speeds. Furthermore, they decrease quickly with depth. For wind speeds less than 3 m/s, the normalized amplitudes drop to the background noise level for -ky greater than 0.2. At higher wind speeds, this number increases to 0.3. On the other hand, $\hat{r}_{12}$ is much smaller than either $\hat{r}_{11}$ or $\hat{r}_{22}$ and remains near the noise level for practically all wind speeds and depths.

The phase lags $\theta_{\tilde{r}_{ij}}$ stay very close to 180° in experiments with wind speeds less than 4 m/s. At u_∞ = 4.1 m/s, there is a fair amount of data scatter, but the overall trend of the phase angles stay in the neighborhood of 180°. At the highest wind speed, the phase lags do not have any trend with depth. The apparent data scatter at high wind speeds may be due to the large amount of harmonics present, thus making it difficult to determine the phase lags at the first harmonic.

The wave-induced wave stresses are defined as $\widetilde{\tilde{u}_i\tilde{u}_j}$. They can be found by multiplying $\tilde{u}_i$ and $\tilde{u}_j$ over the period of the main wave and removing the mean wave-induced shear stresses $\overline{\tilde{u}_i\tilde{u}_j}$ from the products. It is shown in Sec. 4.2.6 that $\tilde{u}_i$ is almost sinusoidal, so we can characterize $\tilde{u}_i$ as follows:

$$\tilde{u}_i = \hat{u}_i \cos(\omega t - \theta_i) + \text{harmonics}$$

Therefore, $\tilde{u}_i\tilde{u}_j$ becomes,

$$\tilde{u}_i\tilde{u}_j = \frac{\hat{u}_i\hat{u}_j}{2}[\cos(2\omega t - \theta_i - \theta_j) + \cos(\theta_i - \theta_j)] + \text{harmonics} \qquad (4\text{-}6)$$

Then $\widetilde{\tilde{u}_i\tilde{u}_j}$ is just simply the time-varying part of Eq. 4-6. It is obvious that $\widetilde{\tilde{u}_i\tilde{u}_j}$ has a dominant frequency twice that of the excitation frequency and has an amplitude of $\hat{u}_i\hat{u}_j/2$. The harmonic content of $\tilde{u}_i$ is very small, consequently the harmonic content of $\widetilde{\tilde{u}_i\tilde{u}_j}$ relative to the dominant frequency is also negligible. For this set of experiments, $\hat{u}_i\hat{u}_j/2$ is very much larger than $\hat{r}_{ij}$. The implication of this can only be resolved by further analysis of the effects of measurements made in a non-wave-following coordinate system and the governing equations (see Chap. 5).

4.3 MECHANICAL WAVE IN WAVE-FOLLOWING EULERIAN FRAME

4.3.1 Water Surface Conditions

A one-hertz, sinusoidal, mechanically generated wave was also used in this set of experiments. The measured amplitudes of the one-hertz wave components are given in Table 1. Time traces of the wave-height-gauge signal under different wind speeds are shown in Fig. 42, with each trace being two seconds in duration. The variation of surface "roughness" $(\overline{\eta'^2})^{1/2}$ with wind speed u_∞ is plotted in Fig. 43. The wind speeds, wave shapes, and reflection coefficients of the traveling wave train are virtually identical to those of the fixed-frame mechanical-wave experiments.

4.3.2 Surface Drift Velocity

The mean Lagrangian and Eulerian surface drift velocities versus wind speeds are shown in Fig. 44. The results agree with those for the

fixed-frame mechanical-wave case; thus, the remarks made for those experiments are applicable here also.

4.3.3 Mean Velocity Profiles

Under the proposed coordinate transform (Sec. 2.4.1), the depth is now $-y^*$ instead of $-y$. However, the mean position of the LDA probe volume when observed in the laboratory frame is $\overline{y^*} = y$. Then, as noted in Sec. 2.5, the interpretation of the measured quantities in the wave-following frame is different from that of the fixed frame.

The mean velocity defect ($\overline{u}_s - \overline{u}$) profiles are presented in Fig. 45, showing that the mean velocity defect increases with wind speed. Similar to the fixed-frame, mechanical-wave experiments, the computed mean Eulerian surface drift velocity and the measured mean velocity are negative at zero wind speed. Most importantly, we see that the wave-following system enables measurements very close to the wavy surface. For low wind-speed runs, where the ripples on the one-hertz dominant wave were small, it was possible to reach a y^* of -1 to -2 mm. Even at the highest wind speed, where $(\overline{\eta'^2})^{1/2}$ was about 2 mm, the probe was still able to make measurements at $y^* = -5.6$ mm.

It is important to stress that, although the measured velocity is in a wave-following frame, the velocities are still Eulerian quantities. Therefore, the mean Eulerian surface drift is used in computing the mean velocity defect. Of course, the measured mean Eulerian surface drift is perfect for use in this wave-following coordinate system since the velocity was obtained by measuring the mean Lagrangian surface drift exactly at $y^* = 0$, and then removing the mean Stokes surface drift.

The mean velocity defect profiles in wall coordinates are shown in Figs. 46 and 47. Each figure uses a different set of u_* values. The u_*'s obtained from the fixed-frame experiments are used for normalization in Fig. 46. The u_*'s obtained by stress continuity at the interface from the experiments of Hsu et al. (1983) are used in Fig. 47. A discussion of the validity of using either of these u_* values is given in the next section.

In Fig. 46, the two low wind-speed profiles lie close together and fall between the smooth-wall and rough-wall data lines with a strong bias towards the latter line. Near the interface, the profiles follow the $u^+ = -y^{*+}$ line. Then, the profiles become logarithmic for $-y^{*+}$ greater than 20. For the two high wind-speed cases, the profiles also cluster together, but lie below those for the lower speed runs, as well as below the data line representing the fully rough flow regime on solid walls. Furthermore, the profiles exhibit logarithmic trends for $-y^{*+}$ greater than 50.

Results similar to the above are observed in Fig. 47 where a different set of u_* was used in normalization. The two low-speed mean velocity defect profiles now lie almost totally between the smooth and fully rough flow regime. However, the two high wind-speed profiles remain relatively unchanged.

The mean vertical velocity profiles are shown in Fig. 48. The mean velocity lies within $\pm$ 5 mm/s about zero for wind speeds from 0 to 4.1 m/s. At the highest wind speed, the mean vertical velocity is positive and is about 2 to 9 mm/s for the whole profile. Again, the mean vertical velocity gradient (with depth $-y^*$) is small compared to the mean horizontal velocity gradient.

4.3.4 Mean Turbulent Quantities

Due to data scatter, well-defined friction velocities (u_*) cannot be found from the measured mean turbulent shear stress via the usual curve-fitting method as used in the two previous sets of experiments. However, good estimates of u_* can be obtained by the following methods:

Method 1. For the two low wind-speed experiments, the first point ($y^* \sim 0$) of the velocity profile may lie in the viscous sublayer where the velocity gradient is linear. Then, the friction velocity can be estimated as:

$$u^+ = -y^{*+}$$

$$\frac{\bar{u}_s - \bar{u}}{u_*} = \frac{-y^* u_*}{\nu}$$

$$u_*^2 = \nu \left. \frac{\bar{u}_s - \bar{u}}{-y^*} \right|_{\text{1st data point}}$$

The u_* values estimated by this method for the two low-speed runs are given in Table 8.

Method 2. Hsu et al. (1983) found friction velocities on the air side in a transformed coordinate system under similar experimental conditions. Utilizing the u_* values for the air flow and assuming stress continuity across the interface, we can find the interpolated or extrapolated friction velocities for the water flow given in Table 8.

Method 3. The u_* values obtained in the mechanical-wave fixed-frame experiment may be good estimates for the u_* values in a transformed coordinate system and these are also given in Table 8 for comparison.

It can be seen from Table 8 that for the two low wind-speed runs, there is little difference between the u_*'s obtained by Methods 1 and

3. Although the u_*'s given by Method 2 are lower than those by Method 3, especially for the lowest wind-speed run, they are of comparable magnitude. The low u_* value for Method 2 at 1.7 m/s may be due to the curve-fitting procedure used by Hsu et al. (1977). As pointed out by Papadimitrakis (1982), the u_* values can vary as much as 10% by using different fitting methods, and each method is very sensitive to the fitting region. At higher wind speeds, Method 1 is not applicable because of large random ripples present on the main wave. Method 2 now yields higher u_* values than Method 3. If the difference is truly significant and not a result of uncertainty, then the difference might be attributed to the fact that a portion of the momentum from the wind goes into wave growth, thus, less shear stress is measured in the water.

The friction velocities given by the mechanical-wave, fixed-frame experiments are likely to be the best estimates for u_* for the present case also. Therefore, they are used throughout for all mechanical-wave experiments unless stated otherwise. In any case, it is true that none of the interpretations of the data set are changed significantly by the estimates for u_*.

For completeness, the measured mean turbulent shear stresses in the transformed coordinate system are tabulated in Appendix D. They are also shown in normalized form in Fig. 49. At zero wind speed, the mean turbulent shear stress is very small and is of the order of 5.0×10^{-6} m^2/s^2, which is very close to the resolution limit of the LDA. There is quite a bit of data scatter as can be seen in Fig. 49. In addition, the normalized mean turbulent shear stress does not go to one near the interface but is about 15 for $u_\infty = 1.7$ m/s, 5 for $u_\infty = 2.5$ and 4.1 m/s, and roughly unity at $u_\infty = 6.1$ m/s. This result suggests

the shear stress may vary over the main wave with possibly a minimum at the wave trough.

The RMS u' and v' are normalized by the wave parameters and shown in Figs. 50 and 51. The wave parameters are used here because they have less uncertainty. The RMS u' and v' both increase with wind speed and decrease with depth. There is little anisotropy, except at the two higher wind speeds where the RMS v' is slightly higher near the interface and lower than RMS u' away from the surface. Furthermore, there is no data collapse because the wave number k and the RMS orbital velocity at the surface are not the appropriate scales for turbulent processes.

Since the mechanical-wave fixed-frame u_*'s are used in this case, the corresponding turbulent boundary-layer thicknesses (δ) may also be suitable length scales to use. Figures 52 and 53 show the RMS u' and v' normalized by u_* and δ. Data collapse is fair, thus implying that u_* and δ may also be the appropriate scales for the turbulent processes in the transformed coordinates. Comparing Figs. 52 and 53 with Figs. 31 and 32 for the fixed-frame case, one sees that the wave-following results appear as extensions to those of the fixed-frame experiments to shallower depths.

4.3.5 Mean Wave-Induced Quantities

The mean wave-induced shear stress profiles are shown in Fig. 54. The mean wave-induced shear stress is mostly negative, except for the case of u_∞ = 2.5 m/s, where a positive peak occurs at $-ky^* \simeq 0.25$. In terms of physical units (mm^2/s^2), the magnitude of $(-\overline{\tilde{u}\,\tilde{v}})$ seems to increase with wind speed but there is quite a bit of data scatter (see Appendix D). With the exception of the run at u_∞ = 2.5 m/s and

of a lower magnitude in general, the trends are similar to those for the fixed-frame experiments.

The RMS wave-induced velocity components are plotted in normalized coordinates in Figs. 55 and 56. Data collapse is excellent despite a slightly larger scatter for the RMS $\tilde{u}$. Again, RMS $\tilde{v}$ is always larger than RMS $\tilde{u}$ at equivalent wind speeds and depth. By comparing Figs. 55 and 56, and Figs. 35 and 36 for the fixed-frame case, one sees again that the wave-following results appear as extensions to the fixed-frame plots to shallower depths. The normalized RMS $\tilde{u}$ approaches a value of about 0.9, and the normalized RMS $\tilde{v}$ attains a limiting value of about unity near the interface.

4.3.6 Wave Perturbation Velocities

Similar to the fixed-frame experiments, the wave perturbation velocities $\tilde{u}$ and $\tilde{v}$ are almost sinusoidal. The normalized amplitude and the phase angles of the periodic velocities at the excitation frequency are shown in Fig. 57. In each experiment, the amplitudes decay exponentially with depth. The vertical amplitude component $\hat{v}$ is always larger than the horizontal component $\hat{u}$, especially for non-zero wind speed runs. Both $\hat{u}$ and $\hat{v}$ decrease slightly with wind speed at equivalent depths; the wind seems to have a lesser effect on $\hat{v}$ than on $\hat{u}$. The normalized profiles for $\hat{u}$ or $\hat{v}$ approach unity as $-ky^*$ goes to zero regardless of wind speeds. Even though this trend is also observed in fixed-frame experiments, it is more vividly shown here in the wave-following coordinates.

The total harmonic energy content for $\tilde{u}$ and $\tilde{v}$ at each depth are summarized in Appendix D. Both $\tilde{u}$ and $\tilde{v}$ have higher harmonic content near the interface than at deeper depths. Furthermore, the $\tilde{u}$ usually

has more harmonic components than $\tilde{v}$, except at $u_\infty = 2.5$ m/s where the reverse is true. At greater depths, both $\tilde{u}$ and $\tilde{v}$ have roughly the same amount of harmonic energy content of about 1.4%.

The phase lag of $\hat{u}$ with respect to the phase of $\hat{n}_S$ varies at most between -3° and +2° in the neighborhood of zero at all depths except at points where there are obvious data scatter. The data scatter was partially due to the lower signal-to-noise ratio of the backward-scatter collection method for the LDA; especially at deeper depths where $\tilde{u}$ and $\tilde{v}$ were smaller than near the surface. These data points are not discarded because even though the phase angles may have a larger error, other statistical quantities are still valid. The phase difference, $\theta_{\tilde{u}} - \theta_{\tilde{v}}$ stays at 90° ± 2°. The decrease of the phase difference at $u_\infty = 6.2$ m/s present in the fixed-frame experiment is not found here.

The cosine-fitting technique was also used to determine the velocity amplitudes and phase angles. Similar to the fixed-frame experiments, the results agree with those given by the spectral method. The plots of all $\tilde{u}$ and $\tilde{v}$ are collected in a separate report and their numerical values are stored on 800 BPI tapes.

4.3.7 Wave-Induced Stresses

The amplitudes $\hat{r}_{ij}$ (normalized by u_*^2) and the phase angles $\theta_{\tilde{r}_{ij}}$ of the wave-induced turbulent stresses $\tilde{r}_{ij}$ at the excitation frequency are shown in Fig. 58. There is some data scatter and a few extraneous points are eliminated in these plots, but their numerical values are retained in Appendix D for completeness.

At zero wind speed (not plotted), the $\hat{r}_{ij}$ are very small and most likely represent the background noise level rather than any physical quantities. At $u_\infty = 1.7$ and 2.5 m/s, $\hat{r}_{11}$ and $\hat{r}_{22}$ are roughly of equal

magnitudes while $\hat{r}_{12}$ is usually smaller than both of them. The $\hat{r}_{ij}$ all decay rapidly with depth to the noise level for -ky* greater than 0.3. At u_∞ = 4.1 and 6.1 m/s, the $\hat{r}_{ij}$ are quite high near the surface but decrease quickly to the noise level for -ky* bigger than 0.3. There is no systematic increase of $\hat{r}_{ij}$ with wind speed as observed in the fixed-frame experiments. The apparent increase in $\hat{r}_{ij}$ at larger -ky* is attributed to data scatter. The data scatter is partly due to a lower signal-to-noise ratio in the backward-scatter LDA system than in the forward-scatter system. Furthermore, the mechanically generated waves were highly distorted at such high wind speeds; a small error in obtaining $\tilde{u}$ or $\tilde{v}$ due to a lower signal-to-noise ratio can contribute to a significant error in $\tilde{r}_{ij}$.

At u_∞ = 0.0 and 1.7 m/s, the phase lag $\theta_{\hat{r}_{12}}$ seems to stay around 180° while $\theta_{\hat{r}_{11}}$ and $\theta_{\hat{r}_{22}}$ are equal to 0 near the surface and reach 180° at large -ky*. Similar trends are also observed at u_∞ = 2.5 m/s despite large amounts of data scatter. For the two high-speed experiments, $\theta_{\hat{r}_{ij}}$ seem to start from 360° (or 0°) for small -ky* and decrease gradually to around 90° at large -ky*.

The comments about the wave-induced wave stresses $\widetilde{\tilde{u}_i\tilde{u}_j}$ in Sec. 4.2.7 are also valid here. In general, $\hat{u}_i\hat{u}_j/2$ is also very much larger than $\hat{r}_{ij}$.

Table 8

Determination of Friction Velocities
for Wave-Following Frame Experiments

u_∞ (m/s)	Method 1 From $u^+ = -y^{*+}$ u_* (mm/s)	Method 2 From Hsu et al. (1983) u_* (mm/s)	Method 3 From Fixed-Frame Data u_* (mm/s)
1.7	2.34	1.86	2.20
2.5	3.09	3.11	3.35
4.1	-	6.02	5.35
6.1	-	10.84	9.23

NB: The uncertainties for u_* are estimated to be about ± 10%.

CHAPTER 5

DISCUSSION

The representative results of the experiments were presented in Chap. 4. The experiments provide a comprehensive data set for the flow field directly beneath an air-water interface in a well-defined test facility for a wide range of wind speeds, surface conditions, and reference coordinate systems. The objectives of obtaining velocity data have been accomplished. However, it is crucial to sort out the implications of these data and to understand the physical reasons for the observed behavior of the flow. This is the main goal of this chapter. Whenever possible, the data interpretation will be compared to some simple analyses of the governing equations or well-established results.

5.1 CHARACTERISTIC SCALES

5.1.1 Case I: Wind Wave in Eulerian Frame

In this set of experiments, the air-water interface was subjected to the shearing action of the turbulent air flow. Thus, shear layers developed adjacent to the interface. The flow was turbulent in the water boundary layer even at the lowest wind speed. The definition of turbulence is based upon the highly diffusive nature of the flow (other than due to molecular diffusion). This was observed by injecting small amounts of dye in the water layer during some preliminary experiments. It is important not to confuse the random wind-generated waves with turbulence. The random waves are not in turbulent motion because they are essentially irrotational. In addition, the waves are mostly nondissipative (though they often are dispersive), while turbulence is essentially dissipative (Tennekes and Lumley, 1972). This is the main reason why we

can decompose the flow field into three parts: the mean, the wave-induced component, and the fluctuating or turbulent component. Furthermore, it may be possible to derive some scales or parameters which characterize each of these components.

For wind speeds less than 3 m/s, the water surface remained relatively smooth even though capillary-type disturbances were present. The wave-induced quantities were expected to be very small. Therefore, the water boundary layer developed would have features similar to those of flows over flat plates. Of course, it was necessary to convert the water velocity into the velocity defect form $(\overline{u}_s - \overline{u})$ in such comparisons. When the mean velocity defect profiles are plotted in wall coordinates (Fig. 12), they agree with profiles of flows over rigid surfaces. The profiles are logarithmic which is usually taken as evidence for the existence of the inertial sublayer. In addition, the profiles extend to follow the $u^+ = -y^+$ line, which suggests the existence of the viscous sublayer. Hence, the velocity and length scales appropriate for flows over solid surfaces are also applicable for the water boundary layer at low wind speeds.

In the inertial sublayer, the characteristic velocity is the friction velocity u_* and the characteristic length is proportional to the distance from the still water level (i.e., $-\kappa y$) provided that $-yu^*/\nu \gg 1$ and $-y/\delta \ll 1$. Of course, in the viscous sublayer, the viscous shear stress dominates and the contribution of the turbulent shear stress becomes insignificant. So in the viscous sublayer, the length scale becomes ν/u_*, while u_* remains as the correct velocity scale. In the outer layer, where the "mean" flow dominates (i.e., $\overline{u} \approx 0$, $\overline{u}_s - \overline{u} \approx \overline{u}_s$), the obvious choice of the velocity scale is the mean

AD-A154 117 A STUDY OF THE TURBULENT LAYER IN THE WATER AT AN AIR-WATER INTERFACE(U) STANFORD UNIV CALIF DEPT OF CIVIL ENGINEERING T K CHEUNG JAN 85 TR-287 2/3

UNCLASSIFIED N00014-84-K-0242 F/G 8/3 NL

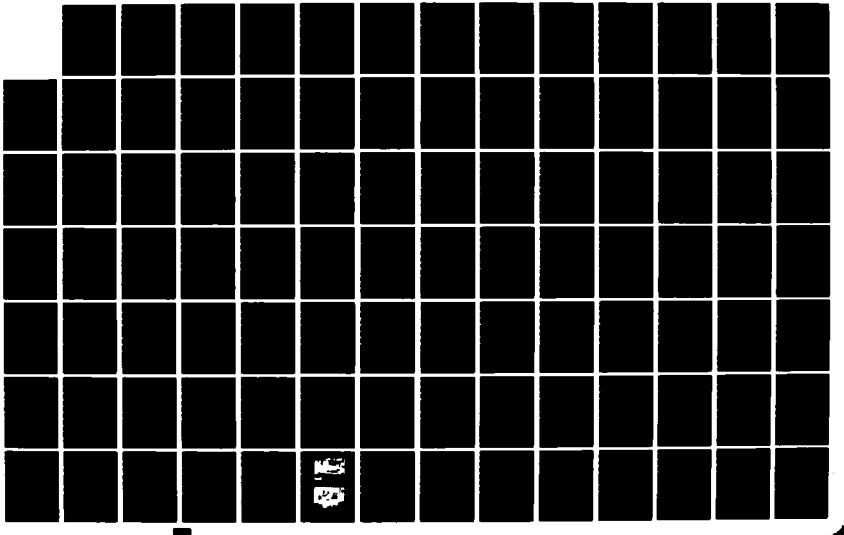

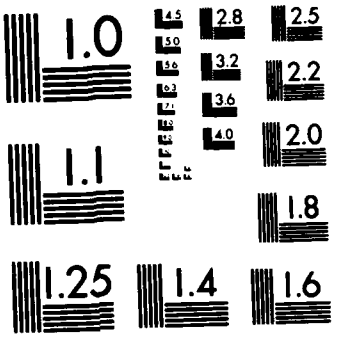

MICROCOPY RESOLUTION TEST CHART
NATIONAL BUREAU OF STANDARDS-1963-A

Eulerian surface drift velocity $\bar{u}_s$. The corresponding length scale is the turbulent boundary-layer thickness δ. In addition, the fetch L can also be a significant length scale.

At high wind speeds (> 3 m/s), waves were present at the interface. The mean velocity profiles in wall coordinates are also logarithmic. However, the slopes of some of the profiles are different from those at low wind speeds. Furthermore, there is an apparent change of slope in some of the profiles, such as those at wind speeds between 3.2 and 9.9 m/s. There is no change of slope in the profile at the highest wind speed but the slope of the profile is clearly different from the low wind-speed experiments. The possible explanation of such behavior is discussed in Sec. 5.2. Here, we focus our attention on finding the relevant parameters characterizing the flows.

The inertial sublayer most likely persists at high wind speeds because of the logarithmic trend of the velocity profiles. Consequently, the friction velocity u_* and $-\kappa y$ are the proper scaling velocity and length in this layer. However, we must keep in mind that within the inertial sublayer, the wave-induced quantities may affect the flow dynamics in the sublayer. In the outer layer, where the effects of turbulence and waves are weak, the mean Eulerian surface drift $\bar{u}_s$ and the turbulent boundary-layer thickness δ remain the appropriate scales for the outer mean flow.

The turbulent intensities or RMS u' and RMS v' profiles when normalized by u_* and δ coalesce into narrow bands (Figs. 16 and 17). Clearly, u_* and δ are the characteristic scales relating turbulent intensities and their decay with depth. The fact that δ is the appropriate length scale is intuitively obvious, because the largest

turbulent eddy is probably on the order of the thickness of the turbulent boundary layer. Similarly, because u_* is derived from the turbulent shear stress, which is directly responsible for turbulence generation, the turbulent intensities should scale with u_* as shown here.

So far, the relevant scales for the mean and turbulent parts of the flows are shown to be similar to those for wall-bounded shear flows. It is well known that wall-bounded shear flows have multiple scales. Here, the wind-generated waves complicate the problem further by introducing additional velocity and length scales. The wind-generated waves are usually considered irrotational and of small amplitude. Thus, some suitable scales for the wave field may be derived from the small-amplitude linear water-wave theory. Some obvious velocity scales are the phase velocity of the dominant wave or the RMS wave orbital velocity at the surface. The phase velocity is always bigger than the mean surface drift velocity in the experiments. Hence, there is no counterpart of the critical layer, which is known to exist on the air side of the interface, in the water. In addition, the phase velocity does not relate directly with the measured water orbital velocity. Therefore, the phase velocity is not an important velocity scale in analyzing the water motion. On the other hand, the linear water-wave theory can be used to compute the orbital velocity at the surface from the surface displacement (Eq. 4-4). This RMS orbital velocity $(\overline{\tilde{u}_o^2})^{1/2}$ is closely related to the measured wave-induced velocities. Associated with this computed RMS orbital velocity is the integrated wave number ($1/y_\eta$, see Eq. 4-5). The excellent data collapse resulting by using these scales (Figs. 19 and 20) suggests that they are the characteristic scales for the wave-induced quantities.

Another length scale of interest is the RMS wave height $(\overline{\eta^2})^{1/2}$. This length scale may give some insight into the surface roughness as defined in boundary-layer type flows (Schlichting, 1979). The velocity profiles in wall coordinates show a downward shift with increasing wind speed which is usually associated with changes in surface roughness. Kays and Crawford (1980) gave a law of the wall, which incorporates a roughness Reynolds number, for fully rough flows with no pressure gradient and no transpiration:

$$u^+ = \frac{1}{\kappa} \ln y^+ + B \qquad (5\text{-}1)$$

$$B = \frac{1}{\kappa} \ln \frac{32.6}{Re_k} \quad ; \qquad Re_k = \frac{u_* k_S}{2}$$

k_S = characteristic length of the roughness element

If the RMS wave height is the only parameter in determining the "surface roughness," then k_S should be proportional to the RMS wave height, i.e., $k_S = c(\overline{\eta^2})^{1/2}$ for some constant c. Since the velocity profile for $u_\infty = 3.2$ m/s lies on the line corresponding to the start of the fully rough flow regime, it was used to calibrate the simple model. The constant c was found to be 13.5. Next, the various values of B were calculated for higher wind speeds. The relationships given by Eq. 5-1 were compared with the measured profiles. These relationships gave only very rough correlation with the data. One apparent reason is that measured profiles have a different slope. More importantly, similar to the air flow, the actual roughness most likely does not depend on the entire wave spectrum; hence, the total RMS wave height should not be included in such calculation as suggested by Kitaigorodskii (1973), Kondo (1973), and Phillips (1977).

The RMS wave height actually has been considered as a length scale in calculating the surface RMS orbital velocity $(\overline{u^2})^{1/2}$, because it is obtained from the surface elevation spectrum. It may seem paradoxical that the RMS wave height, which is a wave-related quantity, would have an effect on the surface roughness, which is related to turbulence generation. On close examination, this is not at all unreasonable, because the waves may in fact have some effects on surface roughness and give rise to wave-induced turbulence.

5.1.2 Case II: Mechanical Wave in Eulerian Frame

The main distinction between this case and the wind-wave case (Case I) is the presence of the mechanically generated waves. In Case I, the waves were generated solely by the wind. Here, the dominant waves were generated by mechanical means. The mechanically generated waves were then acted upon by the turbulent air flow. As a result, shear layers developed on both sides of the interface. The water layer was turbulent for any non-zero wind speed used in this study ($\geq$ 1.7 m/s). Small wavelets, hereafter referred to as ripples, were also generated by the wind. The ripples randomly distorted the mechanically generated wave profile from that of an almost pure sinusoid.

The mean velocity profiles are logarithmic (Fig. 27), thus implying the existence of the inertial sublayer. Although the slopes of the profiles are not 2.5 (= 1/0.4) they are practically identical to those in the high wind-speed wind-wave experiments. So the significant velocity scale is u_* and the velocity defect distribution varies with $-\kappa y$. Of course the value of κ may not necessarily be equal to that usually taken by the von Karman constant (0.4) because of a different slope of the velocity profiles, but the constant should remain at the same order

as 0.4 in the scaling length. At u_∞ = 1.7 and 2.5 m/s, the profiles deviate from the logarithmic regions as the interface is approached (i.e., small $-y^+$). The data near this region behave as if the profiles were in the viscous sublayer but at a higher $-y^+$ than the expected $-y^+ \sim 11$. The explanation of this behavior is given in Sec. 5.2.

The friction velocity u_* is the characteristic scale for the RMS u' and v', while the turbulent boundary-layer thickness δ is the parameter that governs their decay with depth (see Figs. 31 and 32). Once more, we must emphasize the difference in the definition of the fluctuating quantity η' between Case I and Case II. In Case I, even though the frequency of some of the surface waves may not be the same as that of the dominant wave, they are still classified as surface waves. In the present case, any non-periodic components, or any components which do not have a fixed-phase relationship with the mechanically generated wave are considered as fluctuating components. For example, the wind-generated ripples are considered as the fluctuating component of η. The ripples, of course, contribute to parts of the RMS u' or v'. Although η' has a "wave-like" nature, the RMS u' and v' certainly do not scale with any attributes of the dominant wave.

It is relatively straightforward to characterize the mechanically generated wave train because its frequency and mean amplitude are well-defined. The proper length scale for the wave-induced water motion is the inverse of the dominant wave number 1/k. This length scale is a special case of Eq. 4-5 for a <u>monochromatic</u> wave, that is,

$$S_{\eta\eta}(f) = \frac{\hat{\eta}_S^2}{2} \delta(f - f_D) \qquad (5\text{-}2)$$

where $\delta(f)$ is the Dirac delta function, f_D is the frequency of the wave, and $\hat{\eta}_S$ its amplitude. The wave decay depth y_η then becomes $1/k$. Similarly, using the above expression for $S_{\eta\eta}(f)$ and substituting into Eq. 4-4, the velocity scale $(\overline{\tilde{u}_o^2})^{1/2}$ becomes $2\pi f_D \hat{\eta}_S/\sqrt{2}$. The reason for not using the whole η spectrum in deriving the wave velocity scale has already been given in Sec. 4.2.5 and is not repeated here.

The turbulence level is low at a depth of δ or near the outer layer. However, the wave quantities are still significant in this region as shown in Figs. 37 and 38. This is quite different from the wind-wave case where both the turbulent and wave quantities are small in the outer layer.

For the mean flow, the clear choice of the velocity scale is the mean Eulerian surface drift and the length scale is δ where there is substantial mean velocity gradient. The growth of the boundary layer is related to another length scale--the fetch L.

5.1.3 Case III: Mechanical Wave in Wave-Following Eulerian Frame

The surface conditions in this case were identical to those of fixed-frame mechanical-wave experiments (Case II). The major difference between Case II and the present one is in the reference coordinate. Here, all the measurements were made in the wave-following frame but the obtained data are still Eulerian in nature. Apparently, the relevant velocity and length scales in Case II apply here. Consequently, most comments made in the previous section also follow.

The logarithmic trends of the mean velocity profiles persist; thus, u_* is the velocity scale and the velocity defect varies with $-\kappa y$ in the inertial sublayer. As compared to Case II, the velocity probe was able to reach very close to the interface. At the two lowest wind speeds,

the velocity probe was able to sample at depths near the viscous sublayer as indicated by data points which follow the $u^+ = -y^{*+}$ line.

Unfortunately, the friction velocity u_* and the turbulent boundary-layer thickness δ cannot be found from the measured turbulent shear stress. However, the estimated u_*'s and δ's seem to collapse the turbulent intensities (RMS u' and v') equally well. Therefore, the turbulent motion has a length scale of the order of δ and u_* is of the correct magnitude for the turbulent fluctuations.

The wave field has a characteristic velocity of $2\pi f_D \hat{n}_S/\sqrt{2}$ and a length scale of 1/k. The RMS $\tilde{u}$ and $\tilde{v}$ collapse into narrow bands even for $|y| < |\tilde{n}|$, where ordinarily $\tilde{u}_i(x, |y| < |\tilde{n}|, t)$ are not well-defined. The wave-following frame does not seem to have any major effect on the wave-related velocities.

Lastly, the mean Eulerian surface drift is the velocity scale and the estimated δ is the length scale for the mean flow. The fetch may also be a relevant length scale for the mean flow.

5.1.4 Summary

In Secs. 5.1.1 to 5.1.3, we clearly showed the various important length and velocity scales that relate to different components or regions of the flow field. Many of these characteristic scales have been suggested by other investigators, such as Navrotskii (1967) and Kitaigorodskii et al. (1982), but the existence of these scales has never been experimentally demonstrated. Also, instead of finding, say, the bulk momentum transfer coefficient at the air-water interface, we focus our inquiry on the relevant scales of the fundamental principles that govern the transfer process.

Some of the characteristic scales are summarized in Table 9. Note that not all the scales are listed, because others can easily be derived from those tabulated. The absolute magnitudes of these scales sometimes are not as important as their relative magnitudes. For example, in the wind-wave experiments, y_η is always much smaller than δ. On the other hand, δ is always less than the corresponding y_η in all mechanical-wave experiments.

The turbulent boundary-layer thickness δ is larger in the wind-wave case than in the mechanical-wave case at comparable wind speeds. This may be due to the suppression of the wind-generated ripples by the mechanical waves as suggested by Bole and Hsu (1969). However, the friction velocities remain the same order of magnitude at equivalent wind speeds regardless of surface conditions. Of course, all y_η's and δ's are small compared to the fetch of 13 m.

5.2 MEAN VELOCITY PROFILES IN WALL COORDINATES

Some mean velocity profiles in Cases I and II, where waves were dominant, have slopes different from 2.5 in the logarithmic region. Furthermore, there is a change of slope in a number of these profiles. Such behavior is not found in typical two-dimensional boundary-layer type flows, even under mild pressure gradients. Tennekes and Lumley (1972) pointed out that the pressure gradient can have an effect on the slope of the velocity profile, but we will show that the pressure gradient cannot be the cause of the change in slope or the slopes being less than 2.5 in some of the mean profiles. At low wind speeds, say $u_\infty <$ 3 m/s in both Case I and II, the pressure gradient due to water set-up or surface tilt was negligible. In Case I, the slopes of the mean profiles for $u_\infty < 3$ m/s follow a 2.5 slope while the profiles in Case II

have a smaller slope. The primary distinction between Cases I and II is the presence of the mechanically generated waves in Case II. Of course in Case I, the wind was not strong enough to generate any waves of significant magnitude. Hence, by comparing the low wind-speed experiments in Cases I and II, we conclude that the pressure gradient is not the primary cause for the anomalous slopes of the mean velocity profiles.

Another possible cause is that the flow might not be two-dimensional. The law of the wall (Eq. 5-1) does not hold for three-dimensional flows (White, 1972). The low wind-speed experiments in Case I were nearly two-dimensional near the channel center-line and the mean profiles follow the expected trend of such flows. In Case II, the mechanically generated waves were two-dimensional and the ripples were even smaller than those in Case I at low wind speeds, so the flow field beneath the waves should also be nearly two-dimensional. Although there are data scatter in the mean velocities, any unsteadiness or net three-dimensional effect of the flow cannot give such consistent trends in the mean profiles. Three-dimensionality of the mean flow was not present and therefore cannot be the cause of the usual slopes of the mean velocity profiles.

The law of the wall given by Eq. 5-1 can be rewritten as:

$$u^+ = \frac{1}{\kappa} \ln\left(\frac{-y}{y_o}\right) \quad \text{for} \quad y < 0 \tag{5-3}$$

where the various constants are absorbed into y_o. In Cases I and II, measurements of the mean profiles were made at fixed depths. If the mean flow with velocity distribution given by Eq. 5-3 above follows the motion of the dominant waves, then Eq. 5-3 should be modified as follows:

$$u^+ = \frac{1}{\kappa} \overline{\ln\left(\frac{h - y}{y_o}\right)}$$

$$= \frac{1}{\kappa} \left[\overline{\ln(h - y)} - \ln y_o\right] \qquad (5\text{-}4)$$

where $h = h(t) \approx \eta(t)$ = surface elevation. The difference (Δu^+) between Eq. 5-3 and Eq. 5-4 gives the change in u^+ due to the logarithmic profile moving up and down with the dominant waves. It is clear that the biggest difference should occur at points very close to the surface and for large $|\eta|$. Consider a typical run in Case II where $|\eta|$ was large, with the sign of Δu^+ aside, the difference is at most 1.3 u^+ units. This difference can account for the apparent drop in u^+ at small $-y^+ \sim 50$ (see Fig. 27) for low wind-speed experiments. However, away from the interface, Δu^+ is considerably less than the deviation of the measured profile from the relation given by Eq. 5-4. A more elaborate scheme of calculating Δu^+ was suggested by Phillips (1977). This scheme was incorporated into the data analysis program and the results are tabulated in Appendix D. The two estimates for Δu^+ agree, but both are too small to account for the observed discrepency at large $-y^+$ values. If indeed the anomalous slopes were due to kinematics of the waves and measurements being made in a fixed frame, then the anomaly should vanish in the wave-following experiments (Case III). The mean velocity profiles in Case III also have slopes smaller than 2.5 in the logarithmic region. Thus, the change in slope or the profiles having slopes less than 2.5 cannot be the effect of measuring velocities at fixed depths.

Numerous possible explanations for the observed trends of the mean profiles were rejected based on the above discussions. A logical deduction is that the dynamics of the waves are responsible for the unusual mean profiles. The normalized RMS u' and RMS $\bar{u}$ in Case I are

plotted versus $-y^+$ in Figs. 59 and 60, respectively. Hence, it is possible to compare the change in relative magnitudes of RMS u' and RMS $\tilde{u}$ with $-y^+$. For $u_\infty < 3$ m/s, the RMS u' is always larger than RMS $\tilde{u}$ at all depths. At higher wind speeds, there are values of $-y^+$ at which RMS u' > RMS $\tilde{u}$ and also for RMS u' < RMS $\tilde{u}$. If the waves do affect the mean profiles, then in the region where RMS u' < RMS $\tilde{u}$, the mean profiles may deviate from the 2.5 slopes. On the other hand, the slopes should approach 2.5 in regions where RMS u' > RMS $\tilde{u}$. For Case I, it is found that in the region where RMS u' > 2 (RMS $\tilde{u}$), the mean profiles have slopes nearly equal to 2.5; and where RMS u' < RMS $\tilde{u}$, the slopes are smaller than 2.5. Furthermore, the slopes change from 2.5 to less than 2.5 at depths where RMS u' ≈ 2 (RMS $\tilde{u}$), such as those for 3.2 m/s < u_∞ < 9.9 m/s. These observations were derived from experiments in Case I; if these observations are the outcomes of some basic physical principles, then they should apply to Cases II and III also. This is indeed the case, because generally RMS u' < RMS $\tilde{u}$ in mechanical-wave experiments and the mean profiles were found to have slopes less than 2.5. In addition, there is no change of slope (in the logarithmic region) in the profiles for Cases II and III, because there does not exist any region where RMS u' ≈ RMS $\tilde{u}$. So in the light of the experimental evidence, the waves seem to have an effect on the mean flow.

5.3 POSSIBLE EVIDENCE OF WAVE-GENERATED TURBULENCE

In Case I, the turbulent intensity (RMS u' or v') profiles are very similar to those in a steady pure shear flow. That is, the turbulence is non-isotropic with RMS u' > RMS v'. In addition, the RMS $\tilde{u}$ exceeds RMS u', but at most by a factor of about two. Although the wave fluctuation is strong, it remains at the same order as the turbulent motion.

Also, the wave motion decays fairly rapidly with depth. On the other hand, the vertical and horizontal turbulent intensities in Case II are almost equal in magnitude, i.e., the turbulence is nearly isotropic. The RMS $\tilde{u}$ now exceeds RMS u' by more than a factor of two. This factor attains a value of 10 in low wind-speed experiments when waves were predominant. The decay of the wave motion with depth is not as rapid as that in Case I because the mechanical waves have a longer wavelength. Thus, if there is wave-generated turbulence, the phenomenon ought to be more prominent in mechanical-wave experiments. The apparent deviation of the turbulent intensities in Cases II and III from those of the wind-wave experiments may indicate such a phenomenon.

If the waves are truly irrotational, the mean wave-induced shear stress ($-\overline{\tilde{u}\,\tilde{v}}$) should be zero, and the wave would have no interaction with either the mean or the turbulent flow fields. It is clear from the data that the waves are not truly irrotational, thus, the mean wave-induced shear stress is non-zero. This shear stress may contribute to turbulence production directly or indirectly. The mean wave-induced shear stress is much larger in Cases II and III than in Case I. This again implies that the effect of the mean wave-induced shear stress is stronger in mechanical-wave experiments.

The experimental data support the postulate that the waves can affect the mean flow as discussed in Sec. 5.2. It is well-known that turbulence can only be maintained by drawing energy from the mean flow, or as suggested above, from the waves also. Hence, the mean, wave, and turbulent fields are closely coupled. Although the experimental evidence for such coupling is strong, it is crucial to demonstrate, from a theoretical viewpoint, that the governing equations allow such interactions.

5.4 ANALYSIS OF THE FIXED-FRAME GOVERNING EQUATIONS PERTAINING TO THE EXPERIMENTAL OBSERVATIONS

The boundary-layer equations for two-dimensional incompressible flows can be derived from the Navier-Stokes equations by an order-of-magnitude analysis. In many flow situations, such as those over flat plates, the characteristic scales are well-known. Therefore, one can proceed directly to the boundary-layer equations without rederiving them. Here, some of the characteristic scales and their relative magnitudes are not known a priori. Hence, an order-of-magnitude analysis of the governing equations is impossible unless the relevant scales are found experimentally or otherwise. The characteristic scales for different parts of the flow are found experimentally in Sec. 5.1; thus, an order-of-magnitude analysis can now be performed on the governing equations.

5.4.1 Primary Estimates

To do an order-of-magnitude analysis of the governing equations, variables will be replaced by their "typical" magnitudes. The changes in the variables are taken to be of the same order as the typical values. The symbol "Δ" that preceeds a variable denotes changes in that variable. The notation "$\sim$" denotes a typical value of order-of-magnitude accuracy regardless of the sign. This should not be confused with the superposed "~" which stands for wave quantities. In the fixed-frame equations, the following typical values are used:

$$\Delta x \sim L \quad \text{for mean quantities}$$

$$\sim c\Delta t \sim c/\omega \sim y_\eta \quad \text{for wave quantities}$$

$$\Delta t \sim 1/\omega$$

$$\Delta y \sim \delta \quad \text{for mean quantities}$$

$$\sim y_\eta \sim 1/k \quad \text{for wave quantities}$$

$$y_\eta < \delta \quad \text{in Case I}$$

$$y_\eta \sim \delta \quad \text{in Case II}$$

$$\bar{u} \sim u_S \sim \bar{u}_S$$

$$\tilde{u},\ \Delta\tilde{u} \sim a\omega$$

$$\tilde{v},\ \Delta\tilde{v} \sim a\omega$$

where

L = length scale in the streamwise direction

ω = circular frequency of the dominant wave

δ = turbulent boundary-layer thickness ($\delta \ll L$)

y_η = wave-decay depth ($y_\eta \ll L$)

u_S = mean Eulerian surface drift velocity

a = amplitude of the dominant wave

k = dominant wave number

c = dominant wave speed ($= \omega/k$).

It is assumed that the mean turbulent quantities

$$\Delta(\overline{u'u'}),\ \Delta(\overline{u'v'}),\ \Delta(\overline{v'v'}) \sim \epsilon^2 u_S^2 \tag{5-5}$$

where ϵ^2 is a multiplicative factor (usually $\ll 1$) whose magnitude will be determined in the analysis. This order-of-magnitude estimate is arrived at by the following reasoning. The mean turbulent quantities, such as $\overline{u'^2}$, are of the order of u_*^2, and u_* is found to be roughly proportional to u_S, so that the mean turbulent quantities are of the order of $\epsilon^2 u_*^2$.

The order-of-magnitude changes in $\widetilde{u'u'}$, $\widetilde{u'v'}$, and $\widetilde{v'v'}$ are derived as follows. The phase-averaged value $\langle u'u' \rangle$ is assumed to be given by:

$$\langle u'u' \rangle \sim \epsilon^2 \langle u_S \rangle^2$$

where $\langle u_S \rangle$ is the phase-averaged Eulerian surface drift velocity. This estimate is a generalization of Eq. 5-5, which applies to the mean quantities. Now, if $\langle u_S \rangle$ is given by:

$$\langle u_S \rangle \sim u_S + a\omega \cos \omega t$$

then

$$\langle u_S \rangle^2 \sim u_S^2 + 2u_S a\omega \cos \omega t + a^2\omega^2 \cos^2 \omega t$$

$$= u_S^2[1 + 2(\frac{a\omega}{u_S}) \cos \omega t + (\frac{a\omega}{u_S})^2 \cos^2 \omega t]$$

$$= u_S^2[1 + 2\alpha \cos \omega t + \alpha^2 \cos^2 \omega t]$$

where $\alpha = a\omega/u_S$.

From the experimental results, $\alpha \gtrsim 1$ in Cases II and III, so $\widetilde{u'u'}$, $\widetilde{u'v'}$, $\widetilde{v'v'} \sim \epsilon^2 u_S^2$. It is unnecessary to consider Case I because the wave-induced turbulent stresses are not defined. From the above analysis, $\widetilde{u'u'}$ is of the same order as $\overline{u'u'}$, and similarly for the other components. This result is quite different from those of Carr (1981a,b) and Jayaraman et al. (1982) for the unsteady boundary layer. They found that $\widetilde{u'u'}$ is much smaller than $\overline{u'u'}$.

5.4.2 Continuity Equations

The mean continuity equation (Eq. 2-17a) has two terms and their order-of-magnitude estimates are given by:

$$\frac{\partial \bar{u}}{\partial x} \sim \frac{u_S}{L} \quad \text{and} \quad \frac{\partial \bar{v}}{\partial y} \sim \frac{\Delta \bar{v}}{\delta}$$

Each term must be of the same order for the equation to hold, so we must have:

$$\Delta \bar{v} \sim u_S \frac{\delta}{L}$$

that is, the change in the mean vertical velocity is very small. This agrees with the experimental observations that the mean vertical velocity gradient is very small and the mean vertical velocity is very close to zero.

Care must be taken in analyzing the wave continuity equation (Eq. 2-17b) in order to avoid some pitfalls. The wave-induced or periodic velocities are known to be of the same order of magnitude, and the two terms in the equation must also be of the same order. Thus, the length scales Δx and Δy must be of the same size. However, Δx cannot be the same as the primary estimate for the mean variables L; otherwise Δy would be L, which is impossible. Instead, we know that

$$\frac{\partial \tilde{v}}{\partial y} \sim \frac{a\omega}{y_\eta}$$

$$\tilde{u} \sim a\omega$$

$$k \sim 1/y_\eta \quad \text{and} \quad c = \omega/k$$

Since we require a balance between the x and y derivatives,

$$\frac{\partial \tilde{u}}{\partial x} \sim \frac{\partial \tilde{v}}{\partial y} \sim \frac{a\omega}{y_\eta} \sim \frac{a\omega^2}{c}$$

and because

$$\frac{\partial \tilde{u}}{\partial x} \sim \frac{a\omega}{\Delta x} ,$$

it follows that the required x scale is $\Delta x \sim c/\omega = c\Delta t$; this gives the typical Δx value for wave quantities.

5.4.3 Mean Momentum Equations

There are nine terms in the mean x-momentum equation (Eq. 2-18). The order-of-magnitude estimate of each term is as follows:

Term 1 $$\frac{\partial}{\partial x}(\bar{u}\,\bar{u}) \sim \frac{u_S^2}{L}$$

Term 2 $$\frac{\partial}{\partial y}(\bar{u}\,\bar{v}) \sim \frac{u_s u_s \delta}{\delta L} = \frac{u_s^2}{L}$$

Term 3 $$\frac{1}{\rho}\frac{\partial \bar{p}}{\partial x} \sim \frac{1}{\rho}\frac{\Delta \bar{p}}{L}$$

Term 4 $$\nu \frac{\partial^2 \bar{u}}{\partial x^2} \sim \nu \frac{u_s}{L^2} = \frac{u_s^2}{L}\frac{\nu}{u_s L}$$

Term 5 $$\nu \frac{\partial^2 \bar{u}}{\partial y^2} \sim \nu \frac{u_s}{\delta^2} = \frac{u_s^2}{L}\frac{\nu}{u_s L}\frac{L^2}{\delta^2}$$

Term 6 $$\frac{\partial}{\partial x}(\overline{u'u'}) \sim \frac{1}{L}\varepsilon^2 u_s^2 = \frac{u_s^2}{L}\varepsilon^2$$

Term 7 $$\frac{\partial}{\partial y}(\overline{u'v'}) \sim \frac{1}{\delta}\varepsilon^2 u_s^2 = \frac{u_s^2}{L}\varepsilon^2\frac{L}{\delta}$$

Term 8 $$\frac{\partial}{\partial x}(\overline{\tilde{u}\,\tilde{u}}) \sim \frac{1}{L}a^2\omega^2 = \frac{u_s^2}{L}\frac{a^2\omega^2}{u_s^2} = \frac{u_s^2}{L}\alpha^2$$

Term 9 $$\frac{\partial}{\partial y}(\overline{\tilde{u}\,\tilde{v}}) \sim \frac{1}{y_\eta}a^2\omega^2 = \frac{u_s^2}{L}\frac{a^2\omega^2}{u_s^2}\frac{L}{y_\eta} = \frac{u_s^2}{L}\alpha^2\frac{L}{y_\eta}$$

Term 4 is negligible compared to Term 5, and Term 6 is negligible compared to Term 7, because $\delta \ll L$. As $y_\eta \ll L$, Term 9 is much bigger than Term 8. The estimate in Term 8 is for Case I, because when the waves are generated by the wind, the wave orbital velocity has acquired a magnitude of $a\omega$ at the fetch L. This term should even be smaller compared to Term 9 for Case II, because there is little growth of the mechanically generated waves over the distance L for the wind speeds used in the experiments. The viscous term (Term 5) is important when

$$\frac{\nu}{u_s L}\frac{L^2}{\delta^2} \sim 1 \quad \text{or} \quad \frac{\delta}{L} \sim \left(\frac{u_s L}{\nu}\right)^{-1/2}$$

or in regions very close to the interface. The turbulent term (Term 7)

is significant when

$$\epsilon^2 \sim \frac{\delta}{L}$$

and this yields the order-of-magnitude estimate of ϵ^2. The parameter α is always on the order of one or larger, except for low wind-speed experiments in Case I, so Term 9 is always significant when waves are present. Finally, for the pressure term to be of any importance, we need to have

$$\Delta\bar{p} \sim \rho \frac{Lu_S^2}{L} = \rho u_S^2$$

After discarding the insignificant terms, the mean x-momentum equation simplifies to:

$$\frac{\partial}{\partial x}(\bar{u}\,\bar{u}) + \frac{\partial}{\partial y}(\bar{u}\,\bar{v}) = -\frac{1}{\rho}\frac{\partial\bar{p}}{\partial x} + \nu\frac{\partial^2\bar{u}}{\partial y^2} - \frac{\partial}{\partial y}(\overline{u'v'} + \overline{\tilde{u}\,\tilde{v}}) \qquad (5\text{-}6)$$

This equation is similar to the steady boundary layer x-momentum equation except for the extra mean wave-induced shear stress term $-\overline{\tilde{u}\,\tilde{v}}$. The mean wave-induced shear stress and its vertical gradient are not small near the interface when waves are present, especially in mechanical-wave experiments. Hence, the waves, which lead to $-\overline{\tilde{u}\,\tilde{v}}$, can affect the mean flow. In Sec. 5.2, it was pointed out that the mean velocity profiles in wall coordinates change slope at depths where RMS u' ≈ 2(RMS $\tilde{u}$). The mean wave-induced shear stress is related to the wave-induced velocity $\tilde{u}$, which of course is represented by RMS $\tilde{u}$. On close examination of the data (e.g. Appendix D), the depth at which RMS u' ≈ 2(RMS $\tilde{u}$) corresponds to the distance over which there is substantial change in the mean wave-induced shear stress. In Case I, the low wind-speed experiments have negligible $-\overline{\tilde{u}\,\tilde{v}}$, so Eq. 5-6 is identical to the mean x-momentum equation for a <u>steady</u> boundary layer. However, this asymptotic result does not

hold for low wind-speed experiments in Case II, because $-\overline{\tilde{u}\,\tilde{v}}$ is still significant due to the mechanically generated waves. It is clear that the experimental observations, such as those in Sec. 5.2, agree with the implications of the simplified mean x-momentum equation (Eq. 5-6).

The mean y-momentum equation (Eq. 2-19) also has nine terms as well as the body-force term. Their order-of-magnitude estimates are as follows:

Term 1 $$\frac{\partial}{\partial x}(\bar{u}\,\bar{v}) \sim \frac{u_S}{L}\frac{u_S\delta}{L} = \frac{u_S^2\delta}{L^2}$$

Term 2 $$\frac{\partial}{\partial y}(\bar{v}\,\bar{v}) \sim \frac{u_S\delta}{L}\frac{u_S\delta}{L}\frac{1}{\delta} = \frac{u_S^2\delta}{L^2}$$

Term 3 $$\frac{1}{\rho}\frac{\partial \bar{p}}{\partial y} \sim ?$$

Term 4 $$\nu\frac{\partial^2\bar{v}}{\partial x^2} \sim \nu\frac{u_S\delta}{L}\frac{1}{L^2} = \frac{u_S^2\delta}{L^2}\frac{\nu}{u_S L}$$

Term 5 $$\nu\frac{\partial^2\bar{v}}{\partial y^2} \sim \nu\frac{u_S\delta}{L}\frac{1}{\delta^2} = \frac{u_S^2\delta}{L^2}\frac{\nu}{u_S L}\frac{L^2}{\delta^2}$$

Term 6 $$\frac{\partial}{\partial x}(\overline{u'v'}) \sim \frac{1}{L}\varepsilon^2 u_S^2 = \frac{u_S^2\delta}{L^2}\varepsilon^2\frac{L}{\delta}$$

Term 7 $$\frac{\partial}{\partial y}(\overline{v'v'}) \sim \frac{\varepsilon^2 u_S^2}{\delta} = \frac{u_S^2\delta}{L^2}\varepsilon^2\frac{L^2}{\delta^2}$$

Term 8 $$\frac{\partial}{\partial x}(\overline{\tilde{u}\,\tilde{v}}) \sim \frac{1}{L}a^2\omega^2 = \frac{u_S^2\delta}{L^2}\frac{a^2\omega^2}{u_S^2}\frac{L}{\delta} = \frac{u_S^2\delta}{L^2}\alpha^2\frac{L}{\delta}$$

Term 9 $$\frac{\partial}{\partial y}(\overline{\tilde{v}\,\tilde{v}}) \sim \frac{1}{y_\eta}a^2\omega^2 = \frac{u_S^2\delta}{L^2}\frac{a^2\omega^2}{u_S^2}\frac{L}{\delta}\frac{L}{y_\eta} = \frac{u_S^2\delta}{L^2}\alpha^2\frac{L}{\delta}\frac{L}{y_\eta}$$

It is readily seen that Term 4 is negligible compared to Term 5, Term 6 is much smaller than Term 7, and Term 9 is usually much larger than Term 8. So in this first step of simplification, we have:

$$\frac{\partial}{\partial x}(\bar{v}\,\bar{u}) + \frac{\partial}{\partial y}(\bar{v}\,\bar{v}) = -\frac{1}{\rho}\frac{\partial \bar{p}}{\partial y} + \nu\frac{\partial^2 \bar{v}}{\partial y^2} - \frac{\partial}{\partial y}(\overline{v'v'}) - \frac{\partial}{\partial y}(\overline{\tilde{v}\,\tilde{v}}) - g$$

If the order-of-magnitude estimate for $\varepsilon^2 \sim \delta/L$ is used in the analysis, then Terms 1, 2, and 5 are also negligible, because $u_S L/\nu$ is generally large. Thus, the equation is further simplified to:

$$\frac{1}{\rho}\frac{\partial \bar{p}}{\partial y} = -g - \frac{\partial}{\partial y}(\overline{v'v'} + \overline{\tilde{v}\,\tilde{v}}) \qquad (5\text{-}6)$$

In experiments where waves are insignificant, we have in the limit:

$$\overline{\tilde{v}\,\tilde{v}} \sim 0 \quad \text{and} \quad \frac{\partial}{\partial y}(\overline{\tilde{v}\,\tilde{v}}) \sim 0$$

An order-of-magnitude estimate for the pressure term (Term 3) now becomes:

$$\Delta\bar{p} \sim \rho g\delta + \rho\frac{u_S^2\delta}{L}$$

$$\sim \rho g\delta$$

That is, Term 7 is small compared to the body force. So in this special case, the pressure term is just equal to the hydrostatic pressure. When waves are present, we have:

$$\Delta\bar{p} \sim \rho g\delta + \rho\frac{u_S^2\delta}{L} + \rho\frac{a^2\omega^2}{y_\eta}$$

$$\sim \rho g\delta + \rho\frac{a^2\omega^2}{y_\eta}\delta$$

In almost all experiments $a^2\omega^2/y_\eta \ll g$, so we arrive again at:

$$\Delta\bar{p} \sim \rho g\delta$$

So the hydrostatic assumption of the pressure term holds in all cases, and Eq. 5-6 simply becomes:

$$\frac{\partial \bar{p}}{\partial y} = -\rho g$$

5.4.4 Wave-Perturbed or Periodic Momentum Equations

The periodic momentum equation in the x direction (Eq. 2-20) has 11 terms. Each of these terms has the following order-of-magnitude estimates:

Term 1 $$\frac{\partial \tilde{u}}{\partial t} \sim \frac{a\omega}{(1/\omega)} = \frac{a\omega u_S}{L}\frac{\omega L}{u_S}$$

Term 2 $$\frac{\partial}{\partial x}(\tilde{u}\,\bar{u}) = \tilde{u}\frac{\partial \bar{u}}{\partial x} + \bar{u}\frac{\partial \tilde{u}}{\partial x} \sim \frac{a\omega u_S}{L} \text{ or } \frac{a\omega u_S}{y_\eta}$$

Term 3 $$\frac{\partial}{\partial y}(\bar{u}\,\tilde{v}) = \bar{u}\frac{\partial \tilde{v}}{\partial y} + \tilde{v}\frac{\partial \bar{u}}{\partial y} \sim \frac{a\omega u_S}{y_\eta} \text{ or } \frac{a\omega u_S}{\delta}$$

Term 4 $$\frac{\partial}{\partial y}(\tilde{u}\,\bar{v}) = \bar{v}\frac{\partial \tilde{u}}{\partial y} + \tilde{u}\frac{\partial \bar{v}}{\partial y} \sim \frac{u_S\delta}{L}\frac{a\omega}{y_\eta} \text{ or } \frac{a\omega u_S\delta}{L}\frac{1}{\delta}$$

Term 5 $$\frac{1}{\rho}\frac{\partial \tilde{p}}{\partial x} \sim \frac{1}{\rho}\frac{\Delta \tilde{p}}{y_\eta}$$

Term 6 $$\nu\frac{\partial^2 \tilde{u}}{\partial x^2} \sim \nu\frac{a\omega}{y_\eta^2} = \frac{a\omega u_S}{L}\frac{\nu}{u_S L}\frac{L^2}{y_\eta^2}$$

Term 7 $$\nu\frac{\partial^2 \tilde{u}}{\partial y^2} \sim \nu\frac{a\omega}{y_\eta^2} = \frac{a\omega u_S}{L}\frac{\nu}{u_S L}\frac{L^2}{y_\eta^2}$$

Term 8 $$\frac{\partial}{\partial x}\widetilde{(\tilde{u}\,\tilde{u})} \sim \frac{a^2\omega^2}{y_\eta} = \frac{a\omega u_S}{L}\frac{a\omega}{u_S}\frac{L}{y_\eta} = \frac{a\omega u_S}{L}\alpha\frac{L}{y_\eta}$$

Term 9 $$\frac{\partial}{\partial x}\widetilde{(u'u')} \sim \frac{\epsilon^2 u_S^2}{y_\eta} = \frac{a\omega u_S}{L}\frac{u_S}{a\omega}\epsilon^2\frac{L}{y_\eta} = \frac{a\omega u_S}{L}\frac{1}{\alpha}\epsilon^2\frac{L}{y_\eta}$$

Term 10 $$\frac{\partial}{\partial y}\widetilde{(\tilde{u}\,\tilde{v})} \sim \frac{a^2\omega^2}{y_\eta} = \frac{a\omega u_S}{L}\frac{a\omega}{u_S}\frac{L}{y_\eta} = \frac{a\omega u_S}{L}\alpha\frac{L}{y_\eta}$$

Term 11 $$\frac{\partial}{\partial y}\,\widetilde{(u'v')} \sim \frac{\epsilon^2 u_S^2}{y_\eta} = \frac{a\omega u_S}{L}\,\frac{u_S}{a\omega}\,\epsilon^2\,\frac{L}{y_\eta} = \frac{a\omega u_S}{L}\,\frac{1}{\alpha}\,\epsilon^2\,\frac{L}{y_\eta}$$

There are two estimates for each term of Terms 2 through 4 because each of them has two characteristic length scales. The larger of the two estimates is used in comparing the terms. Terms 9 and 11 contain turbulent quantities, but because the phase average is used, the wave length scale is used instead of the turbulent length scale. The predominant term clearly is Term 1. Other terms, except Term 5 are roughly of the same size. Thus, none of them can be neglected without further assumptions. If the estimate $\epsilon^2 \sim \delta/L$ is used, then Terms 9 and 11 are small compared to Terms 8 and 10. Furthermore, if $(\nu/u_S L)(L^2/y_\eta^2) \lesssim 1$, then the viscous terms (6 and 7) are negligible. Hence, we have the following simplified equation:

$$\frac{\partial \tilde{u}}{\partial t} + 2\,\frac{\partial}{\partial x}\,(\tilde{u}\,\bar{u}) + \frac{\partial}{\partial y}\,(\bar{u}\,\tilde{v} + \tilde{u}\,\bar{v}) = -\frac{1}{\rho}\,\frac{\partial \tilde{p}}{\partial x} - \frac{\partial}{\partial x}\,\widetilde{(\tilde{u}\,\tilde{u})} - \frac{\partial}{\partial y}\,\widetilde{(\tilde{u}\,\tilde{v})}$$

Comparing Term 1 with the remaining terms, we see that only the pressure term is large enough to balance the equation. Furthermore, the wave-induced waves stresses $-\widetilde{\tilde{u}_i \tilde{u}_j}$ have a dominant frequency twice that of $\tilde{u}$ as pointed out in Sec. 4.2.7; the interaction of these terms with Term 1 must be nonlinear and is generally small. Thus, we end up with:

$$\frac{\partial \tilde{u}}{\partial t} = -\frac{1}{\rho}\,\frac{\partial \tilde{p}}{\partial x}$$

which is just the equation of motion in the x direction for small amplitude gravity waves on an ideal fluid (Landau and Lifshitz, 1959). This simple analysis shows that the mean and the turbulent fields have little effect on the wave field. However, this does not imply the reverse, that is, the waves may have some significant impact on the mean and turbulent fields due to the nonlinear terms.

The periodic y-momentum equation (Eq. 2-21) also has 11 terms. They are listed with their order-of-magnitude estimates as follows:

Term 1
$$\frac{\partial \tilde{v}}{\partial t} \sim \frac{a\omega}{(1/\omega)} = \frac{a\omega u_S}{L}\frac{\omega L}{u_S}$$

Term 2
$$\frac{\partial}{\partial x}(\bar{v}\,\tilde{u}) \sim \frac{u_S \delta}{L}\frac{a\omega}{y_\eta} \text{ or } \frac{u_S \delta}{L^2}$$

Term 3
$$\frac{\partial}{\partial x}(\tilde{v}\,\bar{u}) \sim \frac{a\omega u_S}{L} \text{ or } \frac{a\omega u_S}{y_\eta}$$

Term 4
$$\frac{\partial}{\partial y}(\bar{v}\,\tilde{v}) \sim \frac{u_S \delta}{L}\frac{a\omega}{y_\eta} \text{ or } a\omega\frac{u_S \delta}{L\delta}$$

Term 5
$$\frac{1}{\rho}\frac{\partial \tilde{p}}{\partial y} \sim \frac{1}{\rho}\frac{\Delta \tilde{p}}{y_\eta}$$

Term 6
$$\nu\frac{\partial^2 \tilde{v}}{\partial x^2} \sim \nu\frac{a\omega}{y_\eta^2} = \frac{a\omega u_S}{L}\frac{\nu}{u_S L}\frac{L^2}{y_\eta^2}$$

Term 7
$$\nu\frac{\partial^2 \tilde{v}}{\partial y^2} \sim \nu\frac{a\omega}{y_\eta^2} = \frac{a\omega u_S}{L}\frac{\nu}{u_S L}\frac{L^2}{y_\eta^2}$$

Term 8
$$\frac{\partial}{\partial x}\widetilde{(\tilde{u}\,\tilde{v})} \sim \frac{a^2\omega^2}{y_\eta} = \frac{a\omega u_S}{L}\alpha\frac{L}{y_\eta}$$

Term 9
$$\frac{\partial}{\partial x}\widetilde{(u'v')} \sim \frac{\varepsilon^2 u_S^2}{y_\eta} = \frac{a\omega u_S}{L}\frac{\varepsilon^2}{\alpha}\frac{L}{y_\eta}$$

Term 10
$$\frac{\partial}{\partial y}\widetilde{(\tilde{v}\,\tilde{v})} \sim \frac{a^2\omega^2}{y_\eta} = \frac{a\omega u_S}{L}\alpha\frac{L}{y_\eta}$$

Term 11
$$\frac{\partial}{\partial y}\widetilde{(v'v')} \sim \frac{\varepsilon^2 u_S^2}{y_\eta} = \frac{a\omega u_S}{L}\frac{\varepsilon^2}{\alpha}\frac{L}{y_\eta}$$

Similarly to the periodic x-momentum equation, Term 1 and Term 5 are the dominant terms. If the other terms are neglected, the equation of

motion becomes the periodic y-momentum equation for small-amplitude gravity waves of an irrotational fluid:

$$\frac{\partial \tilde{v}}{\partial t} = -\frac{1}{\rho}\frac{\partial \tilde{p}}{\partial y}$$

The body force due to gravity is not included in the equation because it is accounted for in the mean equation:

$$\frac{1}{\rho}\frac{\partial \bar{p}}{\partial y} = -g$$

Let us compare the above analysis with the experimental data. The RMS wave-induced velocity was computed at each depth according to the linear water-wave theory. These values are listed in Appendix D with the measured RMS $\tilde{u}$ and $\tilde{v}$. The RMS $\tilde{v}$ are within 5% of the theoretical values. The RMS $\tilde{u}$ are always less than the theoretical values, and less than the measured RMS $\tilde{v}$ also. One may argue that in the wind-wave experiments, the waves may not propagate strictly in the downstream direction but at some angle to it. Hence, only a portion of the RMS $\tilde{u}$ was measured. However, similar results are found in Case II where the mechanical waves are two-dimensional. One explanation is that Terms 2 and 3 in the horizontal wave momentum equation are bigger than Terms 2 and 3 in the corresponding equation in the vertical direction (see Sec. 5.4.4). That is, the interaction of the waves with the mean flow is stronger in the horizontal direction than in the vertical direction. Thus, more energy is "lost" by the waves in the horizontal direction which results in a smaller RMS $\tilde{u}$ than the theoretical value.

5.4.5 Energy Equations

The momentum equations presented in Sec. 5.4.4 show that coupling exists among the mean, wave, and turbulent fields; but the interaction

among the three fields is best illustrated by the energy equations. The kinetic energy equations can be obtained from the momentum equations as shown by Reynolds and Hussain (1972). The procedure is straightforward and is not presented here.

The average kinetic energy at a point is given by:

$$\frac{1}{2}\overline{u_i u_i} = \frac{1}{2}\bar{u}_i\bar{u}_i + \frac{1}{2}\overline{\tilde{u}_i\tilde{u}_i} + \frac{1}{2}\overline{u_i'u_i'} \tag{5-7}$$

The three terms on the right-hand side of Eq. 5-7 represent the kinetic energy for the mean, wave, and turbulent fields, respectively. The energy equations for these terms are listed below:

$$\begin{aligned}\frac{\bar{D}}{Dt}\left(\frac{1}{2}\bar{u}_i\bar{u}_i\right) = &- \frac{\partial}{\partial x_i}\left(\bar{p}\,\bar{u}_i\right) - \underbrace{\left(-\overline{\tilde{u}_i\tilde{u}_j}\right)\frac{\partial \bar{u}_i}{\partial x_j}}_{\text{I}} - \underbrace{\left(-\overline{u_i'u_j'}\right)\frac{\partial \bar{u}_i}{\partial x_j}}_{\text{II}} \\ &- \frac{\partial}{\partial x_j}\left[\bar{u}_i\left(\overline{\tilde{u}_i\tilde{u}_j} + \overline{u_i'u_j'}\right)\right] - F_i\bar{u}_i \\ &+ \nu\frac{\partial}{\partial x_j}\left[\bar{u}_i\left(\frac{\partial \bar{u}_i}{\partial x_j} + \frac{\partial \bar{u}_j}{\partial x_i}\right)\right] - \nu\left(\frac{\partial \bar{u}_i}{\partial x_j} + \frac{\partial \bar{u}_j}{\partial x_i}\right)\frac{\partial \bar{u}_i}{\partial x_j}\end{aligned} \tag{5-8}$$

$$\begin{aligned}\frac{\bar{D}}{Dt}\left(\frac{1}{2}\overline{\tilde{u}_i\tilde{u}_i}\right) = &- \frac{\partial}{\partial x_j}\left[\overline{\tilde{u}_j\left(\frac{\tilde{p}}{\rho} + \frac{1}{2}\tilde{u}_i\tilde{u}_i\right)}\right] - \underbrace{\overline{\tilde{u}_i\tilde{u}_j}\frac{\partial \bar{u}_i}{\partial x_j}}_{-\text{I}} \\ &- \underbrace{\left(-\overline{\langle u_i'u_j'\rangle\frac{\partial \tilde{u}_i}{\partial x_j}}\right)}_{\text{III}} - \frac{\partial}{\partial x_j}\left(\overline{\tilde{u}_i\langle u_i'u_j'\rangle}\right) \\ &+ \nu\frac{\partial}{\partial x_j}\left[\overline{\tilde{u}_i\left(\frac{\partial \tilde{u}_i}{\partial x_j} + \frac{\partial \tilde{u}_j}{\partial x_i}\right)}\right] - \nu\overline{\left(\frac{\partial \tilde{u}_i}{\partial x_j} + \frac{\partial \tilde{u}_j}{\partial x_i}\right)\frac{\partial \tilde{u}_i}{\partial x_j}}\end{aligned} \tag{5-9}$$

$$\frac{\overline{D}}{Dt}\left(\frac{1}{2}\,\overline{u_i'u_i'}\right) = -\frac{\partial}{\partial x_j}\left[\overline{u_j'\left(\frac{p'}{\rho}+\frac{1}{2}\,u_i'u_i'\right)}\right] - \underbrace{\overline{u_i'u_j'}\,\frac{\partial \bar{u}_i}{\partial x_j}}_{-II}$$

$$- \underbrace{\overline{\langle u_i'u_j'\rangle}\,\frac{\partial \tilde{u}_i}{\partial x_j}}_{-III} - \overline{\tilde{u}_i\,\frac{\partial}{\partial x_j}\langle\frac{1}{2}\,u_i'u_i'\rangle}$$

$$+ \nu\,\frac{\partial}{\partial x_j}\left[\overline{u_i'\left(\frac{\partial u_i'}{\partial x_j}+\frac{\partial u_j'}{\partial x_i}\right)}\right] - \nu\,\overline{\left(\frac{\partial u_i'}{\partial x_j}+\frac{\partial u_j'}{\partial x_i}\right)\frac{\partial u_i'}{\partial x_j}} \qquad (5\text{-}10)$$

where

$$\frac{\overline{D}}{Dt} = \frac{\partial}{\partial t} + \bar{u}_j\,\frac{\partial}{\partial x_j}$$

is the derivative following a fluid particle in the mean flow.

The energy equation for the mean flow (Eq. 5-7) does not contain any more information than the momentum equation for the mean flow because the former is obtained from the latter by algebraic manipulation. However, additional insight into the dynamics of the flow can be gained from the energy equation. The terms on the right-hand side of Eq. 5-8 that have the form $\partial/\partial x_j[\ ]$ represent transport or redistribution of energy within some volume. The work done by the body force is represented by $-F_i\bar{u}_i$. The last term in the equation stands for viscous dissipation. The terms of primary interest are those defined as I and II. Term I, when it is positive, represents the production of the wave kinetic energy by the mean wave-induced stresses $-\overline{\tilde{u}_i\tilde{u}_j}$. The same term appears with an opposite sign in the equation for wave kinetic energy (Eq. 5-9). Similarly, Term II represents the production of the turbulent kinetic energy by the mean Reynolds stresses $-\overline{u_i'u_j'}$. This term shows up as an energy source term in the equation for turbulent kinetic

energy (Eq. 5-10). The term defined as III in Eqs. 5-9 and 5-10 represents the turbulent energy production by the waves via the action of the phase-averaged turbulent Reynolds stresses $-\langle u_i' u_j' \rangle = -\overline{u_i' u_j'} - \tilde{r}_{ij}$. This term can also be rewritten as $-\overline{\tilde{r}_{ij}(\partial \tilde{u}_i / \partial x_j)}$. It is present in the energy equations for both the wave and turbulence, but with opposite signs.

Terms I, II, and III clearly show the interaction among the mean, wave, and turbulent fields. Term I denotes a summation of 9 terms, among which $-\overline{\tilde{u}\,\tilde{v}}\,(\partial \bar{u}/\partial y)$ is dominant. To find the mean velocity gradient, polynomials were least-square fitted to the mean u velocity profiles and their gradients were computed. Next, the product $-\overline{\tilde{u}\,\tilde{v}}\,(\partial \bar{u}/\partial y)$ was calculated (listed in Appendix D). The mean velocity gradient $\partial \bar{u}/\partial y$ is positive in Cases I and II (for $u_\infty \neq 0$), and $-\overline{\tilde{u}\,\tilde{v}}$ is generally negative. Thus, the wave production term is negative; in other words, we have energy transfer from the wave field to the mean field. Hussain (1983) suggested that negative production is a simple consequence of coherent structures in turbulent shear flows. Here, whether the surface waves can be classified as coherent structures is unimportant; we merely want to point out that negative production from organized flow structures is not an uncommon phenomenon. The production term was found to be more negative near the interface and decays (less negative) rapidly with depth as both $-\overline{\tilde{u}\,\tilde{v}}$ and $\partial \bar{u}/\partial y$ diminish away from the interface. Some typical profiles of this production term are shown in Fig. 61 for Case I and in Fig. 62 for Case II.

The negative production of the waves means that they increase the kinetic energy of the mean flow. If energy is drained from the waves to the mean flow, then how do the waves sustain themselves? Indeed, in

some flow situations, the waves grow with fetch. Thus far, we have neglected energy transfer from the wind at the interface. It is obvious that there exists direct energy transfer from the wind to the mean and wave fields in the water across the interface. The energy production or dissipation terms in the equations just indicate the direction of transfer within the water layer. Therefore, the mean and wave fields in the water sustain themselves by drawing energy from the wind.

Turbulence seems to draw its energy from the mean field through Term II or from the wave field through Term III. Note that the phase average is not defined in Case I; however, the phase average used in the wave and turbulent kinetic energy equations may be interpreted as some generalized phase average based on the dominant wave. Although the generalized phase average is not computed, it still allows us to gain some insight from the energy equations.

The dominant component in Term II is $-\overline{u'v'}(\partial\bar{u}/\partial y)$, and it is always positive in the experiments. Thus, energy is drained from the mean field to the turbulent field. The dominant turbulence production term was computed and summarized in Appendix D for Cases I and II. Some representative profiles for the dominant turbulence production term are shown in Figs. 63 and 64. In wind-wave experiments, the magnitude of the turbulence production Term II is higher than the magnitude of the wave production Term I at all wind speeds. However, both terms are about the same order of magnitude near the interface in some cases. On the other hand, the wave-production term is higher in magnitude than the turbulence-production term in mechanical-wave experiments. Thus, the sum of Terms I and II is positive in the mean kinetic energy equation (Eq. 5-7). That is, the net effect of the two production terms is

similar to the turbulence production term in a pure shear flow--a net drain of energy from the mean flow. This may be the reason why the turbulent intensities (RMS u' and v') have trends similar to those for flows over flat plates. However, the net production is negative in mechanical-wave experiments, which may explain the unusual trends of the turbulent intensities for mechanical-wave experiments.

There are four dominant components in Term III, namely,

$$-\overline{\tilde{r}_{11}\frac{\partial\tilde{u}}{\partial x}},\quad -\overline{\tilde{r}_{12}\frac{\partial\tilde{u}}{\partial y}},\quad -\overline{\tilde{r}_{12}\frac{\partial\tilde{v}}{\partial x}},\quad \text{and}\quad -\overline{\tilde{r}_{22}\frac{\partial\tilde{v}}{\partial y}}$$

If we assume the following

$$\tilde{u}_i = \hat{u}_i \cos(kx - \omega t - \theta_{u_i}) \tag{5-11}$$

$$\frac{\partial\tilde{u}_i}{\partial y} = k\tilde{u}_i \tag{5-12}$$

$$\tilde{r}_{ij} = \hat{r}_{ij} \cos(kx - \omega t - \theta_{r_{ij}}) \tag{5-13}$$

then the components in Term III can easily be found from the data summary in Appendix D. However, in fixed-frame experiments, there is much uncertainty in $\theta_{r_{ij}}$. The uncertainty is not due to instrumentation but to kinematics. All $\theta_{r_{ij}}$ seem to have a value about 180° relative to $\tilde{\eta}$. The $\tilde{r}_{ij}$ are expected to be higher near the interface. Since the measurements were made in a fixed-frame, the probe was closest to the interface at the wave trough, which is the 180° phase angle point of $\tilde{\eta}$. So the phase angles of $\tilde{r}_{ij}$ may be due to kinematics of the waves and not due to dynamics. The effects of the wavy motion may not be as severe at deeper depths and $\theta_{r_{ij}}$ may indeed be the true phase angles, but Term III at such depths (~ 1/k) is most likely negligible.

The last term in Eqs. 5-8 to 5-10 denotes viscous dissipation. The dissipative time scale is usually much smaller than the time scale of the waves and the large eddies. Thus, the viscous dissipation term in the mean or wave kinetic energy equation is small. Most of the kinetic energy is dissipated by the viscous dissipation term in the turbulent kinetic energy equation.

5.4.6 Summary

In Sec. 5.4, the characteristic scales obtained in the experiments were used to simplify the governing equations. Not only do the simplified equations give further theoretical insight to the present research, but also they bear out many of the experimental observations. The mean, wave, and turbulent flow fields are shown to be closely coupled in the energy equations. Some of the production terms are estimated using the experimental data and the directions of transfers are identified. It is not the aim of this study to solve these equations, but they do lend themselves for future research and analysis.

5.5 IMPLICATIONS OF THE WAVE-FOLLOWING FRAME RESULTS

The wave-following coordinate system is the most logical reference frame for the mechanical-wave experiments from either an experimental or theoretical viewpoint. This system allows velocity measurements above the wave trough and clearly defines the interfacial boundary for the governing equations. However, this reference frame has some minor shortcomings. An order-of-magnitude analysis was performed on the fixed-frame governing equations in Sec. 5.4. A similar analysis can certainly be done on the wave-following frame equations. Unfortunately, such a task is quite formidable, because the coordinate transform introduces many extra inhomogeneous terms into the equations. A complete

analysis is beyond the scope of this study. Instead, analytical relationships are developed in Sec. 5.5.1 which relate the measured quantities in (x,y,z,t) and (x*,y*,z*,t*). Not only do these relationships allow us to compare some of the measured quantities in the two coordinate systems, but they also demonstrate the significance of utilizing the wave-following frame as is shown in Sec. 5.5.2.

5.5.1 Relationships Between Measured Quantities in (x,y,z,t) and (x*,y*,z*,t*) Coordinates and Their Implications

The phase average is well-defined in both (x,y,z,t) and (x*,y*,z*,t*) coordinates provided $-y > a$. If $x = x^*$ and $z = z^*$, as in the experiments $(x, y = h + f\tilde{\eta})$ and $(x^*, y^* = h)$ with $-h > a$ represent the same spatial point. Then, as shown by Hsu et al. (1977), the phase averages in the two reference frames are related by:

$$\langle g\rangle(x,y,t)\Big|_{y=h+f\tilde{\eta}} = \langle g\rangle(x^*,y^*,t^*)\Big|_{y=h} \tag{5-14}$$

By use of a Taylor series expansion, $\langle g\rangle(x,y,t)\Big|_{y=h}$ can be written as

$$\begin{aligned}
&\langle g\rangle(x,y,t)\Big|_{y=h} \\
&\quad = \langle g\rangle(x,h + f\tilde{\eta} - f\tilde{\eta},t) \\
&\quad = \langle g\rangle(x,h + f\tilde{\eta},t) - \left[\frac{\partial}{\partial y}\langle g\rangle(x,h + f\tilde{\eta},t)\right] f\tilde{\eta} \\
&\qquad + \left[\frac{\partial^2}{\partial y^2}\langle g\rangle\ (x,h + f\tilde{\eta},t)\right] \frac{f^2\tilde{\eta}^2}{2} + O(\tilde{\eta}^3)
\end{aligned} \tag{5-15}$$

The above expression is valid for all values of $f\tilde{\eta}$ provided $\langle g\rangle$ is continuous together with its higher derivatives (say up to second or third order) on an interval containing h and $h + f\tilde{\eta}$. A rigorous proof is not given here to show that $\langle g\rangle$ satisfies these conditions; instead a heuristic argument is given below. Since $\langle g\rangle$ is obtained by phase

averaging, it is periodic and usually sufficiently smooth to satisfy the above conditions. For example, $\tilde{u}$ and $\tilde{v}$ are almost sinusoidal, so their derivatives exist almost everywhere. In addition, owing to their sine-like behavior, convergence of the series expansion is implied. Then, using Eq. 5-14 and the chain rules in evaluating the derivatives, Eq. 5-15 become

$$\langle g\rangle(x,y,t)\Big|_{y=h} = \langle g\rangle(x^*,y^*,t^*)\Big|_{y^*=h} - f\tilde{\eta}\left.\frac{\partial\langle g\rangle}{\partial y^*}\right|_{y^*=h} + \tilde{\eta}^2\left.\frac{\partial}{\partial y^*}\left(\frac{f^2}{2}\frac{\partial\langle g\rangle}{\partial y^*}\right)\right|_{y^*=h} + O(\tilde{\eta}^3) \qquad (5\text{-}16)$$

Next, we decompose $\langle g\rangle$ into $\bar{g}$ and $\tilde{g}$ and obtain, for $-h > a$,

$$\bar{g}(x,y)\Big|_{y=h} = \left[\bar{g}(x^*,y^*) - f\overline{\tilde{\eta}\frac{\partial\tilde{g}}{\partial y^*}} + \overline{\tilde{\eta}^2}\frac{\partial}{\partial y^*}\left(\frac{f^2}{2}\frac{\partial\bar{g}}{\partial y^*}\right)\right]_{y^*=h} + O(\tilde{\eta}^3) \qquad (5\text{-}17)$$

$$\tilde{g}(x,y,t)\Big|_{y=h} = \tilde{g}(x^*,y^*,t^*)\Big|_{y^*=h} - f\tilde{\eta}\left.\frac{\partial\bar{g}}{\partial y^*}\right|_{y^*=h} + O(\tilde{\eta}^2) \qquad (5\text{-}18)$$

These two equations show the relationships for a measured quantity in the two coordinate systems at the same <u>mean</u> depth. The difference between $\bar{g}(x,y)$ and $\bar{g}(x^*,y^*)$ is of second order in the wave quantity. The difference in $\tilde{g}(x,y,t)$ and $\tilde{g}(x^*,y^*,t^*)$ is of first order. Although these equations are similar to those of Hsu et al. (1977), the wave quantities are much larger in this study and the equations have different implications here.

If g represents the horizontal velocity u, then even though the difference between the mean velocity is of second order in the wave quantity, the higher-order term may not be small because $\bar{u}$ is of the same order as $\tilde{u}$. The magnitude of the second term in Eq. 5-17 is

$$\overline{f\tilde{\eta}\,\frac{\partial \tilde{g}}{\partial y^*}} \sim a\,\frac{a\omega}{y\eta} \sim ka(a\omega) \qquad (5\text{-}19)$$

Using the linear water-wave theory, one finds that this term is about 5 mm/s near the surface for the present experiments. The measured mean horizontal velocity is higher in the wave-following frame experiments than in the fixed-frame experiments at equivalent mean depths and wind speeds. The difference is attributed to the higher-order terms in Eq. 5-17, especially the second term (Eq. 5-19). They are on the order of 5-10 mm/s, which agree with the observed differences. Away from the interface, the second-order terms are negligible due to the decay of the wave and the function f with depth. Although, the higher-order terms in Eq. 5-17 may be large compared to the mean velocity, they represent only a small percentage of the mean velocity defect $\overline{u}_s - \overline{u}$. So the mean velocity defect in the wave-following frame can be interpreted as the same quantity in the fixed frame. Similarly, if g represents the vertical velocity v, the second term in Eq. 5-17 is small even though $\tilde{v}$ is big, because $\tilde{\eta}$ and $\tilde{v}$ are almost 90° out of phase; the third term is also small because $\overline{v}$ ~ constant and $\partial\overline{v}/\partial y \sim 0$. Thus, the mean vertical velocity can be taken to be the same in both coordinates also.

The mean square wave quantities $\overline{\tilde{g}^2}$ in the two coordinates are related by:

$$\overline{\tilde{g}^2}(x,y)\big|_{y=h} = \left[\overline{\tilde{g}^2}(x^*,y^*) - 2\overline{\tilde{g}\tilde{\eta}}\,\frac{\partial \overline{g}}{\partial y^*} + f^2\overline{\tilde{\eta}^2}\left(\frac{\partial \overline{g}}{\partial y^*}\right)^2\right]_{y^*=h} + O(\eta^3) \qquad (5\text{-}20)$$

If $\tilde{g}$ represents $\tilde{u}$, we have the following order-of-magnitude estimate for Eq. 5-20:

Term 1 $\quad \overline{\tilde{u}^2} \sim a^2\omega^2$

Term 2 $\quad \overline{\tilde{u}\tilde{\eta}} \frac{\partial \bar{u}}{\partial y^*} \sim \frac{a^2 \omega u_s}{\delta} = a\omega\left(\frac{au_s}{\delta}\right)$

Term 3 $\quad f^2 \overline{\tilde{\eta}^2}\left(\frac{\partial \bar{u}}{\partial y^*}\right)^2 \sim \left(\frac{au_s^2}{\delta}\right)$ because $f \sim 1$ near the interface

Term 2 is small because $a < \delta$, but cannot be ignored entirely, especially near the interface where the mean velocity gradient $\partial\bar{u}/\partial y^*$ is not negligible. However, in the region $-y^* \geq a$, $\partial\bar{u}/\partial y^*$ is not changing rapidly, so Term 2 remains very small. Term 3 is very much smaller than Term 1 and can be neglected. When $\tilde{g}$ represents $\tilde{v}$, Term 2 is even smaller than that for $\tilde{u}$, because $\tilde{\eta}$ and $\tilde{v}$ are almost 90° out of phase and the mean velocity gradient $\partial\bar{v}/\partial y^*$ is practically zero. Hence, the RMS $\tilde{u}$ or $\tilde{v}$ can be considered the same in both coordinates.

The above discussion explains why many of the wave-following results, such as RMS $\tilde{u}$ and the velocity defect $u_s - \bar{u}$, appear the same in both coordinates for $-y > a$. Unfortunately, it is not possible to establish a relationship for the turbulent component g' in the two coordinate systems, because higher-order derivatives may not exist for g'.

There is much difficulty in relating the $\tilde{r}_{ij}$ measured in the two reference frames. First, these quantities are generally of small magnitude and have large uncertainties, so the series expansion technique may not be valid. Second, the measured phase angles $\theta_{\tilde{r}_{ij}}$ in the fixed-frame experiments may not represent the actual phase angles due to the kinematics of the waves. Third, despite the data scatter, the $\tilde{r}_{ij}$ do not exhibit any clear trend in the wave-following frame. Hence, we do not attempt to develop any relationships to connect the $\tilde{r}_{ij}$ in different frames.

We have shown that many measured quantities of interest are coordinate independent. Thus, we can compare these quantities without

resorting to complicated equations, but the equivalence of coordinate frames for $-y > a$ need not be valid for higher-order turbulent quantities. As a cautionary note, the equivalence should not be taken as a proof that the fixed-frame equations are applicable to the wave-following frame.

5.5.2 Significance of the Wave-Following Frame Movements

The phase average $\langle g \rangle$ clearly is not defined for $-y < a$. By use of a traditional perturbation scheme, $\bar{g}(x,y)$ and $\tilde{g}(x,y,t)$ at $-y < a$ can be calculated from $\bar{g}(x^*,y^*)$ and $\tilde{g}(x^*,y^*,t^*)$ according to Eqs. 5-17 and 5-18. However, interpretation of the wave-following measurements in such a manner would seem to defeat the purpose of using the wave-following coordinates. Here, we want to point out what we have gained in using the transformed coordinates and suggest possible improvements in future research.

In mechanical-wave fixed-frame experiments (Case II), the mean velocity defect profiles in wall coordinates clearly illustrate the shortcomings of the fixed-frame measurements. The decrease of u^+ at $-y^+$ around 50, as pointed out in Sec. 4.2.3 and Sec. 5.2, is due to averaging velocities at points close to the wave troughs and points some distance ($\simeq 2a$) from the wave peaks. In the wave-following frame (Case III), these kinematic effects of the waves are totally eliminated because the velocity probe is essentially at some constant distance from the mobile interface. Furthermore, the velocity profiles at low wind speeds clearly show the existence of the buffer layer and the viscous sublayer which cannot be revealed in the fixed-frame system. The existence of these layers are known from other experiments, such as those of McLeish and Putland (1975), and Wu (1975). However, their measurements

were Lagrangian and are of limited value in comparing with Eulerian data. Here, the wave-following frame measurements are still Eulerian quantities.

In the wave-following coordinates, the friction velocities for the low wind-speed experiments can be found from the velocity profiles in the viscous sublayer rather than relying on the usual velocity profile curve-fitting procedure. The friction velocities obtained using this technique agree well with the direct turbulent shear stress measurements.

The velocity profile curve-fitting method may not work for the profiles in this study (fixed or wave-following frame) because the waves affect the slopes of the profiles; thus, the slopes need not be constant in the logarithmic region. On the other hand, it is possible to obtain the friction velocity without directly measuring the turbulent shear stress for low wind-speed flows. One just uses the wave-following frame to obtain a mean velocity down or near to the viscous sublayer and the friction velocity is given by: $u_* = [\nu(\overline{u}_s - \overline{u})/(-y^*)]^{1/2}$ as in Sec. 4.3.4, for $-y^*$ in the viscous sublayer.

In Case III, the mean velocity defect profiles in wall coordinates follow the logarithmic trend which implies that the mean profiles follow the undulating motion of the mechanical waves. Thus, the dominant waves do not contribute to the "roughness" of the flow. The ripples, on the other hand, seem to have some effect on the flow "roughness," as the mean profiles shift downward slightly with increasing wind speed.

The turbulent intensities (RMS u' and v') in the wave-following frame appear as an extension of the fixed-frame results to shallower depth ($-y^* < a$). The RMS u' and v' are isotropic and increase in

magnitude as the interface is approached. Similar trends are observed in the fixed-frame experiments, but the behavior of the turbulent intensities near the interface could not have been anticipated from the fixed-frame measurements. The isotropy of the turbulent intensities is unexpected, but may be explained as follows. The distribution of ripples appears fairly uniform, so the random ripple-induced velocities are expected to be isotropic. Furthermore, the ripple-induced velocities are strongest near the interface. In both Cases II and III, the ripple-induced velocities are included in the calculation of RMS u' and v'. Thus, the turbulent intensities near the surface are mostly dominated by the ripple-induced velocities. Therefore, the RMS u' and v' are isotropic due to isotropy of the ripple-induced velocities. However, the RMS u' and v' have been shown to scale with the turbulent velocity and length scales, which leads us to believe that there is no ambiguity in defining the ripple-induced velocities as turbulence. Bole and Hsu (1969) suggested that there are interactions between the ripples and the dominant waves, and since the ripple-induced velocities have turbulent characteristics, there may be interactions of the main waves with turbulence through the action of the ripples.

The linear water-wave theory was shown to give fairly good results for the wave-induced velocities for $-y > a$. In Sec. 5.5.1, we showed that the RMS wave-induced velocities are practically coordinate independent. Here, since $y = h$ and $y^* = h + f\tilde{\eta}$ both have the same mean depth, we can compare the calculated wave-induced velocities given by the linear theory at $y = h$ with the measured values at $y^* = h + f\tilde{\eta}$. The linear theory also gives good results for the wave-induced velocities for $-y^* > a$. It is possible to calculate the wave-induced

velocities for $-y < a$ though these velocities may not be defined in the fixed frame. Again, we can compare the calculated wave-induced velocities for $-y < a$ with the corresponding measured values at $-y^* < a$ because $\overline{y} = y = \overline{y^*}$. The calculated velocities agree with the measurements fairly well at $u_\infty = 0.0$ and 1.7 m/s, the difference is about 10% for the RMS $\tilde{u}$ and only about 6% for the RMS $\tilde{v}$. At higher wind speeds, the agreement is not as good in this region ($-y^* < a$), because the calculated values include the ripple-induced velocities which the measured RMS $\tilde{u}$ and $\tilde{v}$ do not. This exercise shows that even though the calculated velocities are from a linear theory in the fixed frame, the calculated values agree very well with the measured values in the wave-following frame at equivalent mean depths, even at depths less than the wave amplitude.

The mean wave-induced shear stress $-\overline{\tilde{u}\,\tilde{v}}$ appears to have trends similar to those in the fixed-frame experiments, except for the case of $u_\infty = 2.5$ m/s, where $-\overline{\tilde{u}\,\tilde{v}}$ is positive in some regions of the flow. This could be due to data scatter, but the distribution of $-\overline{\tilde{u}\,\tilde{v}}$ with depth is relatively smooth which suggests that the observed trend is not caused by data scatter. Also, at about this wind speed, similar changes in $-\overline{\tilde{u}\,\tilde{v}}$ occur on the air side of the interface as shown by Hsu and Hsu (1983). However, a definitive conclusion cannot be made at this stage, suggesting further experiments around this wind speed.

The turbulent shear stress $-\overline{u'v'}$ measurements are of the correct order of magnitude but there are fair amounts of data scatter. Consistent friction velocities cannot be obtained from these measurements. This, however, does not mean that the wave-following frame is unsuitable for such measurements, but just that the limits of the instruments have been reached.

Although we have not developed the energy equations in the wave-following coordinates, some preliminary analyses show that many of the terms are very similar to those in the fixed-frame equations. Therefore, we made calculations on some of the dominant kinetic energy production terms, such as $-\overline{\tilde{u}\,\tilde{v}}(\partial\bar{u}/\partial y^*)$ and $-\overline{u'v'}(\partial\bar{u}/\partial y^*)$. Their values can be found in Appendix D. Some representative profiles of these terms are shown in Figs. 65 and 66. Despite the data scatter, the term $-\overline{\tilde{u}\,\tilde{v}}(\partial\bar{u}/\partial y^*)$ is generally negative, but it is always positive very close to the interface (the first or second data points). It is unclear whether this is mere coincidence or due to some physical phenomena; only further experimentation may resolve this mystery. If the term $-\overline{\tilde{u}\,\tilde{v}}(\partial\bar{u}/\partial y^*)$ is indeed positive very close to the interface, then this implies the waves draw their energy from the mean flow in that region. This result is not unlike what Hsu and Hsu (1983) found on the air side of the interface.

5.5.3 Summary

This first attempt to extend the wave-following coordinate system from the air side of the interface to the water side has proven to be very successful. Not only is the wave-following frame able to extend the fixed-frame results, but also interesting features which could not have been discovered in a fixed frame are revealed. However, refinement of the LDA is needed in order to resolve higher-order wave or turbulent terms.

Table 9

Summary of Characteristic Scales

Case	u_∞ (m/s)	u_S (mm/s)	δ (mm)	$u_\star$ (mm/s)	$(\overline{\tilde{u}_o^2})^{1/2}$ or $2\pi f_D \tilde{\eta}_S/\sqrt{2}$ (mm/s)	y_η or $1/k$ (mm)	f_D (Hz)
I	1.5	40	141	2.10	0.29	-	-
	2.6	70	310	3.40	4.44	-	6.1
	3.2	73	348	4.94	38.26	9.3	5.2
	4.7	93	264	7.20	76.67	19.9	3.5
	6.7	137	249	11.30	108.34	32.6	2.7
	9.9	204	354	17.50	139.84	45.1	2.4
	13.1	270	298	27.50	194.06	58.2	2.0
II	0.0	-16	-	-	97.39	248	1.0
	1.7	24	99	2.20	93.61	248	1.0
	2.5	41	102	3.35	97.08	248	1.0
	4.1	62	168	5.35	98.23	248	1.0
	6.2	108	171	9.23	92.68	248	1.0
III	0.0	-15	-	-	94.59	248	1.0
	1.7	24	99†	2.20†	92.99	248	1.0
	2.5	43	102†	3.35†	97.43	248	1.0
	4.1	60	168†	5.35†	95.70	248	1.0
	6.1	110	171†	9.23†	90.95	248	1.0

†From Case II.

CHAPTER 6

CONCLUSIONS AND RECOMMENDATIONS

6.1 CONCLUSIONS

The main objectives of this study have been accomplished. The following conclusions can be drawn from the results and discussions presented in Chaps. 4 and 5.

1. This study presents a comprehensive data set on momentum transfer at an air-water interface under a wide range of surface conditions and in two coordinate systems. The data set should prove very useful in evaluating current or future computational schemes as well as turbulence models for air-sea interaction.
2. A nonintrusive wave-following velocity probe extends the wave-following coordinate system (Hsu et al., 1981) from the air side of the interface to the water side. The wave-following velocity probe can reveal features in the flow which could not have been found from a fixed frame.
3. It is possible to separate the flow field beneath the air-water interface into three constituent fields: the mean, the wave, and the turbulent fields. Each of these fields can be characterized by significant velocity and length scales.
4. A simple analysis of the governing equations using the experimentally obtained characteristic scales show that there are interactions among the mean, wave, and turbulent fields.
5. The wave field affects the mean flow directly, which leads to a change in slope in the steady form of the law of the wall, although

the logarithmic region persists in the velocity profiles. Also, the kinetic energy of the mean flow is augmented by the waves.

6. Small-amplitude water-wave theory gives good predictions for the measured wave quantities.

7. Turbulence draws its energy mainly from the mean flow. Turbulence can be augmented by the waves because the waves affect the mean flow.

8. Turbulent intensity profiles in wind-wave experiments are similar to flows over flat plates, for example Klebanoff (1955).

9. In mechanical-wave experiments, the turbulent intensity profiles have very different trends from those in wind-wave experiments. This may be due to the interaction of the ripple-induced velocities with that of the dominant wave.

10. Direct interactions between the waves and turbulence, such as $-\overline{\tilde{r}_{ij}(\partial\tilde{u}_i/\partial x_j)}$ in the energy equations, cannot be quantified satisfactorily. These interaction terms are probably small compared to other types of interactions.

6.2 RECOMMENDATIONS FOR FUTURE WORK

The results documented here represent the major part of the study. Further analysis of the data may include the following:

1. A careful study of the velocity spectra may reveal how the various spectral components of the wave and turbulence vary with depth and wind speed. Then, from this information, we can examine the frozen turbulence model postulated by Lumley and Terray (1982).

2. Velocity profiles at fixed phase angles along the waves can be obtained for mechanical-wave experiments. This can give valuable

information as to how the wave and mean velocities change with phase (i.e., position) along the main wave.

3. The mean and wave momentum equations in the wave-following coordinates need to be derived. An order-of-magnitude analysis can then be performed on these equations which may provide some further insights into the wave-following frame results.
4. An analysis of the energy equations in the form as those of Hsu et al. (1982) may further quantify the partition of energy in the vertical and horizontal directions.

The merits of experimental studies about the air-water interface are clearly illustrated in this study. The following are some recommendations for future research:

1. The wave-following LDA system needs to be improved to allow more accurate measurements of the turbulent shear stresses.
2. The present experimental program can be run at different fetches to quantify the effects of wave growth on water velocity. This enables us to examine the gradual development of the interactions between the waves and the mean flow.
3. It may be possible to develop a wave-following coordinate system for the wind-wave experiments. This is a non-trivial task because the random nature of the wind waves pose the biggest challenge in data acquisition and reduction. However, a great deal can be learned from a successful wave-following attempt in this case.
4. A complete three-dimensional map of the velocity field in the water can improve on the present data set. The total kinetic energy for the mean, wave, and turbulent flow fields can then be determined. This, when coupled with simultaneous three-dimensional velocity

measurements on the air side, may very well be the ultimate experiment for momentum and energy transfers at an air-water interface.

5. A study of the total energy transfer can be achieved by mapping out the temperature field in some of the above-mentioned experiments.

APPENDIX A

WAVE-SEPARATION METHOD

The theoretical framework for the wave-separation method is outlined in Sec. 2.2.2 and Howe et al. (1981). Some of the essential steps are given below.

Let $\hat{x}$ and $\hat{y}$ be some measured quantities (such as u, v) at a fixed fetch. Each quantity can be decomposed into three parts, i.e.,

$$\hat{x} = \bar{x} + \tilde{x} + x'$$

$$\hat{y} = \bar{y} + \tilde{y} + y'$$

Then, after defining

$$x = \tilde{x} + x'$$

$$y = \tilde{y} + y',$$

a linear operator L is defined as follows:

$$\tilde{x}(t) = \int_{-\infty}^{\infty} L_x(\alpha)\eta(t - \alpha)d\alpha = L_x(t) * \eta(t) \qquad (A.1)$$

and

$$\tilde{y}(t) = \int_{-\infty}^{\infty} L_y(\beta)\eta(t - \beta)d\beta = L_y(t) * \eta(t) \qquad (A.2)$$

where $\eta(t)$ denotes the water surface elevation at the same fetch, and * denotes the convolution process.

The cross-correlation of $\tilde{x}$ and $\tilde{y}$ is defined as:

$$\overline{\tilde{x}(t)\tilde{y}^*(t - \tau)} = \int_{-\infty}^{\infty}\int_{-\infty}^{\infty} L_x(\alpha)L_y^*(\beta)\overline{\eta(t - \alpha)\eta^*(t - \tau - \beta)}d\alpha d\beta$$

where * denotes the complex conjugate. If it is assumed that $\tilde{x}$ and $\tilde{y}$ are the outcomes of stationary random processes, then the cross-correlation function is:

$$R_{\tilde{x}\tilde{y}}(\tau) = \int_{-\infty}^{\infty}\int_{-\infty}^{\infty} L_x(\alpha)L_y^*(\beta)R_{\eta\eta}(\tau + \beta - \alpha)d\alpha d\beta$$

$$= L_x(\tau) * L_y^*(-\tau) * R_{\eta\eta}(\tau)$$

Fourier transforming the above equation gives:

$$S_{\tilde{x}\tilde{y}}(f) = L_x(f)L_y(f)S_{\eta\eta}(f) \tag{A.3}$$

Also,

$$\overline{x(t)\eta(t-\tau)} = \overline{[\tilde{x}(t) + x'(t)]\eta(t-\tau)} = \overline{\tilde{x}(t)\eta(t-\tau)}$$

because η is assumed to correlate only with the wave component. Next, use of Eqs. A.1 and A.2 yields:

$$L_x(f) = \frac{S_{xy}(f)}{S_{\eta\eta}(f)} \quad \text{and} \quad L_y(f) = \frac{S_{y\eta}(f)}{S_{\eta\eta}(f)}$$

Therefore, Eq. A.3 can be written as:

$$S_{\tilde{x}\tilde{y}}(f) = \frac{S_{x\eta}(f)S_{y\eta}(f)}{S_{\eta\eta}(f)} \tag{A.4}$$

The orthogonality property of the decomposition also implies:

$$R_{xy}(\tau) = R_{\tilde{x}\tilde{y}}(\tau) + R_{x'y'}(\tau)$$

or in the frequency domain

$$S_{xy}(f) = S_{\tilde{x}\tilde{y}}(f) + S_{x'y'}(f) \tag{A.5}$$

Hence, given x, y, and η, $S_{xy}(f)$, $S_{y\eta}(f)$, and $S_{\eta\eta}(f)$ can be found. Then, from Eqs. A.4 and A.5, $S_{\tilde{x}\tilde{y}}(f)$ and $S_{x'y'}(f)$ can be deduced. The second order statistics of x and y are found by integrating the corresponding spectra, i.e.,

$$\overline{\tilde{x}\,\tilde{y}} = \overline{\tilde{x}(t)\tilde{y}(t)} = \int_{-\infty}^{\infty} S_{xy}(f)df$$

$$\overline{x'y'} = \overline{x'(t)y'(t)} = \int_{-\infty}^{\infty} S_{x'y'}(f)df$$

APPENDIX B

ANALYSIS OF THE OPTICAL WAVE-FOLLOWER SYSTEM

In this appendix, we first outline the procedures used in calculating the intersecting point of the three LDA laser beams when they are scanned through multiple interfaces (air, glass, and water). Then, we show that the Doppler shifts on the laser beams due to the scanning mirror are identically zero when the wave-follower is used in a homogeneous medium. Next, we extend the results for the single medium to the air-glass-water system by providing some heuristic arguments. A complete theoretical treatment of the multiple media problem is too involved to present here. Furthermore, we have demonstrated in the wave-follower qualification tests that the heuristic arguments are indeed correct.

The LDA has three laser beams comprising the two-component, two-color system. The orientation of the beam is shown in Fig. B.1. The blue and the green beams lie in the horizontal plane GOB while the cyan beam is equidistant from both the blue and green beams. Also, the three beams lie on the surface of a cone with its vertex at the focal point O and the base at the front lens of the LDA in Fig. B.1. The mirrors in the wave-follow system simply fold this "cone" at different sections. Therefore, there is no loss of generality in considering the section of the "cone" which begins at the moving mirror instead of at the front lens of the LDA. Thus, the orientation of the three LDA laser beams when they traverse through the air-glass-water media can be represented by Figs. B.2 and B.3. The definitions of the angles and distances in the figures are self-explanatory. In Fig. B.2, the line BOG lies along

the axis of rotation of the scanning mirror and BO' and GO' represent the paths of the blue and green laser beams, respectively. Then in Fig. B.3, CO' represents the path of the cyan beam. Note that OO' in Fig. B.3 represents the projection of the surface BO'G in Fig. B.2 in the plane of the paper. The reader is cautioned that OO' does not represent any laser beam in that plane in Fig. B.3, except perhaps at the point where the blue and the green beams intersect. Therefore, the angles along OO' do not satisfy Snell's law of refraction. In is clear from Fig. B.2 that the blue and green beams always intersect. However, the intersection point of the blue and green beams may not intersect exactly with the cyan beam for non-zero values of θ_s because the sine function in Snell's law is a nonlinear function.

We first find the intersection point (x_{AB}, y_{AB}) of the blue and green beams. This point is taken to be the position of the probe volume. Using Snell's law of refraction, some geometry, and the following nomenclature, one can derive the key relationships.

The nomenclature is

n_a - refractive index of air (1.00)

n_g - refractive index of glass (1.50)

n_w - refractive index of water (1.33)

m - thickness of glass (6.4 mm)

ℓ - distance of axis of rotation of scanner mirror to glass (72 mm)

f - distance of axis of rotation of scanner mirror to measuring point in air (411.5 mm)

a - half distance between the blue and green laser beams at the optical scanner mirror (25.6 mm)

α - half intersecting angle of LDA beams in air (2.5°)

In Fig. B.2, we have then

$$n_a \sin \theta_s = n_g \sin \theta_s' = n_w \sin \theta_s''$$

$$a' = \left(1 - \frac{\ell}{f \cos \theta}\right) a$$

$$a'' = a' - m \sin \alpha' \tan \theta_s'$$

$$\alpha' = \tan^{-1}\left(\frac{\tan \alpha}{\sin \theta}\right)$$

$$x_{AB} = \ell + m + a''\left(\frac{\cot \theta_s''}{\sin \alpha'}\right) \qquad \text{(B-1)}$$

$$y_{AB} = \ell \tan \theta + m \tan \theta_s' \cos \alpha' + a'' \cot \alpha' = f \sin \theta \qquad \text{(B-2)}$$

In Fig. B.3, we have

$$\cos \psi' = \frac{\cos \theta_s'}{\sin \alpha' \sin \theta_s'}$$

$$\cos \psi'' = \frac{\cos \theta_s''}{\sin \alpha' \sin \theta_s''}$$

Note that $\psi' \neq \theta_s'$, $\psi'' \neq \theta_s''$ in general, but $\psi = \theta$.

$$x_{PM}'' = \frac{c_M'' - c_P''}{[\tan \psi'' - \tan(\theta'' + \Delta\theta'')]}$$

$$y_{PM}'' = x_{PM}''(\tan \psi'') + c_P''$$

$$c_P'' = y_P' - x_M(\tan \psi'')$$

$$c_M'' = y_M' - x_M[\tan(\theta'' + \Delta\theta'')]$$

$$y_P' = y_P + (\tan \psi')(x_M - x_\ell)$$

$$y_M' = y_M + [\tan(\theta' + \Delta\theta')](x_M - x_\ell)$$

$$n_a \sin \theta = n_g \sin(\theta' + \Delta\theta') = n_w \sin(\theta'' + \Delta\theta'')$$

$$y_M = y_P - h = y_P - \frac{k \cos \alpha}{\sin(\theta + \alpha)}, \quad k = \tan \alpha(f - \ell \sec \theta)$$

$$y_P = \ell \tan \theta$$

The equation for the line $c''_M O'$ is given by

$$y'_M - [\tan(\theta'' + \Delta\theta'')]\, x_M - c''_M = 0 \qquad (B\text{-}3)$$

Using Eqs. B-1 and B-2, one can calculate the location of the point (x_{AB}, y_{AB}). The minimum distance between (x_{AB}, y_{AB}) and the line $C''_M O'$ (Eq. B-3) gives the limit on the maximum scan angle (θ_s) for a given laser beam width (at the probe volume) because if this distance exceeds the beam diameter near the probe volume, the cyan beam does not intersect with the blue and green beams and the probe volume is undefined. In this study, the beam waist was about 0.15 mm and θ_s was limited to about 7° in scanning through multiple interfaces. At some points along the scan path, the three laser beams may not intersect exactly at the beam waist, leading to perhaps additional broadening of the LDA signal as pointed out by Hanson (1976). However, such broadening cannot be too severe because of the relatively long focal length of the front lens. This was further confirmed by the results of the qualifying experiments.

Figure B.4 depicts the side view of the optical wave-follower when it is used in a homogeneous medium. The definitions of the various angles and lengths are apparent in the figure. The point O', which represents the LDA probe volume, moves with some velocity u_p as the scanning mirror rotates with an angular velocity $\dot{\theta}$. In addition, we have the following relationships:

$$\theta = \theta_{max} \sin \omega_o t$$

$$\dot{\theta} = \frac{d\theta}{dt} = \omega_o \theta_{max} \cos \omega_o t$$

$$\omega_o = 2\pi f_o$$

where f_o is the frequency of oscillation of the scanner mirror and θ_{max} is the maximum scan angle.

In Fig. B.4, CAO' represents the path of the cyan laser beam, GOO' represents the projection of the surface where the blue and green beams lie onto the plane of the figure, and MM' represents the scanner mirror.

Because the direction of u_p is perpendicular to OO', u_p has no velocity component in the plane containing the blue and green beams between OO'. Furthermore, the blue and green beams reflect off the mirror along the rotational axis where the velocity of the mirror is zero. Thus, the blue and green beam frequencies undergo no Doppler shift due to the scanning mirror.

When the mirror rotates through an angle θ, the point O' (see Fig. B.4) moves through an arc length of $f(2\theta)$. There is a factor of 2 because from the law of reflection, a reflected ray rotates twice the angle θ as the mirror rotates through an angle θ. Thus, the tangential velocity of the point O' is the time rate of change of the arc length, i.e., $u_p = f(2\dot{\theta})$. The velocity u_p has a component in the direction of O'A, so we have

$$u_p \cos\left(\frac{\pi}{2} + \alpha\right) = - u_p \sin \alpha = - 2f\dot{\theta} \sin \alpha$$

which causes a frequency shift of $(-2f\dot{\theta} \sin \alpha)/\lambda$ to the cyan beam, where λ is the wavelength of the cyan beam. The point A on the mirror has a tangential velocity $u = r\dot{\theta}$ which has components in the directions AC and AO', and the net frequency change to the cyan beam due to u is $(2u/\lambda) \cos[\pi/2 - (\theta - \beta + \alpha)]$. Therefore, the net change of frequency of the cyan beam as it travels from C to O' is

$$- \frac{2t\dot{\theta} \sin \alpha}{\lambda} + \frac{2r\dot{\theta}}{\lambda} \sin(\theta - \beta + \alpha) \qquad (B\text{-}4)$$

$$= \frac{2\dot{\theta}}{\lambda} [- f \sin \alpha + r \sin(\theta - \beta + \alpha)]$$

$$= 0$$

because

$$f \sin \alpha = r \sin(\theta - \beta + \alpha) \equiv d \qquad (B\text{-}5)$$

where d is indicated by the dashed line in Fig. B.4. Equations B-4 and B-5 are very general equations, the only constraint is that the light beams originate within the cone of light bounded by the LDA lens and the focal point. Hence, the scanning mirror produces no Doppler shift to the outgoing laser beams and the incoming backscattered light when the wave-follower is used in a homogeneous medium.

When the wave-follower is used in the air-glass-water system, Eqs. B-4 and B-5 are still valid for the following reason. The point O' in Fig. B.3 indicates the actual position of the probe volume inside the test facility. However, to an observer outside the facility, the apparent intersection point of the laser beams, which is defined by the beam angles in the air, is at O". Thus, as far as the receiving optics of the LDA is concerned, the probe volume still appears as if it were in a homogeneous medium and the scanning mirror produces no Doppler shift to the laser beams. The fact that the beams traverse through a series of media and back only constrains the maximum scan angle but does not introduce any further frequency shift to the beams.

In practice, it is almost impossible to have the aluminized surface of the scanner mirror passed through the axis of rotation of the scanner. The effect of this is that the probe volume does not follow

exactly an arc as the mirror rotates. This minor defect can be minimized by aligning the blue and the green laser beams along a line on the scanner mirror closest to the axis of rotation and parallel to it. Then, the maximum deviation of the probe volume path from an arc is 0.1 mm for a scan angle of 10°.

APPENDIX C

LEAST-SQUARES COSINE-FITTING TECHNIQUES

To fit a sequence of data $y_i(t_i)$, $i = 1, 2, \ldots, n$ with a cosine waveform described by:

$$\hat{y} = A \cos(\omega t - \theta) ,$$

one has to find A and θ such that

$$S = \Sigma(y_i - A \cos(\omega t_i - \theta))^2$$

is a minimum. The conditions for the existence of a minimum are:

$$\frac{\partial S}{\partial A} = \frac{\partial S}{\partial \theta} = 0$$

Thus,

$$\Sigma\, y_i \cos(\omega t_i - \theta) = A\, \Sigma \cos^2(\omega t_i - \theta) \qquad (C.1)$$

$$\Sigma\, y_i \sin(\omega t_i - \theta) = A\, \Sigma \sin(\omega t_i - \theta) \cos(\omega t_i - \theta) \qquad (C.2)$$

Let

$$S_1 = \Sigma\, y_i \cos\omega t_i \quad ; \quad S_2 = \Sigma\, y_i \sin\omega t_i$$

$$S_3 = \Sigma \cos^2\omega t_i \quad ; \quad S_4 = \Sigma \sin^2\omega t_i$$

$$S_5 = \Sigma \cos\omega t_i \sin\omega t_i$$

then Eqs. C.1 and C.2 can be written as follows:

$$S_1 \cos\theta + S_2 \sin\theta = A(S_3 \cos^2\theta + S_4 \sin^2\theta + 2S_5 \cos\theta \sin\theta) \qquad (C.3)$$

$$S_2 \cos\theta - S_1 \sin\theta = A(S_5 \cos^2\theta - S_5 \sin^2\theta + (S_4 - S_3)\cos\theta \sin\theta) \qquad (C.4)$$

Solving for θ and A from Eqs. C.3 and C.4 gives:

$$\tan\theta = \frac{S_2S_3 - S_1S_5}{S_1S_4 - S_2S_5}$$

$$A = \frac{S_1 \cos\theta + S_2 \sin\theta}{S_3 \cos^2\theta + S_4 \sin^2\theta + 2S_3 \cos\theta \sin\theta}$$

or

$$A = \frac{S_2 \cos\theta - S_1 \sin\theta}{S_5 \cos^2\theta - S_5 \sin^2\theta + (S_4 - S_3)\cos\theta \sin\theta}$$

APPENDIX D DATA SUMMARY

LIST OF SYMBOLS

E	ETA
ETA	RMS WAVE HEIGHT
TINF	AIR FREE STREAM TEMPERATURE (CENTER LINE OF CHANNEL)
TB	BULK WATER TEMPERATURE (Z=-355 MM)
U	HORIZONTAL VELOCITY, LDA
V	VERTICAL VELOCITY, LDA
UR	VELOCITY RATIO, (USE-U)/USE
US	RMS WAVE VELOCITY AT SURFACE, FROM WAVE SPECTRA
USS	STOKES DRIFT AT SURFACE, FROM WAVE SPECTRA
USSAV	AVERAGE STOKES DRIFT AT SURFACE FROM WAVE SPECTRA
USURF	TOTAL SURFACE DRIFT, FROM PAPER PUNCHINGS
USE	(EULERIAN) SURFACE DRIFT, USURF-USSAV
USTAR	FRICTION VELOCITY
UZ	RMS WAVE VELOCITY AT DEPTH Z, FROM WAVE SPECTRA
UZS	STOKES DRIFT AT DEPTH Z, FROM WAVE SPECTRA
WPRUD	ENERGY PRODUCTION TERM DUE TO MEAN WAVE STRESS, SEE SEC
TPRUD	TURBULENCE PRODUCTION DUE TO MEAN TURBULENT SHEAR STRES
XLN	LOG CORRECTION FOR MEANS, IN U+ UNITS (PHILLIPS,1977)
YETA	DOMINANT WAVE DECAY LENGTH SCALE
Y	VERTICAL COORDINATE - POSITIVE UP

WAVE SEPARATION

TWO QUANTITIES X AND Y WITH ZERO MEAN :

X	TOTAL RMS OF X
XW	RMS WAVE COMPONENT OF X
XT	RMS TURBULENT COMPONENT OF X
XP	WAVE AMPLITUDE OF X DERIVED FROM PHASE AVERAGES
PX	PHASE LAG OF XP REFERENCED TO THE PHASE OF ETA
PXPY	PHASE DIFFERENCE BETWEEN XW AND YW
SHNX	FRACTION OF MEAN SQUARE HARMONIC COMPONENTS IN PHASE AVGE OF X
XYTWP	WAVE AMPLITUDE OF XY FOR TURBULENT SHEAR STRESSES
PXYTW	PHASE LAG OF PXYTW REFERENCED TO THE PHASE OF ETA
SXW	FRACTION OF TOTAL X VARIANCE ASSOCIATED WITH WAVE
XE	COVARIANCE OF X AND ETA
XY	COVARIANCE OF TOTAL X AND TOTAL Y
XYW	COVARIANCE OF WAVE X AND WAVE Y
XYT	COVARIANCE OF TURBULENT X AND TURBULENT Y
SXYW	FRACTION OF TOTAL XY COVARIANCE ASSOCIATED WITH WAVE

** ALL LENGTH DIMENSIONS IN MM **

RMS ETA= .03 AVE. TINF.= 25.09 AVE. THULK= 21.52 RMS U'V' AT SURFACE FROM SPECTRA= .29

YETA = 6.0 FROM= 1.0 HZ DELTA= 181.0 USTAR= 2.1

WIND WAVE, UINF= 1.5 M/S, 8/17/82

ALL LENGTH DIMENSIONS IN MM

USUNF= 60. USSAV= 0. USE= 40. MEAN VELOCITIES AND TEMPERATURES

RUN	-Y	-Y/DELTA	-Y+	ETA	USS	U	UZS	UW	XLN	V	TINF	TR
1	3.5	.02	8.	.03	.0	19.2	.0	.520	.000	-.8	24.47	21.29
2	6.1	.03	10.	.03	.0	18.8	.0	.559	.000	-.5	24.68	21.31
3	8.7	.04	13.	.03	.0	18.6	.0	.635	.000	-.8	24.20	21.31
4	11.3	.06	15.	.03	.0	18.3	.0	.675	.000	-.1	24.05	21.31
5	13.9	.07	17.	.03	.0	18.2	.0	.798	.000	-.8	25.27	21.31
6	16.5	.09	20.	.03	.0	18.0	.0	.811	.000	-.1	25.49	21.31
7	19.1	.10	23.	.03	.0	17.8	.0	.838	.000	-.2	25.45	21.32
8	21.7	.12	26.	.03	.0	17.7	.0	.838	.000	-.3	25.25	21.32
9	24.3	.13	29.	.03	.0	17.5	.0	.912	.000	-.3	25.05	21.32
10	26.9	.15	32.	.03	.0	17.4	.0	.849	.000	-.2	24.91	21.32
11	29.5	.16	35.	.03	.0	17.3	.0	.966	.000	-.2	24.76	21.32
12	32.1	.18	38.	.03	.0	17.2	.0	.971	.000	-.3	24.65	21.32
13	34.7	.19	41.	.03	.0	17.1	.0	.949	.000	-.3	24.53	21.32
14	37.3	.21	44.	.03	.0	17.0	.0	.995	.000	-.7	24.48	21.32
15	39.9	.22	47.	.03	.0	16.9	.0	1.015	.000	-.6	24.26	21.32
16	42.5	.24	50.	.03	.0	16.8	.0	1.078	.000	-.5	24.02	21.32
17	45.1	.25	53.	.03	.0	16.7	.0	1.111	.000	-.6	23.93	21.32
18	47.7	.27	56.	.03	.0	16.6	.0	1.135	.000	-.7	23.77	21.31
19	50.3	.28	59.	.03	.0	16.5	.0	1.154	.000	-.7	23.77	21.31

RMS VELOCITIES

RUN	-Y	US	UZ	U	UW	UT	SUW	V	VW	VT	SVW
1	3.5	.00	.00	.00	.00	.00	.000	.00	.00	.00	.000
2	6.1	.00	.00	.00	.00	.00	.000	.00	.00	.00	.000
3	8.7	.00	.00	.00	.00	.00	.000	.00	.00	.00	.000
4	11.3	.00	.00	.00	.00	.00	.000	.00	.00	.00	.000
5	13.9	.00	.00	.00	.00	.00	.000	.00	.00	.00	.000
6	16.5	.00	.00	.00	.00	.00	.000	.00	.00	.00	.000
7	19.1	.00	.00	.00	.00	.00	.000	.00	.00	.00	.000
8	21.7	.00	.00	.00	.00	.00	.000	.00	.00	.00	.000
9	24.3	.00	.00	.00	.00	.00	.000	.00	.00	.00	.000
10	26.9	.00	.00	.00	.00	.00	.000	.00	.00	.00	.000
11	29.5	.00	.00	.00	.00	.00	.000	.00	.00	.00	.000
12	32.1	.00	.00	.00	.00	.00	.000	.00	.00	.00	.000
13	34.7	.00	.00	.00	.00	.00	.000	.00	.00	.00	.000
14	37.3	.00	.00	.00	.00	.00	.000	.00	.00	.00	.000
15	39.9	.00	.00	.00	.00	.00	.000	.00	.00	.00	.000
16	42.5	.00	.00	.00	.00	.00	.000	.00	.00	.00	.000
17	45.1	.00	.00	.00	.00	.00	.000	.00	.00	.00	.000
18	47.7	.00	.00	.00	.00	.00	.000	.00	.00	.00	.000
19	50.3	.00	.00	.00	.00	.00	.000	.00	.00	.00	.000

COVARIANCES (UE, VE (E-3))

RUN	-Y	UE	VE	UV	UVW	UVT	SUVW	WPROD	TPNOD
1	3.5	.000	-.000	-.1	-.0	-.3	-.06	.03	.46
2	6.1	.000	-.000	-.1	-.0	-.5	-.09	.03	.32
3	8.7	.000	-.000	-.2	-.0	-.5	-.08	.03	2.37
4	11.3	.000	-.000	-.2	-.0	-.7	-.09	.00	.68
5	13.9	.000	-.000	-.2	-.0	-.5	-.07	.00	1.85
6	16.5	.000	-.000	-.2	-.0	-.5	-.07	.00	2.58
7	19.1	.000	-.000	-.2	-.0	-.5	-.07	.00	1.23
8	21.7	.000	-.000	-.2	-.0	-.5	-.07	.00	.53
9	24.3	.000	-.000	-.2	-.0	-.5	-.07	.00	.37
10	26.9	.000	-.000	-.2	-.0	-.5	-.07	.00	.37
11	29.5	.000	-.000	-.2	-.0	-.5	-.07	.00	.19
12	32.1	.000	-.000	-.2	-.0	-.5	-.07	.00	.21
13	34.7	.000	-.000	-.2	-.0	-.5	-.07	.00	.24
14	37.3	.000	-.000	-.2	-.0	-.5	-.07	.00	.04
15	39.9	.000	-.000	-.2	-.0	-.5	-.07	.00	.11
16	42.5	.000	-.000	-.2	-.0	-.5	-.07	.00	.11
17	45.1	.000	-.000	-.2	-.0	-.5	-.07	.00	.11
18	47.7	.000	-.000	-.2	-.0	-.5	-.07	.00	.11
19	50.3	.000	-.000	-.2	-.0	-.5	-.07	.00	.11

RMS ETA= .12 AVE. TINF.= 18.95 AVE. THICK= 16.10 RMS UW AT SURFACE FROM SPECTRA= 4.44

YETA = 9.0 FDOM= 6.1 HZ DELTA= 310.0 USTAR= 3.4

WIND WAVE, UINF= 2.6 M/S, 12/14/82

ALL LENGTH DIMENSIONS IN MM

USURF= 70. USSAV= 0. USE= 70. MEAN VELOCITIES AND TEMPERATURES

RUN	-Y	-Y/DELTA	-Y+	ETA	USS	U	UZS	UR	XLN	V	TINF	TH
1	1.9	.01	8.	.14	.2	55.5	.1	.235	.007	-1.2	19.01	16.11
2	2.5	.01	10.	.17	.2	46.2	.1	.335	.005	-.8	19.05	16.11
3	3.6	.01	15.	.17	.2	43.0	.0	.373	.001	-.7	19.06	16.11
4	5.5	.02	23.	.17	.2	40.8	.0	.408	.000	-.7	19.07	16.11
5	8.1	.03	34.	.17	.2	39.0	.0	.572	.000	-.6	19.07	16.11
6	11.0	.04	46.	.17	.2	38.2	.0	.583	.000	-.6	19.08	16.11
7	14.5	.05	60.	.17	.2	37.4	.0	.630	.000	-.7	19.12	16.11
8	18.8	.06	78.	.17	.2	36.8	.0	.665	.000	-.7	19.02	16.11
9	23.8	.08	99.	.17	.2	36.1	.0	.688	.000	-.3	19.08	16.11
10	30.0	.10	124.	.17	.2	35.7	.0	.729	.000	-.6	19.05	16.10
11	37.6	.12	155.	.17	.2	35.2	.0	.708	.000	-1.0	18.94	16.10
12	47.7	.15	196.	.17	.2	34.8	.0	.722	.000	-.6	18.98	16.10
13	61.7	.20	254.	.17	.2	34.4	.0	.742	.000	-.7	18.90	16.10
14	79.5	.25	329.	.17	.2	34.1	.0	.770	.000	-1.6	18.88	16.10
15	101.8	.33	421.	.17	.2	33.8	.0	.838	.000	-1.1	18.85	16.10
16	128.5	.41	534.	.17	.2	33.6	.0	.897	.000	-1.1	18.86	16.10
17	159.8	.51	662.	.17	.2	33.4	.0	.871	.000	-1.0	18.82	16.10
18	196.2	.63	812.	.17	.2	33.2	.0	.903	.000	-1.2	18.82	16.10
19	237.2	.76	982.	.17	.2	33.1	.0	.909	.000	-1.2	18.81	16.10
20	280.9	.91	1162.	.17	.2	33.0	.0	.974	.000	-1.9	18.87	16.09
21	308.4	.99	1276.	.17	.2	33.0	.0	.995	.000	-.9	18.86	16.09

RMS VELOCITIES

RUN	-Y	US	UZ	U	UW	UT	SUW	V	VW	VT	SVW
1	1.9	4.9	3.6	13.5	6.8	11.5	.26	11.5	10.7	4.2	.87
2	2.5	4.9	3.6	13.5	6.8	11.5	.26	11.5	10.7	4.2	.87
3	3.6	4.9	3.6	13.5	6.8	11.5	.26	11.5	10.7	4.2	.87
4	5.5	4.9	3.6	13.5	6.8	11.5	.26	11.5	10.7	4.2	.87
5	8.1	4.9	3.6	13.5	6.8	11.5	.26	11.5	10.7	4.2	.87
6	11.0	4.9	3.6	13.5	6.8	11.5	.26	11.5	10.7	4.2	.87
7	14.5	4.9	3.6	13.5	6.8	11.5	.26	11.5	10.7	4.2	.87
8	18.8	4.9	3.6	13.5	6.8	11.5	.26	11.5	10.7	4.2	.87
9	23.8	4.9	3.6	13.5	6.8	11.5	.26	11.5	10.7	4.2	.87
10	30.0	4.9	3.6	13.5	6.8	11.5	.26	11.5	10.7	4.2	.87
11	37.6	4.9	3.6	13.5	6.8	11.5	.26	11.5	10.7	4.2	.87
12	47.7	4.9	3.6	13.5	6.8	11.5	.26	11.5	10.7	4.2	.87
13	61.7	4.9	3.6	13.5	6.8	11.5	.26	11.5	10.7	4.2	.87
14	79.5	4.9	3.6	13.5	6.8	11.5	.26	11.5	10.7	4.2	.87
15	101.8	4.9	3.6	13.5	6.8	11.5	.26	11.5	10.7	4.2	.87
16	128.5	4.9	3.6	13.5	6.8	11.5	.26	11.5	10.7	4.2	.87
17	159.8	4.9	3.6	13.5	6.8	11.5	.26	11.5	10.7	4.2	.87
18	196.2	4.9	3.6	13.5	6.8	11.5	.26	11.5	10.7	4.2	.87
19	237.2	4.9	3.6	13.5	6.8	11.5	.26	11.5	10.7	4.2	.87
20	280.9	4.9	3.6	13.5	6.8	11.5	.26	11.5	10.7	4.2	.87
21	308.4	4.9	3.6	13.5	6.8	11.5	.26	11.5	10.7	4.2	.87

COVARIANCES (UE, VE (E-3))

RUN	-Y	UE	VE	UV	UVW	UVT	SUVW	WPWOD	TPWOD
1	1.9	.001	-.000	8.8	4.5	-.1	1.02	-9.55	.15
2	2.5	.001	-.000	-1.3	.8	-2.1	.68	-1.68	4.31
3	3.6	.001	-.000	-4.6	.5	-5.0	.11	-.98	4.95
4	5.5	.001	-.000	-7.3	.3	-7.6	.05	.61	12.11
5	8.1	.001	-.000	-9.3	.1	-9.4	.01	.56	13.37
6	11.0	.000	-.000	-9.6	.1	-9.5	.01	.18	11.47
7	14.5	.000	-.000	-12.1	.0	-11.8	.02	.27	11.83
8	18.8	.000	-.000	-11.5	.0	-11.1	.03	.24	4.13
9	23.8	.000	-.000	-11.4	.0	-11.2	.00	.01	5.59
10	30.0	.000	-.000	-8.5	.0	-8.2	.02	.02	2.09
11	37.6	.000	-.000	-7.5	.0	-7.4	.02	.01	.55
12	47.7	.000	-.000	-11.5	.0	-11.3	.01	.00	-.45
13	61.7	.000	-.000	-9.5	.0	-9.5	.01	.00	-.47
14	79.5	.000	-.000	-8.7	.0	-8.6	.01	.04	-.48
15	101.8	.000	-.000	-11.1	.0	-11.0	.01	.02	2.85
16	128.5	.000	-.000	-5.4	.0	-5.3	.02	.02	-.75
17	159.8	.000	-.000	-5.4	.0	-5.7	.01	.06	-.49

RMS ETA= 1.13 AVE. TINF.= 22.39 AVE. THICK= 20.47 RMS UX AT SURFACE FROM SPECTRA= 38.26

YETA = 4.5 FOUM= 5.2 HZ DELTA= 568.0 USTAR= 4.9

WIND WAVE, UINF= 3.2 M/S, 8/18/82

USURF= 84. USSAV= 11. USE= 73. MEAN VELOCITIES AND TEMPERATURES

ALL LENGTH DIMENSIONS IN CM

RUN	-Y	-Y/DELTA	-Y+	ETA	USS	U	UZS	UR	XLN	V	TINF	TR
1	2.9	.01	15.	1.08	10.2	38.9	4.6	.483	.147	.4	23.24	20.56
2	3.9	.001	19.	1.07	10.0	40.8	3.5	.472	.076	.4	23.14	20.55
3	5.0	.001	25.	1.12	10.9	33.1	2.9	.572	.034	1.1	22.98	20.58
4	6.1	.002	30.	1.11	10.7	35.6	2.2	.551	.020	.4	22.88	20.54
5	7.4	.002	37.	1.11	10.9	31.6	1.6	.606	.011	.4	22.73	20.53
6	8.4	.003	42.	1.11	10.5	30.3	1.1	.626	.006	.7	22.58	20.52
7	11.4	.003	57.	1.11	11.1	28.4	.7	.653	.002	.1	22.46	20.51
8	13.8	.004	69.	1.11	11.5	25.7	.4	.688	.001	.5	22.40	20.50
9	16.2	.005	81.	1.15	10.8	25.2	.3	.697	.000	.5	22.38	20.49
10	20.1	.006	101.	1.10	11.4	24.5	.1	.706	.000	.5	22.29	20.48
11	25.0	.007	126.	1.10	11.1	23.7	.0	.718	.000	.5	22.26	20.47
12	31.3	.009	156.	1.15	10.8	19.6	.0	.766	.000	.8	22.23	20.46
13	39.1	.011	196.	1.12	10.3	17.1	.0	.796	.000	1.1	22.22	20.45
14	49.0	.014	246.	1.10	10.4	20.7	.0	.753	.000	.8	22.19	20.44
15	62.7	.018	308.	1.12	10.4	14.5	.0	.808	.000	.8	22.13	20.43
16	77.7	.022	387.	1.09	9.8	13.5	.0	.839	.000	.8	22.10	20.42
17	97.7	.028	488.	1.10	10.2	6.2	.0	.926	.000	.3	22.05	20.41
18	123.6	.036	615.	1.11	10.2	6.8	.0	.919	.000	1.0	22.04	20.40
19	156.1	.045	777.	1.14	10.7	2.8	.0	.970	.000	.5	22.03	20.38
20	197.5	.57	982.	1.16	10.8	2.5	.0	.974	.000	.5	21.97	20.38
21	243.8	.70	1211.	1.15	10.3	-.3	.0	1.000	.000	1.0	21.94	20.37

RMS VELOCITIES

RUN	-Y	US	UZ	U	UW	UT	SUW	V	VW	VT	SVW
1	2.9	37.2	25.4	23.5	19.0	15.9	.65	24.6	24.1	5.1	.96
2	3.9	36.9	24.4	23.0	17.8	16.5	.60	23.1	22.4	5.5	.94
3	5.0	36.5	24.0	22.1	17.5	15.5	.63	22.1	21.4	5.5	.94
4	6.1	36.1	23.8	21.8	15.9	15.8	.59	20.1	19.2	6.0	.91
5	7.4	36.6	23.6	19.8	16.2	13.8	.51	18.5	17.3	6.6	.87
6	8.4	37.9	23.1	18.7	12.0	14.4	.41	16.4	15.3	5.8	.87
7	11.4	39.3	20.6	15.6	10.5	11.5	.45	14.4	12.9	6.5	.80
8	13.8	39.7	18.8	14.1	8.5	11.5	.36	12.3	10.5	6.5	.72
9	16.2	38.7	16.5	14.2	8.5	12.6	.21	10.7	8.4	6.5	.62
10	20.1	39.8	14.8	12.5	8.8	11.2	.15	8.8	6.6	5.5	.48
11	25.0	39.1	12.8	10.7	4.3	10.2	.09	7.7	5.6	5.5	.28
12	31.3	38.1	10.8	10.2	2.0	10.0	.04	6.5	4.6	5.0	.16
13	39.1	37.7	.0	10.9	.1	10.9	.01	5.8	.0	5.8	.06
14	49.0	38.7	.6	10.8	.1	10.8	.00	5.7	.0	5.7	.02
15	62.7	37.9	.8	10.2	.5	10.2	.00	5.8	.5	5.9	.01
16	77.7	36.8	.3	11.4	.5	11.4	.00	5.6	.4	5.6	.01
17	97.7	38.0	.2	8.5	.5	8.5	.00	4.7	.3	4.7	.00
18	123.6	37.5	.2	11.4	.5	11.5	.00	6.2	.4	6.2	.00
19	156.1	38.5	.1	7.5	.3	7.5	.00	4.2	.2	4.2	.00
20	197.5	38.2	.1	8.0	.3	8.0	.00	4.2	.3	4.3	.00
21	243.8	37.9	.1	5.3	.0	5.3	.01	4.3	.3	4.3	.01

COVARIANCES (UE, VE (E-3))

RUN	-Y	UE	VE	UV	UVW	UVT	SUVW	WPROD	TPWOD
1	2.9	.021	-.002	-3.8	17.7	-21.5	4.66	-24.23	29.83
2	3.9	.020	-.002	-15.2	15.0	-26.1	.98	-16.77	33.81
3	5.0	.021	-.002	-15.1	5.8	-20.8	.56	-6.50	28.77
4	6.1	.019	-.002	-22.2	1.3	-23.5	.06	-1.65	26.77
5	7.4	.017	-.002	-23.0	-.1	-23.0	.00	.06	24.27
6	8.4	.015	-.002	-19.7	-.6	-19.1	.03	.59	19.61
7	11.4	.013	-.001	-22.1	3.2	-25.3	.15	-2.67	21.00
8	13.8	.011	-.001	-21.7	-.2	-21.4	.01	.14	15.50
9	16.2	.009	-.001	-24.5	-.1	-24.4	.00	.06	14.50
10	20.1	.007	-.001	-23.7	-.2	-23.9	.01	.21	11.28
11	25.0	.004	-.000	-25.6	-.2	-25.8	.01	.01	7.97
12	31.3	.003	-.000	-17.0	-.2	-16.8	.01	.05	3.92
13	39.1	.001	-.000	-18.9	-.2	-18.5	.01	.02	2.96
14	49.0	.001	-.000	-25.9	-.2	-25.7	.01	.05	3.40
15	62.7	.000	-.000	-15.5	-.2	-15.2	.01	.04	2.14
16	77.7	.000	-.000	-27.5	-.2	-27.2	.01	.04	3.85
17	97.7	.000	-.000	-18.3	-.0	-18.3	.00	.00	4.58

RMS ETA= 3.22 AVE. TINF.= 16.78 AVE. TAULK= 15.22 RMS UW AT SURFACE FROM SPECTRA= 76.67

YETA = 19.9 FUOM= 3.5 HZ DELTA= 268.0 USTAR= 7.2

WIND WAVE, UINF= 4.7 M/S, 12/10/82

ALL LENGTH DIMENSIONS IN MM

USURF=124. USSAV= 31. USE= 93. MEAN VELOCITIES AND TEMPERATURES

RUN	-Y	-Y/DELTA	-Y+	ETA	USS	U	UZS	UR	XLM	V	TINF	TB
2	8.7	.03	55.	3.11	29.3	25.5	8.8	.723	.125	-.3	17.79	15.38
3	8.6	.03	55.	3.11	29.3	27.6	8.9	.706	.127	-.4	17.66	15.36
4	9.6	.03	61.	3.11	29.3	26.5	9.1	.720	.108	-.1	17.51	15.35
5	11.7	.04	74.	3.11	29.3	26.5	7.7	.738	.062	-.9	17.48	15.38
6	13.6	.05	87.	3.11	29.3	26.5	5.7	.774	.035	-.2	17.30	15.38
8	18.5	.07	118.	3.11	29.3	26.5	4.0	.754	.017	-.2	17.15	15.30
8	18.5	.07	118.	3.11	29.3	26.5	3.0	.807	.010	-.4	17.08	15.29
9	28.5	.10	182.	3.11	29.3	26.5	1.8	.831	.004	-.5	16.82	15.28
10	38.5	.14	246.	3.11	29.3	26.5	.9	.886	.001	-.8	16.72	15.25
11	48.5	.18	309.	3.11	29.3	26.5	.4	.882	.000	-.4	16.61	15.20
12	58.5	.21	373.	3.11	29.3	26.5	.1	.835	.000	-.6	16.53	15.19
13	68.5	.25	437.	3.11	29.3	26.5	.0	.907	.000	-.5	16.48	15.16
14	78.5	.28	501.	3.11	29.3	26.5	.0	.917	.000	-.5	16.38	15.12
15	118.5	.43	756.	3.11	29.3	26.5	.0	.976	.000	-.1	16.30	15.10
16	145.5	.53	929.	3.11	29.3	26.5	.0	1.020	.000	.6	16.21	15.08
17	186.5	.67	1190.	3.11	29.3	26.5	.0	1.027	.000	.2	16.14	15.08
18	218.5	.78	1394.	3.11	29.3	26.5	.0	1.063	.000	.9	16.04	15.06
19	268.0	.96	1710.	3.11	29.3	26.5	.0	1.050	.000	.7	15.95	15.04

RMS VELOCITIES

RUN	-Y	US	UZ	U	UW	UT	SUW	V	VW	VT	SVW
2	8.7	74.2	43.3	42.1	38.1	17.9	.82	85.5	83.8	12.1	.93
3	8.6	74.5	43.5	42.0	38.0	17.9	.82	86.2	84.6	12.1	.93
4	9.6	74.6	44.1	42.0	38.0	18.0	.85	86.2	84.6	12.9	.93
5	11.7	74.7	45.0	39.9	36.0	18.3	.78	85.2	83.7	13.9	.92
6	13.6	74.8	45.8	37.8	34.0	18.6	.78	83.9	82.8	14.0	.92
8	18.5	74.9	46.7	35.7	32.0	18.9	.71	82.8	81.9	14.0	.90
8	18.5	74.9	46.7	35.7	32.0	18.9	.71	82.8	81.9	14.0	.90
9	28.5	75.2	47.5	33.6	30.1	19.2	.70	82.0	81.1	14.2	.87
10	38.5	75.5	48.2	31.6	28.2	19.5	.62	81.3	80.5	14.3	.83
11	48.5	75.7	48.8	29.7	26.4	19.8	.52	80.6	79.9	14.3	.72
12	58.5	75.9	49.3	27.8	24.7	20.0	.39	80.0	79.4	14.3	.57
13	68.5	76.1	49.8	25.9	23.0	20.2	.28	79.5	78.9	14.3	.38
14	78.5	76.3	50.2	24.1	21.4	20.4	.15	79.0	78.5	14.3	.18
15	118.5	77.1	51.4	18.4	16.4	21.0	.00	77.7	77.2	14.3	.01
16	145.5	76.8	51.8	14.9	13.2	21.3	.00	77.3	76.8	14.3	.00
17	186.5	75.0	51.9	9.2	8.2	21.7	.00	76.3	75.8	14.3	.00
18	218.5	75.9	52.0	6.6	5.8	21.9	.00	76.0	75.6	14.3	.00
19	268.0	75.8	52.0	2.7	2.3	22.1	.00	75.9	75.5	14.3	.00

COVARIANCES (UE, VE (E-3))

RUN	-Y	UE	VE	UV	UVW	UVT	SUVW	WPROD	TPROD
2	8.7	-.120	-.005	-45.0	15.6	-60.5	.35	-13.58	52.79
3	8.6	-.122	-.006	-26.7	17.9	-44.6	.67	-15.75	39.15
4	9.6	-.152	-.007	-22.7	20.2	-42.9	.89	-16.86	36.90
5	11.7	-.121	-.007	-37.7	15.3	-53.0	.81	-10.53	36.88
6	13.6	-.104	-.008	-26.8	10.8	-36.5	.58	-6.28	23.00
8	18.5	-.089	-.006	-83.7	3.7	-85.4	.08	-.78	20.52
8	18.5	-.079	-.005	-40.1	3.6	-43.7	.09	-1.21	14.67
9	28.5	-.062	-.005	-33.5	.2	-33.3	-.01	-.48	6.52
10	38.5	-.048	-.005	-56.9	.5	-57.5	-.01	-.03	5.39
11	48.5	-.032	-.002	-42.8	.5	-42.4	-.02	-.03	2.25
12	58.5	-.018	-.001	-41.7	.1	-41.8	-.00	-.01	4.60
13	68.5	-.009	-.001	-58.2	.1	-58.1	-.00	.03	12.54
14	78.5	-.004	-.000	-41.7	.5	-41.1	-.01	.16	12.36
15	118.5	-.001	.000	-33.5	.2	-33.5	-.00	.01	5.78
16	145.5	-.000	.000	-14.5	.2	-14.5	-.01	.01	-.56
17	186.5	-.000	.000	-17.5	.1	-17.6	-.00	.00	1.70
18	218.5	-.000	.000	-2.4	.1	-2.5	.06	-.05	-.88
19	268.0	-.000	.000	-10.3	.0	-10.3	.00	.01	-4.06

RMS ETA= 5.67 AVE. TIMF.= 22.10 AVE. TAULK= 18.50 RMS UX AT SURFACE FROM SPECTRA=104.54

YETA = 32.6 FDOM= 3.2 HZ DELTA= 249.0 USTAR=11.5

WIND WAVE, UINF= 6.7 M/S, 8/31/82

ALL LENGTH DIMENSIONS IN CM

USURF=169. USSAV= 52. USE=137. MEAN VELOCITIES AND TEMPERATURES

RUN	-Y	-Y/DELTA	-Y+	ETA	USS	U	UZS	UR	XLN	V	TIMF	TB
1	13.9	.06	151.	5.67	53.3	27.0	15.0	.778	.179	.6	24.09	18.55
2	13.8	.06	150.	5.62	52.9	30.0	16.9	.762	.178	.2	23.83	18.55
3	14.8	.06	160.	5.80	52.9	30.2	17.8	.788	.149	.2	23.54	18.55
4	16.6	.07	180.	5.70	52.1	32.1	18.8	.821	.098	2.2	23.24	18.55
5	19.5	.08	212.	5.58	49.9	28.5	9.3	.822	.058	.2	22.96	18.55
6	23.5	.09	255.	5.77	53.6	28.5	7.7	.851	.038	2.2	22.80	18.54
7	29.0	.12	315.	5.79	53.2	28.8	5.2	.868	.015	1.8	22.68	18.54
8	36.3	.15	393.	5.87	55.7	29.5	3.5	.882	.007	1.6	22.51	18.53
9	46.8	.18	477.	5.67	50.7	29.2	1.2	.873	.005	1.7	22.15	18.53
10	52.7	.21	573.	5.72	52.0	29.2	1.2	.892	.001	.7	21.98	18.52
11	63.7	.26	691.	5.58	52.6	29.2	.6	.922	.000	1.5	21.45	18.51
12	76.7	.31	832.	5.72	55.1	29.9	.3	.935	.000	.5	21.41	18.50
13	93.7	.38	1016.	5.59	48.5	29.6	.1	.948	.000	1.5	21.48	18.49
14	113.5	.46	1231.	5.46	50.5	29.5	.0	.970	.000	.8	21.27	18.47
15	133.5	.54	1448.	5.47	50.5	29.5	.0	.992	.000	.6	21.12	18.46
16	153.5	.61	1666.	5.46	49.6	29.7	.0	.994	.000	.4	20.97	18.44
17	183.0	.74	1985.	5.66	52.5	29.8	.0	1.003	.000	.5	20.86	18.43
18	212.9	.85	2309.	5.58	50.5	29.8	.0	1.038	.000	2.1	20.81	18.42
19	243.8	.98	2643.	5.77	50.4	29.8	.0	1.078	.000	6.1	20.62	18.40

RMS VELOCITIES

RUN	-Y	US	UZ	U	UW	UT	SUW	V	VW	VT	SVW
1	13.9	110.4	64.3	60.6	54.9	25.7	.82	65.6	63.8	16.8	.93
2	13.8	109.9	63.9	60.6	54.8	27.8	.78	65.5	62.7	18.9	.92
3	14.8	109.1	61.9	58.5	53.8	24.6	.82	65.4	60.6	17.4	.92
4	16.6	108.5	56.8	55.5	49.9	25.2	.79	65.2	56.6	16.5	.92
5	19.5	108.5	50.8	51.1	43.9	26.1	.74	65.2	50.5	16.8	.90
6	23.5	110.3	46.6	46.8	41.0	22.2	.77	66.2	46.5	16.2	.85
7	29.0	109.8	38.6	40.5	34.5	21.8	.71	66.1	39.2	16.7	.85
8	36.3	111.7	31.7	35.2	27.5	20.3	.69	66.1	32.0	16.1	.80
9	46.8	112.7	24.8	30.2	21.3	20.0	.53	66.1	25.2	14.8	.76
10	52.7	108.8	18.3	24.8	16.2	18.8	.63	65.8	19.2	14.0	.76
11	63.7	108.5	15.3	22.5	10.8	19.9	.21	65.8	12.8	13.9	.64
12	76.7	109.8	10.7	20.1	7.6	14.6	.11	66.2	9.1	10.1	.30
13	93.7	108.5	5.5	17.6	4.2	16.2	.00	66.2	5.9	11.2	.06
14	113.5	108.1	3.2	15.8	2.5	15.2	.00	66.2	2.9	11.2	.06
15	133.5	108.2	2.2	14.8	1.9	14.9	.00	66.2	1.9	9.8	.02
16	153.5	108.1	1.6	13.9	1.4	14.2	.00	66.2	1.3	8.2	.01
17	183.0	108.0	1.1	12.9	1.0	13.4	.00	66.2	.9	7.8	.01
18	212.9	108.0	.8	12.2	.7	12.8	.00	66.2	.6	7.8	.01
19	243.8	110.4	.6	11.7	.5	12.2	.00	66.5	.4	5.5	.01

COVARIANCES (UE, VE (E-3))

RUN	-Y	UE	VE	UV	UVW	UVT	SUVW	WPROD	TPROD
1	13.9	.320	-.011	-40.2	63.7	-103.9	1.58	-10.20	16.64
2	13.8	.319	-.0115	-48.8	22.0	-30.8	2.50	-5.50	4.90
3	14.8	.311	-.0115	-75.4	51.2	-164.6	.92	-5.19	17.69
4	16.6	.286	-.0112	-67.8	48.7	-117.6	.75	-4.79	20.78
5	19.5	.250	-.0113	-96.8	30.2	-126.5	.51	-5.77	28.20
6	23.5	.248	-.0115	-124.5	9.3	-133.8	.07	-1.92	27.60
7	29.0	.208	-.0110	-116.2	6.8	-123.0	.06	-1.52	27.09
8	36.3	.169	-.0108	-117.9	-5.1	-124.5	-.04	-.86	26.62
9	46.8	.129	-.0085	-101.1	-1.1	-102.2	-.01	-.21	24.58
10	52.7	.107	-.0065	-105.7	.5	-105.2	.00	-.09	24.58
11	63.7	.067	-.0065	-105.7	.5	-105.2	.00	-.09	24.58
12	76.7	.051	-.0065	-104.8	.5	-104.3	.00	-.09	24.46
13	93.7	.027	-.0061	-77.5	.3	-77.2	.00	-.05	18.46
14	113.5	.015	-.0060	-53.8	.2	-53.6	.00	-.03	12.79
15	133.5	.009	-.0060	-52.8	.2	-52.6	.00	-.03	12.79
16	153.5	.006	-.0060	-35.7	.1	-35.6	.00	-.02	8.64
17	183.0	.003	-.0060	-35.7	.1	-35.6	.00	-.02	8.64
18	212.9	.001	-.0060	-33.7	.1	-33.6	.00	-.02	8.14
19	243.8	.001	-.0060	-32.7	.1	-32.6	.00	-.02	7.90

RMS ETA= 8.58 AVE. TINF.= 20.14 AVE. TBULK= 18.19 RMS UW AT SURFACE FROM SPECTRA=139.48

YETA = 45.1 FOUM= 2.6 HZ DELTA= 354.0 USTAR=17.5

WIND WAVE, UINF= 9.9 M/S, 8/24/82

ALL LENGTH DIMENSIONS IN MM

USURF=280. USSAV= 76. USE=204. MEAN VELOCITIES AND TEMPERATURES

RUN	-Y	-Y/DELTA	-Y+	ETA	USS	U	UZS	UR	FLW	V	TINF	TR
1	18.4	.05	386.	8.37	72.9	37.6	19.8	.795	.211	.4	21.14	18.41
2	19.2	.05	320.	8.50	74.9	83.5	19.6	.775	.193	-2.6	20.93	18.38
3	21.1	.06	352.	8.69	76.9	58.2	18.6	.797	.155	-1.3	20.71	18.35
4	24.0	.07	400.	8.37	73.7	81.8	18.9	.797	.097	-3.1	20.53	18.32
5	29.1	.08	485.	8.58	75.6	32.3	12.5	.840	.058	-1.5	20.31	18.28
6	34.8	.10	574.	8.51	72.3	33.3	9.3	.888	.032	-.7	20.17	18.25
7	42.1	.12	702.	8.67	78.1	28.2	6.8	.875	.016	3.0	20.04	18.22
8	52.9	.15	867.	8.65	75.6	21.6	4.4	.907	.007	-.2	19.96	18.20
9	63.9	.18	1065.	8.78	78.3	20.4	2.7	.918	.003	-.7	19.92	18.16
10	76.8	.22	1280.	8.67	77.5	17.2	1.5	.933	.001	1.8	19.89	18.14
11	91.8	.26	1530.	8.71	76.6	14.8	.8	.944	.001	-.2	19.85	18.11
12	112.5	.32	1871.	8.74	80.4	6.9	.4	.974	.000	8.7	19.81	18.09
13	132.5	.37	2208.	8.52	76.6	-13.3	.2	1.011	.000	3.0	19.78	18.06
14	162.5	.46	2704.	8.58	74.9	-10.5	.1	1.037	.000	2.9	19.76	18.04
15	199.1	.56	3316.	8.48	74.5	-15.0	.0	1.056	.000	2.1	19.75	18.01
16	246.0	.69	4100.	8.43	74.6	-19.4	.0	1.069	.000	2.4	19.73	17.99

RMS VELOCITIES

RUN	-Y	US	UZ	U	UW	UT	SUW	V	VW	VT	SVW
1	18.4	136.6	79.8	71.6	59.1	40.3	.68	77.6	72.8	26.8	.88
2	19.2	138.6	79.7	71.0	57.6	41.1	.67	78.3	73.5	26.9	.89
3	21.1	141.5	77.1	71.8	60.3	38.0	.71	77.1	72.5	26.5	.88
4	24.0	137.1	69.8	65.5	54.2	36.9	.68	73.0	68.4	26.2	.86
5	29.1	140.1	69.8	69.1	58.0	36.6	.65	69.3	64.8	26.2	.88
6	34.8	138.8	59.4	66.8	56.8	34.3	.65	59.7	57.3	25.6	.85
7	42.1	141.4	48.4	68.2	58.0	34.4	.65	52.7	48.2	25.6	.77
8	52.9	140.5	38.7	65.9	58.5	34.5	.68	45.8	37.8	25.8	.69
9	63.9	142.3	30.8	62.0	53.8	34.6	.72	37.6	29.8	25.8	.63
10	76.8	141.1	22.8	57.0	47.8	33.5	.73	32.0	22.8	25.3	.57
11	91.8	141.1	17.1	53.2	43.7	33.7	.75	27.6	18.8	25.4	.57
12	112.5	140.1	11.7	49.2	39.7	33.6	.75	22.8	13.9	25.6	.54
13	132.5	139.0	7.7	46.2	36.7	33.7	.76	19.4	10.9	19.6	.24
14	162.5	138.5	4.8	43.6	34.5	33.5	.77	16.7	7.1	18.9	.13
15	199.1	138.1	2.9	41.9	33.0	33.4	.78	15.7	5.1	18.8	.09
16	246.0	138.3	1.6	41.3	32.4	33.4	.78	15.2	4.2	18.8	.07

COVARIANCES (UE, VE (E-3))

RUN	-Y	UE	VE	UV	UVW	UVT	SUVW	WPROD	TPROD
1	18.4	.511	-.011	-177.7	20.9	-198.6	.12	-14.05	134.27
2	19.2	.510	-.013	-189.2	86.1	-275.3	.45	-57.20	182.95
3	21.1	.539	-.018	-234.8	30.0	-264.8	.13	-19.50	171.58
4	24.0	.465	-.015	-264.7	29.4	-298.1	.11	-18.32	185.73
5	29.1	.488	-.012	-227.5	73.4	-300.9	.32	-42.09	172.43
6	34.8	.395	-.011	-217.8	45.2	-263.0	.21	-23.58	136.00
7	42.1	.346	-.011	-214.5	67.2	-281.7	.31	-29.89	123.66
8	52.9	.298	-.009	-220.3	50.1	-320.8	.19	-17.69	113.09
9	63.9	.238	-.006	-242.0	14.8	-296.6	.05	-4.12	83.45
10	76.8	.174	-.006	-250.1	4.6	-254.7	.02	-1.18	64.92
11	91.8	.135	-.003	-264.3	5.2	-271.4	.02	-1.43	75.01
12	112.5	.089	-.001	-158.7	8.0	-164.7	.08	-2.11	58.05
13	132.5	.058	-.002	-256.8	.8	-257.6	.00	-.35	103.26
14	162.5	.034	-.000	-96.7	.8	-97.6	.01	-.25	27.01
15	199.1	.017	-.000	-146.5	-1.7	-144.7	-.01	-.22	-17.49
16	246.0	.008	.000	-79.4	-.6	-78.7	-.01	.44	79.55

RMS ETA= 13.08 AVE. TINF.= 19.34 AVE. THULK= 17.08 RMS UA AT SURFACE FROM SPECTRA=194.04

YETA = 58.2 FDOM= 2.0 HZ DELTA= 298.0 USTAR=27.5

WIND WAVE, UINF=13.1, 8/25/82

USURF=814. USSAV=144. USE=270. MEAN VELOCITIES AND TEMPERATURES ALL LENGTH DIMENSIONS IN CM

RUN	-Y	-Y/DELTA	-Y+	ETA	USS	U	UZS	UR	XLM	V	TINF	TR
1	27.1	.09	689.	13.44	146.7	53.0	29.8	.800	.226	1.9	20.79	17.38
2	30.2	.10	770.	12.59	137.3	57.6	23.5	.804	.142	1.9	20.53	17.35
3	35.0	.12	891.	13.55	150.0	46.0	22.0	.827	.107	1.6	20.31	17.32
4	42.0	.14	1069.	12.97	141.1	37.6	15.7	.871	.052	1.9	20.14	17.29
5	49.8	.17	1269.	13.18	146.5	34.9	12.2	.886	.038	3.3	19.97	17.26
6	58.4	.20	1488.	13.29	143.2	24.1	9.8	.919	.018	5.2	19.86	17.22
7	67.3	.23	1714.	12.98	142.2	29.1	8.5	.914	.009	6.3	19.78	17.19
8	77.9	.26	1985.	13.65	149.6	19.8	8.8	.941	.005	5.9	19.61	17.15
9	99.1	.33	2525.	12.72	138.3	24.3	2.1	.924	.002	2.3	14.51	17.12
10	110.6	.37	2818.	13.28	140.1	7.6	1.6	.978	.001	8.7	19.37	17.09
11	125.3	.42	3191.	13.65	145.8	-.2	1.0	.998	.001	6.9	19.18	17.05
12	146.0	.49	3719.	12.88	144.2	-9.5	.5	1.022	.000	5.4	19.00	17.01
13	162.3	.54	4136.	13.05	141.4	-7.6	.3	1.017	.000	2.9	18.86	16.99
14	192.8	.65	4908.	13.17	145.3	-19.8	.1	1.047	.000	0.0	18.77	16.95
15	218.4	.72	5458.	12.88	139.8	-20.4	.1	1.049	.000	12.8	18.59	16.90
16	238.2	.79	5963.	12.80	138.9	-21.0	.0	1.051	.000	8.8	18.50	16.87
17	253.8	.85	6465.	13.28	144.9	-20.8	.0	1.072	.000	14.6	18.37	16.83
18	278.3	.92	6986.	12.96	145.2	-30.2	.0	1.073	.000	18.3	18.27	16.80
19	293.4	.98	7471.	13.05	142.1	-29.8	.0	1.072	.000	12.6	18.13	16.76

RMS VELOCITIES

RUN	-Y	US	UZ	U	UA	UT	SUA	V	VA	VT	SVA
1	27.1	197.1	104.8	94.4	74.5	57.9	.62	101.7	93.9	39.1	.85
2	30.2	188.7	93.8	88.9	68.6	56.5	.60	92.9	84.4	38.9	.83
3	35.0	200.3	92.3	90.6	70.9	56.3	.61	96.8	85.8	40.4	.82
4	42.0	191.7	76.9	78.5	57.5	53.5	.54	81.3	72.5	36.7	.80
5	49.8	195.4	67.9	73.8	51.6	52.2	.49	78.7	65.1	36.7	.76
6	58.4	195.3	66.1	66.3	48.7	48.1	.52	66.9	57.8	34.3	.74
7	67.3	193.1	49.8	63.3	39.1	49.7	.38	59.1	48.0	34.6	.66
8	77.9	198.8	43.5	59.0	34.0	47.6	.35	54.6	41.7	33.2	.58
9	99.1	189.7	29.3	51.5	26.3	44.2	.26	46.1	31.7	33.5	.47
10	110.6	196.8	25.6	45.8	20.5	40.5	.20	38.4	26.2	28.1	.47
11	125.3	195.0	20.8	40.8	16.8	37.4	.16	34.6	20.7	27.8	.36
12	146.0	193.0	14.8	38.8	11.4	36.6	.09	27.9	14.2	28.0	.26
13	162.3	193.2	12.2	33.0	9.5	31.6	.08	25.0	11.3	22.8	.20
14	192.8	195.4	9.1	32.4	6.6	31.7	.04	21.0	6.9	19.9	.11
15	218.4	190.8	6.0	26.1	4.6	25.6	.03	20.8	5.4	19.6	.07
16	238.2	190.3	4.9	28.3	3.7	28.1	.02	20.2	4.4	19.7	.05
17	253.8	195.1	4.3	20.3	3.0	20.0	.02	18.7	3.4	18.4	.03
18	278.3	193.7	3.4	20.3	2.3	20.2	.01	18.2	2.8	18.0	.02
19	293.4	193.7	3.0	21.7	2.4	21.6	.01	20.3	2.6	20.1	.02

COVARIANCES (UE, VE (E-5))

RUN	-Y	UE	VE	UV	UVA	UVT	SUVA	APROD	TPROD
1	27.1	1.032	.007	-827.9	221.1	-648.9	.52	-826.28	1250.82
2	30.2	.891	-.019	-691.1	36.5	-727.7	.05	-59.66	1184.56
3	35.0	.991	-.016	-762.8	33.4	-796.8	.08	-42.07	945.86
4	42.0	.781	-.015	-625.2	-2.8	-620.8	-.00	1.97	518.20
5	49.8	.720	-.008	-632.0	37.6	-669.7	.06	-19.99	355.69
6	58.4	.666	-.010	-460.5	91.5	-552.0	.20	-31.70	191.29
7	67.3	.555	-.012	-538.8	-16.7	-521.6	-.03	4.56	142.08
8	77.9	.516	-.013	-672.5	24.5	-697.0	.04	-6.91	196.56
9	99.1	.370	-.009	-563.2	-13.5	-549.9	-.02	2.59	251.97
10	110.6	.309	-.008	-353.1	2.8	-355.8	.01	-1.36	174.07
11	125.3	.247	-.009	-341.2	8.1	-350.3	.03	-4.73	182.89
12	146.0	.178	-.008	-380.8	-2.1	-378.4	-.01	.95	169.67
13	162.3	.143	-.005	-210.9	1.5	-212.5	.01	-.98	69.79
14	192.8	.100	-.003	-305.7	-5.5	-300.1	-.02	.56	30.28
15	218.4	.066	-.002	-151.0	-2.7	-148.5	-.02	.20	10.26
16	238.2	.053	-.000	-234.6	.4	-235.4	.00	-.15	19.18
17	253.8	.042	-.001	-78.2	-.3	-77.9	-.00	.04	21.47
18	278.3	.031	-.001	-36.2	-.1	-35.1	-.00	-.01	5.08
19	293.4	.024	.000	-138.8	-.5	-137.4	-.00	-.52	-41.28

RMS ETA= 15.52 AVE. TINF.= 21.59 AVE. TBULA= 21.10

YETA = 248.0 FOOM= 1.0 HZ DELTA= 000.0 USTAR= 1.0

MECHANICAL WAVE, FIXED PROBE, HATCH OPENED, 6/18/83

USURF= 0. USSAV= 16. USE=-16. MEAN VELOCITIES AND TEMPERATURES

ALL LENGTH DIMENSIONS IN MM

RUN	-Y	-Y/DELTA	-Y+	ETA	USS	U	UZS	UR	XLN	V	TINF	TB
1	22.8	.02	23.	15.67	16.9	-9.8	11.5	*****	1.026	-1.2	23.18	21.06
2	25.5	.02	26.	15.68	16.7	-6.8	10.9	*****	.767	-1.4	23.35	21.08
3	30.6	.03	31.	15.81	16.8	-6.3	10.3	*****	.510	-1.6	23.90	21.09
4	38.5	.03	39.	15.82	16.8	-7.0	9.8	*****	.303	-1.6	23.43	21.10
5	50.8	.04	52.	15.88	16.8	-7.2	8.2	*****	.162	-1.3	23.35	21.12
6	65.9	.05	67.	15.59	16.8	-5.4	6.9	*****	.088	-1.6	23.05	21.12
7	83.1	.06	85.	15.78	17.1	-4.6	6.0	*****	.048	-1.8	23.05	21.12
8	98.4	.08	100.	15.88	16.8	-2.6	5.0	*****	.030	-1.6	23.65	21.12
9	112.7	.09	115.	15.88	16.6	-2.3	4.8	*****	.321	-1.8	23.50	21.11
10	130.5	.10	133.	15.97	16.6	-1.9	3.7	*****	.0149	-1.9	23.72	21.11
11	150.2	.12	153.	15.97	16.6	-1.8	2.5	*****	.0069	-1.7	23.88	21.11
12	171.5	.14	175.	15.98	16.6	-1.5	2.1	*****	.0006	-1.7	23.88	21.11
13	195.6	.16	200.	15.99	16.6	-1.3	1.6	*****	.0005	-1.8	23.96	21.11
14	225.0	.18	230.	15.99	16.6	-1.1	1.2	*****	.0002	-1.8	23.89	21.11
15	251.4	.20	257.	15.99	16.6	-1.0	1.0	*****	.0001	-1.8	23.69	21.10
16	276.4	.23	283.	15.99	16.6	-.9	.8	*****	.001	-1.8	23.60	21.10
17	302.7	.25	310.	15.99	16.6	-.9	.7	*****	.001	-1.9	23.88	21.10
18	332.6	.27	340.	15.99	15.7	-1.1	.7	*****	.001	-1.9	23.39	21.09

RMS VELOCITIES

RUN	-Y	US	UZ	U	UR	UT	SUR	V	VR	VT	SVR	UP	PU	VP	PV	PU-PV	SHMU	SHMV
1	22.8	102.9	89.7	83.8	83.3	3.5	1.00	87.5	87.4	3.6	1.00	116.3	357.4	122.9	268.8	88.6	.046	.012
2	25.5	102.4	87.9	82.4	82.2	2.3	1.00	86.8	86.9	2.5	1.00	112.5	357.5	121.3	269.0	88.3	.025	.011
3	30.6	102.5	85.5	80.6	80.6	1.6	1.00	86.9	86.9	1.7	1.00	112.5	357.5	119.4	269.0	88.5	.022	.011
4	38.5	102.4	82.5	77.8	77.8	1.0	1.00	82.2	82.2	1.0	1.00	107.7	357.5	115.1	268.9	88.5	.019	.011
5	50.8	102.6	78.5	73.8	73.8	.7	1.00	77.7	77.7	.7	1.00	102.2	357.5	109.8	268.8	88.6	.017	.011
6	65.9	102.4	73.8	69.0	69.0	.4	1.00	72.4	72.3	.4	1.00	95.5	357.7	101.8	268.9	88.7	.016	.011
7	83.1	102.5	67.1	64.5	64.5	.3	1.00	67.9	67.9	.3	1.00	90.5	357.7	95.6	268.9	88.6	.015	.011
8	98.4	102.5	62.2	59.8	59.8	.2	1.00	63.7	63.7	.2	1.00	84.5	357.7	89.6	268.8	88.8	.015	.011
9	112.7	102.2	58.8	56.5	56.4	.2	1.00	59.7	59.7	.2	1.00	79.6	358.1	84.6	268.8	88.8	.015	.011
10	130.5	101.6	53.8	52.3	52.3	.1	1.00	55.1	55.1	.1	1.00	73.6	357.8	77.8	268.8	88.9	.015	.011
11	150.2	101.3	49.5	47.9	47.9	.1	1.00	50.7	50.7	.1	1.00	67.8	358.0	71.8	268.8	89.0	.015	.011
12	171.5	100.8	45.5	44.0	44.0	.1	1.00	46.8	46.8	.1	1.00	61.8	358.2	65.8	268.8	89.0	.015	.011
13	195.6	100.6	41.8	40.3	40.3	.1	1.00	42.8	42.8	.1	1.00	56.2	358.3	59.8	268.8	89.0	.015	.011
14	225.0	100.4	37.8	36.3	36.3	.1	1.00	38.5	38.5	.1	1.00	50.4	358.3	52.8	268.8	89.0	.015	.011
15	251.4	100.3	33.8	32.3	32.3	.1	1.00	34.2	34.2	.1	1.00	45.1	358.4	47.5	268.8	89.0	.015	.011
16	276.4	99.9	31.0	29.5	29.5	.1	1.00	31.2	31.2	.1	1.00	41.0	358.5	43.2	268.8	89.1	.015	.011
17	302.7	100.1	28.8	26.3	26.3	.1	1.00	28.2	28.2	.1	1.00	37.8	358.6	39.9	268.8	89.1	.015	.011
18	332.6	100.0	26.0	23.4	23.3	.1	1.00	24.2	24.2	.1	1.00	32.8	358.6	34.2	268.8	89.1	.015	.011

COVARIANCES (UE, VE (E-5))

RUN	-Y	UE	VE	UV	UVR	UVT	SUVR	UUTRP	PUUTR	UVTRP	PUVTR	VVTRP	PVVTR	RPRUU	TPRUU
1	22.8	1.259	-.030	225.7	224.5	1.2	.99	12.2	16.5	8.8	186.8	11.1	190.0	22.20	.12
2	25.5	1.248	-.025	190.1	188.7	1.3	.99	8.7	184.6	7.6	185.6	9.7	179.5	18.62	.15
3	30.6	1.218	-.022	237.0	236.0	.9	.99	7.5	184.6	6.2	178.5	7.9	183.2	22.77	.13
4	38.5	1.176	-.022	199.4	199.1	.3	1.00	6.8	183.9	6.5	187.2	7.6	185.2	23.74	.13
5	50.8	1.118	-.025	127.1	127.0	.1	1.00	8.7	184.9	8.5	188.0	8.5	188.1	11.66	.13
6	65.9	1.059	-.022	89.2	89.2	.0	1.00	8.9	184.7	8.4	188.8	8.5	188.9	6.42	.13
7	83.1	.998	-.022	97.5	97.5	.0	1.00	8.8	184.5	8.3	188.8	8.5	188.6	6.54	.13
8	98.4	.922	-.020	75.0	74.9	.0	1.00	7.8	184.5	7.5	188.7	7.7	188.5	6.12	.13
9	112.7	.854	-.017	66.1	66.1	.0	.99	7.8	184.5	7.5	188.7	7.7	188.5	6.12	.13
10	130.5	.797	-.011	74.5	73.5	.0	.99	7.8	184.5	7.5	188.7	7.7	188.5	6.12	.13
11	150.2	.751	-.011	36.7	36.6	.0	.99	7.8	174.3	7.5	191.7	7.7	190.1	6.12	.13
12	171.5	.668	-.005	44.1	44.0	.0	.99	7.8	174.3	7.5	176.7	7.7	176.5	6.12	.13
13	195.6	.610	-.005	43.7	43.6	.0	.99	8.2	200.5	7.9	201.8	8.1	200.1	6.12	.13
14	225.0	.543	-.003	33.4	33.4	.0	.99	7.7	199.2	7.4	198.8	7.6	199.0	6.12	.13
15	251.4	.488	-.003	15.6	15.6	.0	.99	7.7	199.2	7.4	198.8	7.6	199.0	6.12	.13
16	276.4	.448	-.003	10.5	10.5	.0	.99	7.7	174.3	7.4	174.0	7.6	174.2	6.12	.13
17	302.7	.399	-.003	9.5	9.5	.0	.99	7.6	174.3	7.3	174.0	7.5	174.2	6.12	.13
18	332.6	.355	-.003	9.4	9.2	.0	.99	7.6	174.3	7.3	174.0	7.5	174.2	6.12	.13

RMS ETA= 14.98 AVE. TINF.= 22.85 AVE. TAULK= 20.49

YETA = 248.0 FDUM= 1.0 HZ DELTA= 99.0 USTAR= 2.2

MECHANICAL WAVE, FIXED PROBE, UINF= 1.7 M/S, 6/20/83

USURF= 39. UBSAV= 15. USE= 24. MEAN VELOCITIES AND TEMPERATURES ALL LENGTH DIMENSIONS IN

RUN	-Y	-Y/DELTA	-Y+	ETA	USS	U	UZS	UW	RLN	V	TINF	TB
1	21.6	.22	48.	15.12	16.1	3.2	10.6	.649	1.029	-1.0	25.41	20.51
2	23.1	.23	51.	15.08	15.7	2.2	10.3	.684	.987	-.7	23.25	20.51
3	25.3	.26	56.	15.08	15.8	1.3	10.0	.713	.726	-.6	23.23	20.51
4	28.9	.29	64.	14.99	15.5	.4	9.5	.751	.538	-.6	23.04	20.51
5	35.2	.36	78.	14.98	15.3	.4	8.7	.767	.342	-.6	23.06	20.51
6	43.1	.43	95.	15.00	15.4	.0	8.1	.790	.217	-.6	23.14	20.51
7	53.5	.54	118.	14.96	15.5	-1.4	7.2	.831	.130	-.6	23.15	20.51
8	66.4	.67	147.	15.00	15.8	-1.3	6.3	.872	.077	-.5	23.04	20.50
9	81.4	.82	180.	14.75	15.6	-1.5	5.3	.904	.045	-.5	23.10	20.50
10	99.4	1.00	220.	14.83	15.8	-1.9	4.5	.933	.027	-.5	23.00	20.49
11	119.4	1.21	265.	14.81	14.9	-2.8	3.7	.957	.016	-.4	22.98	20.49
12	139.5	1.41	309.	14.89	15.0	-2.8	3.1	.981	.010	-.3	22.83	20.49
13	161.1	1.63	357.	14.97	15.3	-3.3	2.6	1.017	.007	-.3	22.55	20.49
14	186.1	1.88	412.	14.85	15.1	-3.2	2.1	1.028	.004	-.2	22.36	20.48
15	211.3	2.13	468.	14.85	15.2	-3.8	1.7	1.054	.003	-.2	22.16	20.47
16	238.6	2.41	528.	14.78	14.7	-3.6	1.3	1.058	.002	-.2	22.13	20.47
17	267.2	2.70	592.	14.69	14.6	-4.1	1.1	1.077	.001	-.1	22.15	20.46
18	298.7	3.02	662.	14.67	14.7	-4.3	.8	1.071	.001	-.1	22.06	20.45
19	333.8	3.37	740.	14.80	14.9	-4.3	.7	1.092	.001	.0	22.09	20.44

RMS VELOCITIES

RUN	-Y	US	WZ	U	UW	UT	SUW	V	VW	VT	SVW	UP	PU	VP	PV	PUPV	SW*U	SW*V
1	21.6	99.0	86.5	77.4	77.1	6.8	1.00	86.1	85.9	6.1	1.00	107.7	359.5	120.1	271.7	87.8	.065	.025
2	23.1	98.8	85.5	77.4	77.0	5.7	1.00	85.6	85.4	5.3	1.00	107.7	359.8	119.5	271.5	88.1	.026	.017
3	25.3	98.5	84.5	78.1	77.9	5.7	1.00	84.9	84.8	5.3	1.00	108.8	359.8	118.7	271.5	88.7	.023	.017
4	28.9	97.7	82.4	77.4	77.1	5.9	1.00	83.5	83.3	5.7	1.00	107.8	359.8	116.8	271.5	88.9	.020	.016
5	35.2	97.5	79.6	75.2	75.1	6.5	1.00	81.0	80.9	6.0	1.00	105.1	.0	115.3	271.5	88.8	.022	.016
6	43.1	97.7	76.9	73.4	73.3	5.2	1.00	78.7	78.7	5.0	1.00	102.7	.0	110.3	271.5	88.7	.017	.013
7	53.5	97.6	73.0	70.8	70.7	2.8	1.00	75.8	75.7	3.1	1.00	99.1	.2	106.3	271.5	88.6	.013	.010
8	66.4	97.7	68.9	67.1	67.1	2.4	1.00	71.6	71.5	2.7	1.00	94.1	.2	100.5	271.5	88.9	.013	.010
9	81.4	98.2	63.3	63.2	63.1	3.1	1.00	67.4	67.3	3.1	1.00	88.6	.4	94.5	271.5	88.9	.015	.010
10	99.4	98.5	58.8	58.5	58.5	1.6	1.00	62.1	62.1	2.1	1.00	82.1	.4	87.2	271.5	88.9	.014	.009
11	119.4	98.4	53.9	54.1	54.1	1.7	1.00	57.6	57.6	1.9	1.00	75.9	.3	80.9	271.5	88.9	.015	.009
12	139.5	98.3	49.9	49.9	49.9	1.7	1.00	53.1	53.0	2.2	1.00	70.1	.9	74.6	272.1	88.8	.015	.009
13	161.1	97.4	45.9	45.9	45.9	1.6	1.00	48.6	48.6	1.7	1.00	64.5	.6	68.3	271.5	89.0	.015	.009
14	186.1	96.7	41.8	41.8	41.7	2.0	1.00	44.2	44.1	1.9	1.00	58.7	.6	62.0	271.5	89.0	.015	.009
15	211.3	96.8	37.7	37.8	37.8	2.1	1.00	40.0	39.9	2.1	1.00	53.1	1.7	56.1	271.5	89.2	.015	.009
16	238.6	96.9	34.1	33.8	33.8	2.5	1.00	35.5	35.4	2.2	1.00	47.4	1.6	49.8	272.1	89.2	.015	.009
17	267.2	95.5	30.7	30.1	30.0	1.7	1.00	31.6	31.5	1.9	1.00	42.2	1.6	44.3	271.5	89.6	.015	.009
18	298.7	95.6	27.7	26.6	26.6	1.3	1.00	27.9	27.9	1.5	1.00	37.5	1.0	39.2	271.5	89.6	.015	.009
19	333.8	96.2	25.1	23.3	23.2	1.6	1.00	24.2	24.2	1.7	1.00	32.4	1.5	34.0	271.8	89.7	.015	.009

COVARIANCES (UE, VE (E-3))

RUN	-Y	UE	VE	UV	UVW	UVT	SUVW	UUTWP	PUUTW	UVTWP	PUVTW	VVTWP	PVVTW	WPUU	TPUU
1	21.6	1.142	.035	258.5	258.1	.8	1.00	23.9	182.0	13.1	186.9	28.7	197.9	-51.17	-.04
2	23.1	1.141	.030	195.1	198.3	-3.5	1.02	19.8	165.6	15.8	164.9	19.8	199.3	-37.15	-.11
3	25.3	1.152	.028	162.8	166.8	-10.0	1.02	19.5	180.0	9.8	172.8	17.8	218.3	-28.57	-.09
4	28.9	1.136	.025	192.7	193.4	-11.1	1.01	18.3	159.9	13.5	162.1	17.8	205.0	-28.74	-.16
5	35.2	1.108	.027	129.7	133.0	-13.3	1.03	11.2	169.5	7.8	175.8	12.8	204.0	-15.15	-.35
6	43.1	1.082	.025	135.1	134.4	-12.2	1.02	8.4	172.0	5.7	174.7	8.7	186.2	-11.08	-.24
7	53.5	1.042	.011	136.1	138.1	-12.0	1.01	8.7	196.1	7.7	193.0	9.7	198.3	-12.27	-.08
8	66.4	.992	.022	89.2	90.9	-11.7	1.02	7.5	185.4	7.4	185.6	7.4	185.8	-12.22	-.08
9	81.4	.916	.022	85.5	86.5	-9.0	1.01	6.5	177.4	5.3	195.5	10.7	190.2	-11.88	-.08
10	99.4	.858	.028	75.4	77.2	-.1	1.00	7.3	195.5	7.3	195.5	7.3	148.3	-11.88	-.08
11	119.4	.793	.019	60.1	59.6	-.5	.99	6.5	197.8	6.5	197.9	6.8	196.1	-11.69	-.08
12	139.5	.736	.026	54.8	56.2	-.3	1.00	7.2	184.9	7.3	184.9	7.5	183.5	-11.69	-.08
13	161.1	.680	.018	35.0	34.8	-.3	.99	7.4	194.1	7.4	194.2	7.5	193.2	-11.71	-.08
14	186.1	.618	.019	33.5	33.6	-.1	1.00	6.7	174.5	6.7	194.9	6.7	149.2	-11.69	-.08
15	211.3	.556	.016	20.4	21.0	-.2	1.00	7.2	194.4	7.1	174.5	8.3	182.9	-11.12	-.08
16	238.6	.495	.019	9.7	9.3	.4	.95	6.5	181.1	7.4	186.1	7.4	186.2	-10.51	-.08
17	267.2	.437	.015	6.4	6.3	.4	.95	6.5	194.1	6.5	192.5	5.9	191.5	-10.00	-.08
18	298.7	.386	.011	5.4	5.6	.2	.96	7.3	173.0	7.3	174.0	7.3	173.0	-9.53	-.08
19	333.8	.341	.012	5.4	4.2	.6	.94	4.7	144.4	4.7	144.4	7.2	191.0	-9.09	-.08

RMS ETA= 15.51 AVE. TINF.= 26.33 AVE. TBULK= 18.33

YETA = 248.0 FOUM= 1.0 HZ DELTA= 102.0 USTAR= 3.1

MECHANICAL WAVE, FIXED PROBE, UINF= 2.5 M/S, 6/24/83

ALL LENGTH DIMENSIONS IN MM

USURF= 60. USSAV= 19. USE= 41. MEAN VELOCITIES AND TEMPERATURES

RUN	-Y	-Y/DELTA	-Y+	ETA	USS	U	UZS	UR	XLN	V	TINF	TB
1	22.4	.22	72.	15.33	19.1	8.5	11.0	.676	.977	-.5	26.67	18.17
2	24.0	.24	77.	15.46	19.2	7.2	10.9	.698	.855	-.5	26.50	18.20
3	27.0	.27	87.	15.33	18.9	5.6	10.3	.735	.647	-.7	26.25	18.22
4	31.3	.31	100.	15.40	19.1	6.1	9.9	.733	.672	-.8	25.98	18.24
5	37.1	.36	119.	15.49	19.3	5.3	9.3	.756	.324	1.1	25.62	18.27
6	45.2	.44	145.	15.65	19.5	4.1	8.7	.787	.210	-.7	25.35	18.28
7	55.1	.54	176.	15.68	19.5	2.9	7.8	.821	.131	-.7	25.11	18.29
8	67.4	.66	216.	15.57	19.1	2.6	6.8	.838	.079	1.0	24.87	18.31
9	83.0	.81	266.	15.58	19.2	1.8	5.8	.878	.047	1.0	24.83	18.34
10	100.1	.98	320.	15.57	19.1	1.4	4.9	.895	.029	2.1	24.14	18.35
11	120.2	1.18	385.	15.63	19.6	.5	4.1	.924	.018	1.6	23.90	18.36
12	140.3	1.38	449.	15.59	19.5	.0	3.4	.943	.011	1.3	23.68	18.37
13	163.5	1.60	523.	15.46	19.1	-1.1	2.7	.973	.007	2.2	23.45	18.38
14	189.1	1.85	605.	15.42	19.1	-1.3	2.2	.986	.005	1.1	23.23	18.38
15	214.2	2.10	685.	15.48	19.2	-2.1	1.8	1.006	.003	1.4	23.07	18.39
16	242.1	2.37	775.	15.48	19.5	-2.0	1.4	1.009	.002	1.7	22.85	18.40
17	270.6	2.65	866.	15.47	19.2	-1.8	1.1	1.010	.001	1.2	22.62	18.41
18	300.2	2.98	960.	15.46	19.1	-2.3	.9	1.023	.001	1.0	22.40	18.41
19	336.4	3.30	1076.	15.61	19.4	-3.0	.7	1.038	.001	1.4	22.24	18.42

RMS VELOCITIES

RUN	-Y	US	UZ	U	UW	UT	SUW	V	VW	VT	SVW	UP	PU	VP	PV	PUPV	SHMU	SHMV
1	22.4	102.4	87.6	76.0	75.3	9.8	.99	84.7	84.2	9.7	.99	105.8	357.2	117.9	268.4	88.8	.014	.014
2	24.0	103.2	87.6	77.5	77.0	8.8	.99	84.4	84.0	9.0	.99	108.1	357.2	117.7	268.8	88.4	.016	.017
3	27.0	102.2	85.9	76.5	76.0	8.9	.99	82.9	82.4	8.7	.99	106.2	357.1	115.4	268.8	88.5	.014	.019
4	31.3	102.7	83.9	76.1	75.8	7.0	1.00	82.0	81.7	8.7	1.00	106.4	356.9	114.5	269.1	88.7	.014	.014
5	37.1	103.3	81.9	74.6	74.3	7.8	1.00	80.2	79.8	7.7	1.00	104.5	357.5	112.0	269.1	88.4	.014	.017
6	45.2	104.3	78.5	72.8	72.5	6.0	1.00	77.8	77.6	6.0	1.00	101.9	357.7	108.8	268.9	88.4	.013	.016
7	55.1	104.2	75.8	69.7	69.5	5.4	1.00	75.0	74.8	5.8	1.00	97.7	357.8	105.0	269.2	88.6	.013	.015
8	67.4	103.6	71.1	66.1	65.9	5.5	1.00	71.0	70.7	5.7	1.00	92.6	357.8	99.3	269.6	88.5	.013	.015
9	83.0	103.4	66.1	62.2	62.1	4.4	1.00	66.7	66.6	4.9	1.00	87.2	357.6	93.5	269.3	88.3	.013	.013
10	100.1	103.5	61.4	58.4	58.3	4.2	1.00	62.2	62.0	4.9	1.00	81.9	357.9	87.1	269.7	88.2	.012	.013
11	120.2	104.1	56.5	54.5	54.4	3.6	1.00	57.7	57.5	4.4	1.00	76.8	357.9	80.8	269.5	88.4	.012	.013
12	140.3	103.9	51.9	50.3	50.1	3.8	1.00	53.3	53.1	4.2	1.00	70.5	358.1	74.6	269.6	88.5	.012	.012
13	163.5	102.9	46.9	45.7	45.6	3.8	1.00	48.5	48.3	4.4	1.00	64.0	358.3	67.9	269.9	88.6	.012	.012
14	189.1	102.7	42.4	41.4	41.2	4.0	1.00	43.8	43.6	4.5	.99	57.9	358.5	61.3	270.0	88.6	.012	.012
15	214.2	103.1	38.8	37.6	37.5	3.6	1.00	39.6	39.4	4.0	.99	52.6	358.8	55.3	270.0	88.8	.012	.012
16	242.1	103.3	35.1	33.8	33.7	3.8	.99	35.1	34.9	3.8	.99	46.7	359.1	49.1	269.5	89.0	.013	.012
17	270.6	103.0	31.9	30.2	30.0	3.5	.99	31.6	31.3	3.9	.99	42.1	358.9	44.0	269.5	89.0	.013	.012
18	300.2	102.9	29.0	26.6	26.4	3.4	.99	27.9	27.7	3.8	.99	37.1	359.5	38.9	269.7	89.3	.013	.012
19	336.4	103.8	26.2	23.2	23.0	3.3	.99	24.2	24.0	3.7	.99	32.3	359.8	33.7	269.7	89.3	.013	.012

COVARIANCES (UE, VE (E-3))

RUN	-Y	UE	VE	UV	UVW	UVT	SUVW	UUTAP	PUUTW	UVTAP	PUVTW	VVTAP	PVVTW	APPOD	TPPOD
1	22.4	1.136	-.051	121.0	124.6	-3.6	1.03	94.2	177.5	9.5	173.8	104.9	177.1	-50.54	.89
2	24.0	1.168	-.028	179.3	180.5	-1.2	1.01	80.7	176.6	8.8	206.8	88.9	178.1	-41.78	.28
3	27.0	1.146	-.028	151.5	153.0	-1.5	1.01	59.0	185.3	9.3	212.9	89.5	174.7	-31.61	.32
4	31.3	1.147	-.010	132.7	135.4	-2.8	1.02	35.3	188.4	9.0	178.7	31.3	175.1	-23.88	.89
5	37.1	1.138	-.017	157.9	159.9	-2.0	1.01	25.1	190.8	8.1	214.9	14.6	169.7	-22.80	.28
6	45.2	1.118	-.019	115.0	115.8	-.8	1.01	15.0	211.5	9.8	181.8	14.4	177.6	-11.88	.09
7	55.1	1.071	-.015	120.5	121.2	-.6	1.01	12.3	176.5	7.2	193.9	12.2	166.0	-8.86	.08
8	67.4	1.011	-.009	121.7	120.8	.9	.99	15.0	148.4	1.5	184.9	3.5	193.2	-5.55	.04
9	83.0	.951	-.012	123.4	121.2	2.2	.98	10.8	168.8	4.9	195.5	12.0	189.2	-4.08	.07
10	100.1	.896	-.008	115.2	111.2	4.0	.97	8.7	190.2	8.2	179.0	5.0	177.0	-5.56	.15
11	120.2	.839	-.006	94.4	87.6	6.8	.93	8.3	190.1	8.5	190.5	9.9	188.6	-3.18	.28
12	140.3	.772	-.005	76.8	71.2	5.6	.93	8.3	193.1	7.9	177.7	5.6	194.7	-2.67	.21
13	163.5	.696	-.002	66.8	60.6	6.2	.91	8.4	179.9	7.8	145.2	12.1	181.8	-1.96	.26
14	189.1	.628	-.000	49.6	44.3	5.3	.89	8.3	188.5	7.2	186.1	9.9	189.2	-.86	.10
15	214.2	.572	-.000	44.0	41.1	6.9	.86	7.1	202.4	7.0	202.4	7.9	187.6	-.21	.08
16	242.1	.509	-.000	15.9	9.1	6.8	.59	6.6	185.2	6.1	182.8	5.8	190.5	-.05	.02
17	270.6	.458	-.005	17.0	9.7	7.3	.57	7.3	179.7	7.5	180.8	8.5	184.0	-.05	.02
18	300.2	.403	-.002	9.2	2.8	6.4	.30	6.9	179.9	7.5	178.2	7.8	178.5	-.05	.13
19	336.4	.355	-.002	7.1	2.4	4.7	.33	6.1	148.2	6.1	147.9	8.5	183.1	-.05	.05

RMS ETA= 15.77 AVE. TINF.= 22.80 AVE. TRULA= 19.24

YETA = 248.0 FROM= 1.0 HZ DELTA= 168.0 USTAR= 5.8

MECHANICAL WAVE, FIXED PROBE, UINF= 4.1 M/S, 6/22/83

ALL LENGTH DIMENSIONS IN MM

USURF= 94. USSAV= 52. USE= 62. MEAN VELOCITIES AND TEMPERATURES

RUN	-Y	-Y/DELTA	-Y+	ETA	USS	U	UZS	UM	XLN	V	TINF	TH
1	23.6	.14	124.	16.01	32.5	10.8	11.9	.758	.941	-.3	25.41	19.29
2	25.1	.15	131.	15.96	32.0	11.3	11.4	.759	.910	-.2	25.16	19.28
3	24.0	.17	127.	15.95	32.0	9.9	11.0	.787	.840	-.3	24.85	19.28
4	31.9	.19	167.	15.99	33.1	7.7	10.5	.806	.881	-.2	24.59	19.28
5	37.6	.22	197.	15.78	31.9	7.8	9.5	.816	.524	-.2	24.26	19.28
6	45.4	.27	237.	15.82	32.1	6.1	8.7	.882	.211	-.0	24.01	19.28
7	54.8	.33	286.	16.15	33.6	5.8	8.2	.855	.140	-.2	23.77	19.27
8	67.5	.40	353.	15.91	33.3	4.0	7.0	.881	.082	-.0	23.52	19.27
9	82.6	.49	432.	16.23	33.2	2.9	6.2	.903	.051	-.4	23.16	19.26
10	97.5	.58	510.	16.03	33.1	2.6	5.5	.916	.032	-.1	22.98	19.25
11	113.5	.68	594.	16.06	33.0	-.0	4.5	.951	.022		22.73	19.24
12	113.8	.68	595.	15.80	31.8	-.1	4.4	.955	.021	1.0	22.60	19.24
13	134.0	.80	701.	15.78	31.8	-.1	3.6	.978	.013	8.7	22.40	19.25
14	150.7	.90	819.	15.47	30.4	-.2	2.9	.994	.008	5.9	22.30	19.27
15	182.0	1.08	952.	15.69	31.6	-.2	2.4	.981	.005	5.3	22.21	19.26
16	206.6	1.23	1081.	15.73	31.6	-.1	1.9	.986	.004	1.0	22.12	19.25
17	206.6	1.23	1080.	15.54	29.7		1.9	.977	.008	6.4	21.88	19.24
18	236.8	1.41	1236.	15.33	30.4	-.1	1.4	.997	.002	6.6	21.71	19.23
19	269.5	1.60	1409.	15.48	30.4	-.1	.1	.982	.001	2.0	21.56	19.21
20	306.0	1.82	1601.	15.66	32.7		.0	.993	.001	6.0	21.48	19.19
21	336.2	2.00	1758.	15.71	32.6	-.2	.7	1.017	.001	2.7	21.35	19.17
22	193.8	1.15	1011.	15.47	32.2	-.3	2.1	1.014	.004	1.8	21.18	19.15
23	218.8	1.30	1142.	15.65	33.0	-.2	1.7	1.010	.003	2.2	21.08	19.13
24	256.0	1.52	1339.	15.32	29.7	-.2	1.2	1.017	.002	3.4	20.97	19.12

RMS VELOCITIES

RUN	-Y	US	UZ	U	UM	UT	SUM	V	VM	VT	SVM	UP	PU	VP	PV	PUPV	SMPU	SMPV
1	23.6	115.1	90.5	79.2	79.7	19.9	.97	86.6	83.A	21.8	.97	107.2	358.0	117.5	270.1	A7.9	.022	.017
2	25.1	114.A	89.1	80.1	77.8	19.0	.97	85.3	83.0	19.7	.97	106.8	358.3	116.3	270.1	88.2	.022	.015
3	24.0	115.1	87.9	79.1	76.8	18.9	.97	84.2	81.9	19.6	.97	107.6	357.9	114.0	270.0	87.8	.017	.014
4	31.9	115.6	86.6	78.2	76.4	16.7	.98	83.7	81.9	17.2	.98	107.1	358.1	115.0	270.0	88.1	.017	.014
5	37.6	113.9	82.7	75.4	74.4	12.7	.99	79.9	78.9	12.7	.99	104.3	358.3	110.7	270.0	88.1	.016	.012
6	45.4	113.9	79.8	73.6	72.7	11.1	.99	78.0	77.3	10.6	.99	102.1	358.1	108.0	269.9	88.2	.016	.012
7	54.8	116.4	77.7	71.6	70.9	9.0	.99	75.6	75.1	9.1	.99	99.6	357.8	105.5	269.7	88.0	.015	.012
8	67.5	115.5	72.2	67.5	66.7	8.8	.99	71.8	70.9	8.1	.99	93.7	357.6	99.7	269.8	87.8	.015	.012
9	82.6	116.6	68.8	64.2	63.7	8.1	.99	68.1	67.8	7.3	.99	89.5	358.0	95.2	270.0	87.9	.015	.012
10	97.5	115.0	63.6	60.6	60.1	7.8	.99	63.7	63.5	6.9	.99	84.4	357.2	89.0	269.8	87.8	.015	.012
11	113.5	116.5	59.8	56.8	55.9	6.9	.99	59.8	59.5	6.1	.99	78.6	357.7	83.0	270.1	87.9	.012	.012
12	113.8	115.4	58.5	56.8	56.5	6.4	.99	60.0	59.7	5.9	1.00	79.8	358.0	83.9	270.1	87.9	.013	.012
13	134.0	115.0	53.6	51.7	51.4	5.6	.99	54.7	54.3	6.3	.99	72.3	357.5	76.3	270.0	87.5	.013	.012
14	150.7	111.0	48.6	47.6	47.2	5.5	.99	50.0	49.6	5.8	.99	66.4	358.7	69.8	271.0	87.7	.013	.012
15	182.0	113.1	44.1	43.2	42.8	5.3	.98	45.4	44.7	6.2	.98	59.5	358.1	62.8	270.6	87.7	.012	.012
16	206.6	113.2	40.5	39.6	38.9	7.6	.98	41.4	40.7	7.4	.98	54.6	359.2	57.2	271.2	88.0	.013	.012
17	206.6	111.2	39.9	39.2	38.9	5.1	.99	40.9	40.7	4.8	.99	54.7	359.2	57.1	271.2	87.6	.012	.012
18	236.8	110.5	35.9	34.6	34.2	5.7	.99	36.0	35.7	4.8	.99	48.0	358.8	50.2	270.8	88.0	.012	.012
19	269.5	111.1	31.9	30.2	29.6	5.8	.98	31.5	30.8	6.0	.98	41.6	359.5	43.5	270.5	89.2	.013	.012
20	306.0	113.7	28.7	26.8	25.7	6.2	.97	27.8	26.7	6.0	.98	38.1	359.7	37.6	269.6	89.1	.013	.012
21	336.2	113.8	26.2	23.5	22.9	4.8	.96	24.0	23.5	5.0	.98	32.2	359.4	33.0	269.1	90.2	.013	.013
22	193.8	112.5	41.7	40.8	40.1	4.7	.99	42.6	42.3	5.0	.99	56.4	359.0	59.5	270.3	87.8	.012	.012
23	218.8	113.9	38.8	36.7	36.4	4.5	.99	38.5	38.2	4.5	.99	51.2	359.1	53.7	270.3	88.0	.012	.012
24	256.0	110.2	33.0	31.6	31.3	4.4	.99	33.1	32.7	4.3	.99	43.9	358.6	46.0	270.1	88.0	.013	.012

COVARIANCES (UE, VE (E-3))

RUN	-Y	UE	VE	UV	UVM	UVT	SUVM	UUTMP	PUUTM	UVTMP	PUVTM	VVTMP	PVVTM	RMSUU	TRMSUU
1	23.6	1.210	.007	246.9	259.0	-12.0	1.05	805.2	182.5	19.A	164.1	575.6	180.A	-58.24	2.52
2	25.1	1.217	.006	205.7	227.9	-22.3	1.11	378.1	174.A	7.AA	210.3	650.2	181.A	-86.64	4.50
3	24.0	1.211	.004	234.1	253.4	-19.3	1.09	523.2	182.0	3.AA	51.0	372.8	179.2	-89.44	3.77
4	31.9	1.208	.002	191.9	210.1	-18.1	1.09	220.5	173.5	9.6A	254.2	261.4	181.5	-38.56	3.53
5	37.6	1.155	.002	191.5	211.3	-20.0	1.16	124.8	174.5	7.7A	214.6	155.5	180.5	-35.86	3.35
6	45.4	1.132	.002	146.4	170.2	-24.0	1.16	73.2	174.2	6.7A	208.6	MA.A	181.0	-25.33	3.57
7	54.8	1.120	.004	148.4	169.2	-20.5	1.09	49.6	182.4	5.4A	208.3	92.4	177.5	-21.76	2.68
8	67.5	1.085	.004	170.4	185.8	-15.0	1.09	24.4	178.4	4.4A	200.7	47.8	179.5	-19.67	1.64
9	82.6	1.018	.002	144.0	156.2	-15.0	1.09	21.8	182.4	3.4A	206.6	14.6	178.7	-15.48	1.14
10	97.5	.948	.011	133.1	148.7	-15.7	1.12	17.2	179.2	2.1A	201.1	11.2	180.3	-10.07	1.14
11	113.5	.882	.002	129.4	144.1	-14.8	1.07	14.2	180.2	1.1A	222.0	15.2	177.4	-7.31	.64

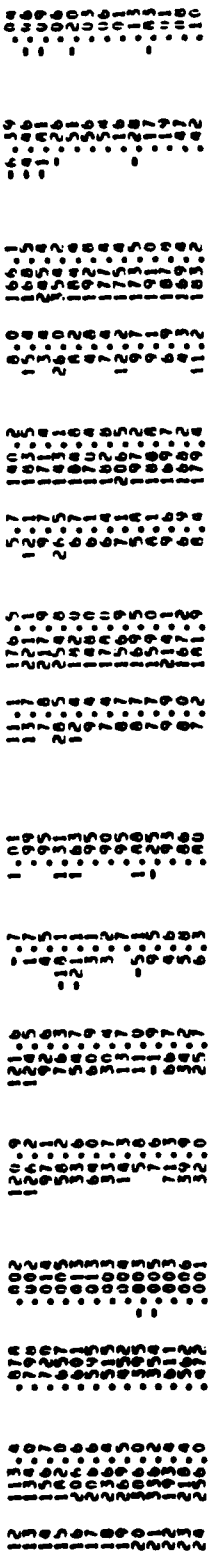

RMS ETA= 15.35 AVE. TINF.= 20.38 AVE. THULK= 17.89

YETA = 248.0 FOUM= 1.0 HZ DELTA= 171.0 USTAR= 9.2

MECHANICAL WAVE, FIXED PROBE, UINF= 6.2 M/S, 6/23/83

ALL LENGTH DIMENSIONS IN MM

USURF=154. USBAV= 46. USE=108. MEAN VELOCITIES AND TEMPERATURES

RUN	-Y	-Y/DELTA	-Y+	ETA	USS	U	UZS	UR	XLN	V	TINF	TH
1	26.7	.16	233.	15.18	43.3	15.6	11.8	.821	.621	1.8	23.11	18.09
2	28.8	.16	285.	15.50	44.2	14.2	12.1	.830	.578	1.6	22.80	18.08
3	31.8	.18	278.	15.17	45.4	10.9	10.1	.861	.444	1.5	22.50	18.08
4	36.9	.20	302.	15.42	45.8	11.3	10.2	.860	.351	1.8	22.17	18.07
5	42.0	.25	372.	15.14	45.0	13.3	8.6	.858	.212	1.2	21.88	18.06
6	50.7	.30	442.	15.28	46.7	10.3	7.8	.882	.185	1.9	21.67	18.08
7	60.0	.35	523.	15.17	44.8	2.7	6.8	.938	.095	3.7	21.39	18.08
8	70.3	.41	615.	15.50	44.8	1.6	6.3	.949	.067	3.5	21.10	18.02
9	82.2	.48	717.	15.34	45.6	1.6	5.8	.959	.048	4.3	20.81	18.00
10	97.1	.57	848.	15.44	47.1	6.6	8.7	.927	.029	3	20.70	17.98
11	97.1	.57	847.	15.27	45.9	-2.6	4.6	.986	.024	5.1	20.57	17.96
12	116.9	.68	1020.	15.44	46.9	-1.2	3.9	.989	.017	5.1	20.21	17.94
13	136.5	.80	1190.	15.26	46.7	-4.8	3.2	1.000	.011	6.1	19.97	17.92
14	156.8	.93	1385.	15.32	48.0	-3	2.6	1.478	.007	4.8	19.76	17.89
15	181.4	1.06	1582.	14.95	48.4	-4.8	2.0	1.013	.005	6.6	19.63	17.87
16	200.2	1.19	1761.	15.34	47.2	-5.5	1.8	1.024	.003	6.1	19.47	17.84
17	228.7	1.36	1945.	15.45	44.7	-3.7	1.5	1.015	.002	7.1	19.25	17.81
18	255.7	1.50	2231.	15.33	47.3	-6.8	1.2	1.036	.002	7.4	19.20	17.78
19	283.7	1.66	2475.	15.71	50.7	-8.5	1.0	1.023	.001	7.3	19.02	17.75
20	313.8	1.84	2730.	15.33	48.0	-5.7	.8	1.032	.001	5.6	18.95	17.71
21	33.5	.19	291.	15.58	45.7	11.7	10.5	.855	.388	2.0	18.88	17.67
22	41.5	.24	360.	15.55	46.4	9.0	9.4	.877	.262	2.8	18.87	17.65
23	49.1	.29	428.	15.62	46.5	9.0	8.2	.888	.162	3.3	18.67	17.62
24	58.6	.32	476.	15.48	47.9	3.2	7.5	.930	.123	3.8	18.97	17.59

RMS VELOCITIES

RUN	-Y	US	UZ	U	UW	UT	SUR	V	VW	VT	SVR	UP	PU	VP	PV	PUPV	SPRU	SPR
1	26.7	122.9	85.8	80.5	73.0	33.6	.91	86.6	78.7	36.9	.91	101.9	356.7	110.3	271.8	84.9	.026	.018
2	28.8	127.6	86.8	81.9	74.2	34.5	.91	86.7	78.5	36.9	.90	106.0	357.5	110.8	272.2	85.2	.026	.018
3	31.8	128.7	83.2	80.6	74.1	31.8	.92	85.8	78.2	33.8	.92	103.9	357.5	109.7	272.1	85.4	.026	.018
4	36.9	125.4	82.6	77.3	71.7	28.9	.93	82.4	76.8	30.1	.93	100.7	355.5	107.7	270.8	85.4	.026	.018
5	42.0	124.2	76.8	75.7	70.9	26.8	.94	79.0	74.5	26.2	.94	99.0	357.3	108.6	271.9	85.5	.026	.018
6	50.7	126.0	74.0	72.0	68.1	25.2	.95	76.6	71.3	24.9	.96	95.7	356.1	106.2	270.2	85.5	.026	.018
7	60.0	123.3	70.1	69.8	65.9	22.8	.95	72.2	68.8	21.6	.95	92.6	356.8	96.7	270.9	85.5	.026	.018
8	70.3	125.1	68.0	65.5	63.2	16.9	.97	68.1	66.3	15.4	.97	88.8	357.3	93.1	271.7	85.6	.026	.018
9	82.2	125.4	65.6	62.4	60.5	15.0	.97	65.3	63.0	13.2	.98	85.1	357.2	89.9	272.1	85.6	.026	.018
10	97.1	126.6	59.9	60.2	58.1	15.9	.96	61.6	60.5	12.7	.98	81.6	356.6	88.8	270.7	85.9	.026	.018
11	97.1	124.9	59.3	59.0	58.0	11.6	.98	61.1	60.2	10.7	.98	81.5	357.4	88.6	272.1	85.5	.026	.018
12	116.9	123.4	55.0	58.7	53.4	10.7	.98	56.5	55.7	9.5	.99	75.8	357.2	78.2	271.1	86.1	.026	.018
13	136.5	124.5	50.6	51.1	50.4	8.7	.99	52.4	51.8	7.6	.99	70.8	357.5	72.8	270.9	85.7	.026	.018
14	156.8	124.0	46.0	47.4	45.6	13.3	.98	47.6	46.8	8.7	.98	64.1	357.5	65.8	271.9	85.7	.026	.018
15	181.4	123.1	40.9	42.3	41.5	7.0	.98	43.3	42.7	6.8	.99	58.4	357.5	60.8	271.7	85.7	.026	.018
16	200.2	120.7	38.0	38.8	37.9	7.0	.98	40.1	39.2	6.6	.98	54.3	357.5	55.1	271.7	85.9	.026	.018
17	228.7	124.0	35.7	35.5	34.8	8.8	.97	36.6	35.6	8.8	.97	48.4	357.1	50.1	270.7	86.0	.026	.018
18	255.7	120.5	32.2	31.6	30.9	6.5	.98	32.5	31.8	6.6	.98	43.4	357.8	44.7	271.4	86.0	.026	.018
19	283.7	130.6	30.0	28.5	27.6	6.9	.97	29.3	28.1	6.1	.96	38.8	358.0	39.6	271.7	86.3	.026	.018
20	313.8	127.0	26.7	25.5	24.5	6.8	.96	26.1	25.0	7.4	.96	34.5	357.5	35.2	270.2	87.3	.026	.018
21	33.5	125.6	82.9	77.5	71.5	30.1	.92	83.4	77.5	30.8	.93	100.2	357.4	108.6	272.1	85.3	.026	.018
22	41.5	127.0	79.7	75.0	70.1	26.7	.93	79.4	74.9	26.5	.94	96.5	358.2	105.2	272.4	85.4	.026	.018
23	49.1	126.5	76.1	72.5	69.0	22.5	.95	75.6	72.4	21.6	.96	90.8	357.1	101.6	271.7	85.4	.026	.018
24	58.6	127.4	73.2	69.7	66.6	20.0	.96	74.4	72.4	18.4	.97	91.8	357.2	101.7	272.1	85.1	.026	.018

COVARIANCES (UF, VE (F-3))

RUN	-Y	UE	VE	UV	UVR	UVT	SUVR	UUTAP	PUUTA	UVTAP	PUVTA	VVTAP	PVVTA	RPRUU	TPRUU
1	26.7	1.043	.057	465.7	515.4	-49.7	1.11	827.2	182.2	81.2	184.4	1177.1	180.6	-171.68	16.37
2	28.8	1.145	.035	429.4	480.8	-51.0	1.12	821.6	181.8	25.5	314.2	1112.5	183.9	-159.02	16.84
3	31.8	1.045	.036	408.1	464.9	-56.8	1.14	820.2	184.5	12.7	184.5	1014.7	188.1	-151.26	18.44
4	36.9	1.078	.004	397.4	439.6	-42.2	1.11	638.2	178.9	23.5	271.5	749.2	179.1	-139.87	13.51
5	42.0	1.055	.029	349.6	423.5	-73.2	1.21	601.2	149.1	62.7	164.2	665.8	180.1	-122.44	21.52
6	50.7	1.010	.008	281.7	351.4	-69.7	1.25	224.7	144.8	28.6	182.8	234.1	184.7	-90.51	17.93
7	60.0	.987	.028	308.1	356.0	-47.9	1.16	161.7	220.7	69.2	184.4	69.8	201.5	-77.08	10.36
8	70.3	.949	.038	257.7	325.2	-67.5	1.26	124.0	195.1	6.9	164.4	110.2	188.8	-55.92	11.51
9	82.2	.949	.035	308.1	335.5	-24.2	1.10	44.5	201.8	21.0	117.4	32.2	178.7	-40.43	5.54
10	97.1	.885	.035	169.5	252.1	-82.7	1.49	52.7	151.5	17.5	150.0	51.5	190.7	-31.45	7.42
11	97.1	.855	.035	267.1	268.9	-21.4	1.00	47.6	187.5	2.7	240.7	45.7	182.1	-21.18	1.74

RMS ETA= 15.02 AVE. TINF,= 17.16 AVE. TRUL= 19.26

YETA= 200.0 FDOM= 1.0 HZ DELTA= 000.0 USTAR= 1.0

MECHANICAL WAVE, WAVE-FOLLOWING MODE, NO WIND, MATCH OPENED, 6/23/83

USURF= 0. USSAV= 15. USE=-15. MEAN VELOCITIES AND TEMPERATURES

ALL LENGTH DIMENSIONS IN cm

RUN	-Y	-Y/DELTA	-Y+	ETA	USS	U	UZS	UW	KLN	V	TINF	TH
1	2.5	.00	2.	15.30	15.4	+9.1	18.6	*****	0.000	-.9	17.82	19.51
2	4.0	.00	4.	15.21	15.2	+8.5	13.8	*****	0.000	-1.1	17.66	19.31
3	7.0	.01	7.	15.16	15.0	+8.1	12.4	*****	0.000	-1.1	17.51	19.31
4	11.1	.01	11.	15.09	15.0	+6.9	12.1	*****	0.000	-1.1	17.50	19.30
5	16.0	.02	16.	15.10	15.0	+5.4	11.3	*****	0.000	-1.1	17.20	19.30
6	21.0	.02	21.	15.06	14.9	+3.5	10.5	*****	0.000	-.9	17.07	19.30
7	27.0	.03	26.	14.99	14.7	+2.5	9.7	*****	0.000	-1.3	16.95	19.29
8	36.1	.04	35.	14.95	14.7	1.6	9.7	*****	0.000	-1.5	16.94	19.28
9	46.5	.05	45.	14.94	14.7	1.4	7.8	*****	0.000	-1.2	16.95	19.28
10	56.5	.06	55.	14.96	14.7	1.9	7.0	*****	0.000	-1.3	16.98	19.28
11	70.6	.07	69.	15.05	14.9	2.4	6.1	*****	0.000	-1.3	16.90	19.28
12	85.0	.08	83.	15.07	15.0	3.0	5.5	*****	0.000	-1.3	16.93	19.27
13	105.0	.11	103.	14.93	14.7	3.4	4.1	*****	0.000	-1.2	17.01	19.26
14	125.0	.13	122.	14.91	14.6	3.2	3.6	*****	0.000	-1.2	17.08	19.26
15	145.0	.15	142.	14.94	14.7	3.5	3.0	*****	0.000	-1.3	17.18	19.25
16	165.0	.16	161.	14.93	14.6	3.5	2.5	*****	0.000	-1.3	17.29	19.24
17	188.0	.19	182.	14.97	14.7	3.4	2.1	*****	0.000	-1.3	17.35	19.24
18	205.0	.21	200.	14.94	14.7	3.2	1.8	*****	0.000	-1.3	17.37	19.24
19	225.0	.23	220.	14.98	14.7	3.1	1.5	*****	0.000	-1.3	17.41	19.23
20	251.0	.25	245.	14.98	14.8	2.5	1.2	*****	0.000	-1.0	17.25	19.22
21	275.0	.28	269.	14.99	14.8	2.0	1.0	*****	0.000	-1.0	17.10	19.21
22	300.0	.30	293.	15.02	14.9	1.9	.9	*****	0.000	-1.0	16.98	19.20
23	325.0	.33	318.	15.00	14.8	1.8	.7	*****	0.000	-1.0	16.89	19.19
24	338.5	.34	331.	15.01	14.8	1.5	.7	*****	0.000	-.9	16.77	19.19

RMS VELOCITIES

RUN	-Y	US	UZ	U	UW	UT	SUW	V	VW	VT	SVW	UP	PU	VP	PV	PUPV	SHRU	SHRV
1	2.5	99.3	97.7	89.0	88.9	4.8	1.00	92.6	92.6	3.1	1.00	124.3	358.6	130.0	269.3	89.3	.023	.014
2	4.0	98.7	96.0	87.7	87.7	3.5	1.00	91.4	91.4	2.3	1.00	122.6	358.8	128.3	269.4	88.9	.022	.013
3	7.0	98.3	95.8	86.4	86.3	3.5	1.00	90.1	90.1	2.3	1.00	120.8	358.8	126.5	269.5	88.9	.020	.013
4	11.1	97.9	91.9	84.7	84.5	5.9	1.00	88.1	88.1	2.3	1.00	118.2	358.5	123.7	269.5	89.0	.021	.013
5	16.0	98.0	88.9	83.2	83.1	3.9	1.00	86.8	86.8	1.5	1.00	116.3	358.3	121.6	269.6	88.9	.020	.013
6	21.0	97.8	86.3	81.5	81.4	5.5	1.00	84.6	84.6	2.3	1.00	113.6	358.5	118.8	269.5	89.0	.021	.013
7	27.0	97.2	83.5	79.2	79.2	3.7	1.00	82.3	82.3	1.9	1.00	110.9	358.6	115.7	269.6	89.0	.021	.013
8	36.1	97.0	79.8	76.1	76.1	3.5	1.00	79.1	79.1	2.1	1.00	106.6	358.5	111.1	269.7	88.9	.021	.013
9	46.5	97.0	75.6	73.0	72.9	3.8	1.00	76.0	76.0	2.1	1.00	102.2	358.4	106.7	269.7	88.9	.021	.013
10	56.5	97.1	72.0	70.3	70.2	2.2	1.00	73.0	73.0	2.1	1.00	98.5	358.3	102.5	269.7	88.7	.021	.013
11	70.6	97.0	67.9	66.6	66.5	4.4	1.00	69.3	69.2	2.1	1.00	93.3	358.3	97.3	269.8	88.7	.021	.013
12	85.0	97.0	63.6	63.0	63.0	2.0	1.00	65.4	65.4	2.1	1.00	88.4	357.9	91.9	269.8	88.6	.021	.013
13	105.0	97.0	57.8	58.1	58.0	2.9	1.00	60.3	60.3	1.6	1.00	81.5	357.8	84.7	269.8	88.5	.021	.013
14	125.0	96.8	53.0	53.8	53.8	2.4	1.00	55.3	55.3	1.6	1.00	74.7	358.2	77.7	269.8	88.6	.021	.013
15	145.0	97.0	48.9	49.8	49.8	2.3	1.00	51.3	51.3	1.7	1.00	69.3	358.0	72.1	269.8	88.6	.021	.013
16	165.0	96.9	45.1	45.9	45.9	1.8	1.00	47.3	47.3	1.6	1.00	64.0	358.2	66.5	269.7	88.5	.021	.013
17	188.0	97.2	41.7	42.1	42.1	1.8	1.00	43.6	43.6	1.6	1.00	59.1	358.3	61.2	269.7	88.5	.021	.013
18	205.0	97.0	38.9	38.9	38.9	1.6	1.00	40.3	40.3	1.6	1.00	54.7	358.3	56.7	269.7	88.7	.021	.013
19	225.0	97.0	36.1	36.1	36.0	1.6	1.00	37.3	37.3	1.6	1.00	50.6	358.4	52.8	269.7	88.7	.021	.013
20	251.0	97.3	33.0	32.9	32.8	2.0	1.00	33.7	33.6	2.5	1.00	45.8	358.7	47.2	269.8	88.9	.021	.013
21	275.0	97.3	30.5	29.7	29.6	2.0	1.00	30.6	30.6	2.5	1.00	41.6	358.7	43.0	269.8	88.9	.021	.013
22	300.0	97.5	28.2	26.7	26.5	3.1	1.00	28.1	27.9	3.0	1.00	37.5	359.2	39.2	270.7	88.5	.021	.013
23	325.0	97.8	26.1	24.4	24.3	2.0	1.00	25.8	25.9	2.0	1.00	34.2	358.9	35.8	269.9	88.8	.021	.013
24	338.5	97.5	25.0	23.0	22.9	1.9	1.00	23.5	23.4	2.0	1.00	32.2	358.8	33.9	269.7	88.1	.021	.013

COVARIANCES (UE, VE (E-3))

RUN	-Y	UE	VE	UV	UVW	UVT	SUVW	UWTWP	PUWT	UVTWP	PUVTW	VVTWP	PVVTW	WPWUP	TPWUP
1	2.5	1.340	-.009	120.6	130.0	-5.4	1.00	7.3	4.2	16.1	185.3	3.1	330.1	50.41	-2.03
2	4.0	1.315	-.006	181.8	183.5	-1.K	1.01	2.6	1K2.K	11.3	1K8.5	8.6	195.7	88.22	-1.65
3	7.0	1.291	-.004	171.2	173.7	-2.5	1.01	5.1	2K8.K	12.9	188.9	1.9	1K8.6	58.49	-1.80
4	11.1	1.259	-.004	152.5	150.8	-2.5	.02	1K.1	.K	12.K	1K6.7	8.5	208.6	47.28	-.77
5	16.0	1.237	-.006	157.2	156.1	.1	.99	11.2	231.K	7.7	17K.1	7.K	178.8	42.28	.28
6	21.0	1.207	-.008	136.8	136.1	.K	.99	8.K	13.9	6.K	2K8.K	5.9	2K1.K	32.88	.18
7	27.0	1.172	-.001	131.6	131.6	.0	1.00	9.2	218.4	3.8	174.3	4.2	212.3	26.70	.01
8	36.1	1.124	-.000	125.4	125.4	-.0	1.00	5.0	2K8.4	1.9	181.8	2.8	281.2	21.32	-.07
9	46.5	1.078	-.001	120.7	120.6	-.4	1.00	7.2	3K.5	1K.0	17K.7	5.3	33K.4	18.79	-.54
10	56.5	1.039	-.001	121.3	122.7	-2.4	1.00	5.8	23K.2	5.6	1K2.2	5.8	227.4	20.49	-.17
11	70.6	.990	-.001	103.7	106.2	-2.4	1.02	2.K	2K8.1	12.5	195.0	3.3	221.4	.53	-.12

RMS ETA= 14.79 AVE. TINF.= 22.77 AVE. TAULK= 19.00

YETA= 248.0 FOOM= 1.0 HZ DELTA= 99.0 USTAR= 2.2

MECHANICAL WAVE, WAVE-FOLLOWING MODE, UINF= 1.7 M/S, 4/26/85

ALL LENGTH DIMENSIONS I: MM

USURF= 39. USSAV= 15. USE= 24. MEAN VELOCITIES AND TEMPERATURES

RUN	-Y	-Y/DELTA	-Y+	ETA	USS	U	UZS	UR	XLM	V	TINF	TH
1	1.0	.01	2.	14.91	15.2	18.7	14.7	.143	0.000	-1.2	23.08	18.98
2	2.8	.02	5.	14.87	15.2	15.5	14.1	.241	0.000	.7	23.21	18.98
3	7.1	.08	14.	14.91	15.2	9.8	13.5	.402	0.000	.2	23.32	18.98
4	7.4	.08	15.	14.85	15.2	5.6	12.5	.535	0.000	.5	23.28	18.98
5	10.0	.11	20.	14.84	15.1	4.6	11.8	.581	0.000	.3	23.21	18.98
6	15.0	.16	30.	14.77	15.1	3.5	10.8	.607	0.000	.7	23.18	18.98
7	20.0	.20	41.	14.81	15.1	3.5	9.8	.660	0.000	.6	23.02	18.99
8	33.9	.34	70.	14.85	15.2	3.5	8.8	.682	0.000	.8	22.92	18.99
9	48.0	.48	99.	14.77	15.1	3.5	7.8	.736	0.000	.8	22.83	18.99
10	53.9	.54	111.	14.81	15.1	3.5	7.0	.781	0.000	.4	22.80	18.99
11	63.9	.64	131.	14.78	15.1	3.5	6.3	.833	0.000	.4	22.76	18.99
12	70.0	.70	144.	14.73	15.0	3.5	5.4	.857	0.000	.5	22.73	18.99
13	93.9	.94	193.	14.79	15.0	3.5	4.7	.890	0.000	.8	22.52	18.99
14	118.0	1.18	243.	14.74	15.0	3.5	3.9	.909	0.000	.8	22.62	19.00
15	133.9	1.34	276.	14.62	14.9	3.5	3.2	.929	0.000	.1	22.64	19.00
16	154.0	1.54	317.	14.66	14.9	3.5	2.7	.942	0.000	.4	22.64	19.00
17	175.0	1.75	360.	14.71	14.9	3.5	2.2	1.000	0.000	.5	22.51	19.01
18	196.0	1.96	403.	14.71	14.9	3.5	1.9	1.014	0.000	.7	22.44	19.01
19	216.0	2.16	445.	14.70	14.9	3.5	1.6	1.008	0.000	.1	22.48	19.03
20	236.0	2.36	485.	14.74	14.9	3.5	1.4	1.008	0.000	.7	22.29	19.03
21	256.0	2.56	526.	14.81	15.0	3.5	1.2	1.022	0.000	.9	22.45	19.04
22	276.0	2.76	567.	14.80	15.0	3.5	1.0	1.026	0.000	.5	22.48	19.04
23	296.0	2.96	609.	14.80	15.0	3.5	.9	1.066	0.000	.2	22.46	19.04
24	325.9	3.29	669.	14.84	15.1	3.2	.7	1.065	0.000	2.1	22.46	19.04

RMS VELOCITIES

RUN	-Y	US	UZ	U	UW	UT	SUW	V	VW	VT	SVW	UP	PU	VP	PV	PUPV	SMPU	SMPV
1	1.0	97.2	96.8	89.2	88.1	13.8	.99	91.4	90.5	12.6	.99	121.9	1.0	126.3	270.1	91.0	.043	.026
2	2.8	97.0	95.2	89.6	88.8	12.5	.99	90.9	90.2	11.6	.99	122.0	.9	125.8	271.6	89.3	.040	.027
3	7.1	97.2	94.8	88.8	88.1	11.1	.99	90.4	89.8	10.3	.99	122.2	.9	125.5	271.5	89.3	.038	.025
4	7.4	96.9	94.3	86.3	85.6	11.1	.99	89.1	88.5	10.3	.99	119.2	.7	124.0	271.5	88.8	.036	.019
5	10.0	96.8	93.8	85.7	84.9	10.4	.99	88.8	88.2	9.7	.99	118.9	.7	122.8	270.8	89.7	.032	.018
6	15.0	96.8	92.9	84.1	83.9	9.7	.99	88.0	87.4	9.0	.99	117.1	.5	120.8	271.1	89.7	.029	.015
7	20.0	96.8	92.3	83.7	83.0	9.0	.99	87.6	86.9	8.3	.99	116.6	.5	119.7	270.8	89.8	.027	.015
8	33.9	96.8	91.6	82.5	81.8	8.3	.99	86.5	85.8	7.7	.99	115.0	.5	118.0	270.5	89.8	.025	.015
9	48.0	96.8	91.0	80.6	80.0	7.7	.99	85.6	85.0	7.1	.99	112.6	.5	115.9	270.5	90.1	.023	.015
10	53.9	96.8	90.8	80.5	79.8	7.1	.99	85.4	84.8	6.5	.99	112.4	.5	115.8	270.5	90.1	.022	.015
11	63.9	96.8	90.6	79.6	78.9	6.5	.99	84.9	84.3	6.0	.99	111.2	.5	114.7	270.5	90.1	.021	.015
12	70.0	96.8	90.3	79.0	78.3	6.0	.99	84.6	84.0	5.5	.99	110.4	.5	114.0	270.5	90.1	.020	.015
13	93.9	96.8	89.8	77.4	76.8	5.5	.99	83.8	83.2	5.0	.99	108.2	.5	111.8	270.5	90.1	.019	.015
14	118.0	96.8	89.5	75.8	75.2	5.0	.99	82.9	82.4	4.5	.99	106.1	.5	109.7	270.5	90.1	.018	.015
15	133.9	96.8	89.3	74.5	74.0	4.5	.99	82.3	81.8	4.1	.99	104.5	.5	108.1	270.5	90.1	.018	.015
16	154.0	96.8	89.2	73.7	73.2	4.1	.99	81.9	81.4	3.7	.99	103.5	.5	107.0	270.5	90.1	.017	.015
17	175.0	96.7	89.1	73.1	72.6	3.7	.99	81.6	81.1	3.4	.99	102.8	.5	106.3	270.5	90.1	.017	.015
18	196.0	96.7	89.0	72.5	72.0	3.4	.99	81.3	80.8	3.1	.99	102.1	.5	105.6	270.5	90.1	.016	.015
19	216.0	96.7	88.9	72.1	71.6	3.1	.99	81.1	80.6	2.8	.99	101.6	.5	105.1	270.5	90.1	.016	.015
20	236.0	96.7	88.8	71.8	71.3	2.8	.99	80.9	80.4	2.6	.99	101.2	.5	104.7	270.5	90.1	.016	.015
21	256.0	96.7	88.8	71.6	71.1	2.6	.99	80.8	80.3	2.4	.99	100.9	.5	104.4	270.5	90.1	.016	.015
22	276.0	96.7	88.7	71.4	70.9	2.4	.99	80.7	80.2	2.2	.99	100.7	.5	104.2	270.5	90.1	.016	.015
23	296.0	96.7	88.7	71.3	70.8	2.2	.99	80.6	80.1	2.1	.99	100.5	.5	104.0	270.5	90.1	.016	.015
24	325.9	96.7	88.7	71.2	70.7	2.1	.99	80.5	80.1	2.0	.99	100.4	.5	103.9	270.5	90.1	.016	.015

COVARIANCES (UE, VE (E-3))

RUN	-Y	UE	VE	UV	UVW	UVT	SUVW	UUTMP	PUUMT	UVTMP	PUVTM	VVTMP	PVVTM	APMUU	TPMUU
1	1.0	1.277	.012	-122.7	+67.3	-55.4	.45	262.0	6.1	101.8	172.8	238.6	6.5	56.65	44.66
2	2.8	1.284	.045	85.5	175.4	+89.9	2.05	215.3	2.3	164.9	176.6	205.8	3.5	+138.75	71.12
3	7.1	1.279	.043	97.5	161.1	+63.5	1.65	156.5	1.4	115.6	177.7	141.7	2.8	+117.70	46.85
4	7.4	1.241	.044	130.5	216.5	+86.1	1.66	150.5	1.5	158.1	181.1	187.8	3.4	+158.47	53.62
5	10.0	1.235	.029	30.5	73.5	+43.0	2.41	78.6	.8	77.8	177.1	72.2	556.9	+38.17	22.33
6	15.0	1.215	.022	70.5	68.5	+19.2	1.20	18.8	5.5	26.8	173.1	14.0	551.3	+33.35	5.61
7	20.0	1.174	.019	29.5	47.8	+18.5	1.29	4.5	350.2	19.8	178.7	3.5	519.4	+8.98	2.02
8	33.9	1.130	.019	-3.1	8.4	+11.0	1.53	4.5	249.8	17.2	178.0	2.8	383.4	+1.42	.68
9	48.0	1.078	.017	38.9	45.9	+8.0	1.28	4.5	352.7	16.5	177.5	2.0	345.5	+1.26	.21
10	53.9	1.035	.024	82.8	88.7	-5.9	1.14	4.5	324.9	16.7	179.5	2.0	357.4	.61	-.01
11	63.9	.993	.022	81.7	80.1	1.6	.47	4.2	141.4	4.0	173.5	4.2	181.2	.94	.05

RMS ETA= 15.55 AVE. TINF.= 22.48 AVE. TBUL= 18.78

YETA= 248.0 FOOM= 1.0 HZ DELTA= 102.0 USTAR= 3.3

MECHANICAL WAVE, WAVE-FOLLOWING MODE, UINF= 2.5 M/S, 5/03/83

USURF= 62. USSAV= 19. USE= 43. MEAN VELOCITIES AND TEMPERATURES

ALL LENGTH DIMENSIONS IN MM

RUN	-Y	-Y/DELTA	-Y+	ETA	USS	U	UZS	UR	XLN	V	TINF	TH
1	2.1	.02	7.	15.58	19.7	23.0	17.2	.341	0.000	1.1	23.54	18.76
2	3.3	.03	11.	15.60	19.8	19.8	16.4	.416	0.000	1.1	23.51	18.76
3	4.9	.05	16.	15.60	19.8	16.5	15.2	.493	0.000	1.7	23.45	18.76
4	6.8	.06	23.	15.62	19.8	14.8	14.7	.530	0.000	2.0	23.30	18.77
5	8.4	.08	27.	15.64	19.8	13.3	13.9	.561	0.000	2.3	23.20	18.77
6	10.5	.10	34.	15.66	19.9	12.3	13.5	.573	0.000	2.6	23.07	18.77
7	13.5	.13	44.	15.66	19.9	10.9	12.9	.621	0.000	2.8	22.81	18.78
8	17.5	.17	57.	15.68	19.9	9.6	11.9	.621	0.000	3.1	22.79	18.78
9	22.5	.22	73.	15.70	19.9	8.6	11.1	.666	0.000	3.3	22.66	18.78
10	28.6	.28	93.	15.72	19.9	8.0	10.3	.691	0.000	3.5	22.78	18.78
11	36.7	.36	119.	15.74	19.9	6.9	9.4	.738	0.000	3.8	22.64	18.78
12	46.9	.46	152.	15.76	19.9	6.3	8.4	.763	0.000	3.9	22.50	18.79
13	57.0	.56	185.	15.78	19.9	6.1	7.8	.782	0.000	4.0	22.35	18.79
14	68.9	.67	224.	15.80	19.9	5.8	6.9	.815	0.000	4.0	22.24	18.79
15	80.9	.79	262.	15.82	19.9	5.6	6.3	.839	0.000	4.0	22.05	18.79
16	90.9	.89	295.	15.84	19.9	5.5	5.9	.858	0.000	4.0	21.99	18.81
17	95.0	.93	308.	15.85	19.9	5.4	5.8	.868	0.000	4.0	21.92	18.82
18	97.2	.95	315.	15.85	19.9	5.4	5.8	.845	0.000	4.0	21.96	18.81
19	99.2	.97	322.	15.86	19.9	5.3	5.6	.906	0.000	4.0	21.86	18.80
20	100.3	.98	326.	15.86	19.9	5.3	5.6	.921	0.000	4.0	21.82	18.79
21	101.4	.99	329.	15.86	19.9	5.2	5.6	.927	0.000	4.0	21.77	18.79
22	103.5	1.00	336.	15.86	19.9	5.2	5.6	.950	0.000	4.0	21.75	18.78
23	216.4	2.12	701.	15.85	19.4	4.4	4.7	.966	0.000	4.0	21.74	18.78

RMS VELOCITIES

RUN	-Y	US	UZ	U	UW	UT	SUW	V	VW	VT	SVW	UP	PU	VP	PV	PUPV	SHEAR U	SHEAR V
1	2.1	103.9	101.5	86.6	84.4	19.4	.97	94.5	92.9	17.3	.98	117.9	.5	129.5	270.8	89.9	.020	.023
2	3.3	104.2	100.6	86.0	85.5	15.7	.98	94.0	93.7	15.5	.99	119.8	358.6	130.4	270.5	88.1	.016	.021
3	4.9	103.1	98.3	85.2	84.1	14.0	.99	93.8	92.9	13.3	.99	118.2	358.7	129.6	270.6	88.1	.015	.021
4	6.8	103.5	97.6	83.3	82.1	13.2	.99	93.8	92.8	13.3	.99	115.3	358.8	124.3	270.8	87.4	.015	.021
5	8.4	103.2	95.8	82.8	81.8	12.9	.99	92.8	92.0	11.8	.99	115.0	359.0	128.6	271.2	87.4	.011	.021
6	10.5	103.6	95.8	82.9	82.1	11.2	.99	92.1	91.5	10.2	.99	115.3	358.5	127.6	270.8	88.1	.010	.020
7	13.5	103.1	93.0	82.4	81.5	10.7	.99	90.9	90.5	8.9	1.00	114.7	1.8	126.1	270.9	90.5	.010	.020
8	17.5	103.5	91.2	80.9	80.5	6.4	.99	89.1	88.8	7.4	1.00	112.9	1.5	125.9	271.1	90.5	.010	.020
9	22.5	103.5	88.8	79.4	79.1	7.5	1.00	87.6	87.3	6.2	1.00	111.1	1.6	121.9	271.1	90.5	.010	.020
10	28.6	103.0	85.8	77.7	77.2	9.0	.99	85.0	84.7	5.3	1.00	108.3	2.0	118.5	271.1	90.5	.010	.020
11	36.7	103.0	82.5	75.6	75.4	6.0	1.00	82.0	81.8	5.3	1.00	105.9	2.0	118.5	271.1	90.2	.010	.020
12	46.9	103.5	78.8	72.6	72.2	7.6	.99	78.8	78.1	7.0	1.00	101.5	1.9	109.8	271.7	90.2	.010	.020
13	57.0	101.8	73.9	68.6	67.7	1.3	.99	76.2	75.8	11.1	.99	95.1	3.1	105.6	272.9	90.1	.010	.020
14	68.9	101.6	69.8	66.0	65.6	7.3	.99	72.0	71.7	6.7	1.00	92.2	2.7	100.5	272.0	90.1	.010	.020
15	80.9	103.3	67.1	63.2	62.9	6.4	.99	68.6	68.3	5.7	1.00	88.4	1.5	95.8	271.6	89.9	.010	.020
16	90.9	103.2	67.0	63.8	63.0	7.1	.99	68.5	68.1	7.2	.99	88.5	1.8	95.5	272.1	89.9	.010	.020
17	95.0	104.1	63.1	59.7	59.4	6.1	.99	64.7	64.4	6.5	.99	83.5	1.7	90.1	271.5	89.9	.010	.020
18	97.2	102.9	58.3	55.9	55.5	6.0	.99	60.1	59.8	5.5	1.00	78.0	1.7	83.8	271.8	89.9	.010	.020
19	99.2	102.6	53.7	51.6	51.3	5.1	1.00	55.5	55.2	5.1	1.00	72.1	1.9	77.5	272.1	89.9	.010	.020
20	100.3	102.6	50.8	49.0	48.7	12.4	.97	52.5	50.9	12.1	.97	68.6	2.5	71.5	270.2	89.5	.010	.020
21	101.4	102.8	46.0	43.8	43.6	4.8	.99	47.6	47.3	5.1	.99	61.2	2.2	66.3	272.4	90.2	.010	.020
22	103.5	102.9	42.3	40.3	40.0	4.5	.99	43.8	43.2	4.6	.99	56.2	1.8	60.8	271.9	89.8	.010	.020
23	216.4	101.7	38.5	35.7	35.3	5.7	.99	40.2	39.8	5.7	.99	49.5	2.7	55.9	272.1	90.6	.010	.020

COVARIANCES (UE, VE (E-3))

RUN	-Y	UE	VE	UV	UVW	UVT	SUVW	UUTRP	PUUTM	UVTRP	PUVTM	VVTRP	PVVTM	APROD	TPROD
1	2.1	1.260	.825	-27.2	-22.1	-5.0	.82	237.6	310.0	46.5	282.0	101.5	340.9	22.47	5.05
2	3.3	1.305	.827	229.7	248.4	-18.6	1.08	1.2	306.4	12.8	280.3	33.5	322.8	-253.54	17.36
3	4.9	1.274	.823	237.1	249.0	-11.9	1.05	30.9	308.9	19.8	191.2	35.8	337.0	-212.37	10.16
4	6.8	1.251	.835	219.3	258.6	-40.3	1.21	54.5	357.4	58.9	180.0	89.5	345.5	-197.49	38.56
5	8.4	1.248	.837	236.5	273.6	-37.1	1.16	60.5	385.2	64.1	194.0	38.9	351.3	-186.68	25.50
6	10.5	1.250	.822	-219.9	243.9	-24.0	1.11	6.8	355.2	22.2	176.6	5.5	255.5	-145.57	18.41
7	13.5	1.257	.854	-112.4	-95.5	-16.9	.45	11.8	98.5	31.8	198.5	7.6	333.5	86.80	4.72
8	17.8	1.239	.857	-98.2	-80.7	-17.5	.98	8.7	248.7	21.3	166.8	8.3	308.6	29.44	4.68
9	22.5	1.220	.862	-75.3	-59.2	-15.2	.79	2.5	350.6	16.2	187.5	8.3	172.9	14.29	1.67
10	28.6	1.190	.855	-137.0	-127.4	-9.6	.93	5.4	157.5	17.9	255.1	11.9	167.2	19.08	1.67
11	36.7	1.165	.863	-38.5	-36.1	-2.2	1.06	5.4	215.8	6.7	142.1	4.1	194.8	5.15	1.67
12	46.9	1.116	.859	-23.1	-34.4	13.5	1.06	5.4	74.4	11.3	91.4	30.2	78.7	12.49	1.67
13	57.0	1.032	.848	-14.1	-24.6	9.2	1.05	88.6	43.4	77.1	124.1	44.4	102.4	1.24	1.51

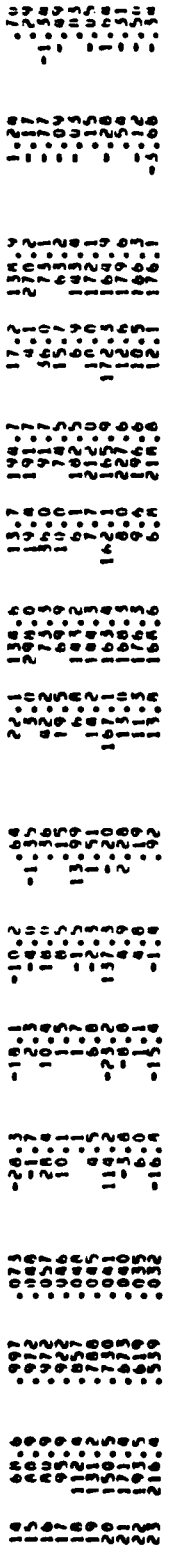

RMS ETA= 15.39 AVE. TINF,= 20.71 AVE. TMULR= 16.52

YETA= 208.8 FDOM= 1.0 HZ DELTA= 160.0 USTAR= 5.4

MECHANICAL WAVE, WAVE-FOLLOWING MODE, UINF= 6.1 M/S, 5/16/83

USURF= 92. USGAV= 32. USE= 60. MEAN VELOCITIES AND TEMPERATURES

ALL LENGTH DIMENSIONS IN CM

RUN	-Y	-Y/DELTA	-Y+	ETA	USS	U	UZS	UR	XLN	V	TINF	TB
1	3.0	.02	15.	15.56	32.3	85.0	23.3	.257	0.000	-11.7	23.35	16.47
2	4.1	.03	20.	15.45	31.2	34.6	20.9	.597	0.000	-2.8	23.05	16.46
3	5.6	.03	27.	15.30	32.0	28.6	14.2	.480	0.000	-5.2	22.78	16.49
4	7.6	.05	37.	15.27	31.1	25.4	10.8	.581	0.000	3.6	22.48	16.50
5	10.6	.06	52.	15.37	30.6	20.3	10.9	.618	0.000	1.1	22.25	16.50
6	14.6	.09	71.	15.42	31.9	18.2	13.2	.658	0.000	1.5	21.93	16.50
7	21.6	.13	105.	15.38	31.5	16.7	11.4	.694	0.000	1.0	21.60	16.51
8	29.6	.18	144.	15.48	32.3	15.3	10.2	.725	0.000	1.4	21.38	16.52
9	39.6	.25	194.	15.31	32.5	13.8	8.7	.777	0.000	.6	21.18	16.52
10	50.6	.31	247.	15.59	32.0	12.7	8.0	.799	0.000	.1	20.99	16.55
11	63.1	.39	308.	15.17	32.0	9.4	6.6	.826	0.000	-.5	20.81	16.54
12	108.1	.68	528.	15.48	32.2	4.7	3.8	.901	0.000	1.0	20.21	16.59
13	125.9	.79	615.	15.33	31.8	1.6	1.7	.943	0.000	1.8	20.07	16.57
14	143.2	.88	700.	15.33	31.8	1.0	1.1	.958	0.000	1.2	19.92	16.56
15	165.2	.98	808.	15.35	32.1	.6	.8	.961	0.000	1.8	19.76	16.55
16	185.6	1.10	906.	15.51	32.0	.2	.2	.973	0.000	1.6	19.68	16.55
17	208.1	1.28	1016.	15.45	31.6	.1	.1	.977	0.000	3.1	19.44	16.54
18	235.9	1.40	1151.	15.43	31.9	.0	.5	.958	0.000	1.7	19.29	16.53
19	266.1	1.58	1299.	15.43	31.7	-.1	.2	.972	0.000	2.5	19.12	16.51
20	296.1	1.76	1447.	15.39	31.7	-.1	.0	.972	0.000	2.6	19.02	16.50
23	77.8	.46	380.	15.27	31.5	.8	.8	.851	0.000	1.6	18.85	16.49
24	93.1	.55	454.	15.36	32.1	0.3	5.0	.877	0.000	1.0	18.57	16.47

RMS VELOCITIES

RUN	-Y	US	UZ	U	UW	UT	SUW	V	VW	VT	SVW	UP	PU	VP	PV	PUPV	SHPU	SHPV
1	3.0	112.9	105.7	93.5	86.8	34.8	.93	103.2	94.9	40.4	.92	120.3	6.2	132.3	269.8	96.8	.080	.038
2	4.1	111.6	102.9	91.7	85.5	33.9	.93	97.7	90.0	37.8	.92	118.8	1.7	125.4	269.6	92.6	.073	.034
3	5.6	112.6	100.5	91.7	85.5	33.9	.93	94.5	88.0	34.8	.93	119.5	358.7	121.6	269.8	89.8	.064	.029
4	7.6	110.0	97.5	90.1	84.0	30.9	.94	93.5	88.0	31.0	.94	118.5	359.0	112.0	269.9	89.9	.054	.024
5	10.6	110.4	95.2	86.4	82.8	28.5	.96	91.7	87.9	26.2	.96	115.5	358.2	121.8	270.2	88.4	.047	.020
6	14.6	111.8	93.3	88.8	81.8	22.9	.96	89.5	86.3	23.6	.96	114.8	358.6	120.3	270.4	88.1	.041	.016
7	21.6	111.7	88.1	88.8	78.8	19.7	.97	85.2	83.4	17.8	.98	109.7	357.7	116.1	269.5	88.1	.031	.010
8	29.6	112.6	84.8	76.0	76.0	15.1	.98	82.8	81.1	15.6	.98	107.3	358.6	113.6	270.3	88.3	.019	.010
9	39.6	111.9	79.3	74.7	73.7	12.0	.99	78.5	77.8	10.5	.99	103.5	358.5	109.2	270.4	88.1	.015	.010
10	50.6	113.4	76.2	71.2	70.4	10.5	.99	75.5	74.9	9.3	.99	98.9	359.2	105.1	271.0	88.2	.014	.010
11	63.1	111.4	70.2	69.9	69.1	9.8	.99	72.0	71.5	8.2	.99	93.9	358.5	100.4	270.2	88.3	.013	.010
14	108.1	112.8	58.8	57.0	55.7	11.9	.98	60.5	59.8	11.2	.98	78.3	.2	83.4	271.7	89.5	.013	.010
15	125.9	111.5	53.5	51.7	51.3	11.8	.98	57.0	55.9	11.2	.98	72.8	.3	78.5	271.1	89.5	.014	.010
16	143.2	111.8	49.6	48.2	47.8	11.8	.98	52.8	51.8	10.5	.99	66.5	.7	72.8	271.4	89.6	.014	.010
17	165.2	111.8	45.0	43.8	43.6	11.8	.97	48.5	47.1	11.0	.97	61.4	1.8	66.2	272.4	89.8	.014	.010
18	185.6	110.6	41.0	40.5	40.2	10.7	.99	44.3	43.9	10.2	.99	56.8	.7	61.7	271.7	89.8	.014	.010
19	208.1	111.3	39.5	38.0	38.0	10.8	.96	40.9	39.5	10.8	.97	51.3	1.1	55.5	271.5	89.6	.015	.010
20	235.9	112.3	35.8	32.8	31.5	9.6	.96	36.8	35.6	9.2	.97	44.1	.6	50.0	271.3	89.2	.018	.010
21	266.1	112.1	32.1	30.8	27.6	13.6	.90	34.3	31.5	13.7	.92	38.7	4.2	44.3	272.6	91.5	.018	.010
22	296.1	111.8	29.1	25.6	22.9	11.8	.89	30.3	28.2	11.1	.93	32.1	4.1	39.6	275.1	89.0	.020	.010
23	77.8	111.9	66.0	64.2	63.5	9.7	.99	67.5	67.0	8.3	.99	89.2	.8	94.1	271.4	89.0	.015	.010
24	93.1	111.9	62.1	59.9	59.0	10.1	.99	63.1	62.5	8.7	.99	83.0	360.0	87.7	270.2	89.7	.015	.010

COVARIANCES (UE, VE (E-3))

RUN	-Y	UE	VE	UV	UVW	UVT	SUVW	UUTWP	PUUWT	UVTWP	PUVTW	VVTWP	PVVTW	WPWUU	TPW3D
1	3.0	1.305	.015	-1051.	-898.6	-154.9	.85	615.1	131.8	571.9	315.2	262.9	27.2	1524.66	263.38
2	4.1	1.289	.008	-383.2	-303.2	-80.0	.88	156.5	187.3	265.8	304.7	274.4	13.1	849.70	64.60
3	5.6	1.298	.009	235.3	157.5	77.8	.67	176.7	81.5	38.9	223.1	326.7	10.7	-255.85	-116.56
4	7.6	1.271	.006	254.7	189.0	65.7	.78	187.5	14.1	85.0	217.4	175.0	7.1	-255.38	-64.80
5	10.6	1.250	.018	294.9	321.7	-24.8	1.08	74.1	.1	24.7	287.5	126.3	356.7	-369.66	28.33
6	14.6	1.240	.028	254.9	267.5	-23.6	1.12	56.7	588.2	12.1	289.5	89.3	337.2	-244.30	24.15
7	21.6	1.192	.003	240.2	255.7	-15.5	1.06	8.8	10.5	25.8	282.7	19.8	102.1	-151.52	9.15
8	29.6	1.168	.020	218.2	213.2	1.0	1.00	75.0	178.6	86.8	186.7	76.2	177.5	-70.08	-.55
9	39.6	1.113	.019	180.0	205.0	-25.1	1.14	21.5	152.9	49.1	228.5	24.2	162.9	-25.64	3.14
10	50.6	1.079	.029	182.8	174.3	+31.4	1.22	19.3	132.7	11.5	285.3	20.8	187.5	-8.71	.80
11	63.0	.998	.014	129.2	152.6	-23.4	1.14	17.8	182.0	8.0	212.3	18.3	158.7	-1.17	.18
14	108.1	.849	.036	188.7	88.0	55.7	.61	121.6	119.5	47.7	120.6	101.5	128.6	-13.84	-8.46
15	125.9	.779	.020	108.7	36.1	72.6	.33	140.4	130.5	120.0	131.0	130.1	131.8	-5.55	-11.17
16	143.2	.714	.031	70.8	43.2	27.3	.61	58.2	88.4	72.0	72.0	57.3	55.1	-8.35	-2.74
17	165.2	.669	.035	107.1	21.6	85.5	.20	149.5	92.4	129.4	74.0	139.7	88.9	-.45	-1.47

18	185.6	.619	.026	35.6	30.8	4.8	.36	21.1	151.1	7.3	203.0	18.0	155.4	1.70	.27
19	208.1	.554	.021	87.8	8.8	79.4	.10	126.0	98.2	122.8	95.5	151.6	97.7	.57	5.39
20	235.9	.477	.017	57.8	13.5	44.5	.23	81.5	116.0	78.6	112.1	83.7	112.8	.34	-1.12
21	206.1	.417	.025	96.6	-24.4	121.1	.25	227.6	102.1	202.7	90.6	238.9	100.8	2.23	-11.08
22	298.5	.345	.082	79.2	9.6	69.5	.12	151.4	111.9	114.9	90.2	127.5	105.7	8.17	36.08
23	77.0	.953	.038	70.6	77.0	-6.4	.09	25.0	144.9	16.8	171.3	22.9	155.6	-3.90	.32
24	93.1	.894	.015	41.7	18.8	22.9	.45	48.6	156.4	52.2	144.8	55.9	146.7	-2.11	-2.57

RMS ETA= 15.12 AVE. TINF.= 18.02 AVE. TBULK= 16.67

YETA= 246.0 FOOM= 1.0 HZ DELTA= 171.0 USTAR= 9.2

MECHANICAL WAVE, WAVE-FOLLOWING MODE, UINF= 6.1 M/S, 5/15/83

ALL LENGTH DIMENSIONS IN MM

USURF=157. USBAV= 47. USE=110. MEAN VELOCITIES AND TEMPERATURES

RUN	-Y	-Y/DELTA	-Y+	ETA	US	U	UZS	UR	XLN	V	TINF	TA
1	5.6	.03	47.	14.98	45.1	41.2	26.6	.567	0.000	-2.1	19.91	16.97
2	7.4	.04	62.	15.21	45.6	33.8	28.5	.62A	0.000	2.1	19.66	16.96
3	9.4	.05	79.	15.17	48.0	29.5	22.6	.66A	0.000	2.1	19.85	16.94
4	11.5	.07	97.	15.35	48.8	31.8	20.9	.667	0.660	1.5	19.26	16.92
5	13.6	.08	115.	15.38	45.8	29.0	18.0	.701	0.000	1.5	19.13	16.91
6	16.4	.10	142.	15.54	48.5	23.3	16.M	.745	0.000	3.4	18.90	16.89
7	20.8	.12	172.	15.25	45.7	25.5	18.1	.748	0.000	4.5	18.71	16.85
8	25.2	.15	213.	15.45	44.6	18.2	12.6	.803	0.000	6.5	18.45	16.84
9	31.7	.19	268.	15.25	46.2	21.3	10.7	.796	0.000	5.8	18.66	16.81
10	38.7	.23	335.	15.18	48.0	10.0	9.1	.821	0.000	5.8	18.34	16.79
11	46.7	.29	420.	15.17	46.9	14.4	7.7	.854	0.000	5.5	18.21	16.76
12	56.1	.35	499.	15.08	46.7	11.5	6.7	.884	0.000	6.4	18.02	16.74
13	70.1	.41	593.	15.00	46.8	13.0	5.9	.880	0.000	6.2	17.77	16.68
14	85.5	.49	706.	15.14	46.0	16.2	6.0	.859	0.000	5.3	17.83	16.59
15	98.6	.58	838.	14.96	46.5	12.1	5.0	.891	0.000	6.0	17.33	16.56
16	117.2	.69	990.	15.20	48.7	9.2	4.5	.913	0.000	6.2	17.24	16.53
17	136.2	.80	1151.	14.85	47.0	6.1	3.5	.939	0.000	6.5	17.18	16.49
18	156.2	.91	1337.	14.84	45.3	2.7	3.0	.964	0.000	6.5	17.07	16.43
19	184.2	1.08	1557.	14.87	45.0	.6	2.5	.990	0.000	7.2	16.95	16.41
20	214.2	1.25	1811.	15.08	45.8	-1.8	2.0	.999	0.000	8.0	16.84	16.37
21	244.5	1.43	2067.	14.89	45.5	-2.7	1.5	1.007	0.000	8.5	16.67	16.33
22	271.8	1.59	2297.	14.97	45.8	-.6	1.2	.98A	0.000	8.5	16.64	16.30
24	307.3	1.80	2598.	14.88	46.9	-1.9	1.0	1.006	0.000	8.9	16.60	16.26

RMS VELOCITIES

RUN	-Y	US	UZ	U	UM	UT	SUM	V	VM	VT	SVM	UP	PU	VP	PV	PUPV	SHMU	SHMV
1	5.6	123.3	107.9	92.8	79.4	48.1	.86	101.5	84.5	56.3	.83	111.0	359.7	117.7	268.9	90.6	.022	.029
2	7.4	120.7	106.2	97.1	82.2	51.0	.85	101.1	84.3	55.9	.83	110.0	358.7	117.7	269.5	89.2	.021	.028
3	9.4	119.3	103.5	95.7	82.8	48.0	.87	99.8	84.7	51.2	.86	110.0	359.7	118.5	271.1	88.6	.019	.027
4	11.5	117.8	101.6	98.9	82.9	46.1	.87	99.1	85.9	49.5	.87	110.0	359.8	119.7	269.9	89.3	.025	.024
5	13.6	115.0	97.9	93.0	81.1	45.6	.87	96.6	84.1	47.5	.87	110.0	.5	117.4	270.8	89.7	.026	.025
6	16.8	112.1	96.2	89.9	80.6	39.9	.90	93.4	84.2	40.5	.90	110.0	.6	117.8	271.1	89.4	.020	.021
7	20.8	110.8	90.7	87.8	78.8	39.5	.89	89.4	80.8	39.8	.90	109.7	.5	113.1	270.7	89.4	.022	.020
8	25.2	108.1	88.2	84.7	77.2	34.9	.91	87.0	80.1	33.0	.92	108.1	.1	112.1	271.4	88.7	.019	.021
9	31.7	105.2	85.1	81.1	73.7	33.8	.91	81.5	76.1	29.8	.93	105.8	359.5	106.8	271.4	87.9	.018	.016
10	38.7	102.3	78.1	76.8	70.8	29.8	.92	79.2	74.7	26.5	.94	99.1	359.9	104.6	271.4	88.5	.021	.020
11	46.7	100.4	73.9	72.5	68.3	24.3	.94	76.9	73.7	21.7	.96	95.7	.3	103.4	271.5	88.8	.018	.017
12	56.1	100.0	69.7	69.8	64.1	25.5	.93	70.3	68.1	17.5	.97	89.9	360.0	95.5	272.1	87.9	.016	.017
13	70.1	100.3	65.7	64.2	61.2	19.6	.95	70.0	67.8	17.4	.97	85.7	.7	95.2	273.4	87.2	.019	.015
14	85.5	100.7	60.5	60.4	55.8	24.1	.92	68.8	62.1	18.3	.96	77.6	1.4	87.2	271.1	90.5	.019	.016
15	98.6	100.6	61.5	56.8	53.3	18.6	.94	61.3	59.5	14.9	.97	74.6	.3	83.5	269.3	91.0	.019	.014
16	117.2	102.3	58.4	51.8	48.5	18.3	.94	57.3	55.4	14.0	.97	67.8	2.7	77.8	273.2	89.5	.020	.015
17	136.2	104.3	52.6	51.3	44.0	26.4	.86	56.1	49.9	25.7	.89	61.6	1.5	69.9	271.9	89.6	.021	.016
18	156.2	103.1	48.6	46.1	41.2	16.2	.94	48.9	46.8	15.5	.95	60.6	1.1	65.2	271.9	89.3	.016	.014
19	184.2	102.9	44.6	40.4	38.2	13.2	.94	44.4	42.5	12.9	.96	53.5	.8	59.7	272.2	88.8	.017	.013
20	214.2	102.2	40.9	36.6	32.6	16.1	.90	41.2	38.3	15.3	.93	46.0	.7	53.8	273.2	87.5	.019	.015
21	244.5	103.4	36.1	31.9	28.8	13.6	.90	35.9	33.8	13.0	.93	40.8	.6	46.9	274.5	87.3	.020	.015
22	271.8	103.7	32.6	28.9	26.8	14.9	.86	33.3	30.0	14.8	.90	34.7	.1	42.2	276.5	86.4	.019	.014
24	307.3	104.7	29.5	26.9	24.9	16.9	.78	30.4	25.6	16.3	.84	29.5	3.5	35.9	278.2	89.5	.017	.017

COVARIANCES (UE, VE (E-3))

RUN	-Y	UE	VE	UV	UVM	UV1	SUVM	UUTAP	PUUAT	UVTAP	PUVTA	VVTAP	PVVTA	APMUU	TPMUU
1	5.6	1.167	.005	30.A	-68.1	98.9	-2.21	168.4	2.5	243.9	258.9	418.1	12.2	85.14	-143.70
2	7.4	1.23M	.015	234.0	122.1	116.9	.51	272.A	345.0	325.1	267.6	353.5	326.9	-141.54	-155.58
3	9.4	1.226	.048	154.5	183.3	-23.8	1.15	106.8	349.5	122.0	275.3	229.8	301.3	-144.80	25.35
4	11.5	1.258	.011	25.9	98.0	-72.2	3.79	88.2	304.9	90.7	261.0	268.8	285.6	-94.55	69.59
5	13.6	1.232	.046	49.9	69.9	-20.0	.71	77.6	278.5	55.5	217.7	288.0	328.8	-45.82	-17.87
6	16.4	1.229	.058	82.4	85.0	-22.1	1.35	11.6	150.5	75.7	224.3	128.4	315.7	-44.89	16.68
7	20.4	1.174	.038	158.1	86.A	71.4	.55	204.2	185.7	131.0	153.2	146.7	178.8	-58.44	-44.98
8	25.2	1.166	.048	123.8	148.1	-24.6	1.17	149.3	148.5	66.4	224.3	145.2	242.9	-70.47	10.08
9	31.7	1.118	.032	143.1	216.0	-72.9	1.51	138.3	248.7	96.1	236.6	88.4	179.0	-72.10	24.34
10	38.7	1.053	.087	215.2	145.6	69.7	1.68	224.2	165.4	150.2	182.2	198.1	160.1	-28.45	-11.80
11	46.7	1.007	.048	100.8	109.0	-8.2	1.08	216.2	142.9	68.7	207.3	155.7	177.5	-10.82	.76
12	56.1	.961	.051	182.5	161.9	19.8	1.18	22.4	159.5	55.5	241.2	85.8	185.5	-6.97	.88
13	70.1	.879	.068	92.2	194.6	-102.4	2.11	100.8	184.2	28.5	145.0	85.0	178.4	-5.85	2.46

15	85.5	.825	.034	-49.2	-18.8	-30.4	.58	169.9	166.3	122.1	162.6	137.9	152.7	.95	1.58
16	98.6	.811	.026	-47.6	-51.5	3.8	1.08	179.1	166.3	99.8	155.8	121.6	163.4	5.00	-.37
17	117.2	.777	.007	11.6	20.2	-8.6	1.74	190.4	151.4	93.1	136.7	98.9	148.7	-3.06	1.30
18	136.2	.688	.048	488.1	10.7	477.8	.02	371.3	158.7	315.1	162.3	345.1	157.5	-1.43	-85.77
19	154.2	.624	.026	112.3	25.8	86.5	.23	187.3	99.8	160.2	77.7	186.6	85.6	-4.25	-18.26
20	184.2	.615	.024	59.5	38.1	21.2	.64	80.7	127.3	56.2	94.6	91.6	116.8	-3.66	-2.04
21	210.2	.551	.027	178.3	52.0	126.3	.29	236.4	154.5	151.2	156.3	198.2	152.0	-.05	-.11
22	240.5	.466	.010	125.1	44.2	80.9	.35	151.8	100.8	135.5	78.1	168.1	95.6	1.88	3.45
23	271.8	.413	.040	131.1	39.5	91.6	.30	195.3	92.8	180.8	67.1	185.1	85.2	-.27	.62
24	307.5	.350	.048	179.3	4.8	174.5	.03	304.0	123.9	249.3	107.6	300.1	120.7	-.56	-15.13

FIGURES

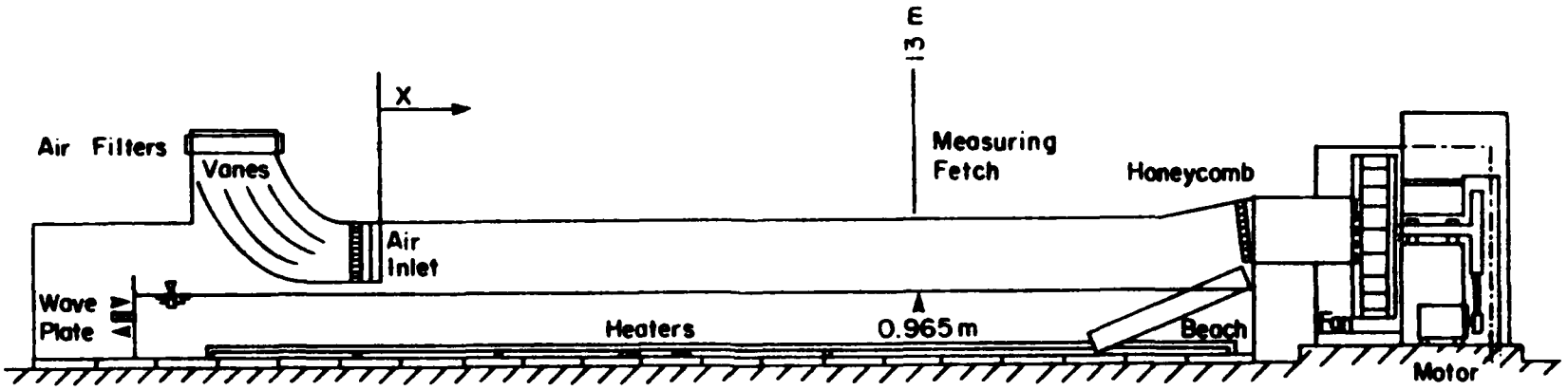

Figure 1. Stanford wind water-wave research facility.

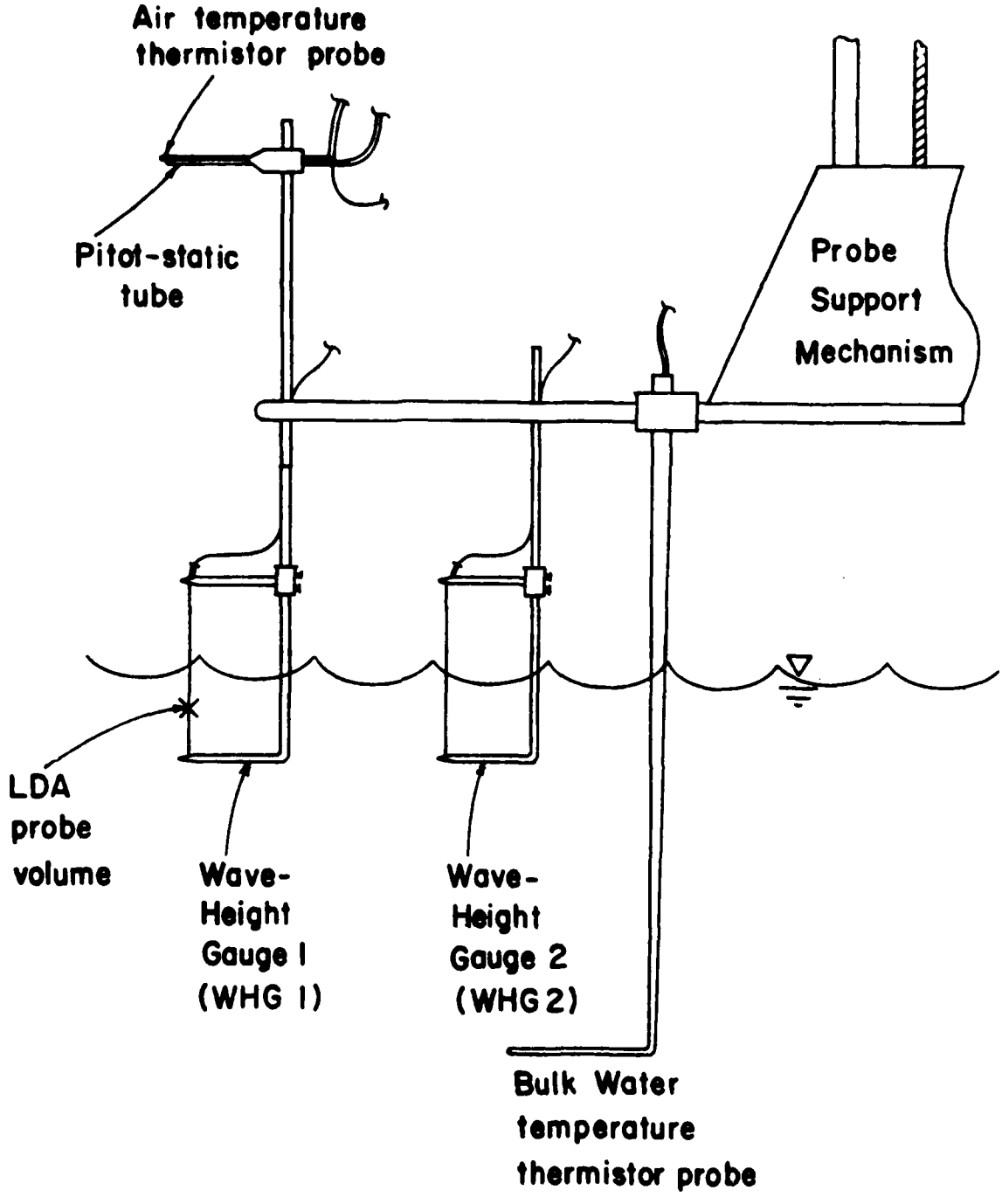

Figure 2. Probe support mechanism.

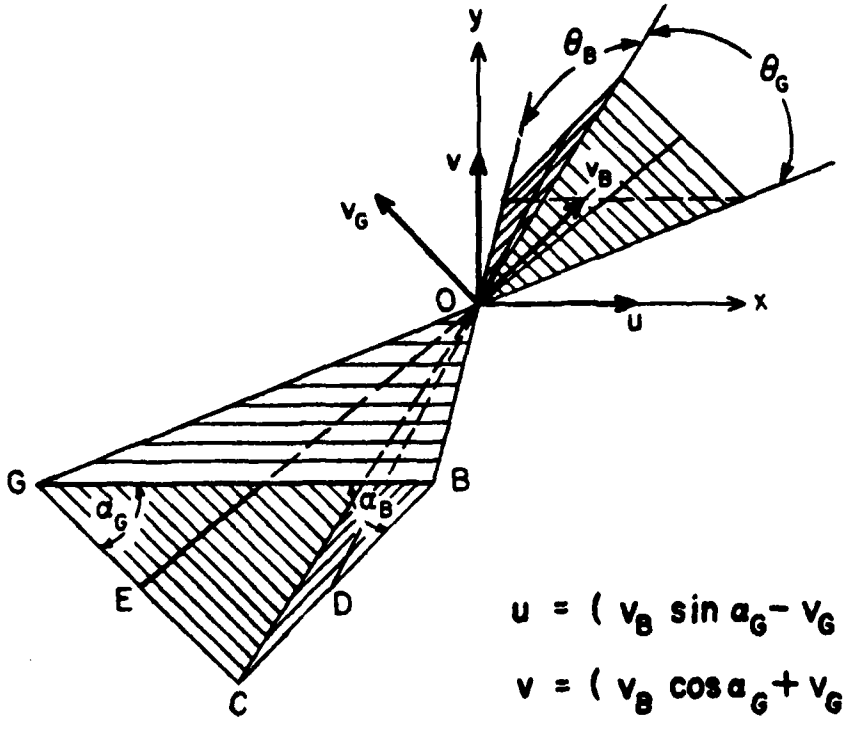

$$u = (v_B \sin \alpha_G - v_G \sin \alpha_B) / \sin (\alpha_B + \alpha_G)$$

$$v = (v_B \cos \alpha_G + v_G \cos \alpha_B) / \sin (\alpha_B + \alpha_G)$$

$v_B \perp$ DO in plane COB

$v_G \perp$ EO in plane COG

BO blue beam

GO green beam

CO cyan beam

Figure 3. Laser Doppler anemometer laser beam configuration.

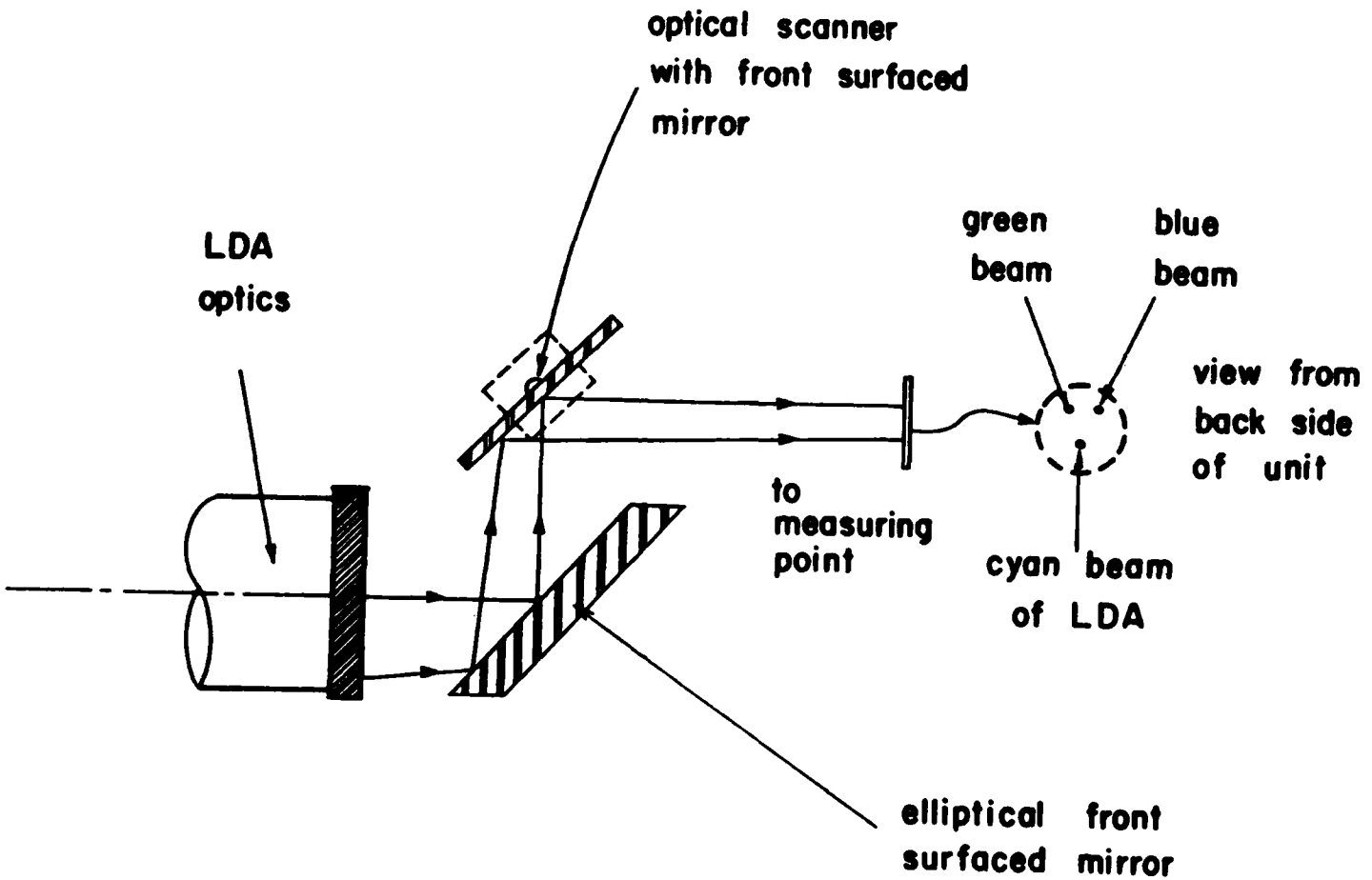

Figure 4. Schematic of optical scanner.

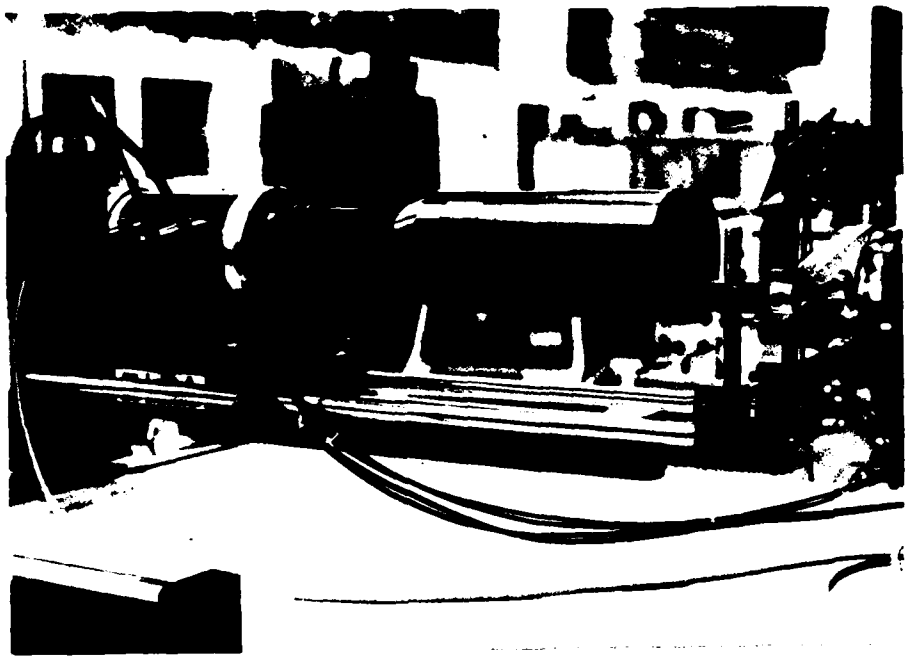

Figure 5. View of optical scanner.

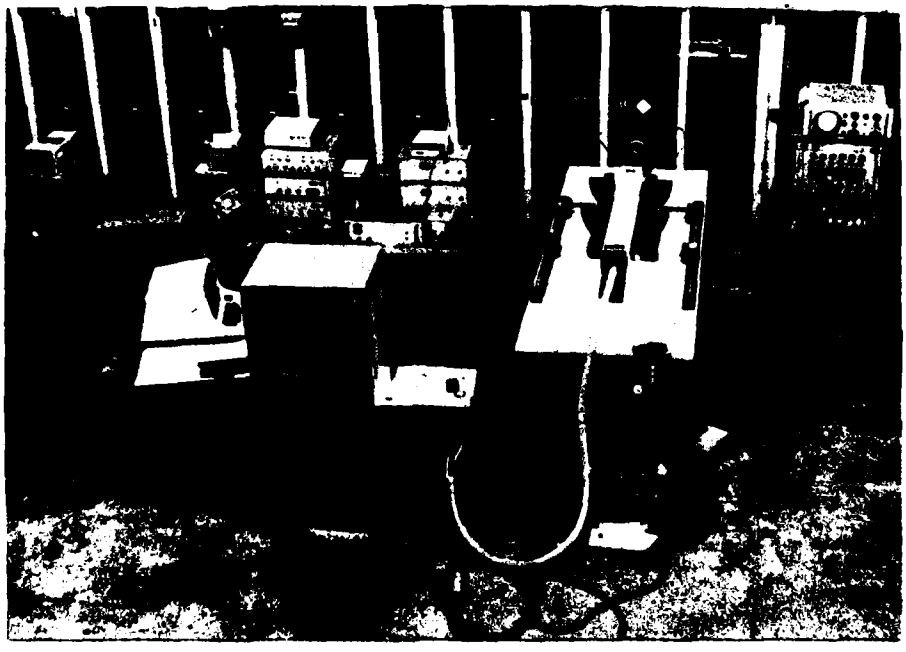

Figure 6. View of optical scanner with the laser Doppler anemometer and test facility.

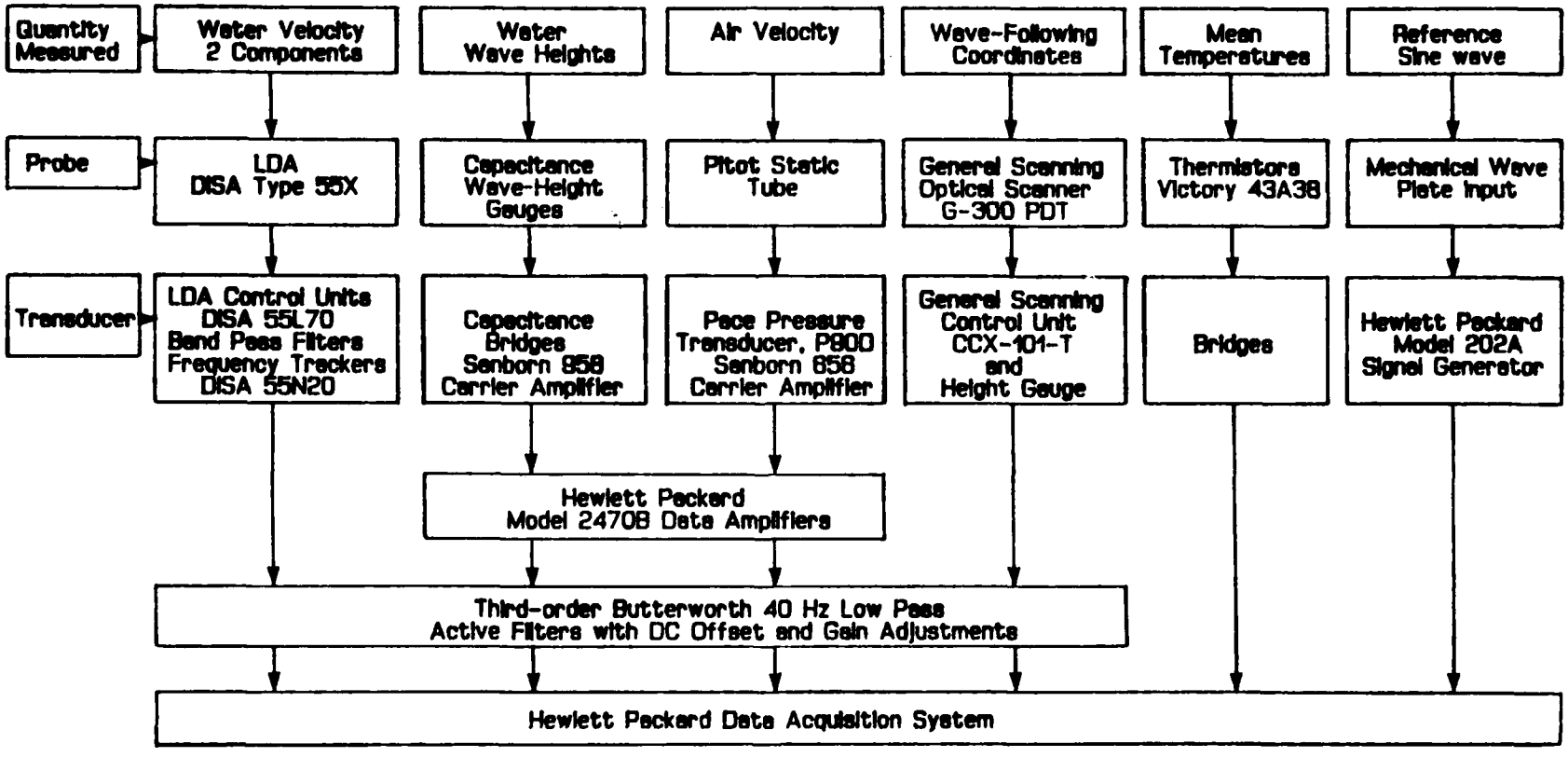

Figure 7. Signal flow chart.

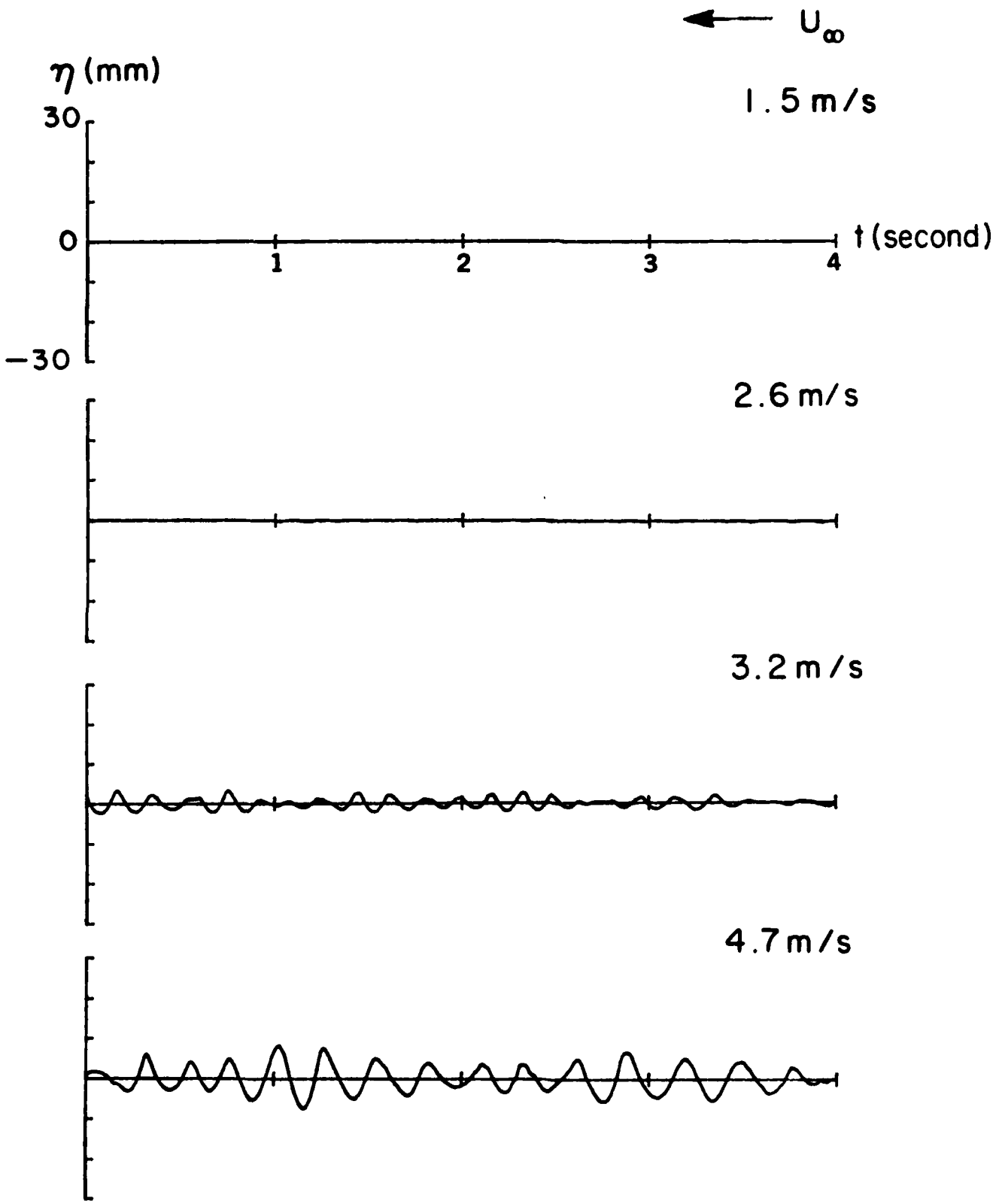

Figure 8 (page one of two).

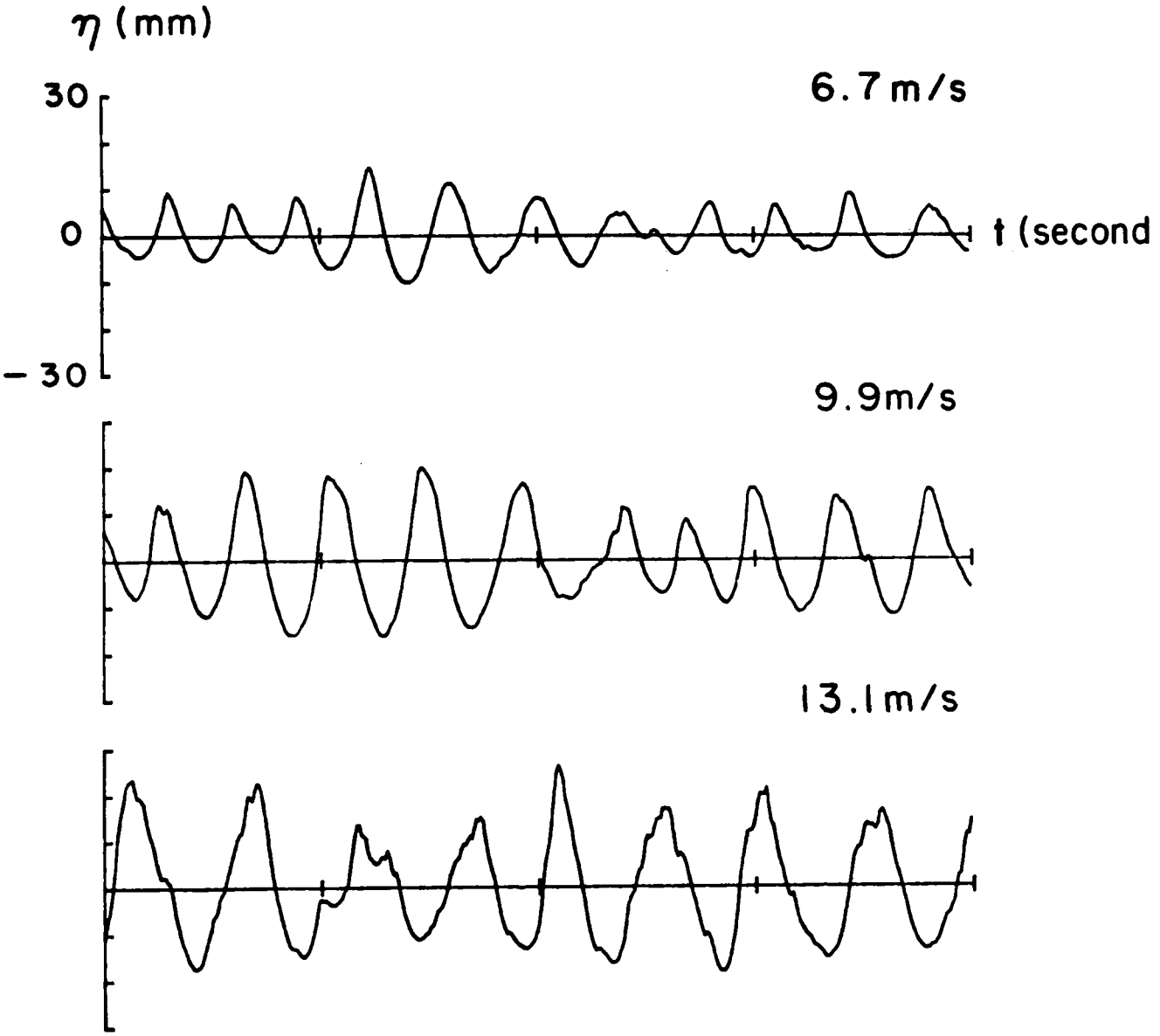

Figure 8. Time traces of water surface displacement at measuring fetch (WW-EF).

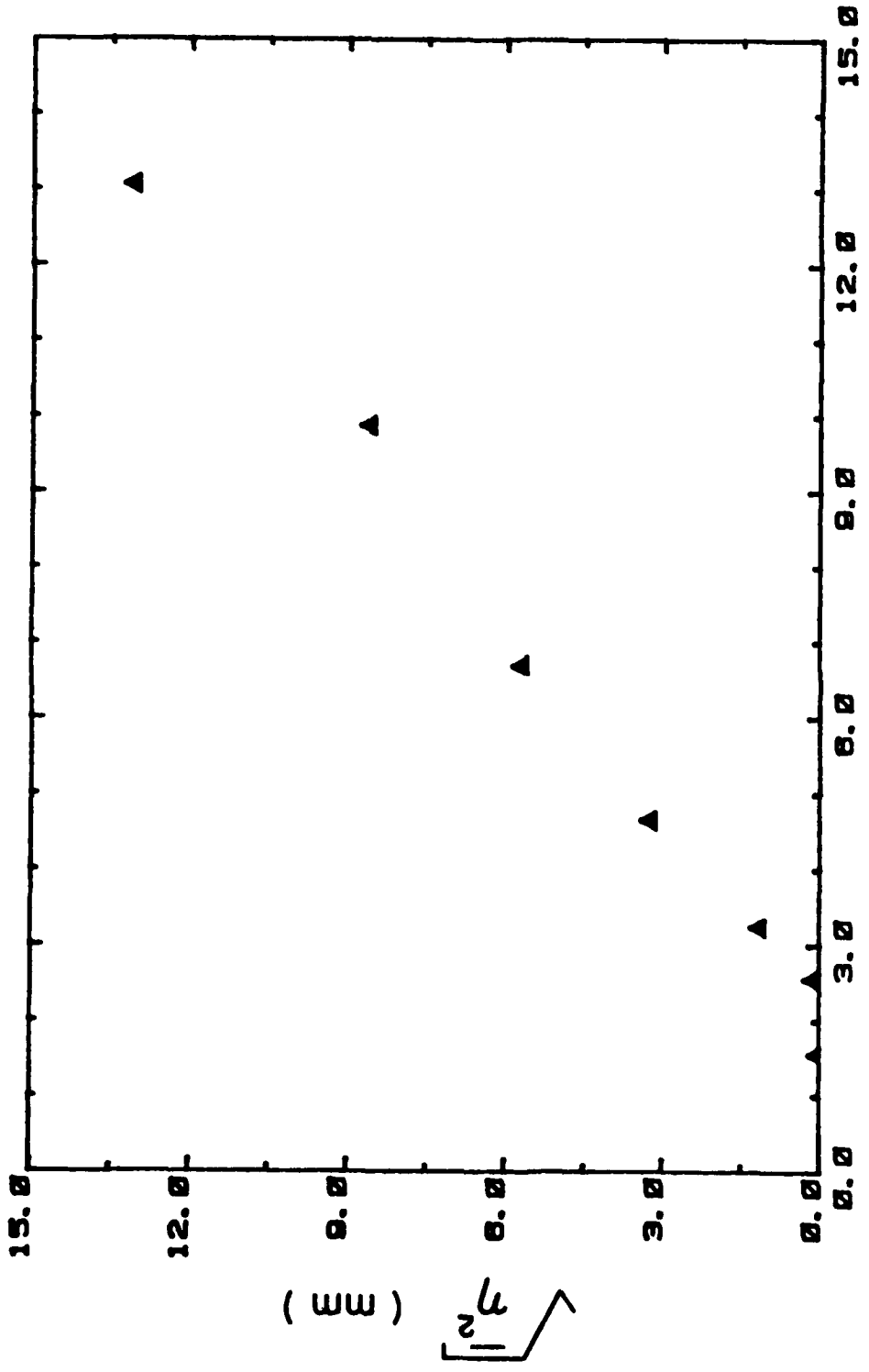

Figure 9. $(\overline{\eta^2})^{1/2}$ versus wind speed (u_∞) (WW-EF).

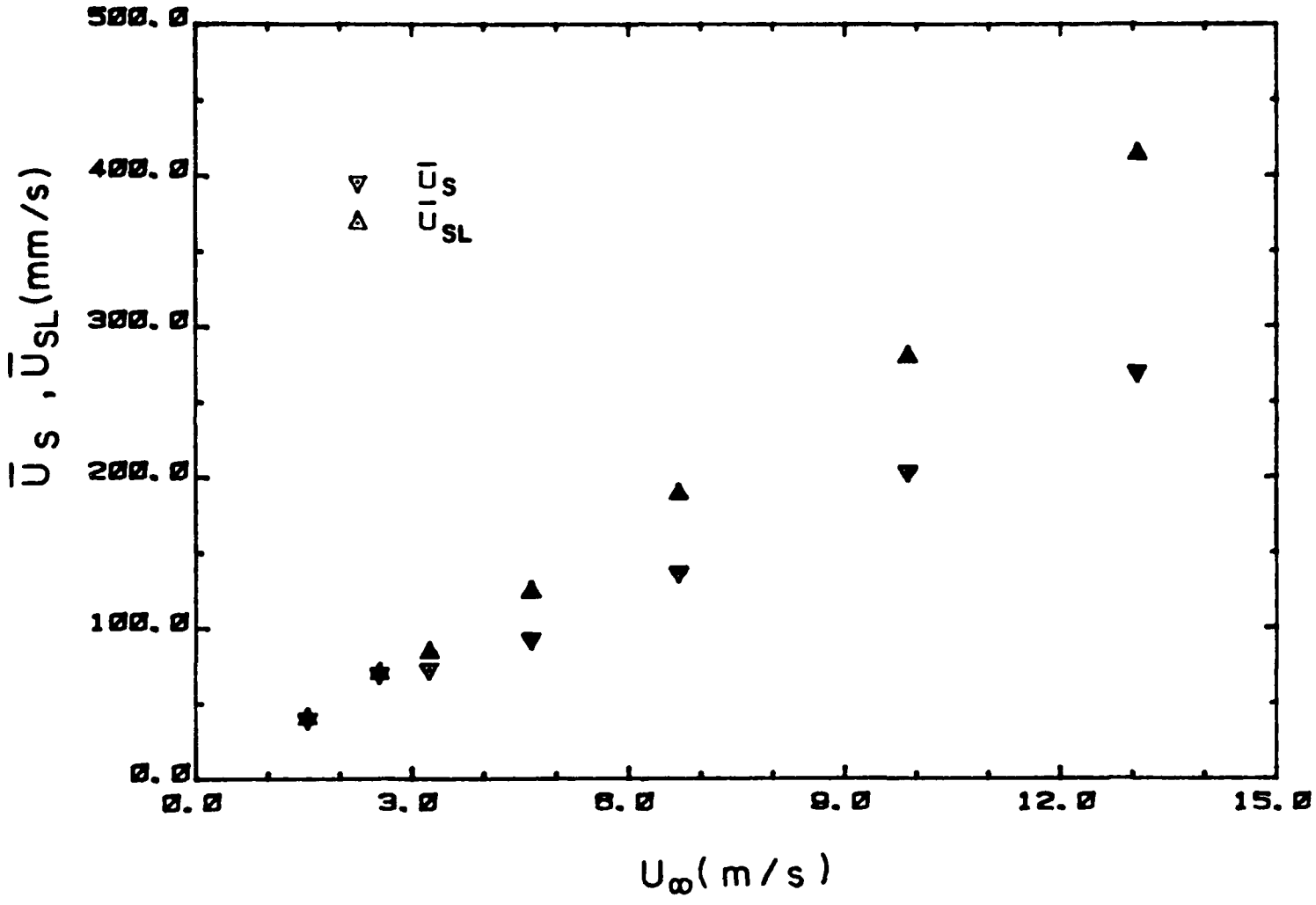

Figure 10. Mean Lagrangian and Eulerian surface drift velocities ($\bar{u}_{SL}$, $\bar{u}_S$) versus wind speed (u_∞) (WW-I

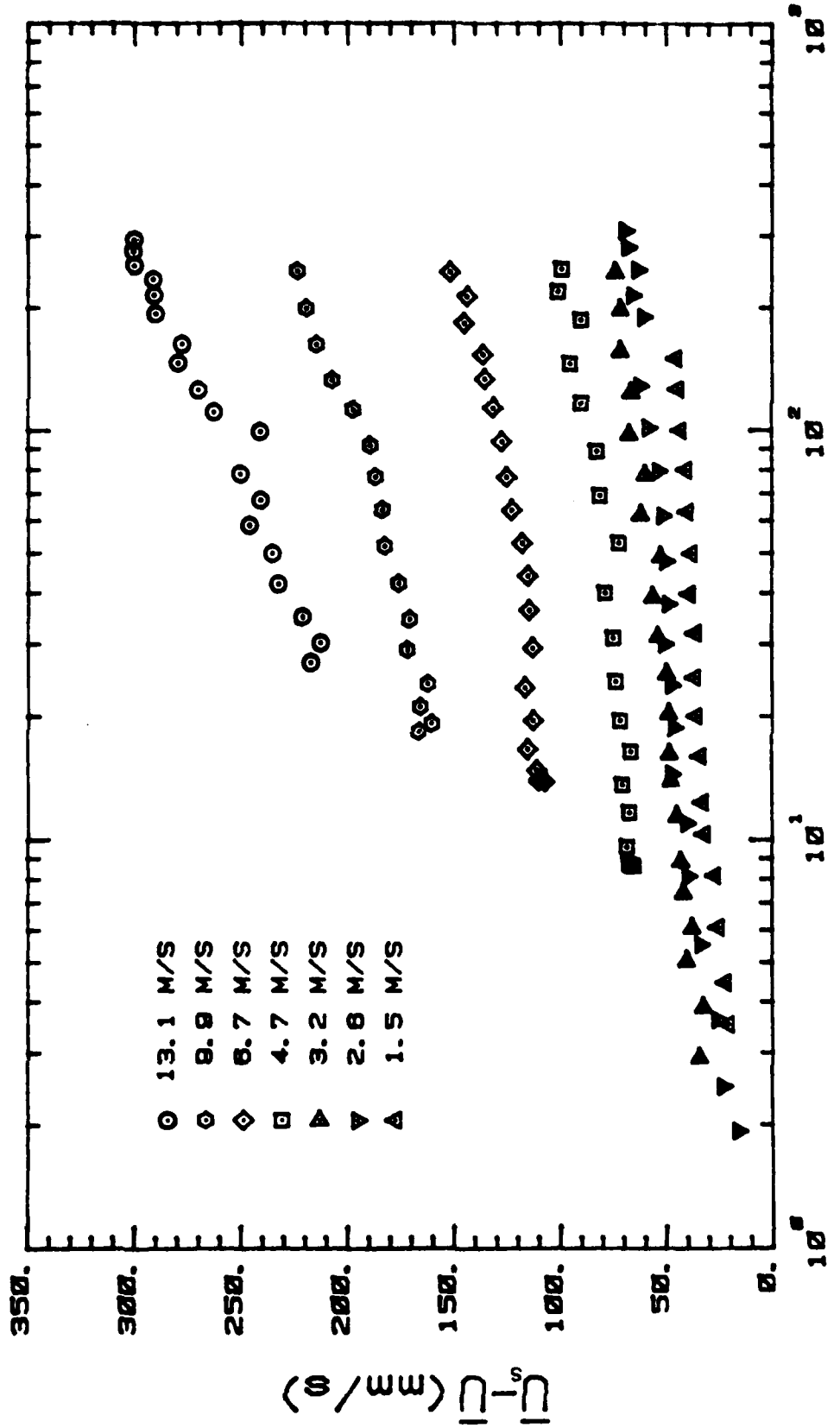

Figure 11. Mean horizontal velocity defect ($\bar{u}_s - \bar{u}$) profiles (WW-EF).

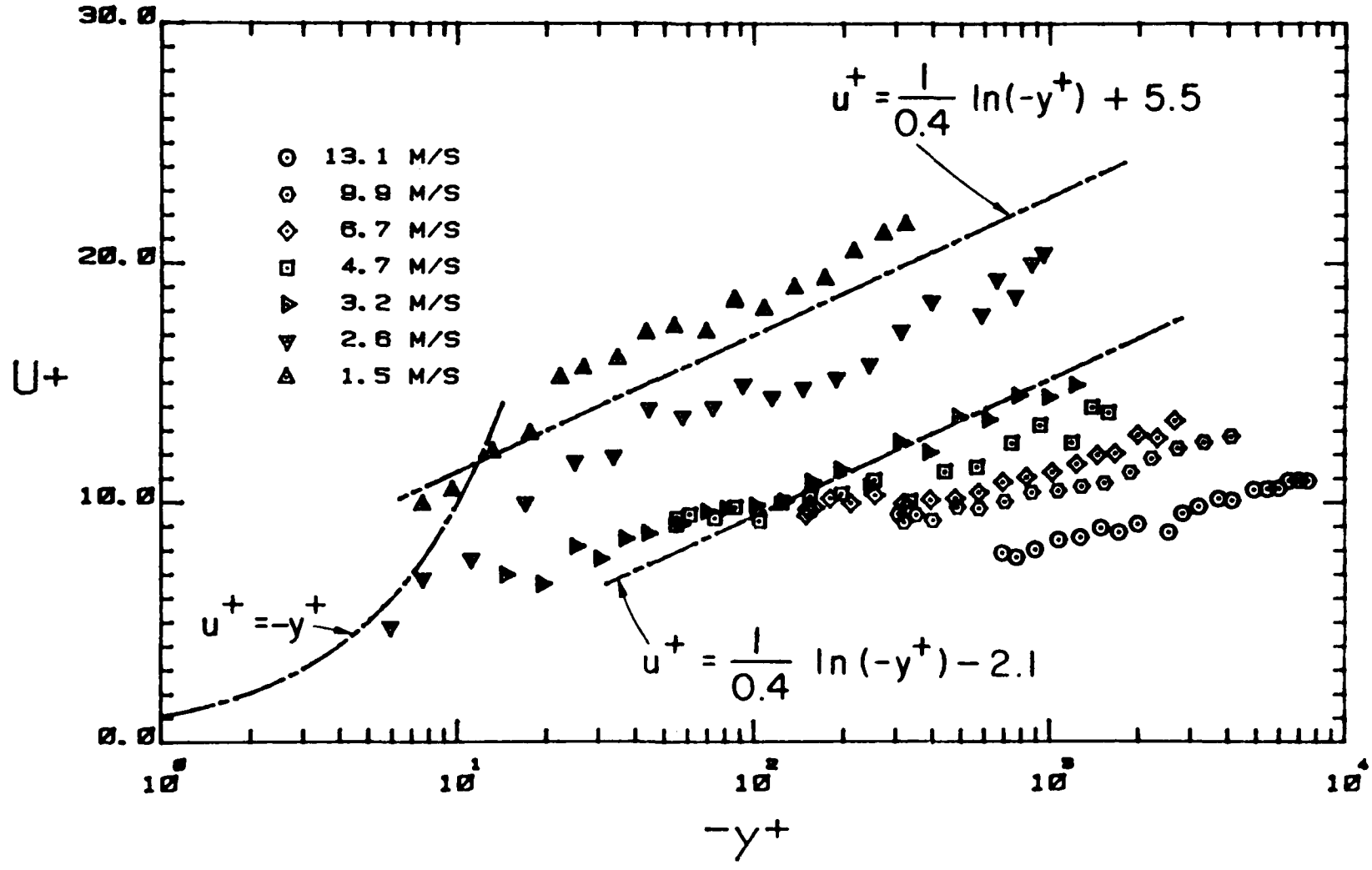

Figure 12. Mean horizontal velocity defect profiles in law-of-the-wall coordinates (WW-EF).

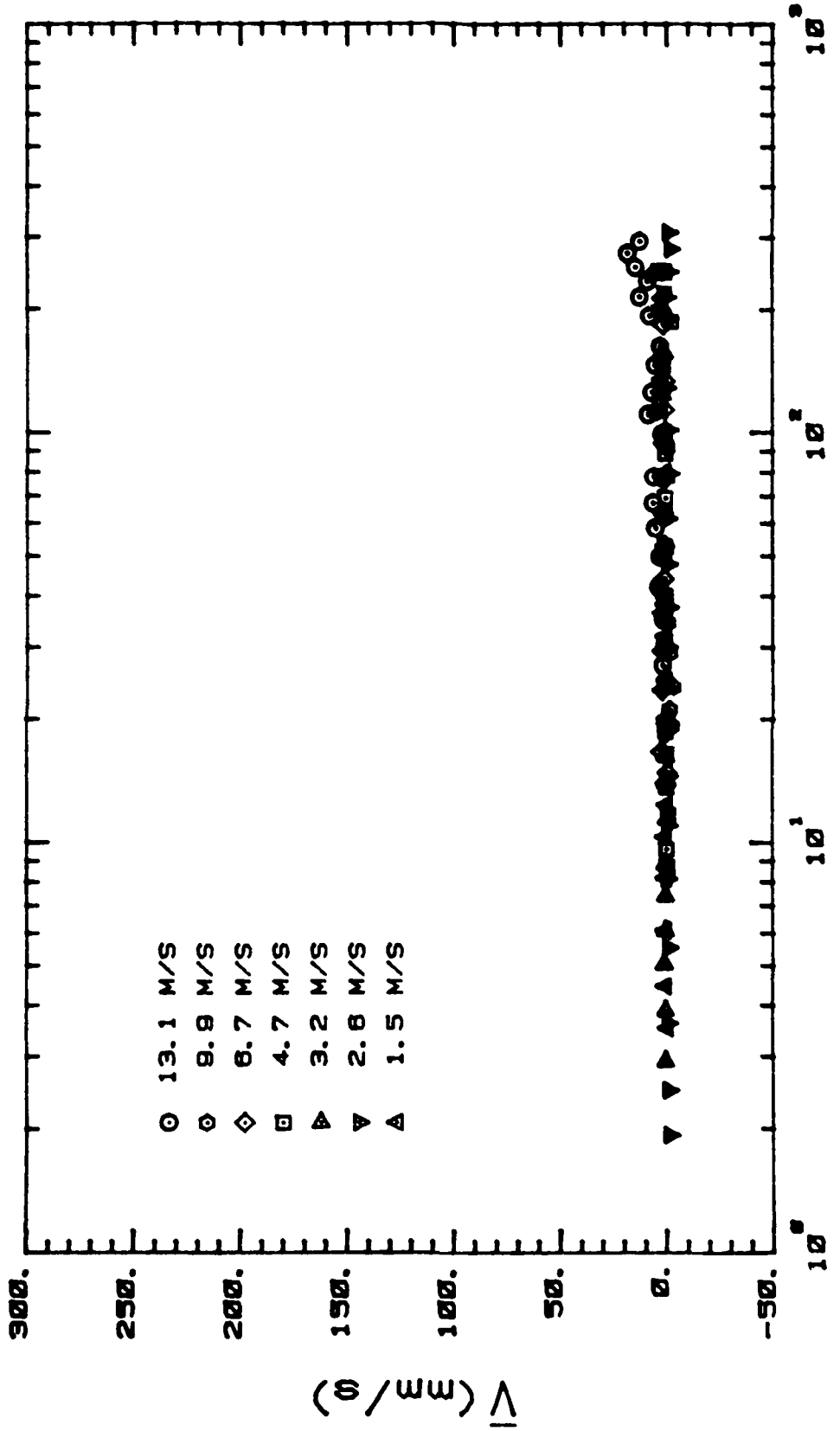

Figure 13. Mean vertical velocity profiles (WW-EF).

AD-A154 117 A STUDY OF THE TURBULENT LAYER IN THE WATER AT AN AIR-WATER INTERFACE(U) STANFORD UNIV CALIF DEPT OF CIVIL ENGINEERING T K CHEUNG JAN 85 TR-287 3/3

UNCLASSIFIED N00014-84-K-0242 F/G 8/3 NL

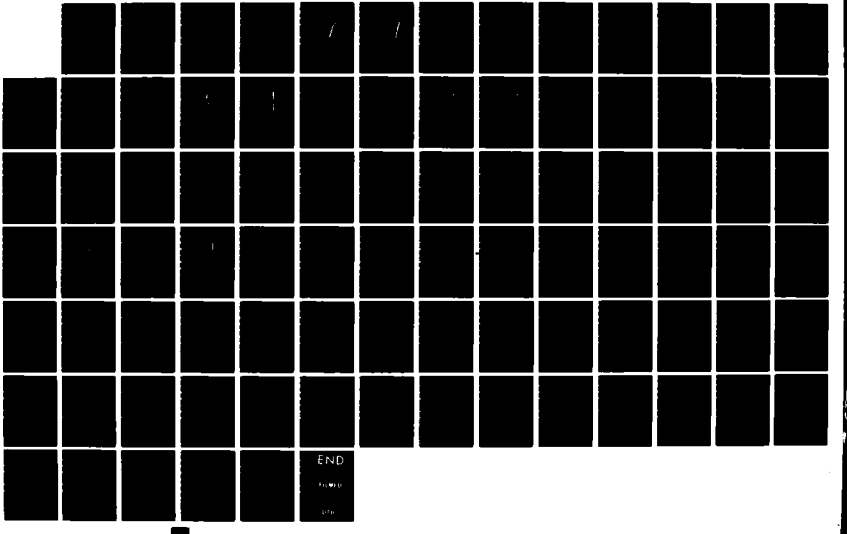

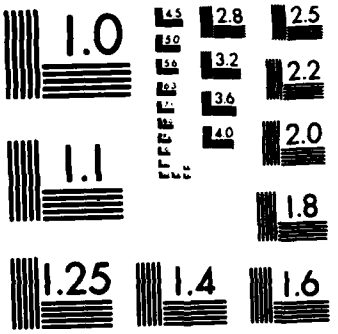

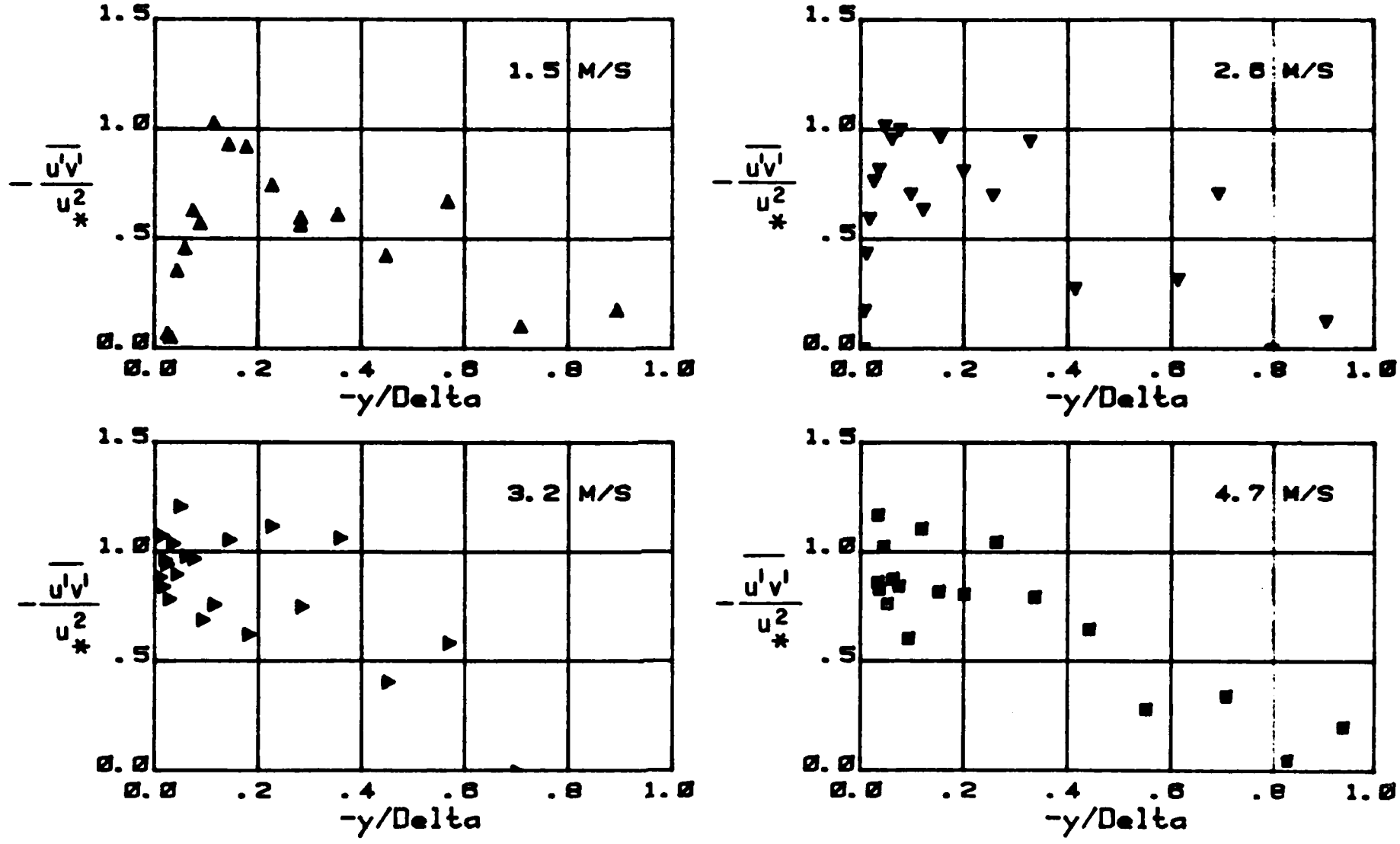

Figure 14 (one of two pages).

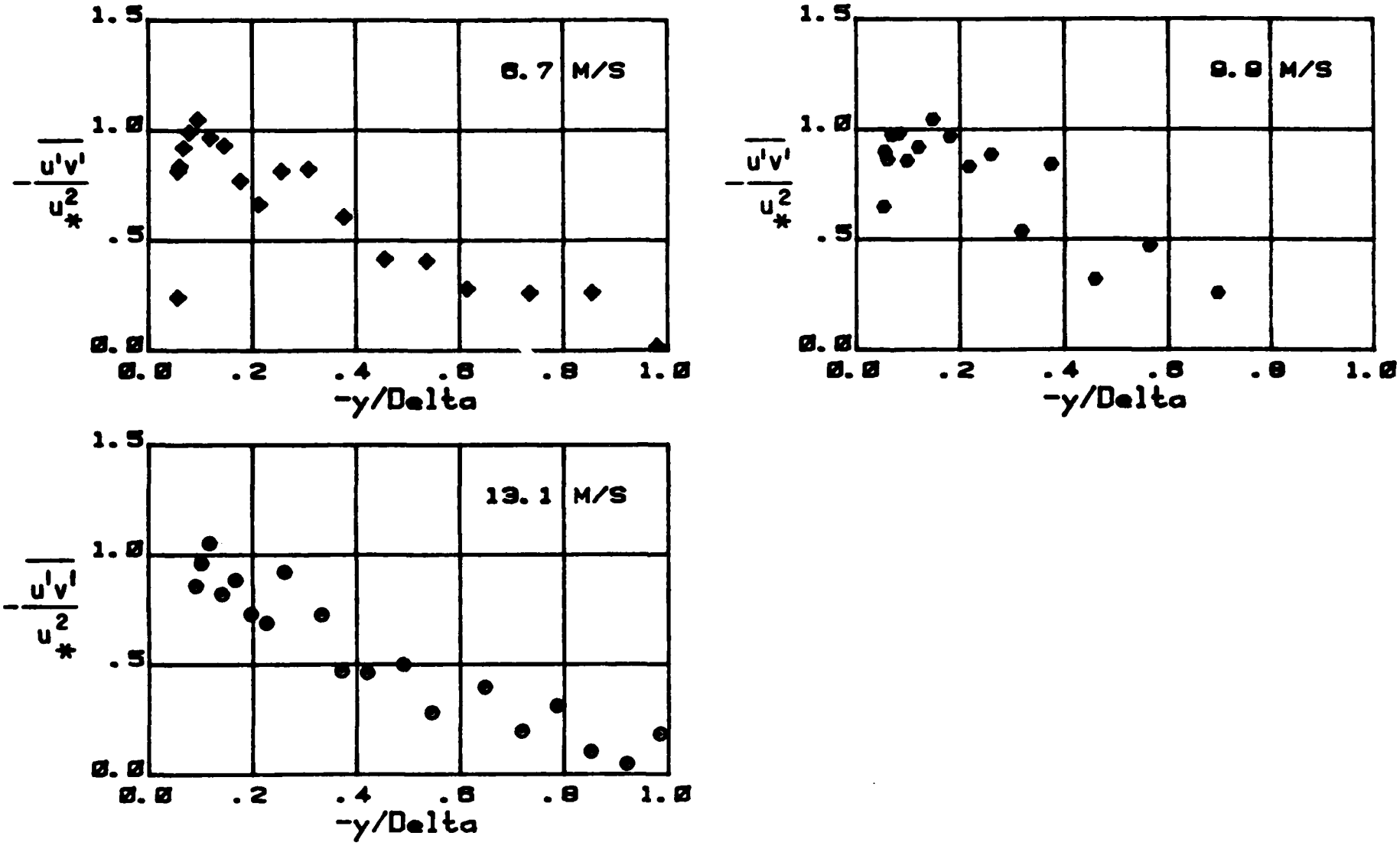

Figure 14. $-\overline{u'v'}/u_*^2$ versus $-y/\delta$ (WW-EF).

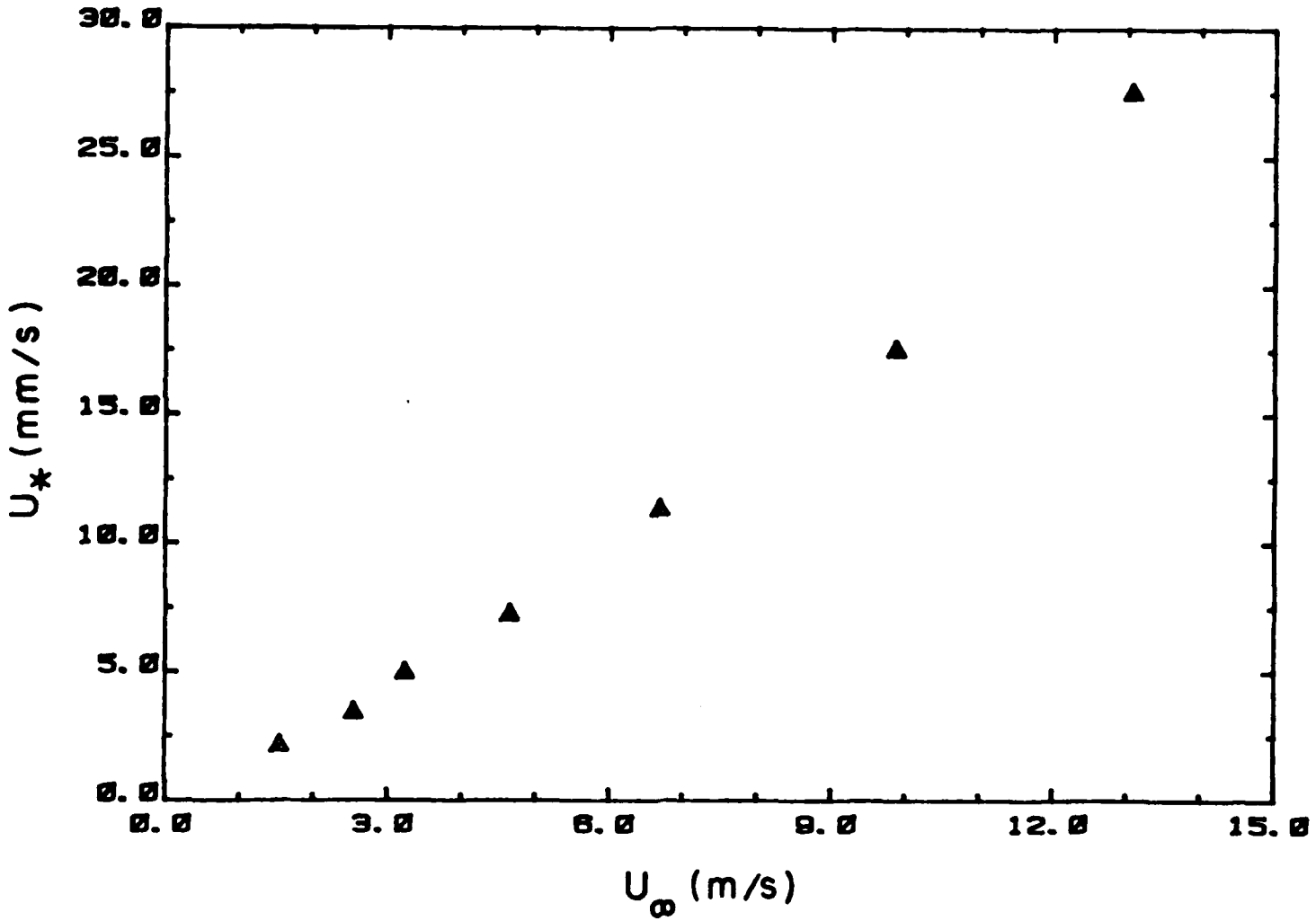

Figure 15. Friction velocity (u_*) versus wind speed (u_∞) (WW-EF).

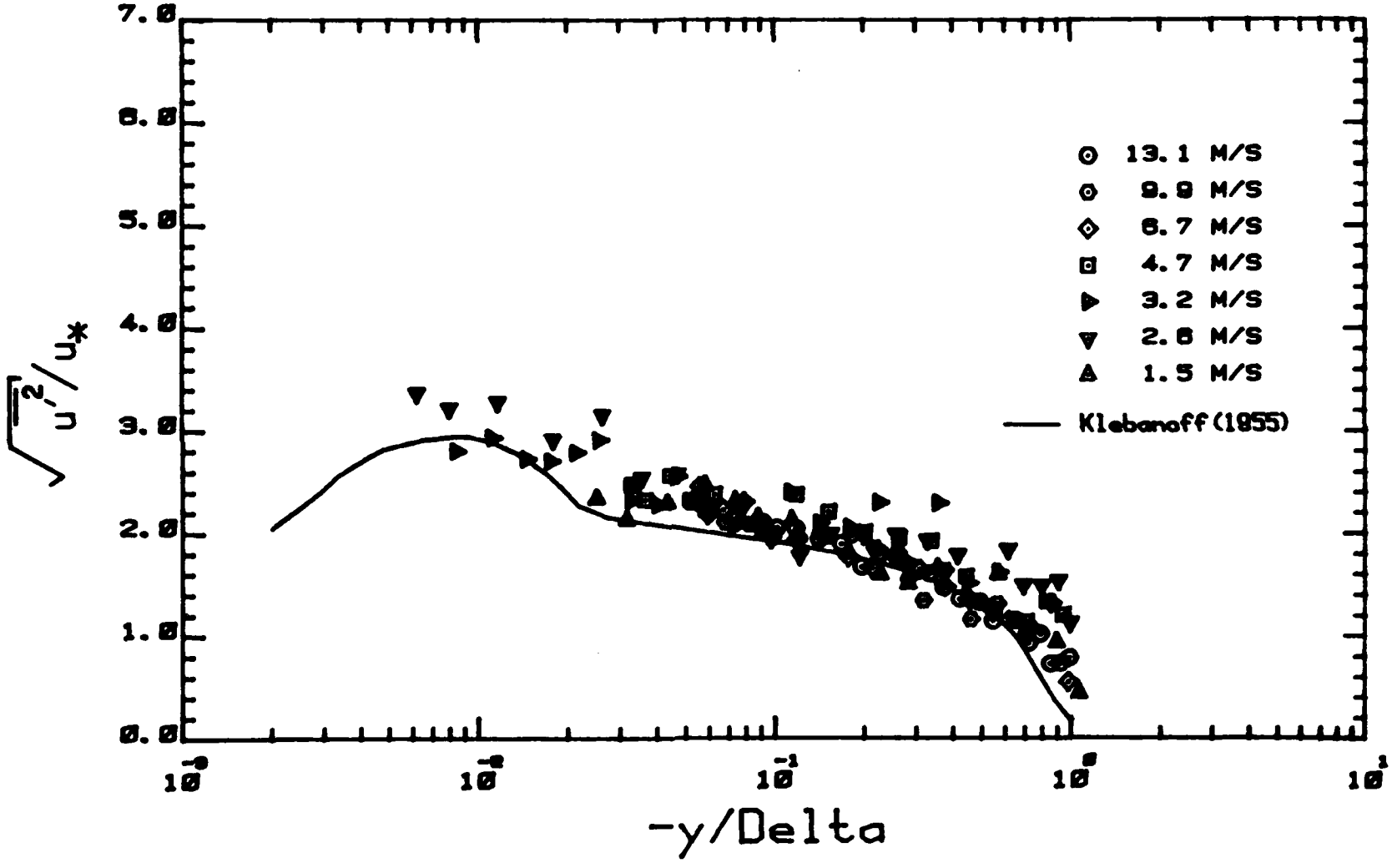

Figure 16. $(\overline{u'^2})^{1/2}/u_*$ versus $-y/\delta$ (WW-EF).

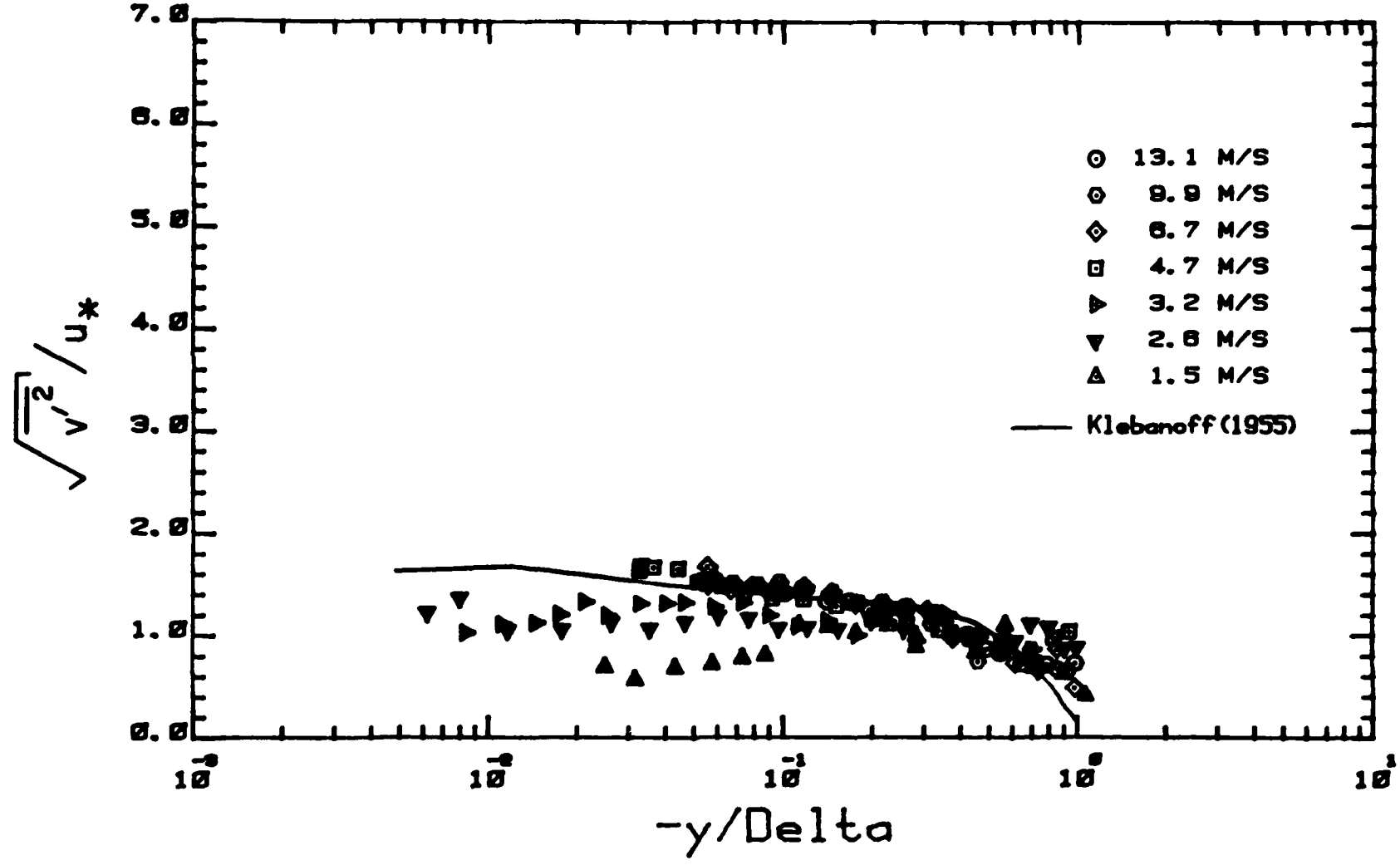

Figure 17. $(\overline{v'^2})^{1/2}/u_*$ versus $-y/\delta$ (WW-EF).

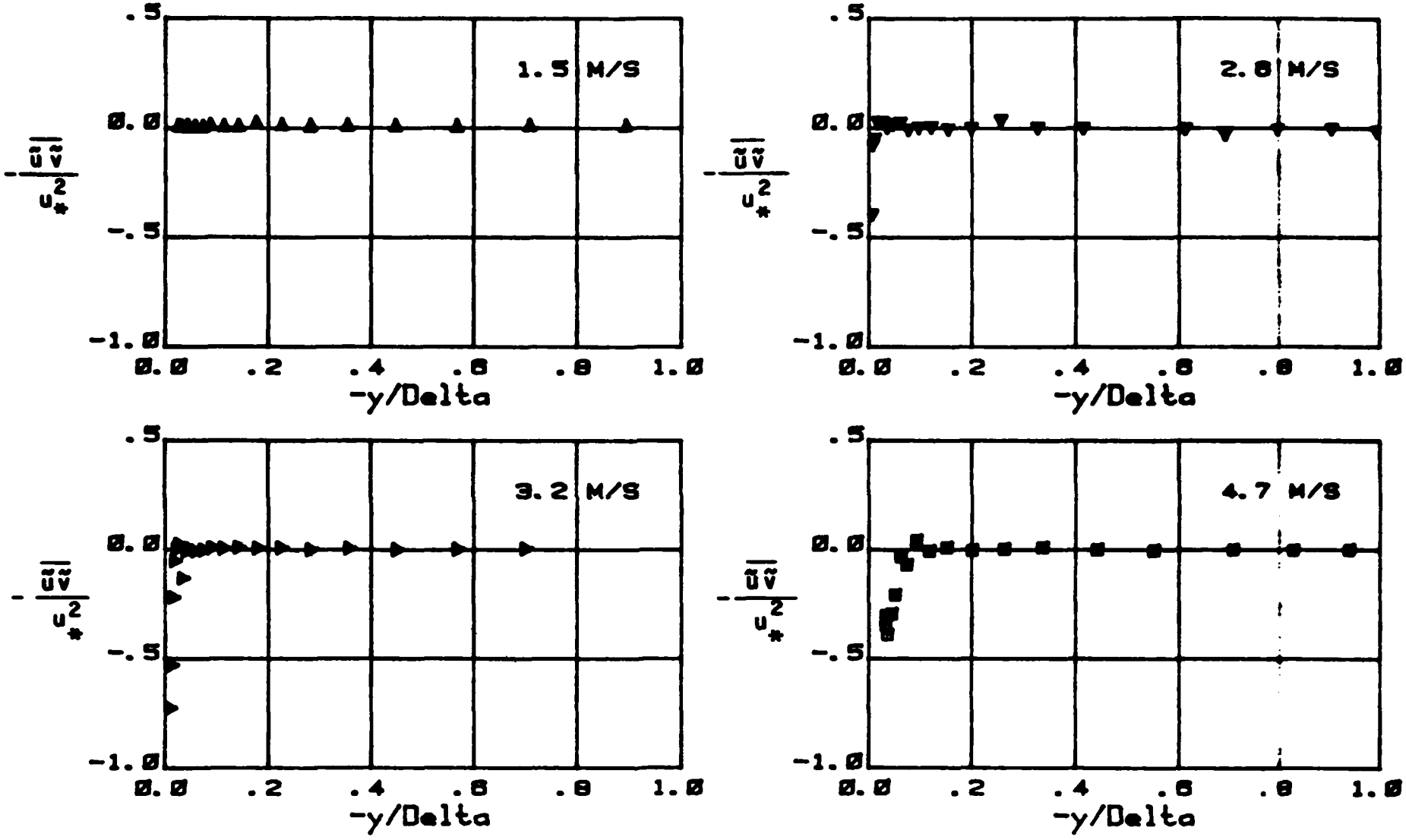

Figure 18 (one of two pages).

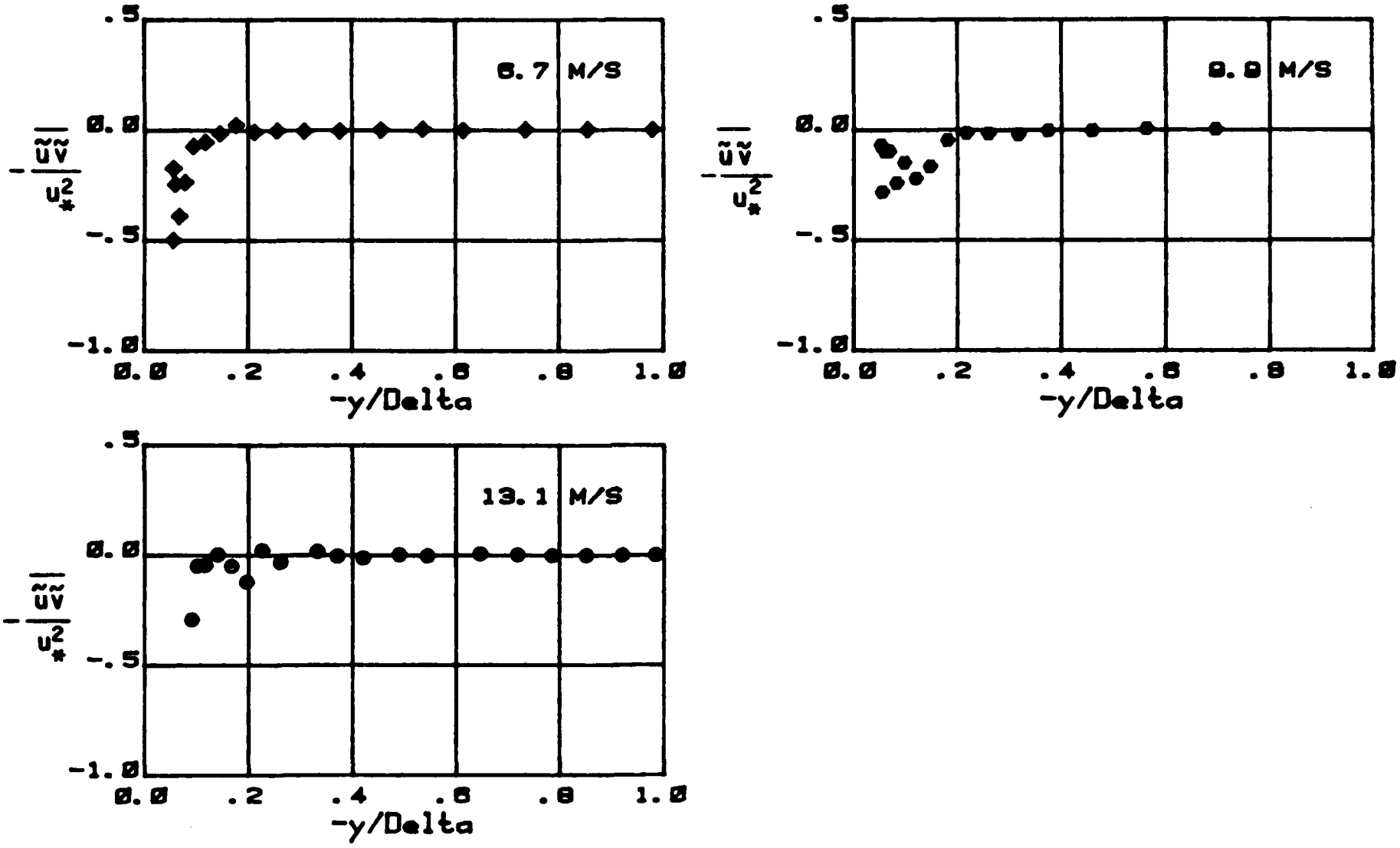

Figure 18. $-\overline{\tilde{u}\tilde{v}}/u_*^2$ versus $-y/\delta$ (WW-EF).

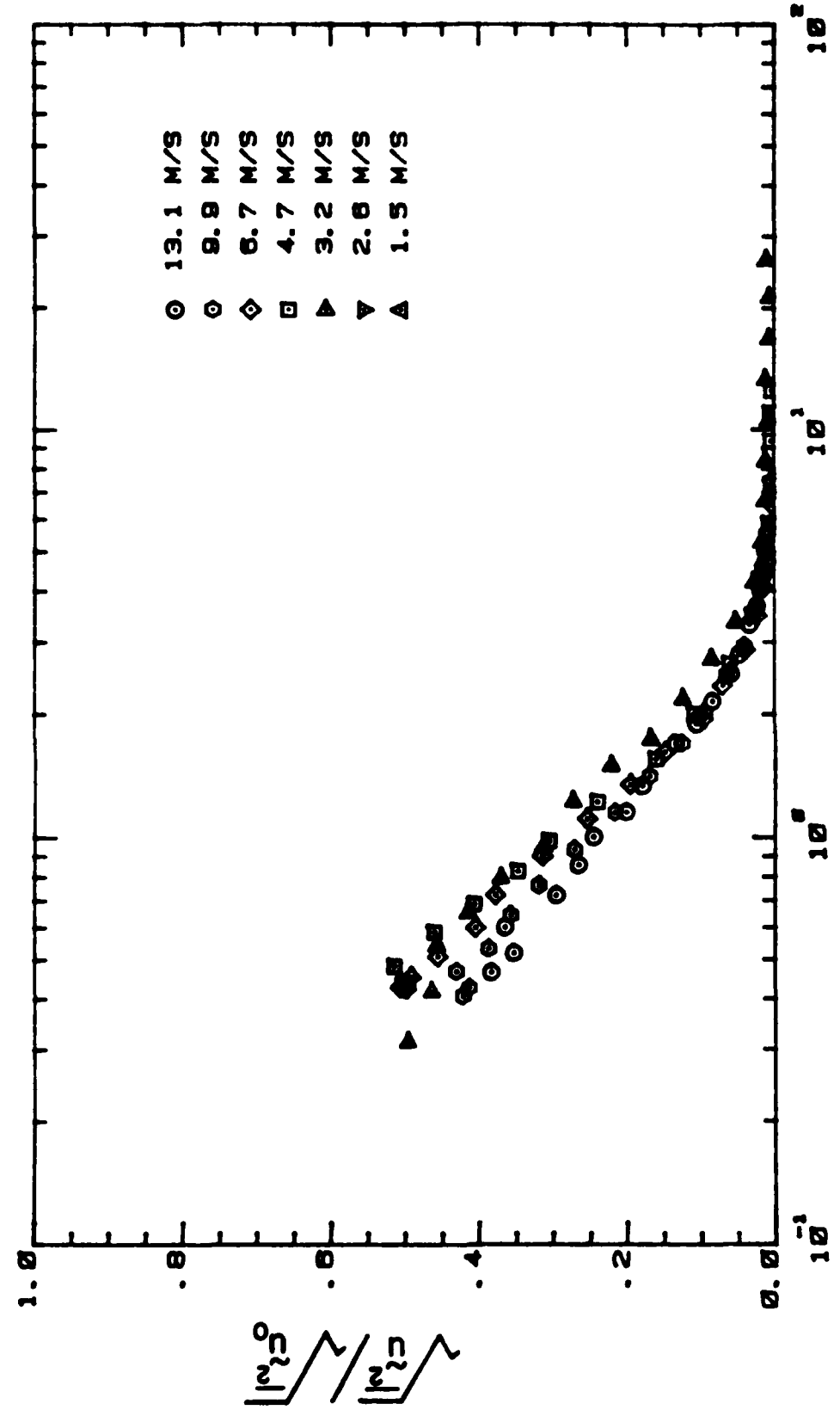

Figure 19. $(\overline{u^2}/\overline{u_o^2})^{1/2}$ versus $-y/y_\eta$ (WW-EF).

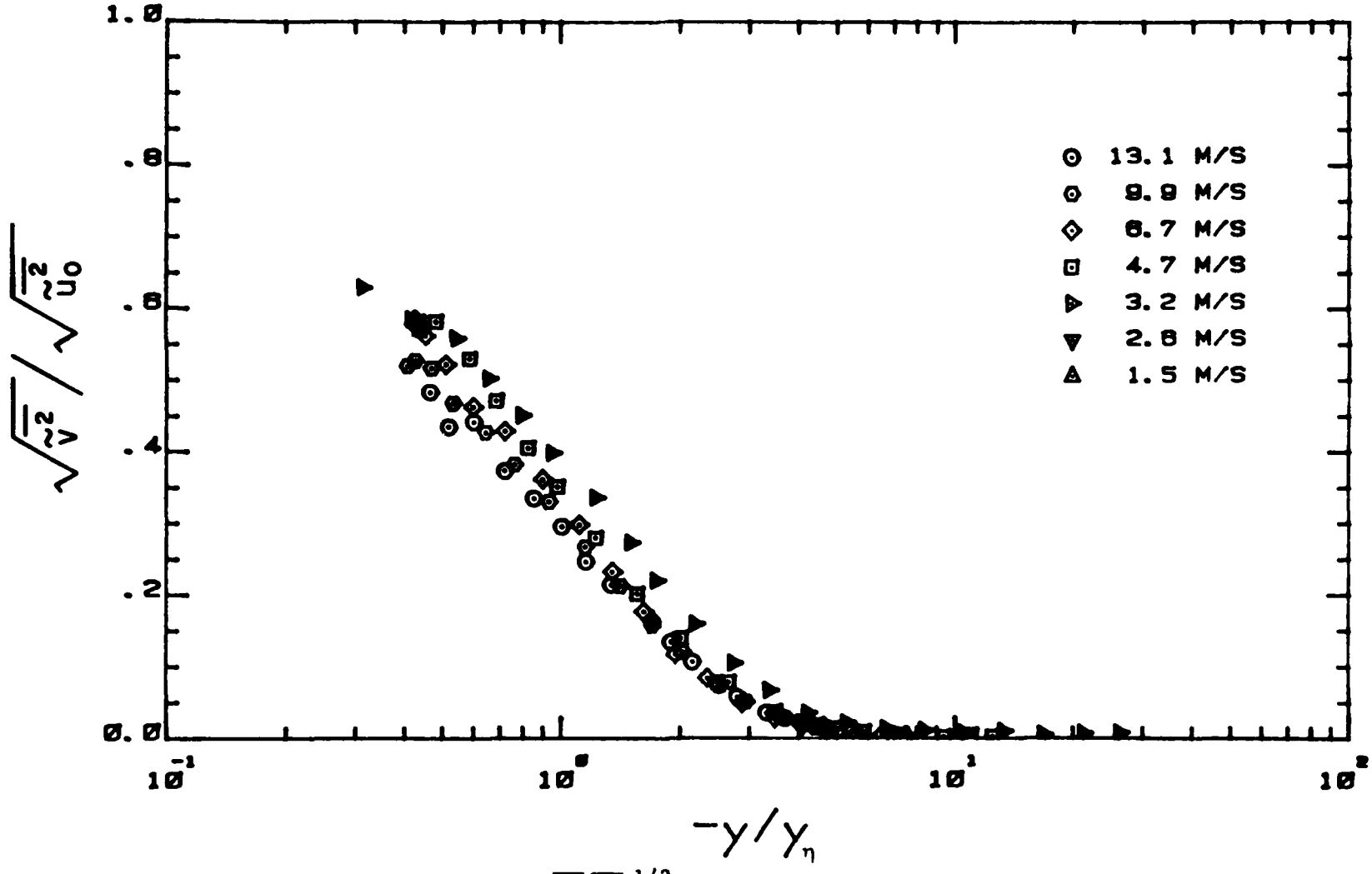

Figure 20. $(\overline{\tilde{v}^2}/\overline{\tilde{u}_o^2})^{1/2}$ versus $-y/y_\eta$ (WW-EF).

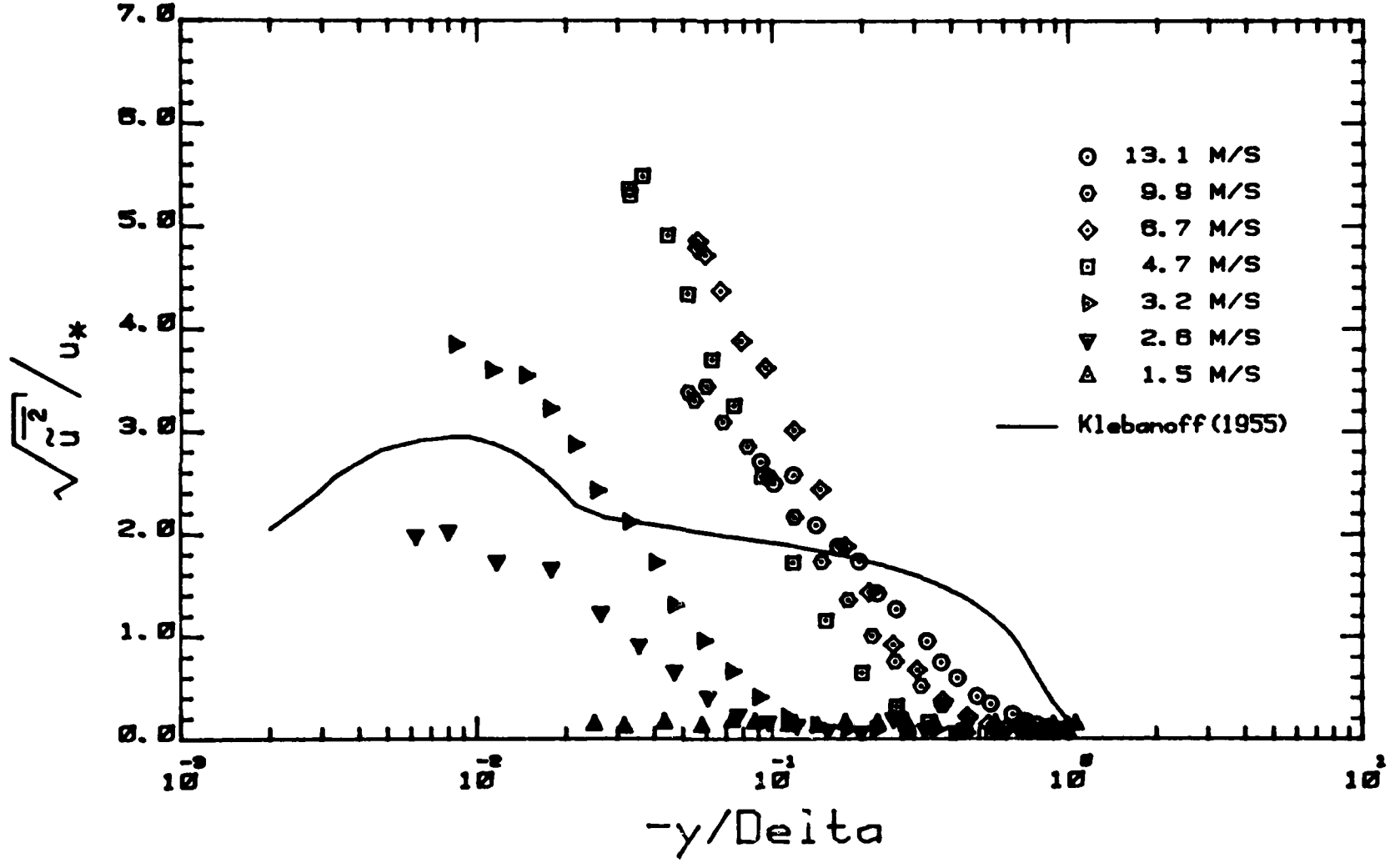

Figure 21. $(\overline{u^2})^{1/2}/u_*$ versus $-y/\delta$ (WW-EF).

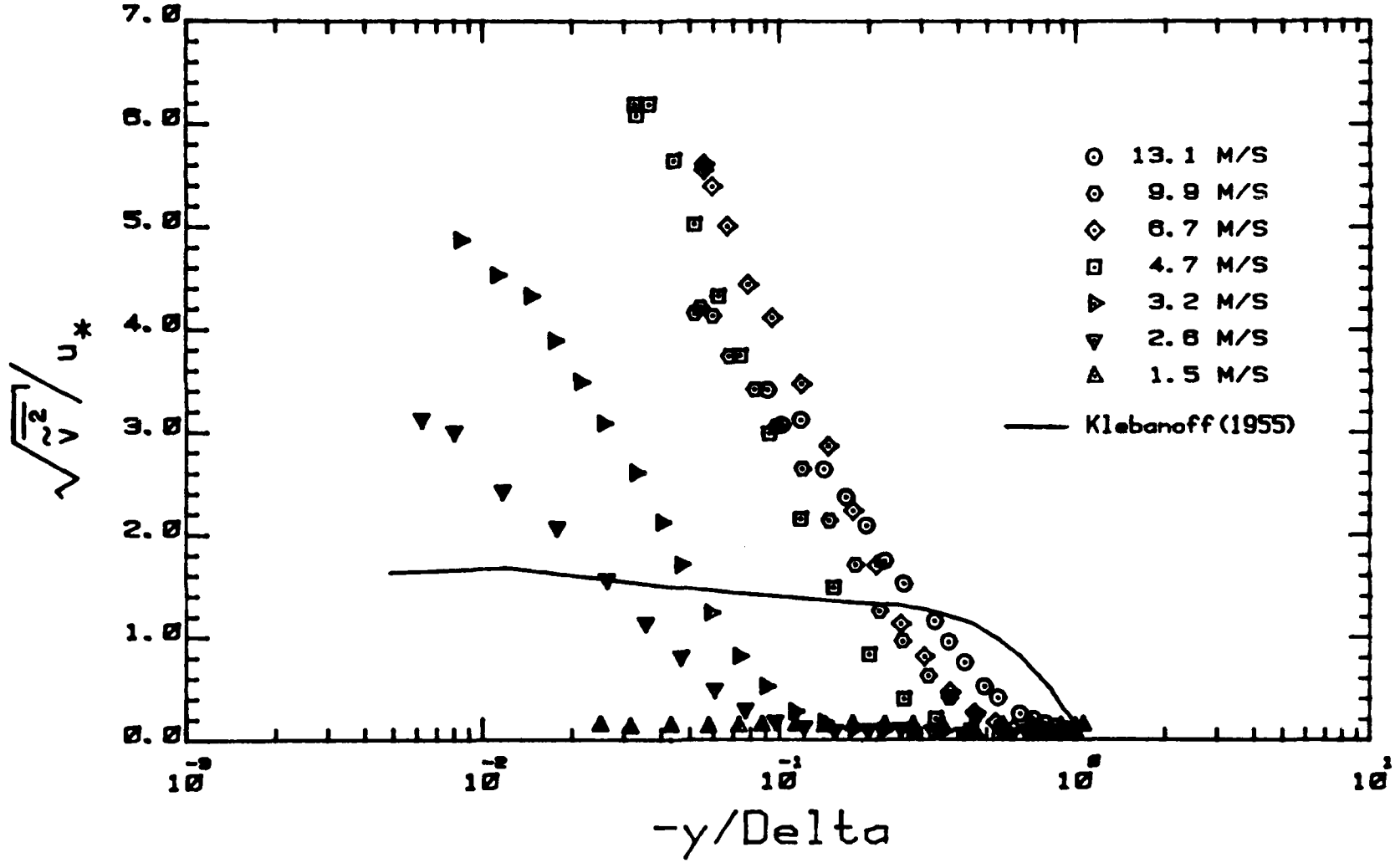

Figure 22. $(\overline{v^2})^{1/2}/u_*$ versus -y/δ (WW-EF).

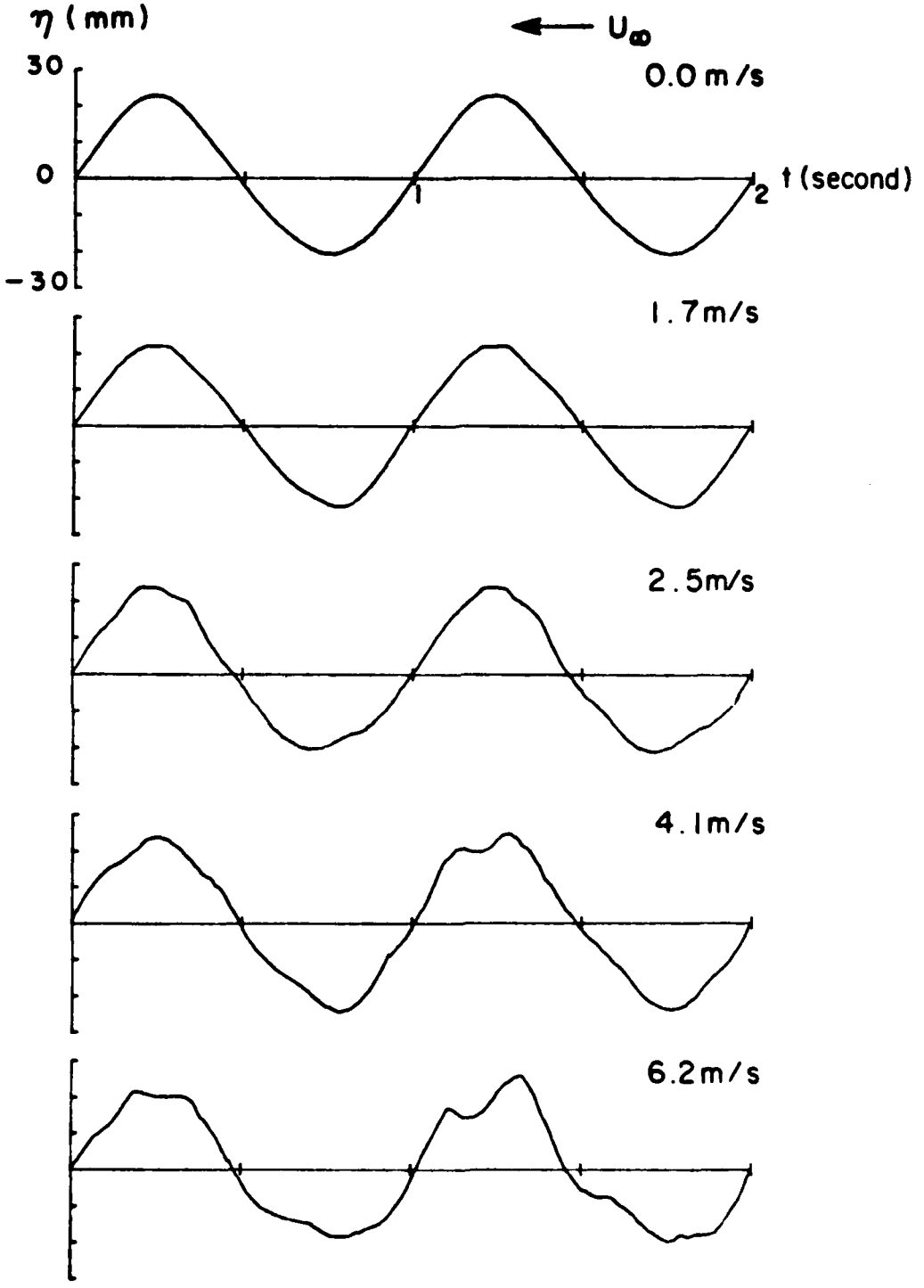

Figure 23. Time traces of water surface displacement at measuring fetch (MW-EF).

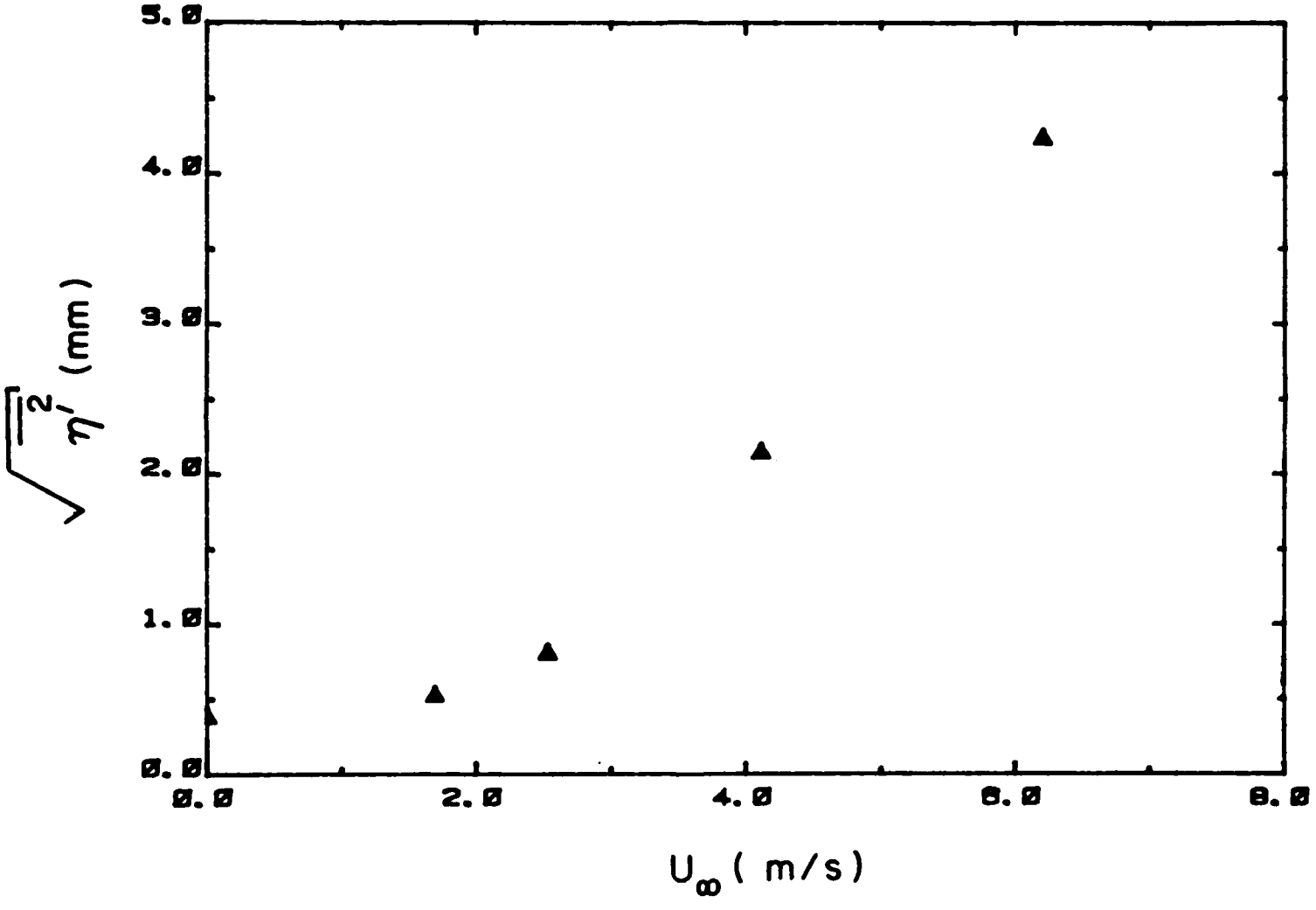

Figure 24. $\left(\overline{\eta'^2}\right)^{1/2}$ versus wind speed (u_∞) (MW-EF).

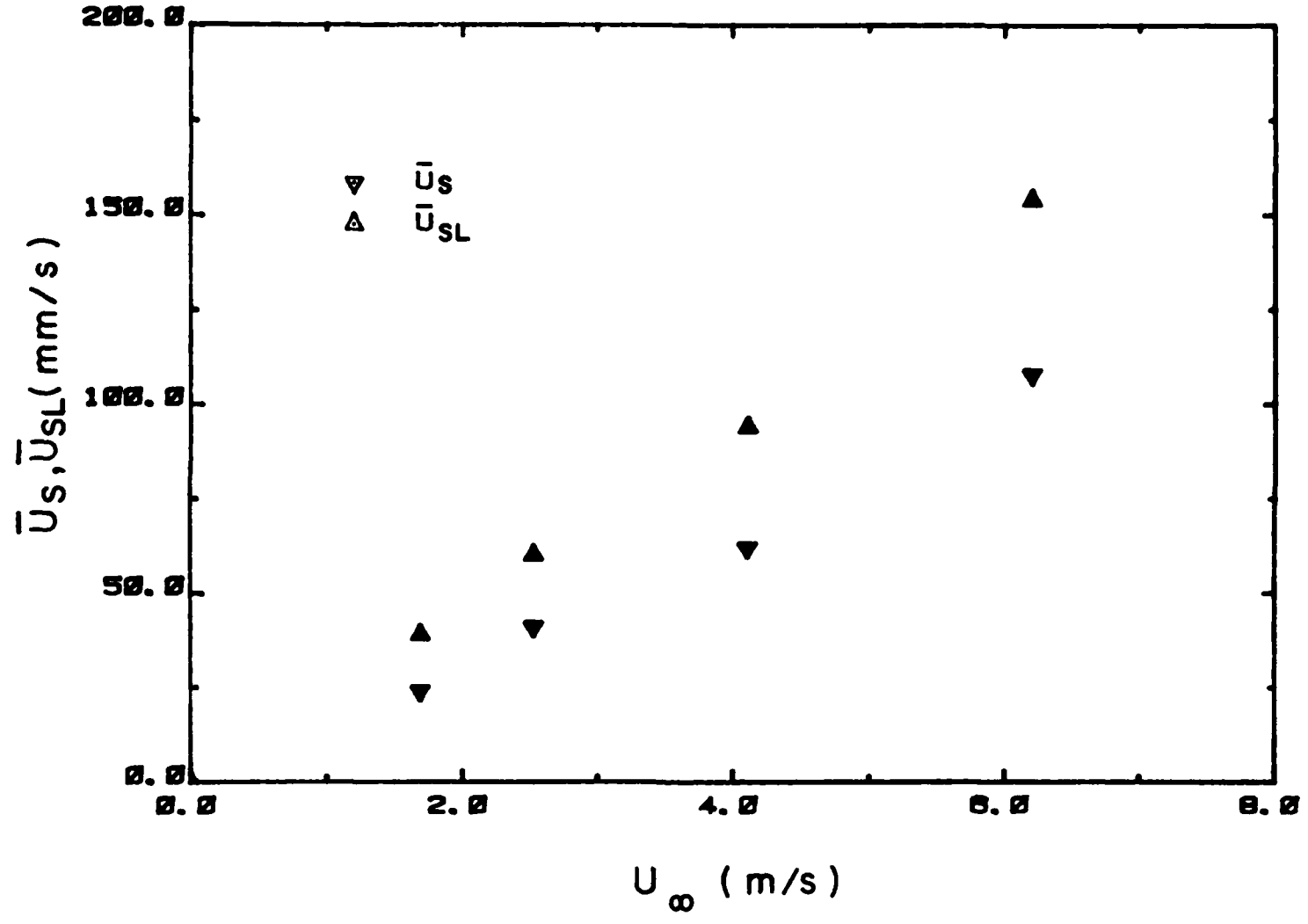

Figure 25. Mean Lagrangian and Eulerian surface drift velocities ($\bar{u}_{SL}$, $\bar{u}_S$) versus wind speed (u_∞) (MW-EF).

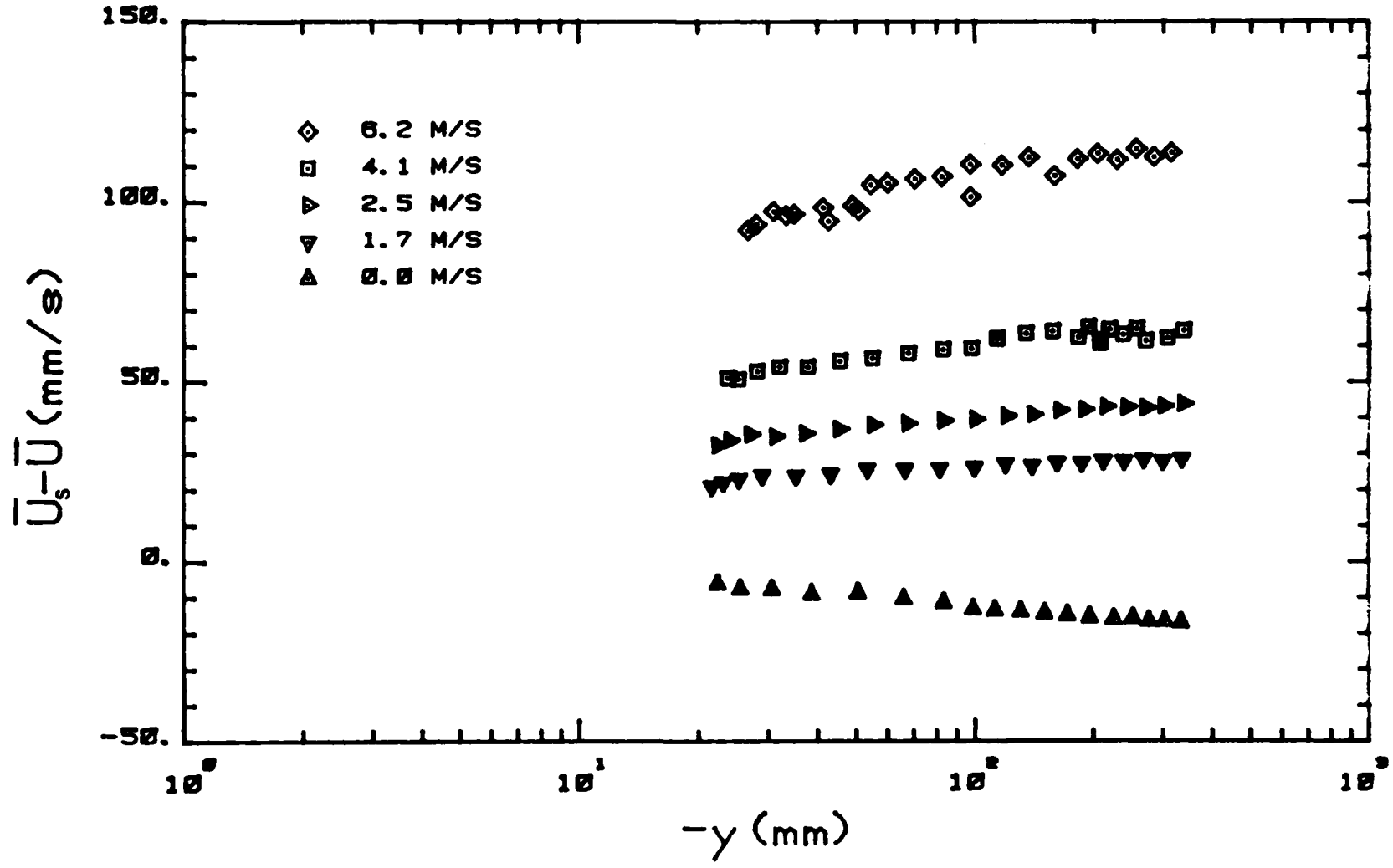

Figure 26. Mean horizontal velocity defect ($\bar{u}_s - \bar{u}$) profiles (MW-EF).

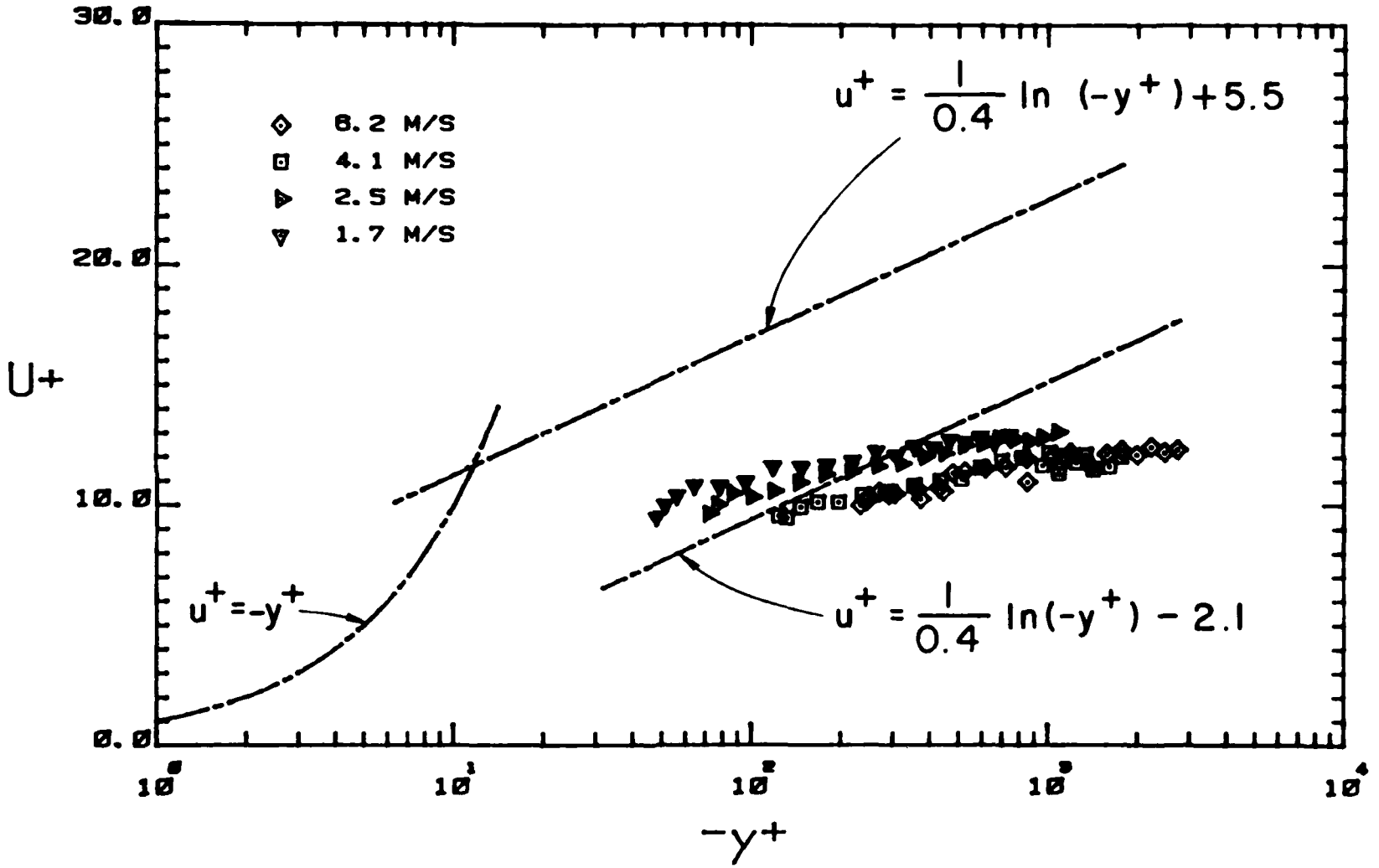

Figure 27. Mean horizontal velocity defect profiles in law-of-the-wall coordinates (MW-EF).

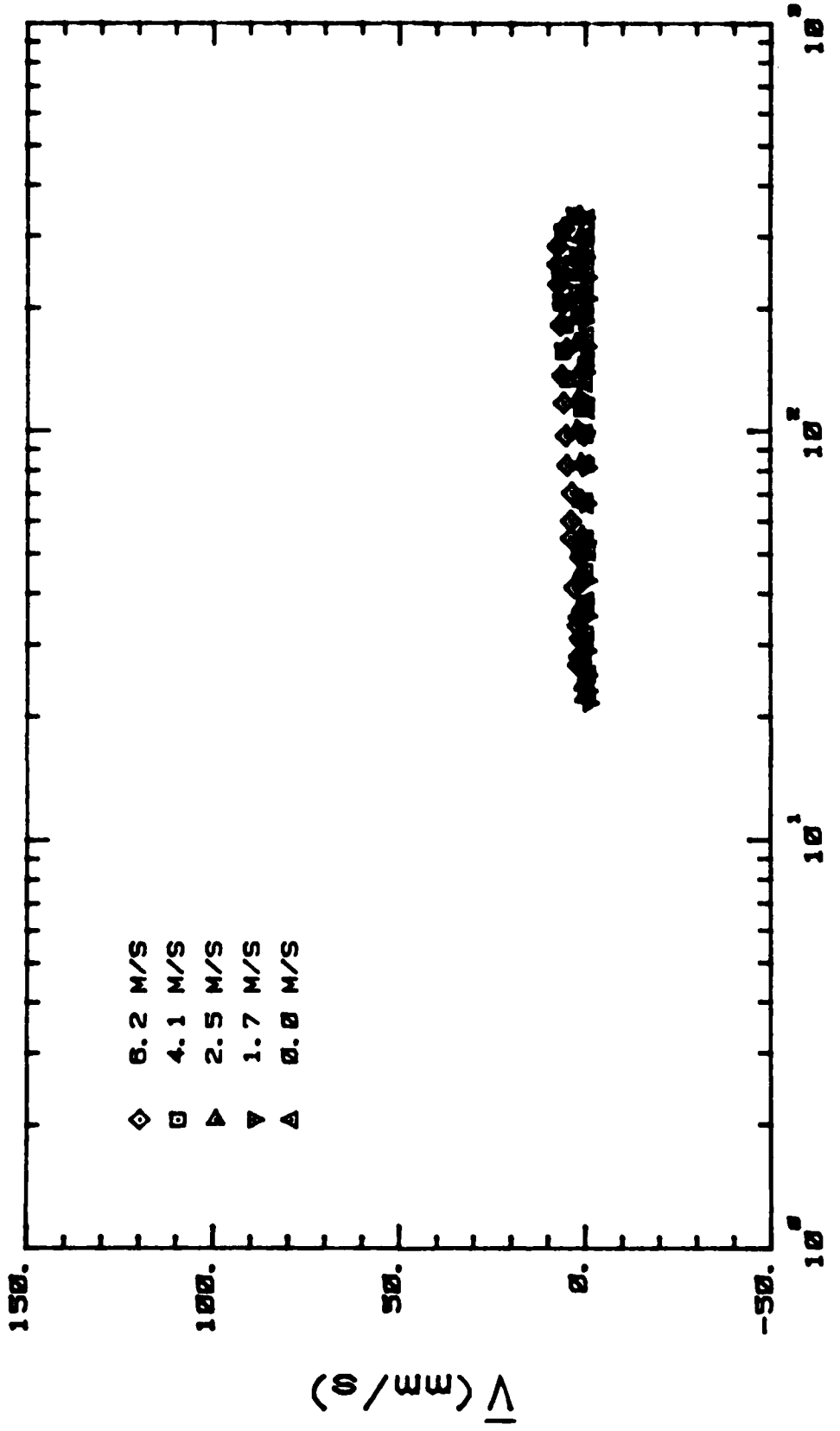

Figure 28. Mean vertical velocity profiles (MW-EF).

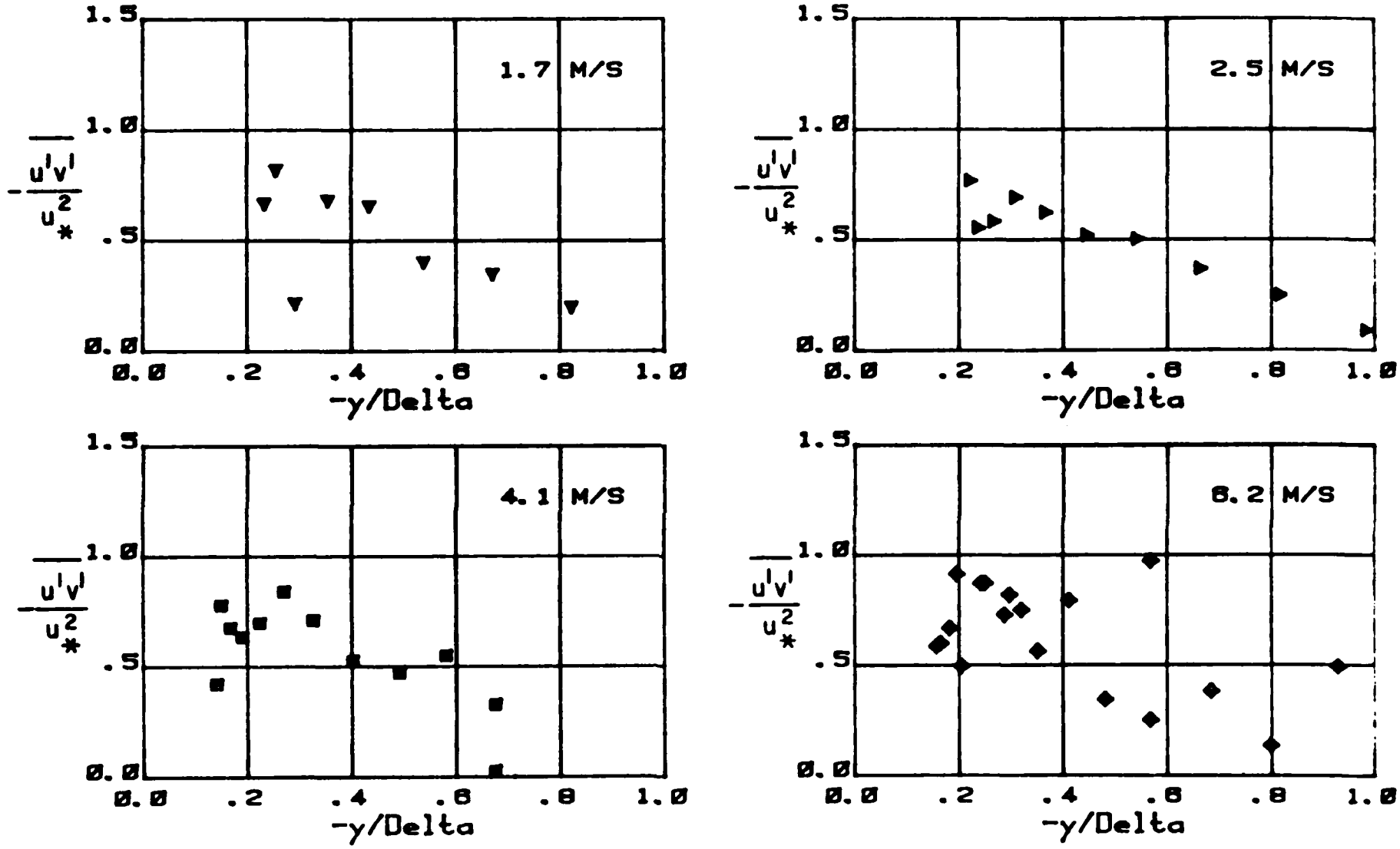

Figure 29. $-\overline{u'v'}/u_*^2$ versus -y/δ (MW-EF).

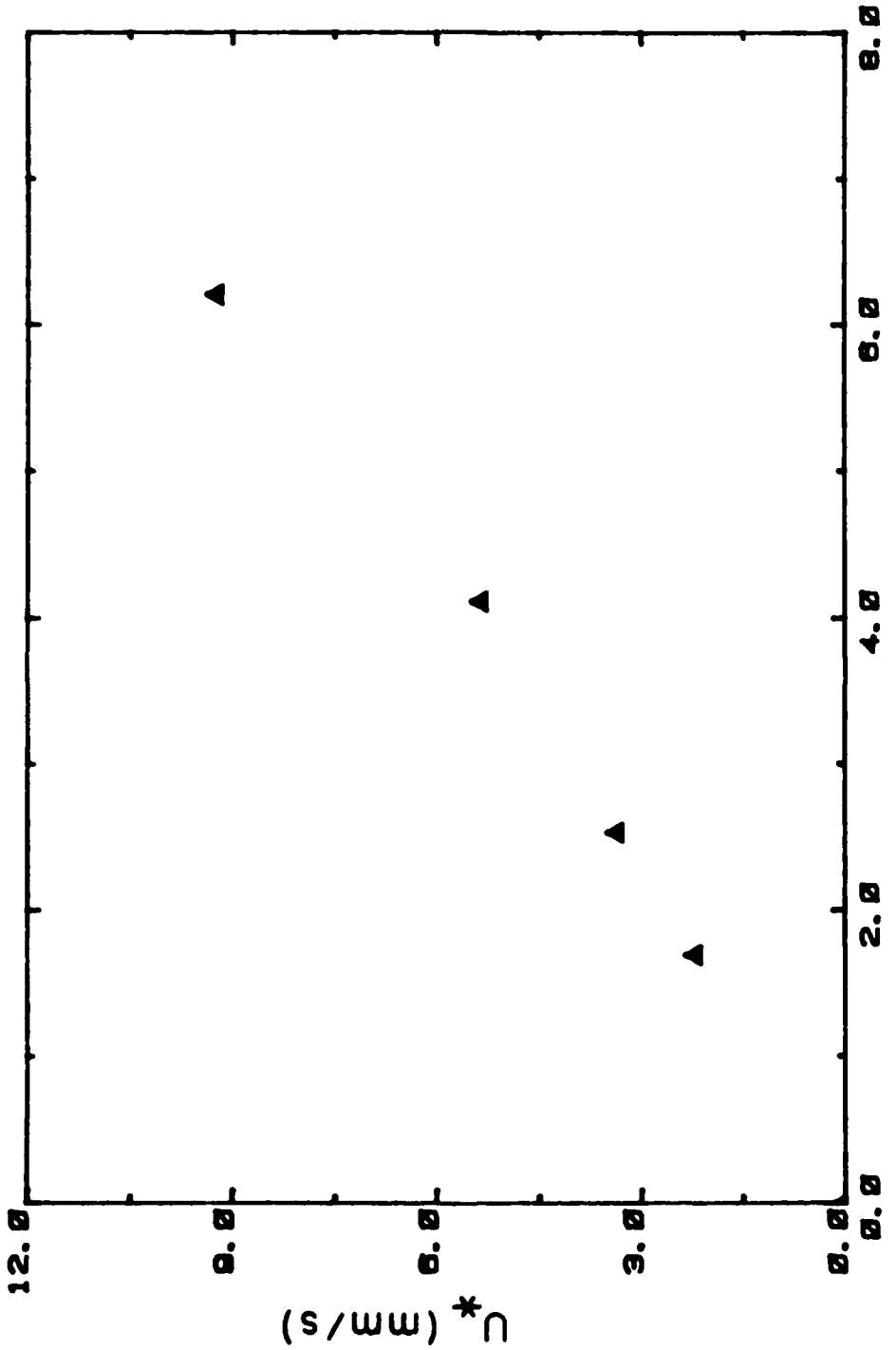

Figure 30. Friction velocity (u_*) versus wind speed (u_∞) (MW-EF).

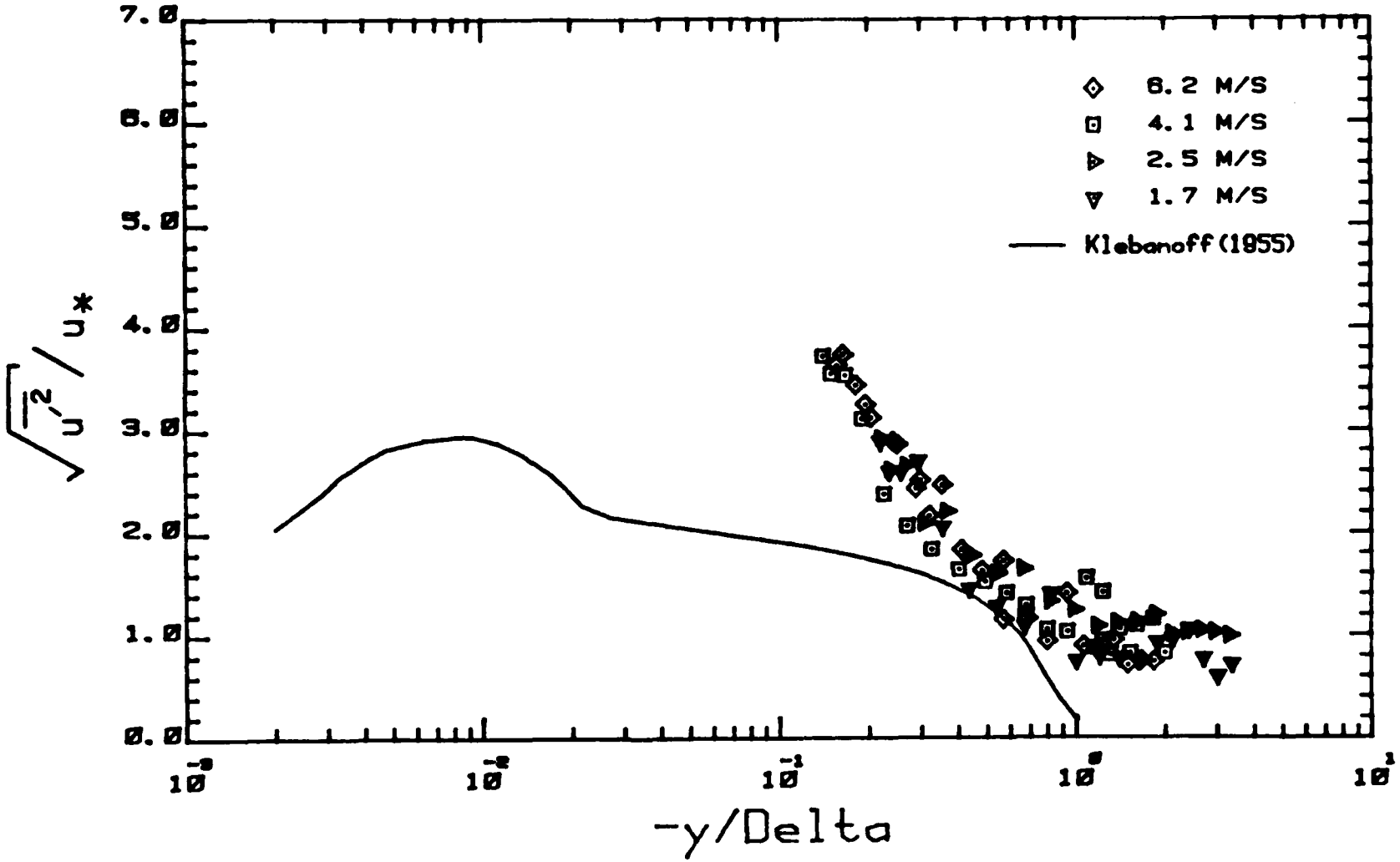

Figure 31. $(\overline{u'^2})^{1/2}/u_*$ versus $-y/\delta$ (MW-EF).

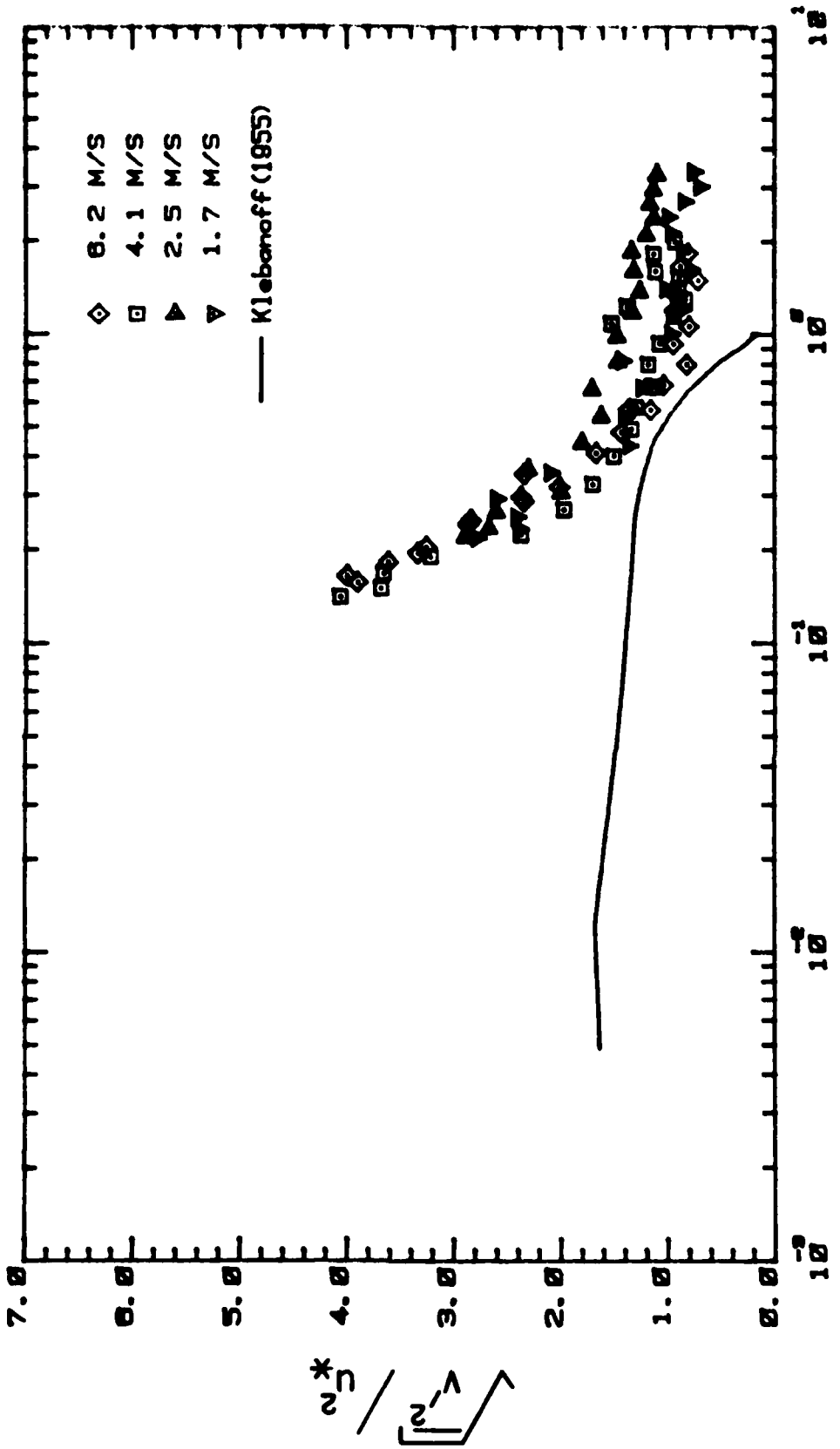

Figure 32. $\overline{(v'^2)}^{1/2}/u_*$ versus $-y/\delta$ (MW-EF).

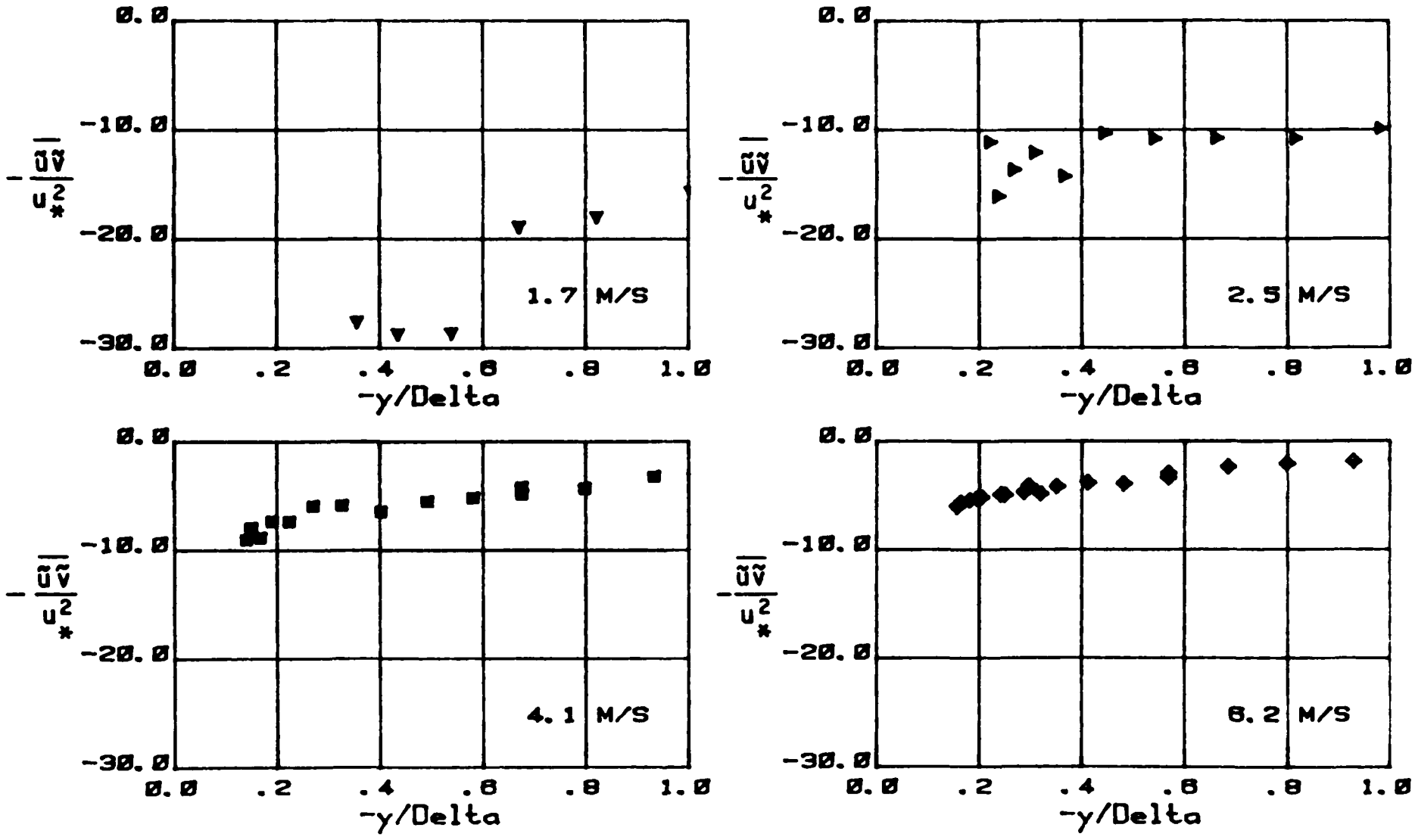

Figure 33. $-\overline{\tilde{u}\tilde{v}}/u_*^2$ versus $-y/\delta$ (MW-EF).

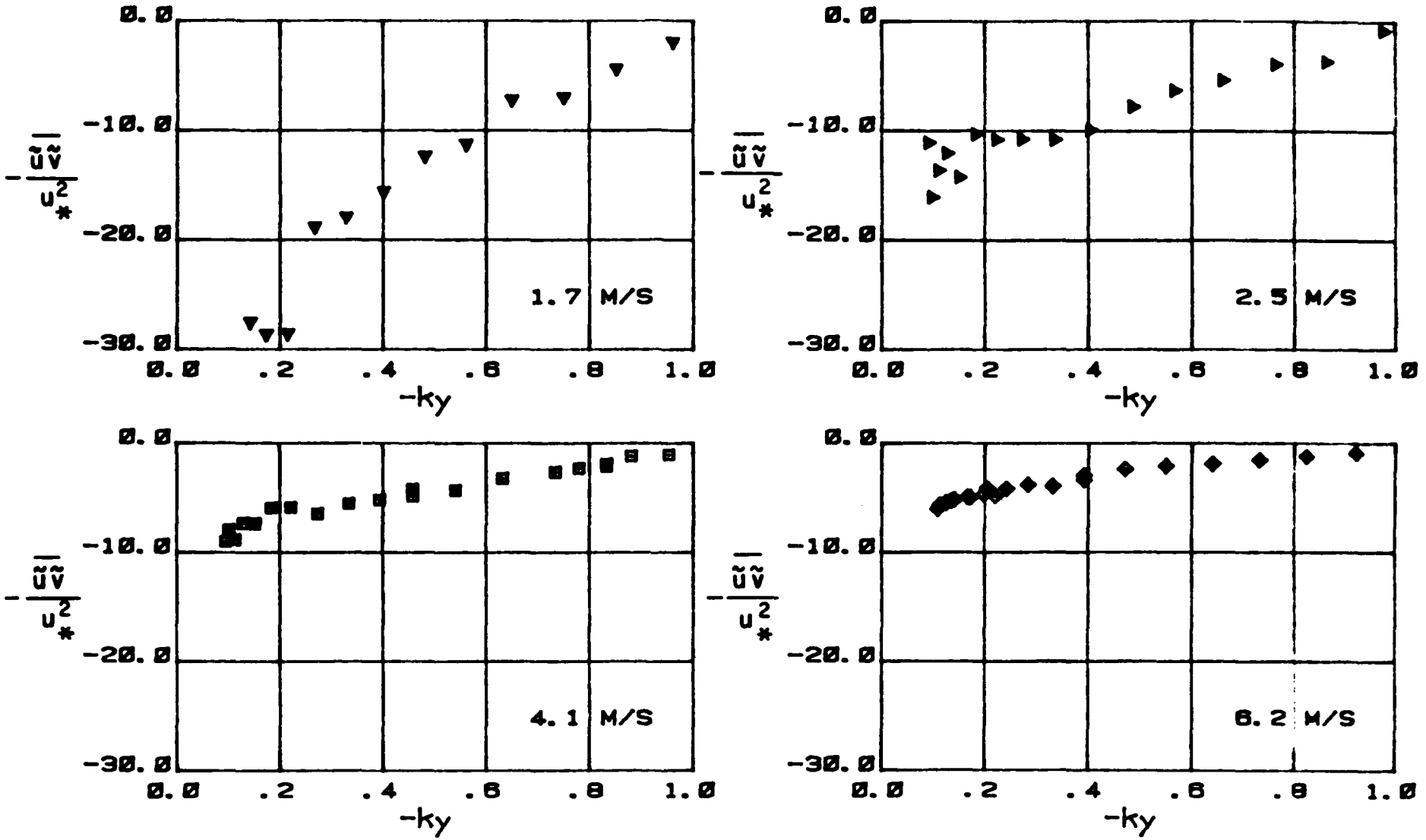

Figure 34. $-\overline{\tilde{u}\tilde{v}}/u_*^2$ versus -ky (MW-EF).

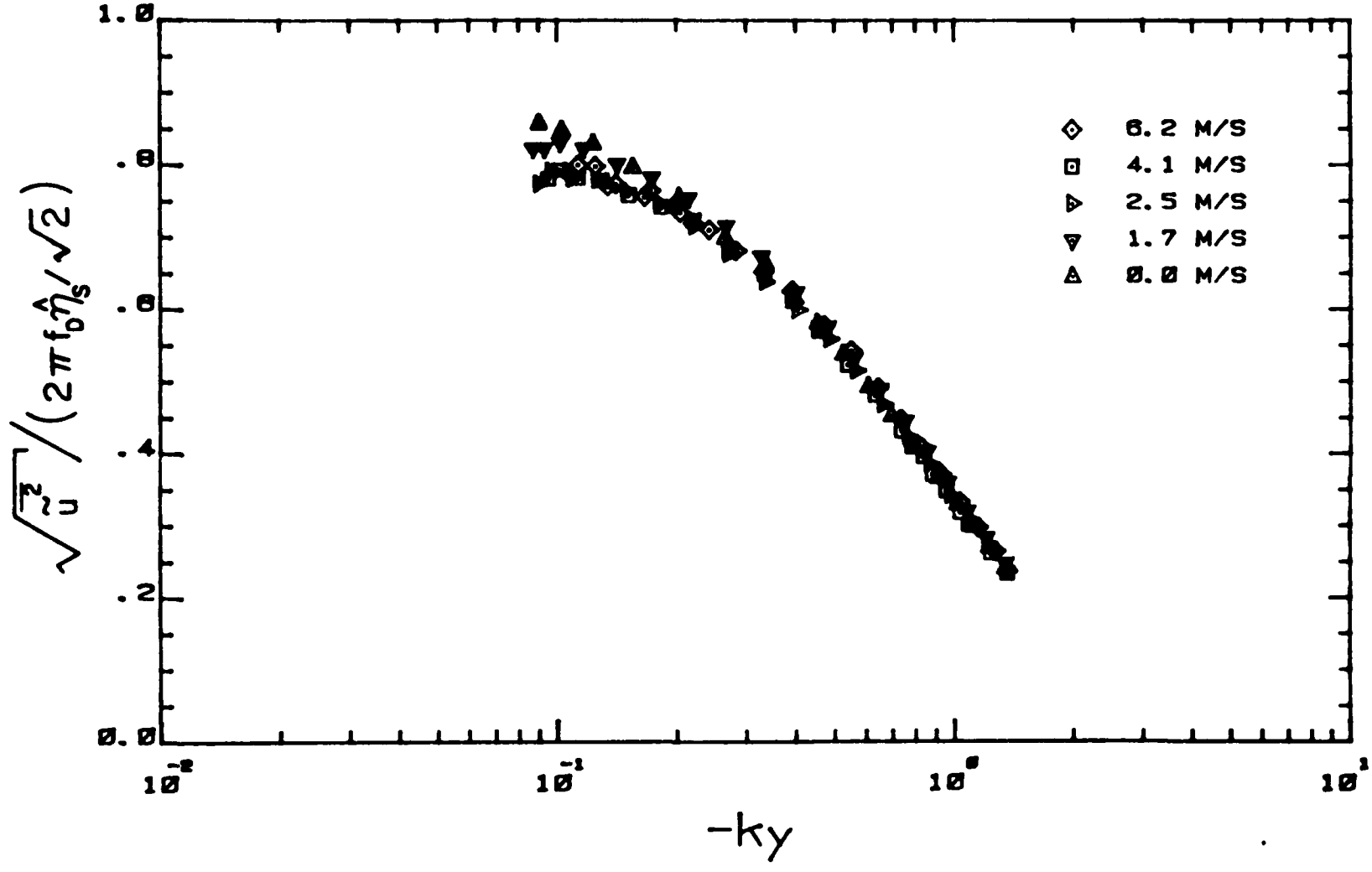

Figure 35. $(\overline{\tilde{u}^2})^{1/2}/(2\pi f_D \hat{n}_S/\sqrt{2})$ versus -ky (MW-EF).

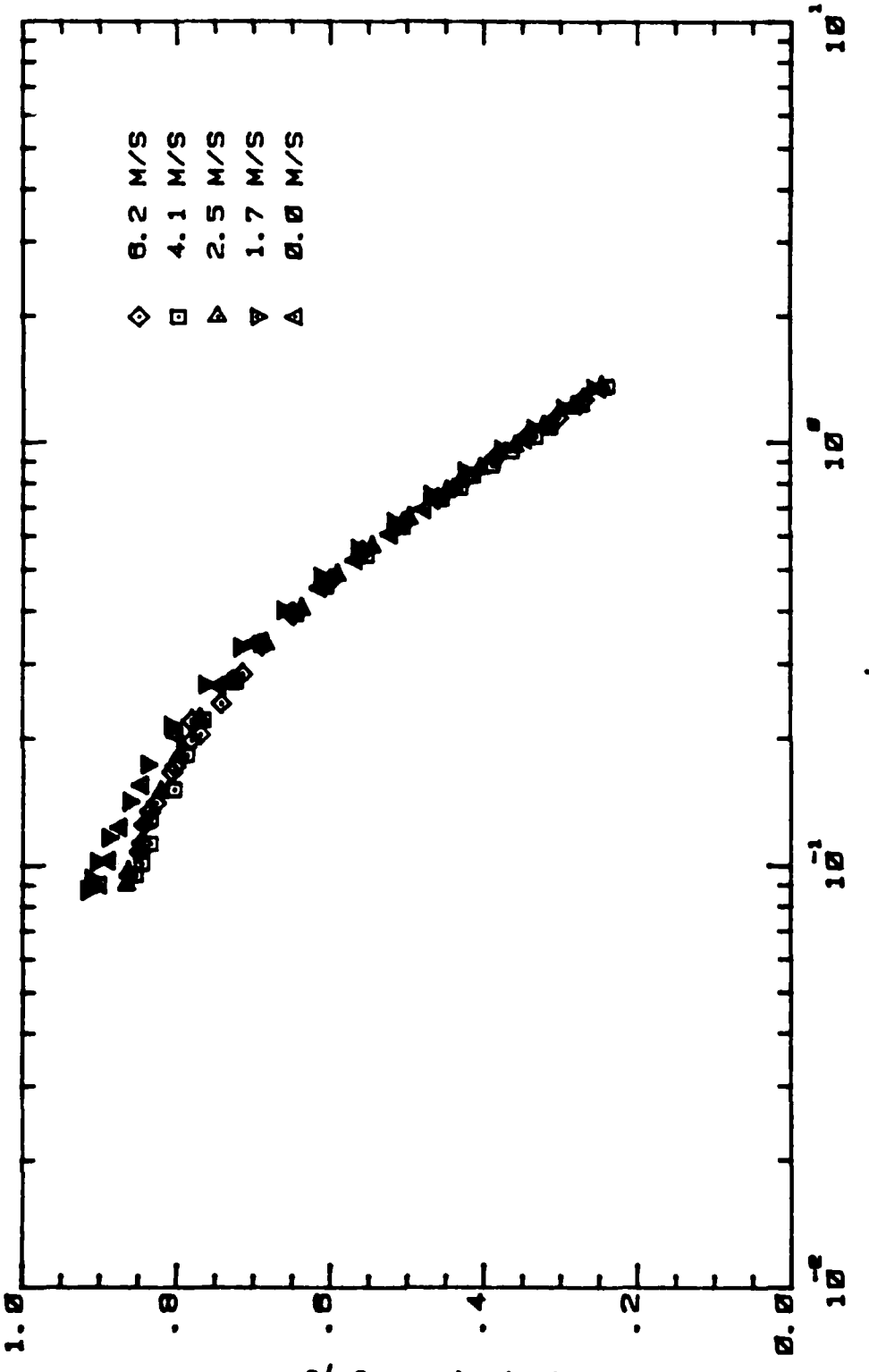

Figure 36. $(\overline{\tilde{v}^2})^{1/2}/(2\pi f_D \hat{\eta}_S/\sqrt{2})$ versus -ky (MW-EF).

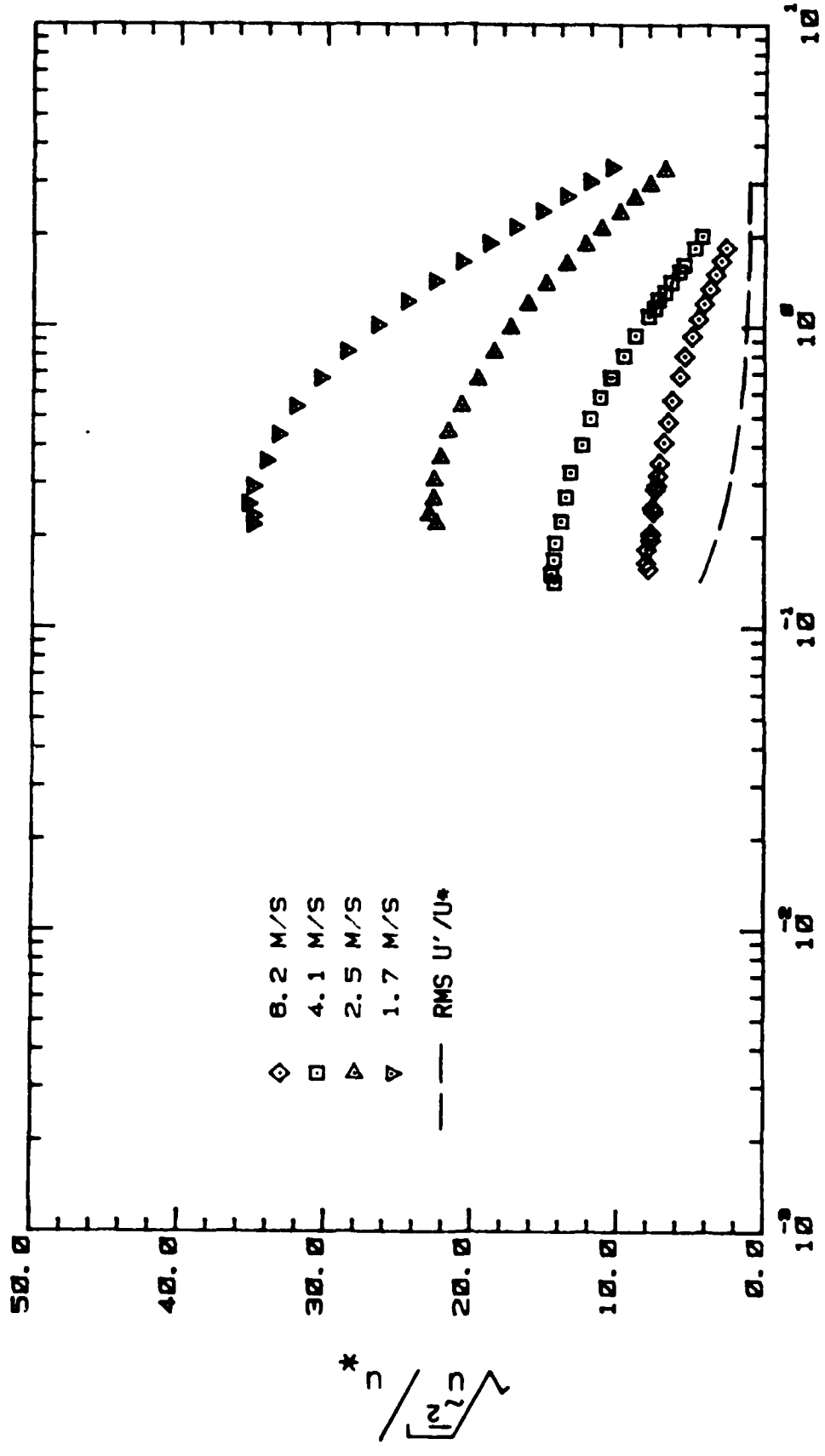

Figure 37. $(\overline{u^2})^{1/2}/u_*$ versus $-y/\delta$ (MW-EF).

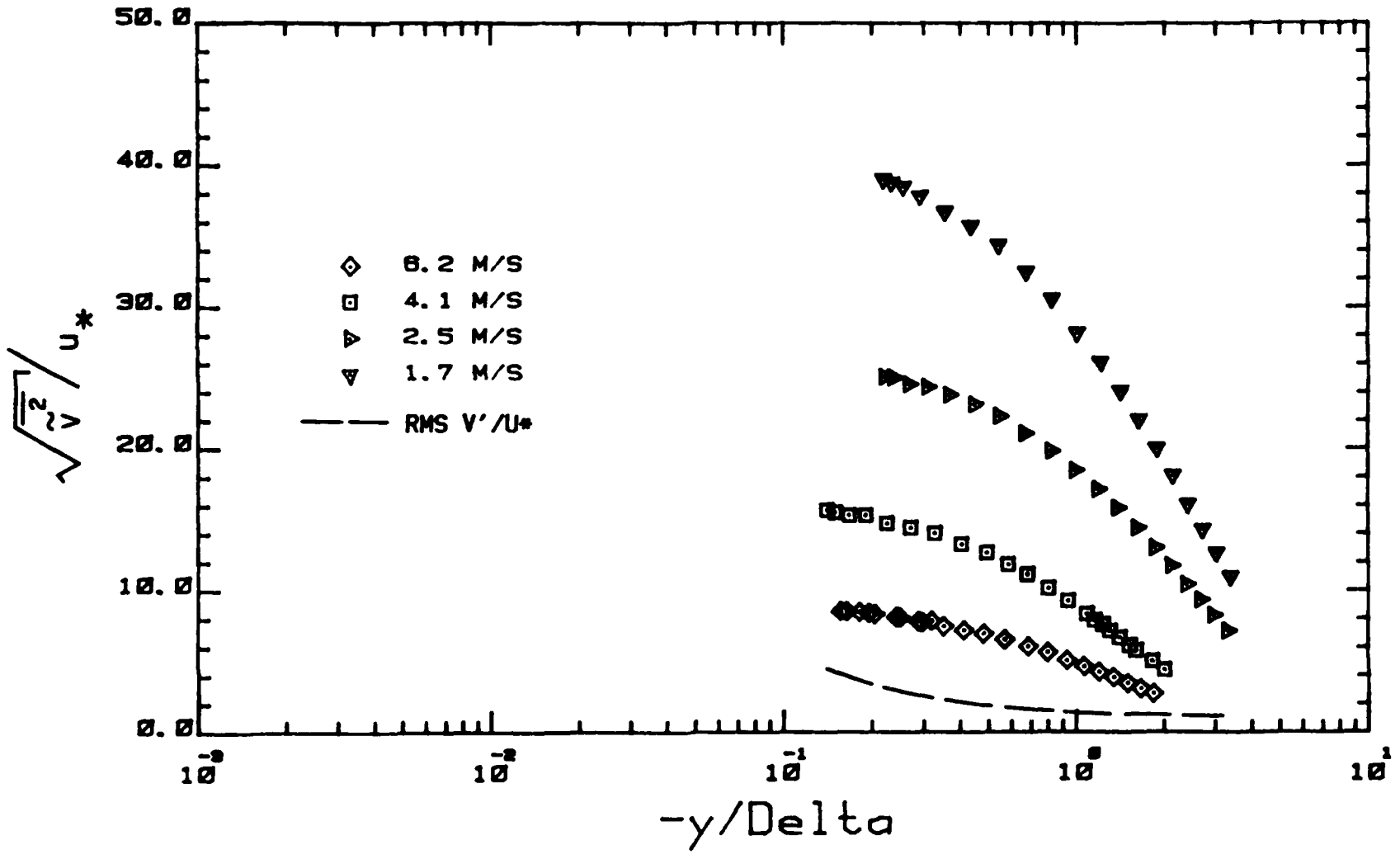

Figure 38. $(\overline{v^2})^{1/2}/u_*$ versus -y/δ (MW-EF).

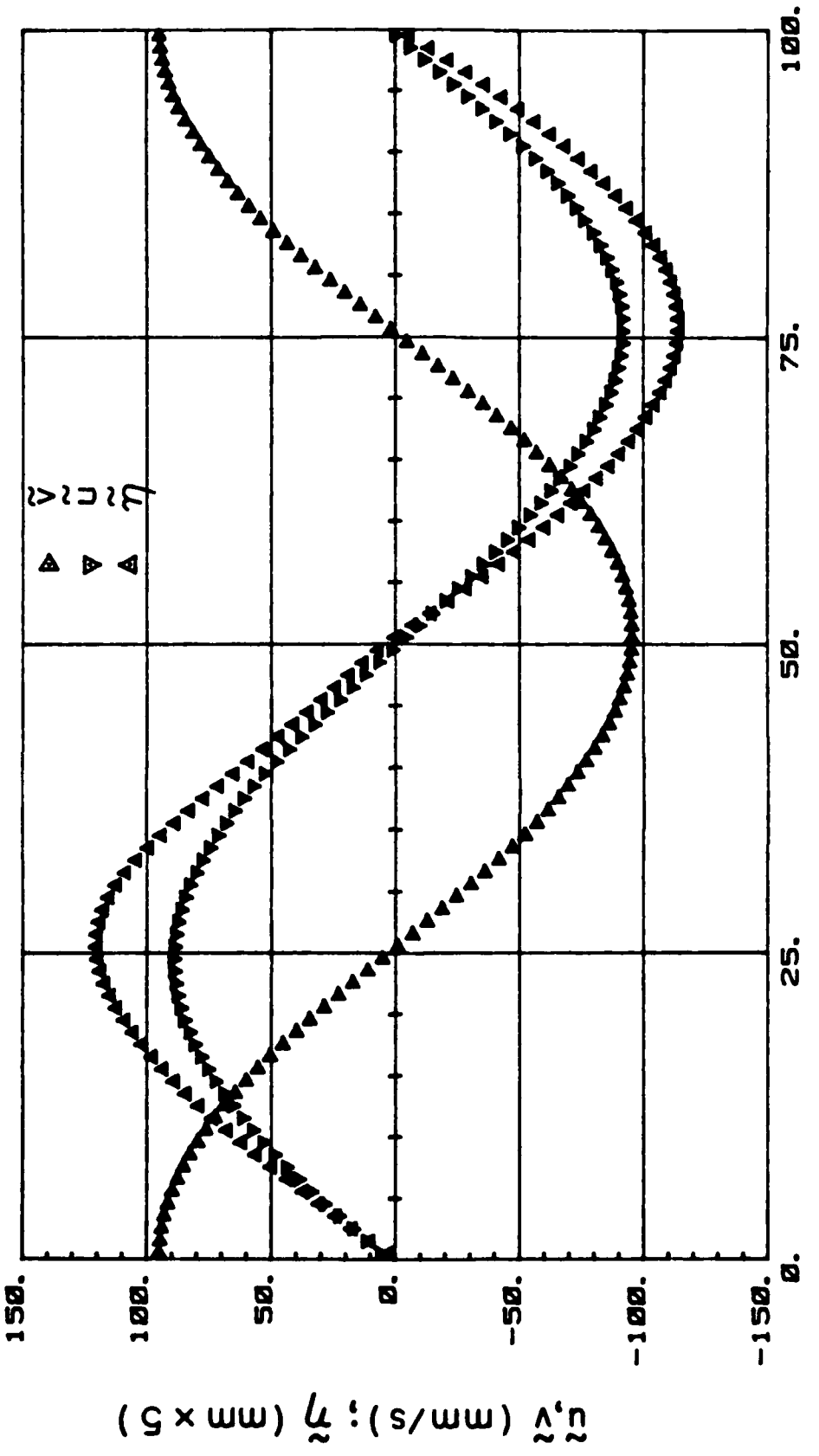

Figure 39. $\tilde{u}$, $\tilde{v}$, and $\tilde{n}$ (MW-EF).

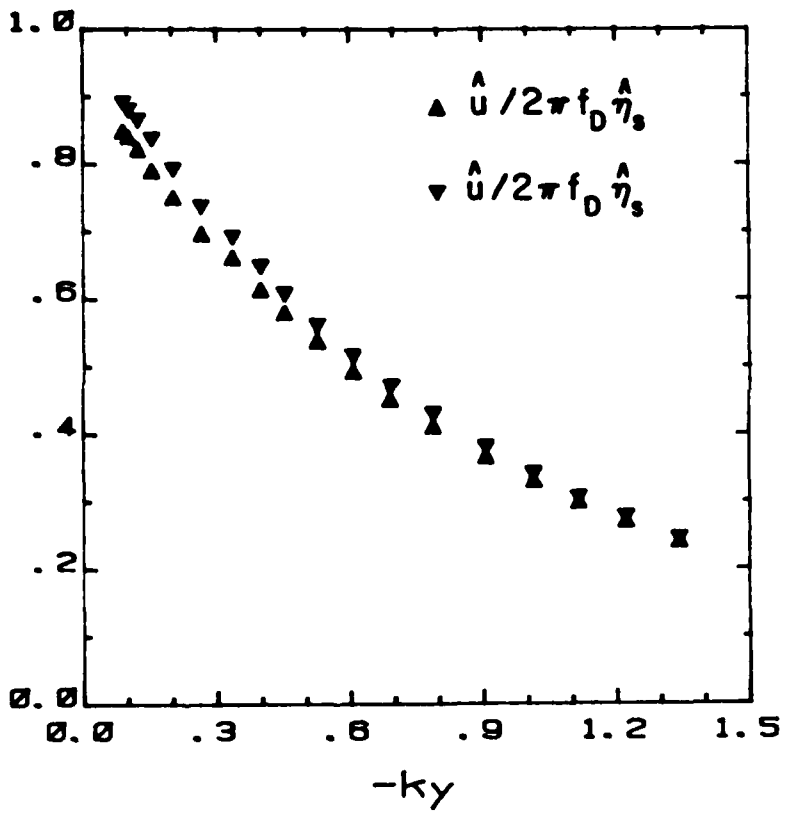

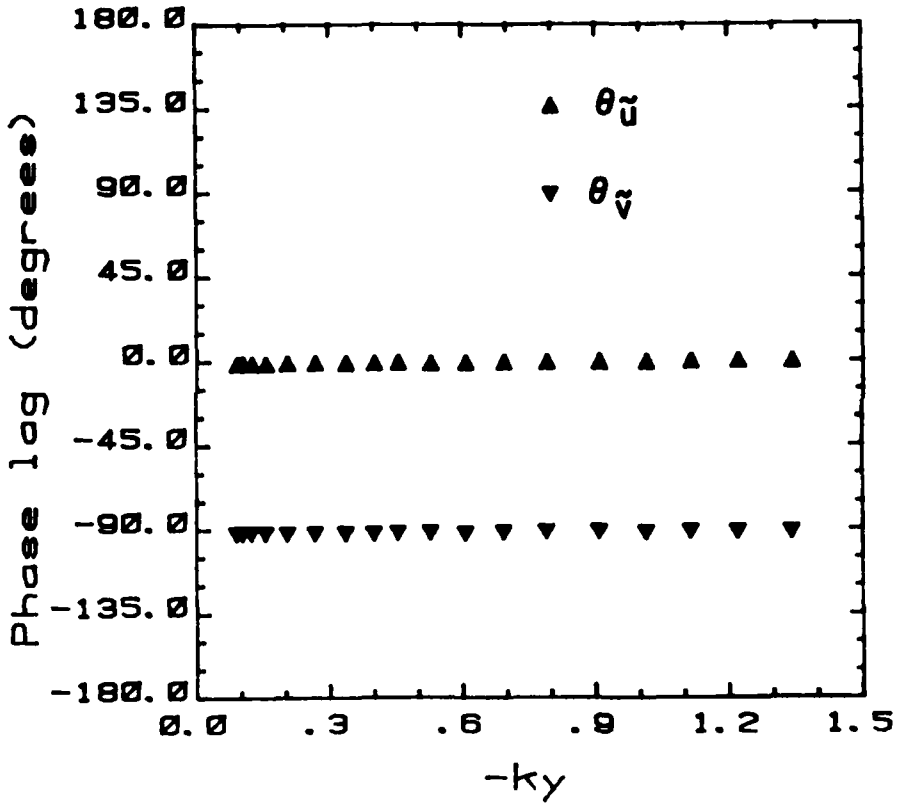

(a) u_∞ = 0.0 m/s

Figure 40. Amplitude and phase distributions of $\tilde{u}$ and $\tilde{v}$ with -ky (MW-EF).

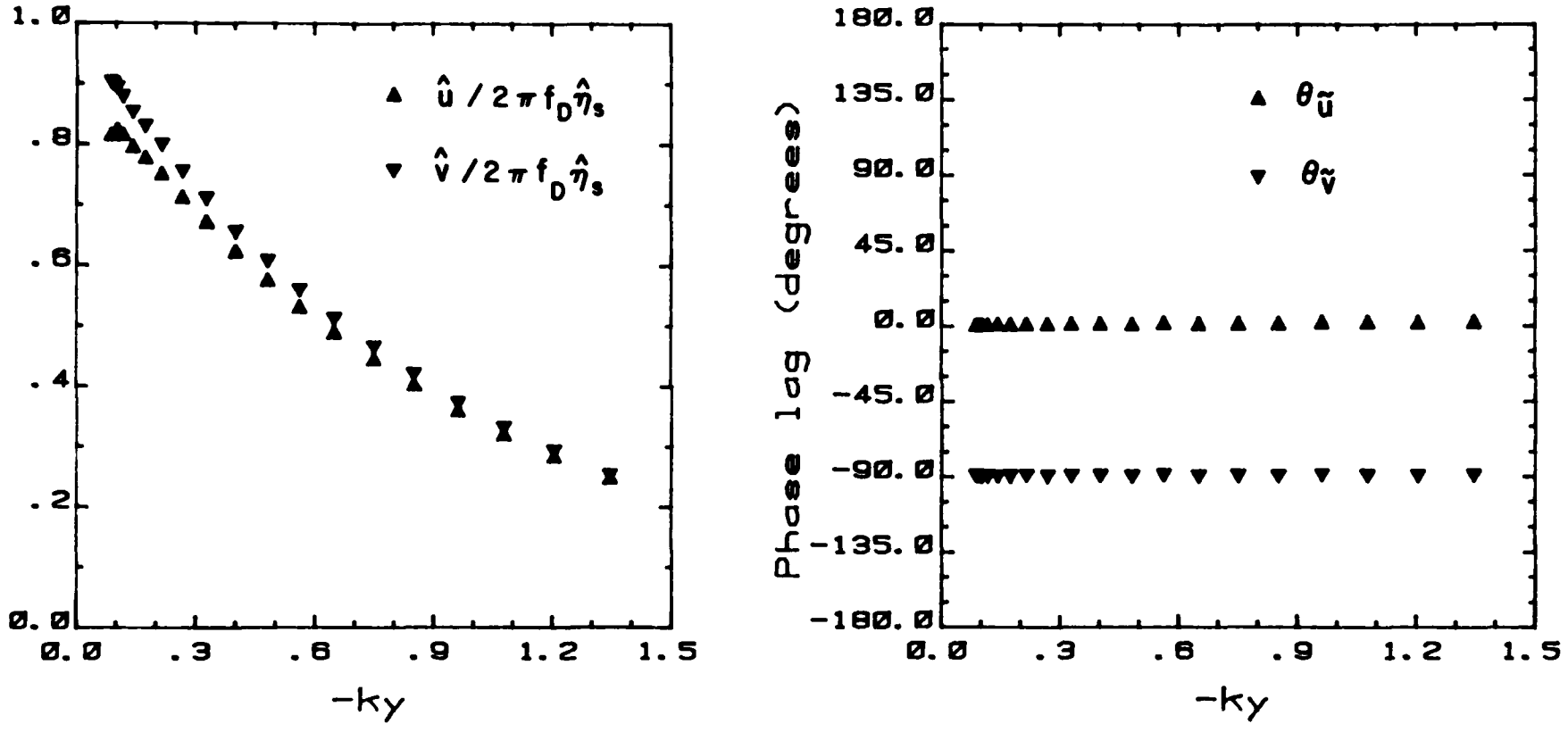

(b) u_∞ = 1.7 m/s

Figure 40. Amplitude and phase distributions of $\tilde{u}$ and $\tilde{v}$ with -ky (MW-EF).

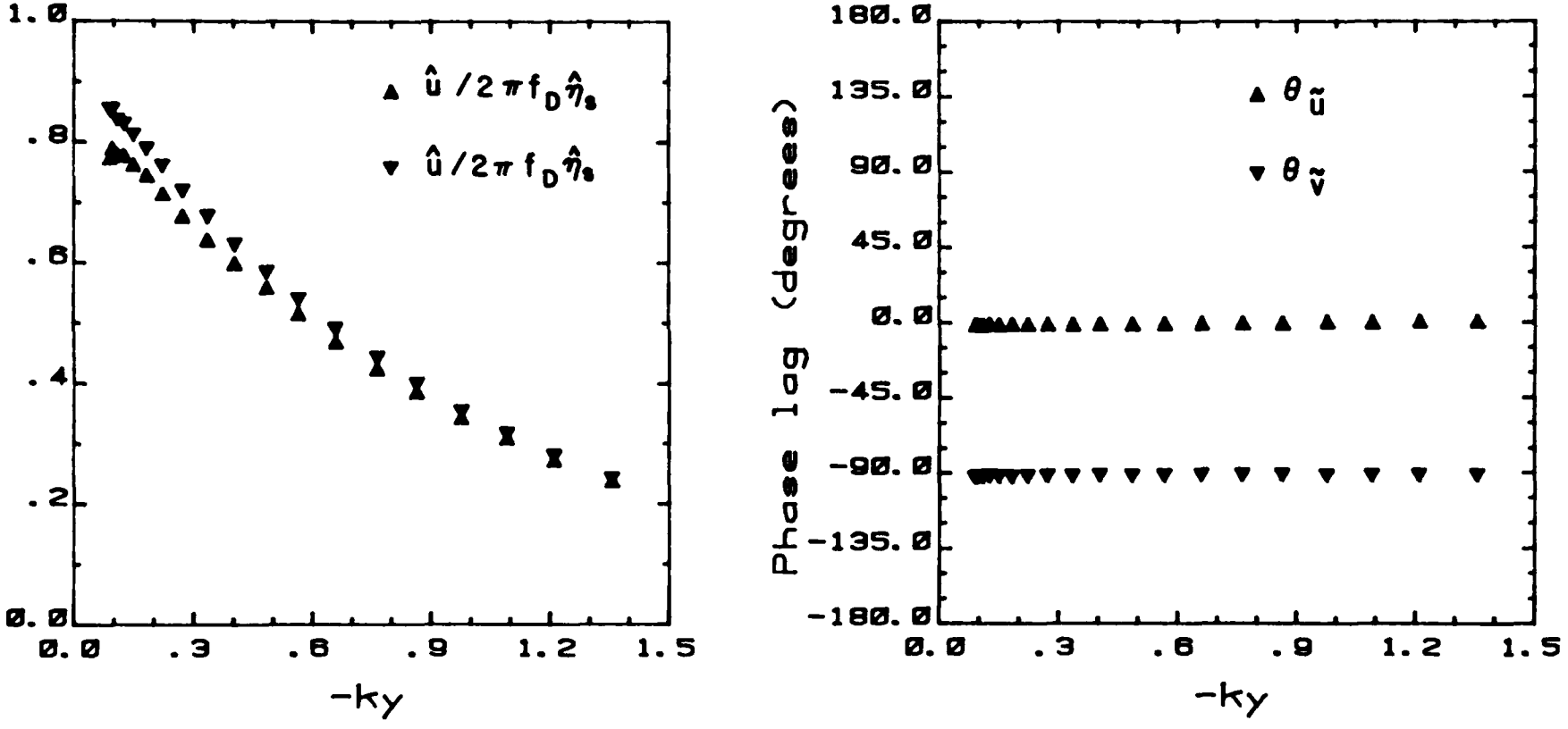

(c) u_∞ = 2.5 m/s

Figure 40. Amplitude and phase distributions of $\tilde{u}$ and $\tilde{v}$ with -ky (MW-EF).

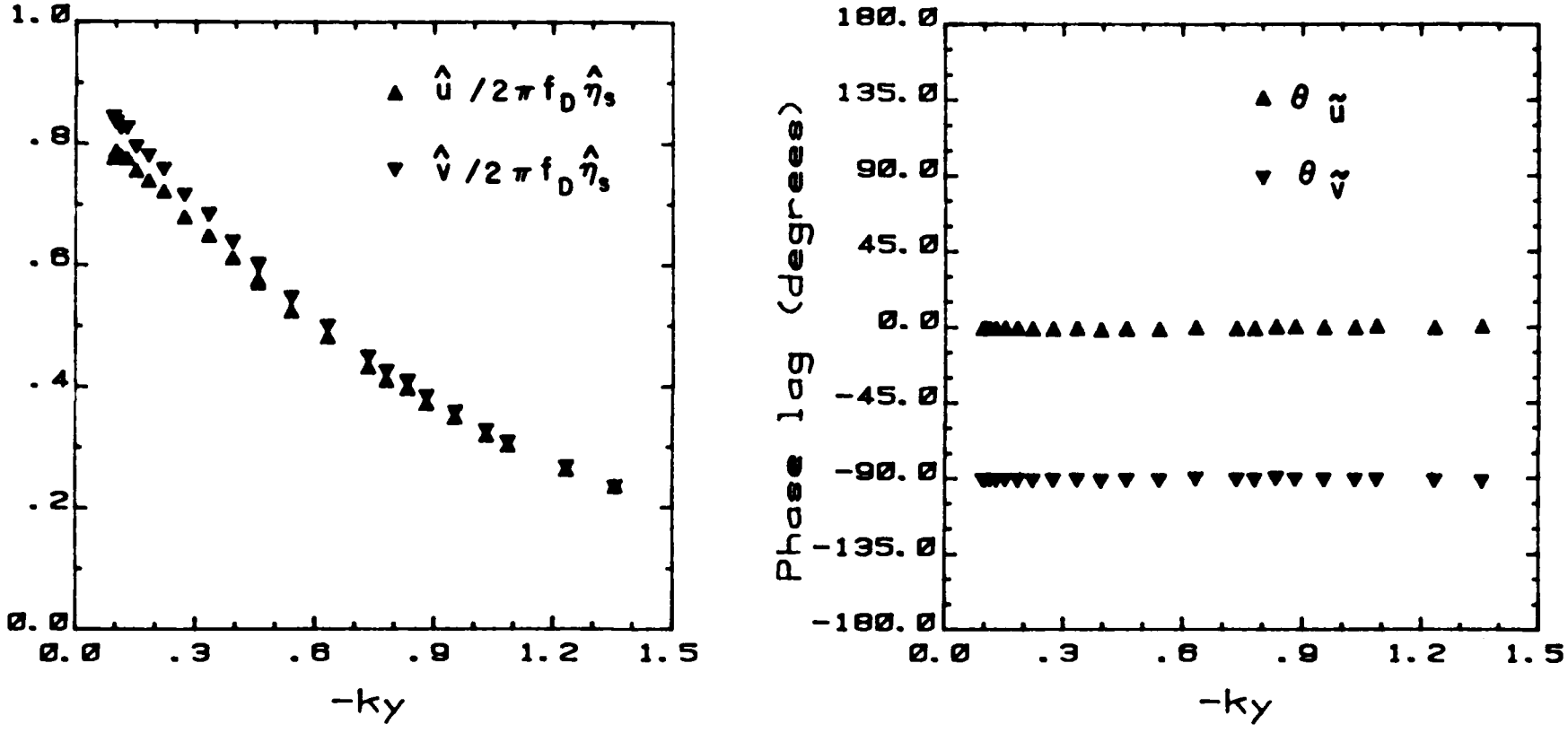

(d) u_∞ = 4.1 m/s

Figure 40. Amplitude and phase distributions of $\tilde{u}$ and $\tilde{v}$ with -ky (MW-EF).

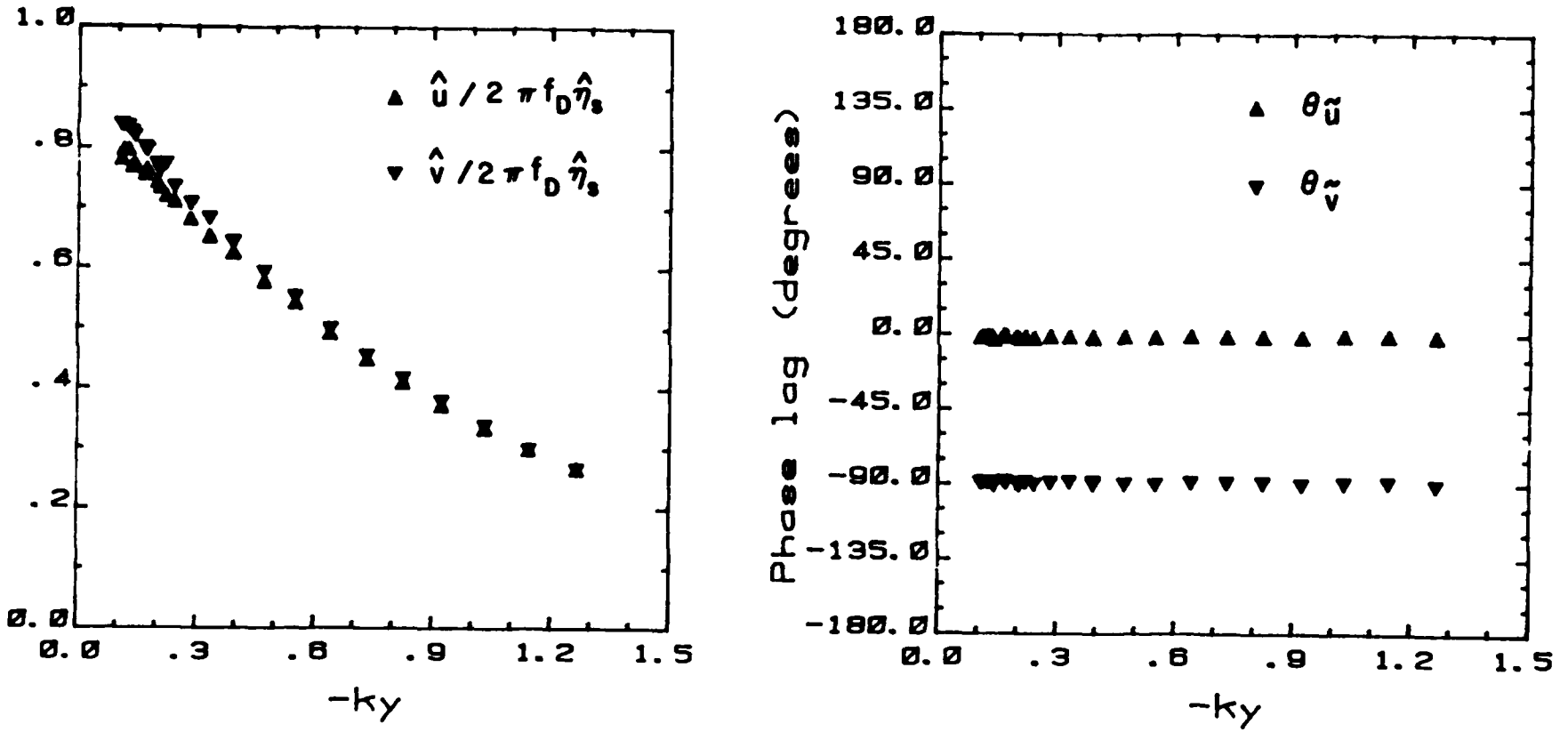

(e) u_∞ = 6.2 m/s

Figure 40. Amplitude and phase distributions of $\tilde{u}$ and $\tilde{v}$ with -ky (MW-EF).

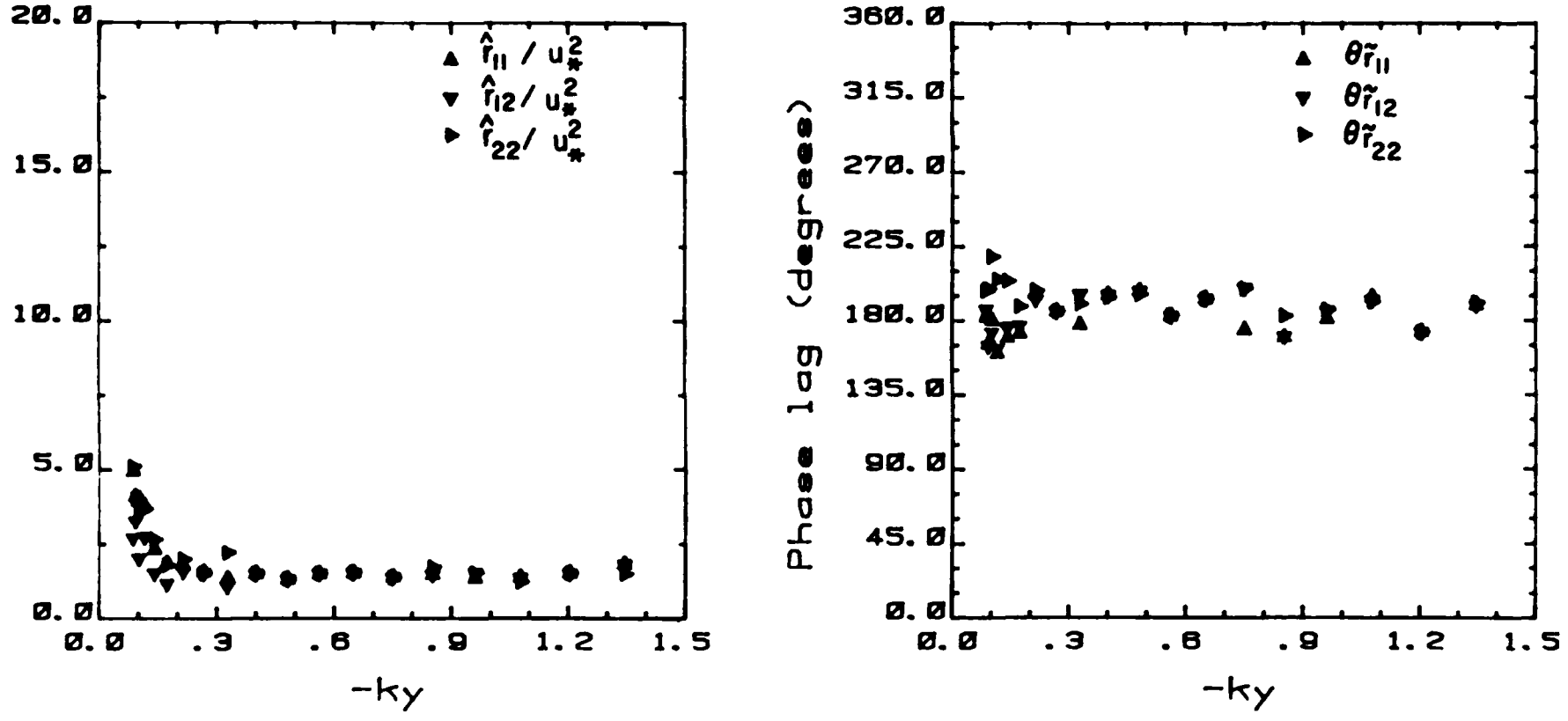

(a) u_∞ = 1.7 m/s

Figure 41. Amplitude and phase distribution of $\tilde{r}_{ij}$ with -ky (MW-EF).

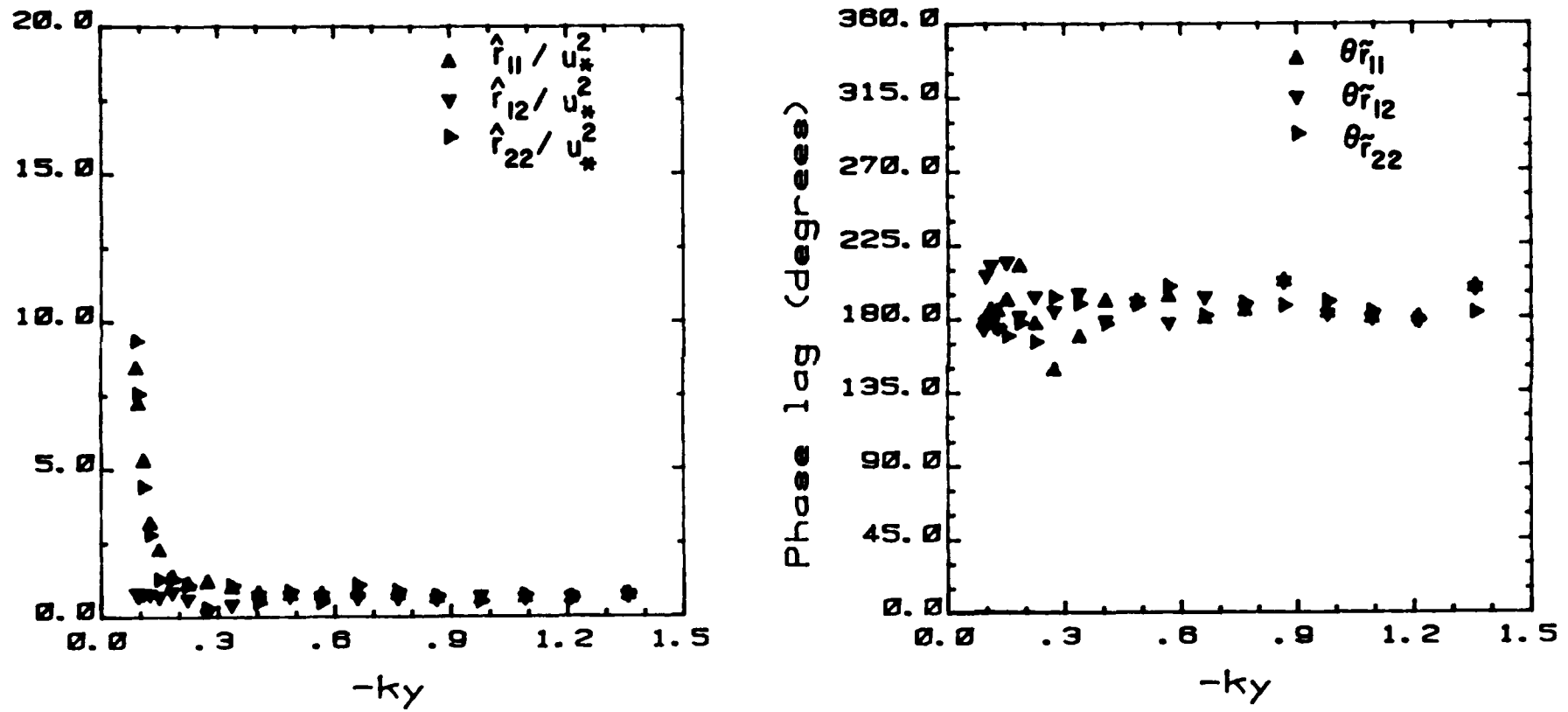

(b) u_∞ = 2.5 m/s

Figure 41. Amplitude and phase distribution of $\tilde{r}_{ij}$ with -ky (MW-EF).

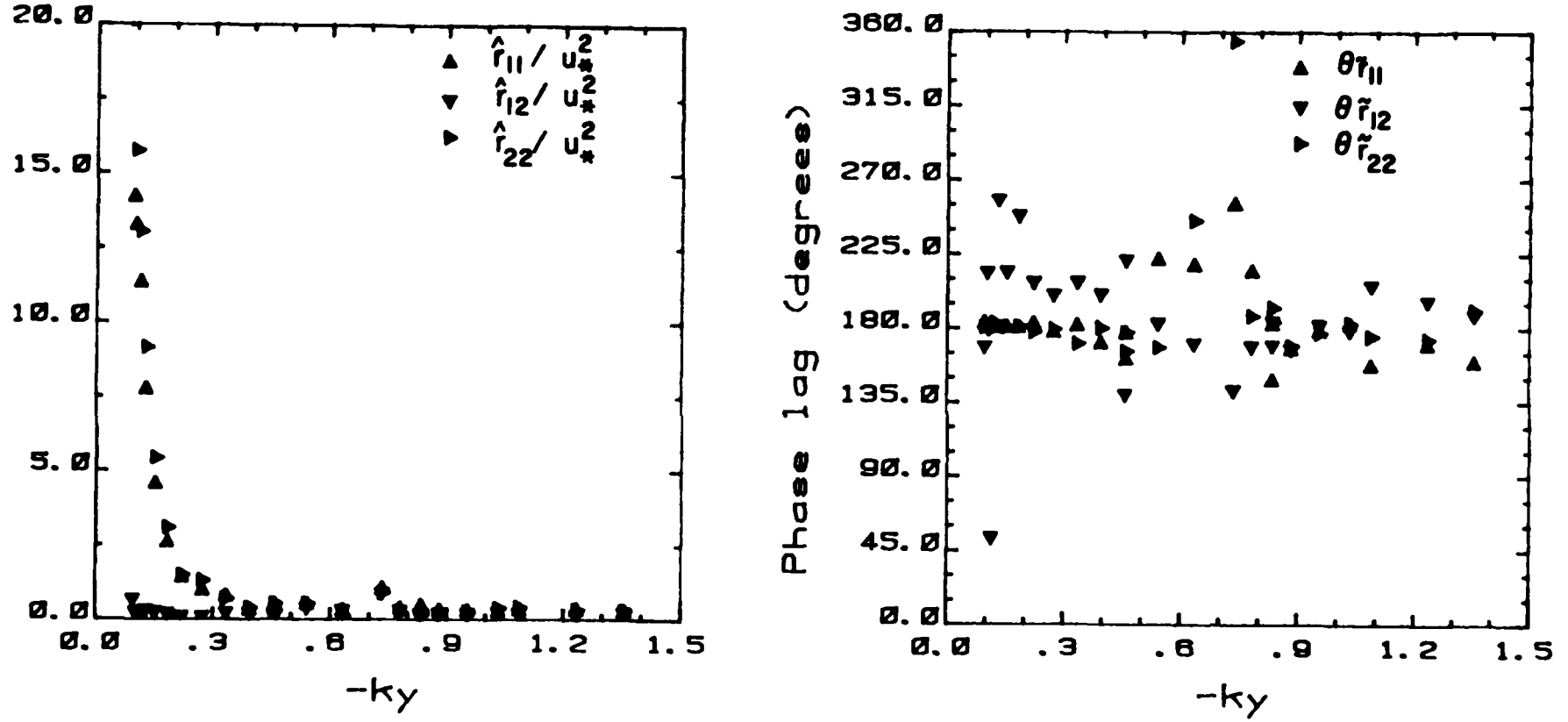

(c) u_∞ = 4.1 m/s

Figure 41. Amplitude and phase distribution of $\tilde{r}_{ij}$ with -ky (MW-EF).

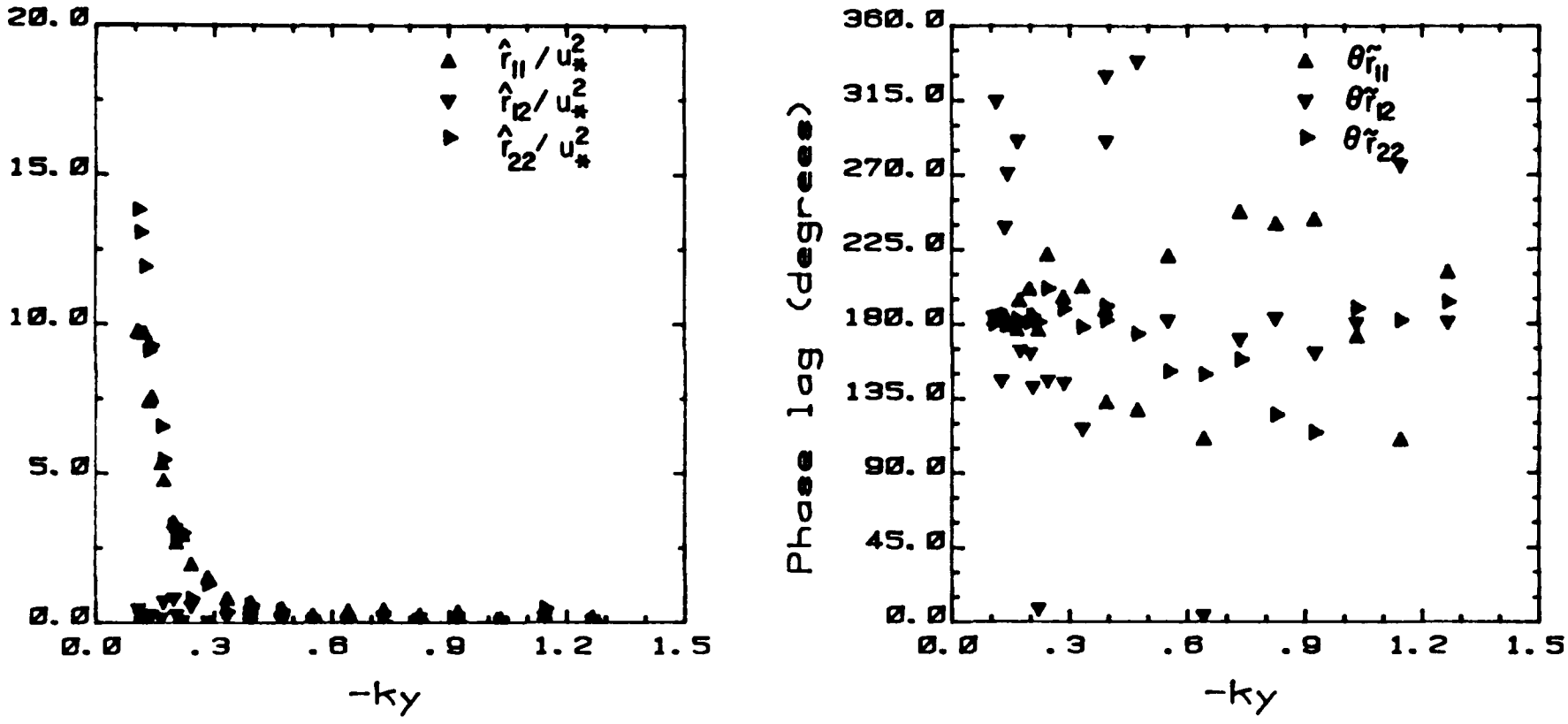

(d) u_∞ = 6.2 m/s

Figure 41. Amplitude and phase distribution of $\tilde{r}_{ij}$ with -ky (MW-EF).

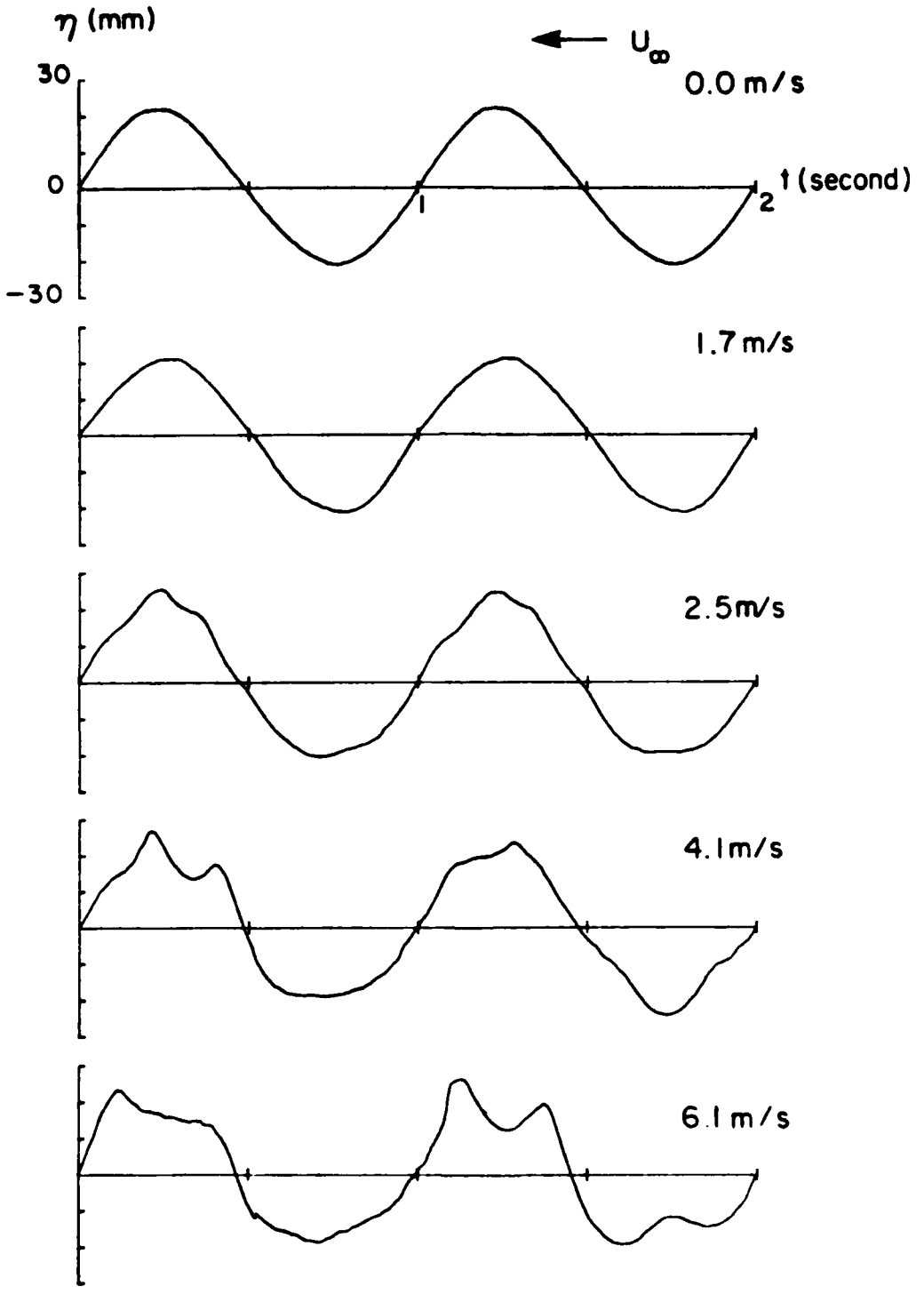

Figure 42. Time traces of water surface displacement at measuring fetch (MW-WF-EF).

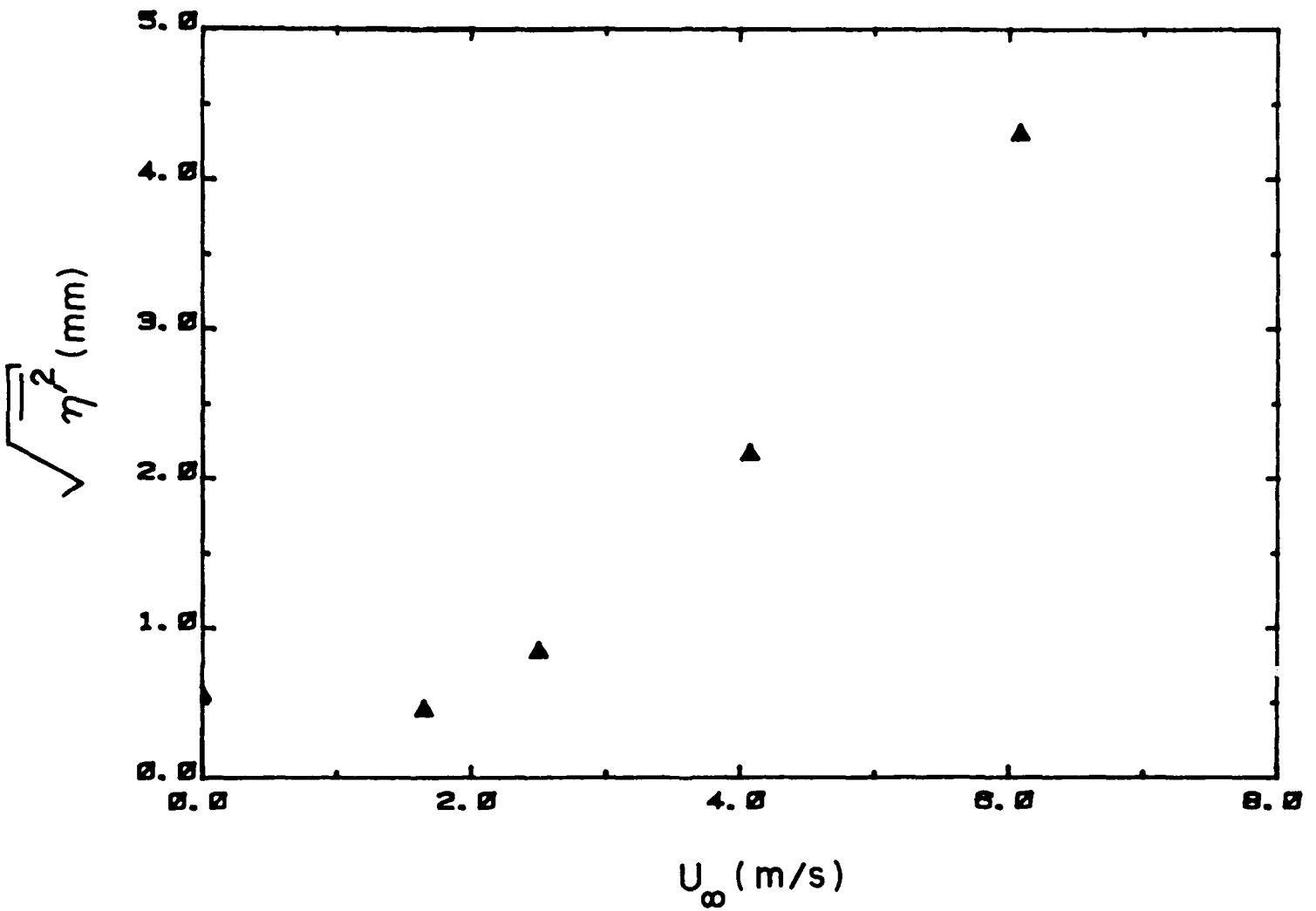

Figure 43. $(\overline{\eta'^2})^{1/2}$ versus wind speed (u_∞) (MW-WF-EF).

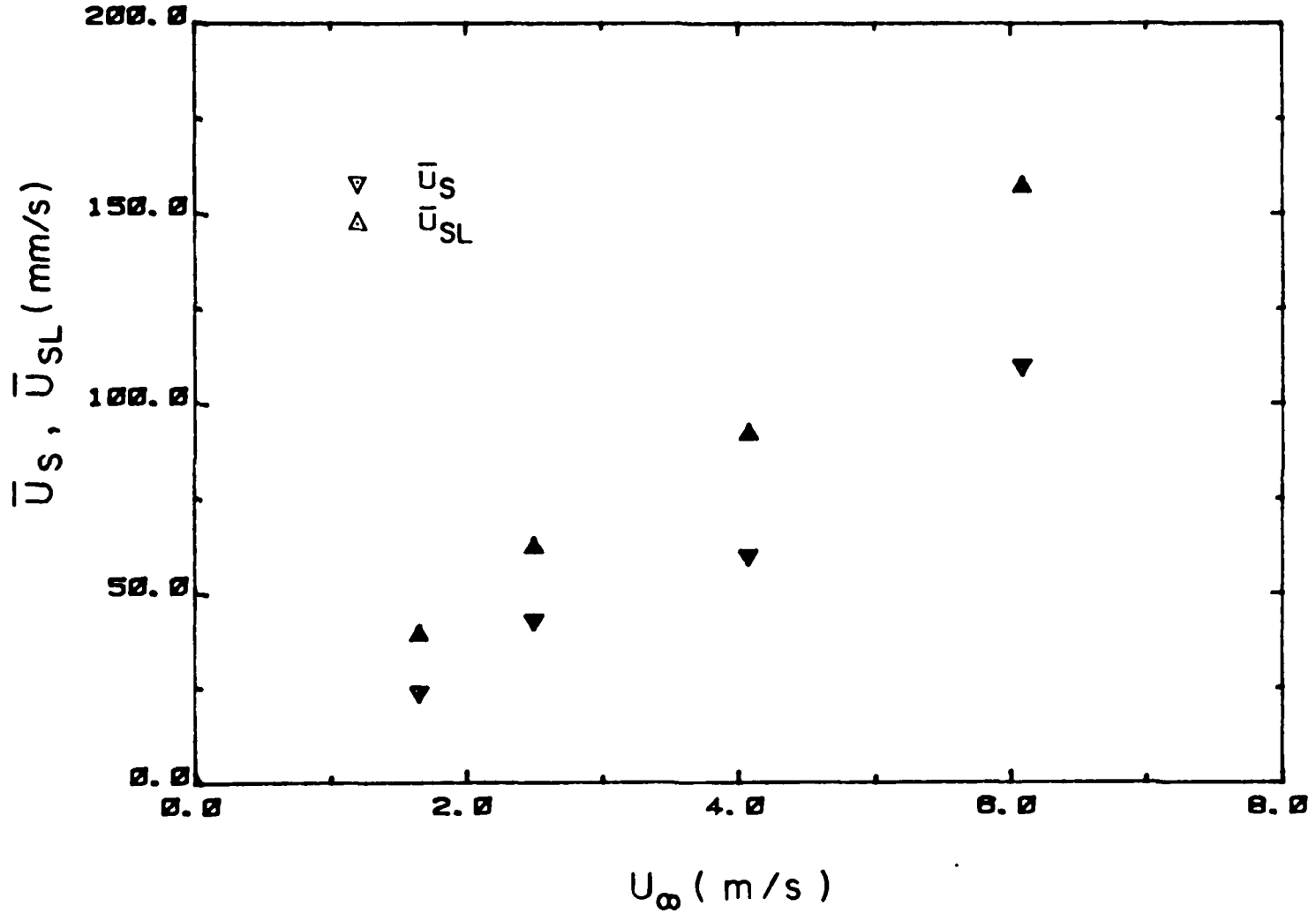

Figure 44. Mean Lagrangian and Eulerian surface drift velocities ($\bar{u}_{SL}$, $\bar{u}_S$) versus wind speed (u_∞) (MW-WF-EF).

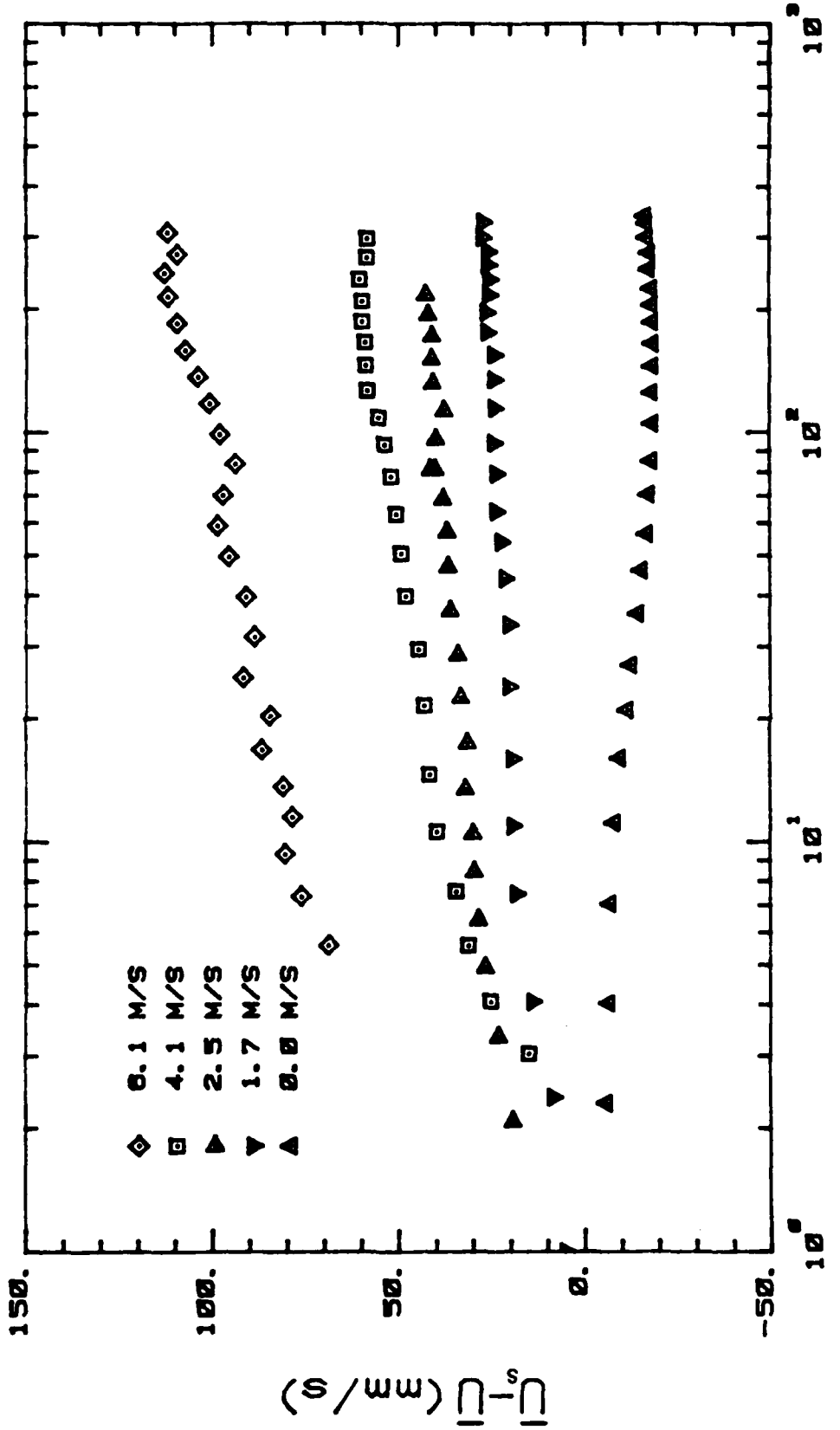

Figure 45. Mean horizontal velocity defect ($\overline{u}_s-\overline{u}$) profiles (MW-WF-EF).

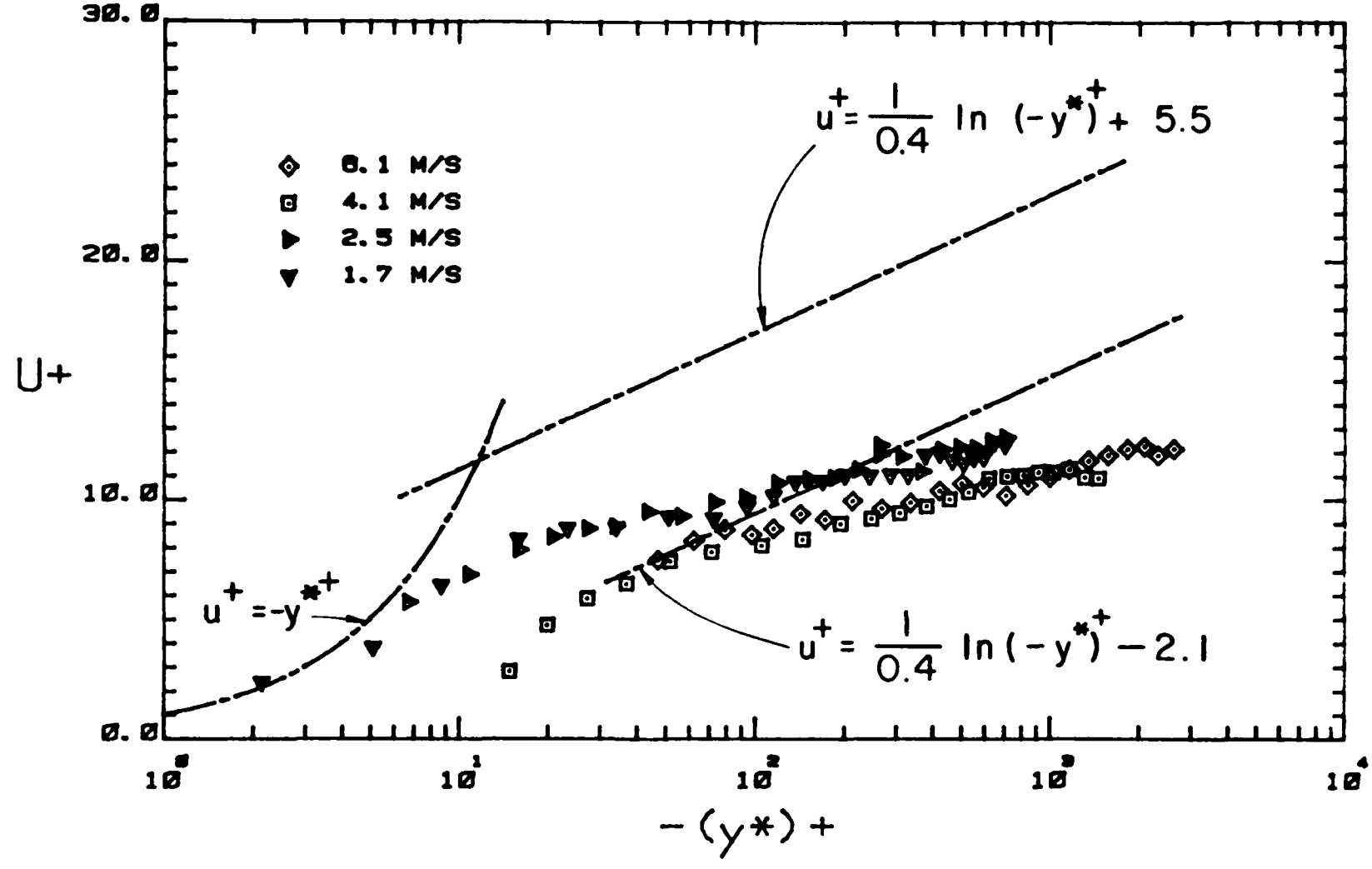

Figure 46. Mean horizontal velocity defect profiles in wave-following law-of-the-wall coordinates using friction velocities of mechanical-wave fixed-frame experiment.

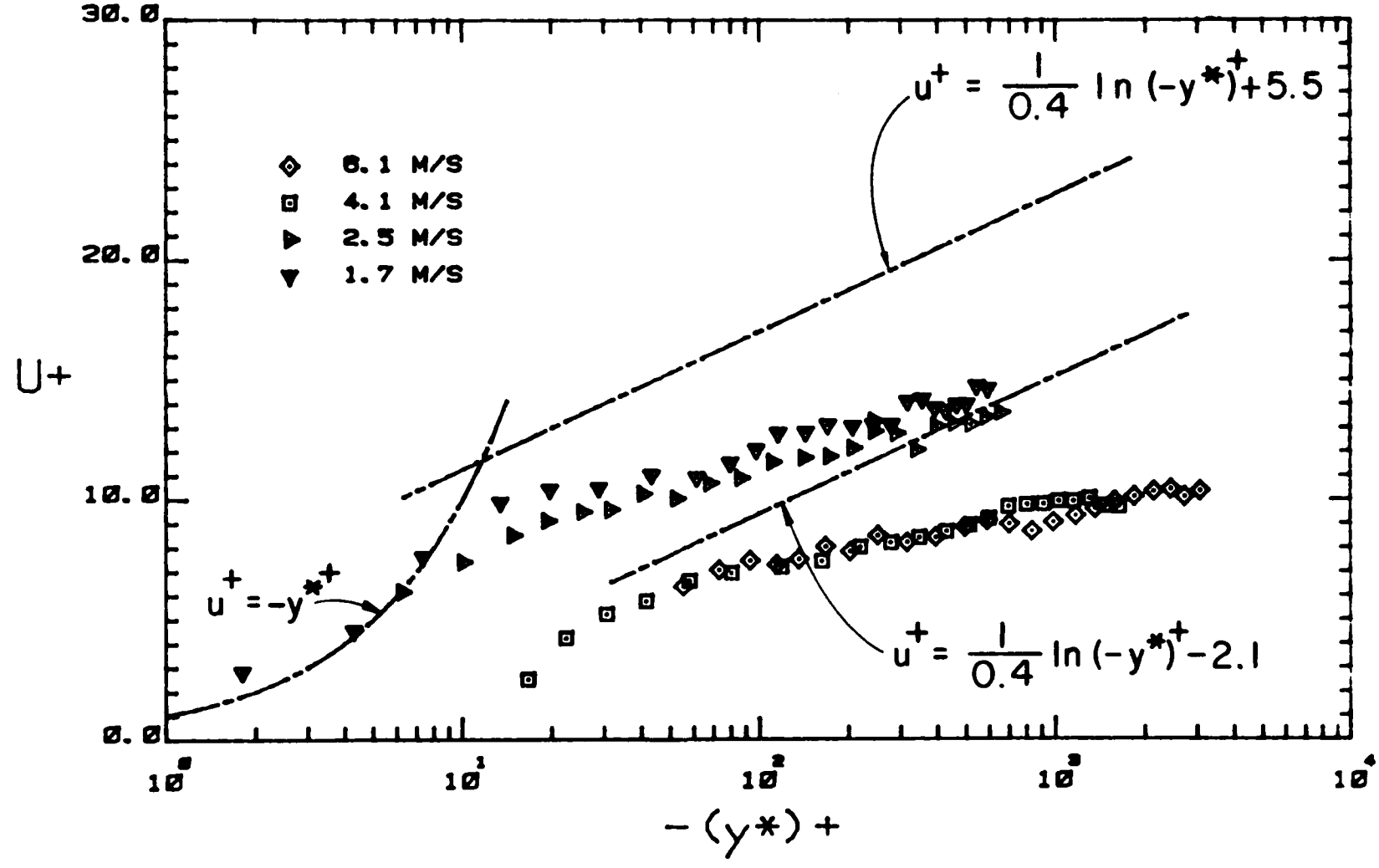

Figure 47. Mean horizontal velocity defect profiles in wave-following law-of-the-wall coordinates using friction velocities of Hsu and Hsu (1983).

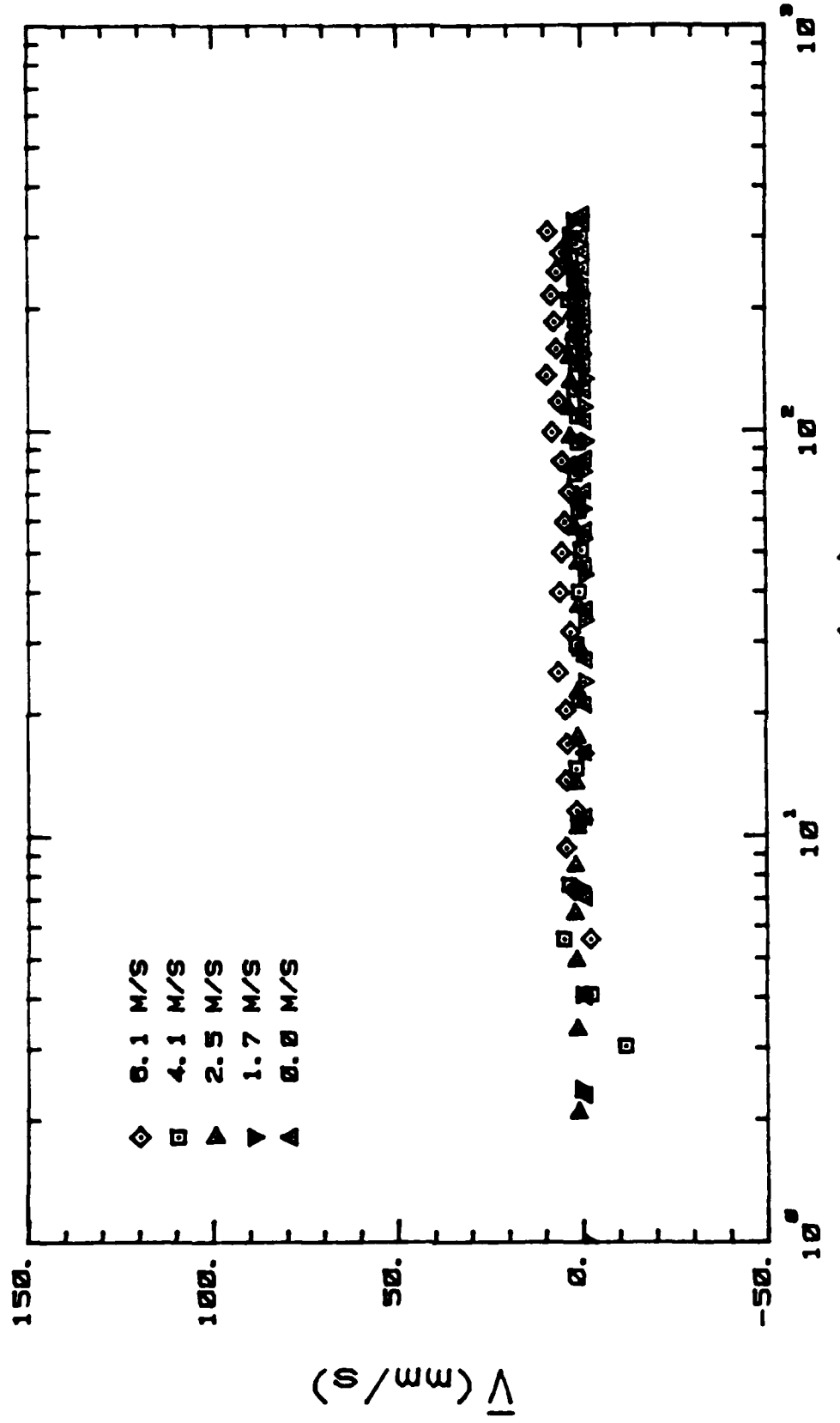

Figure 48. Mean vertical velocity profiles (MW-WF-EF).

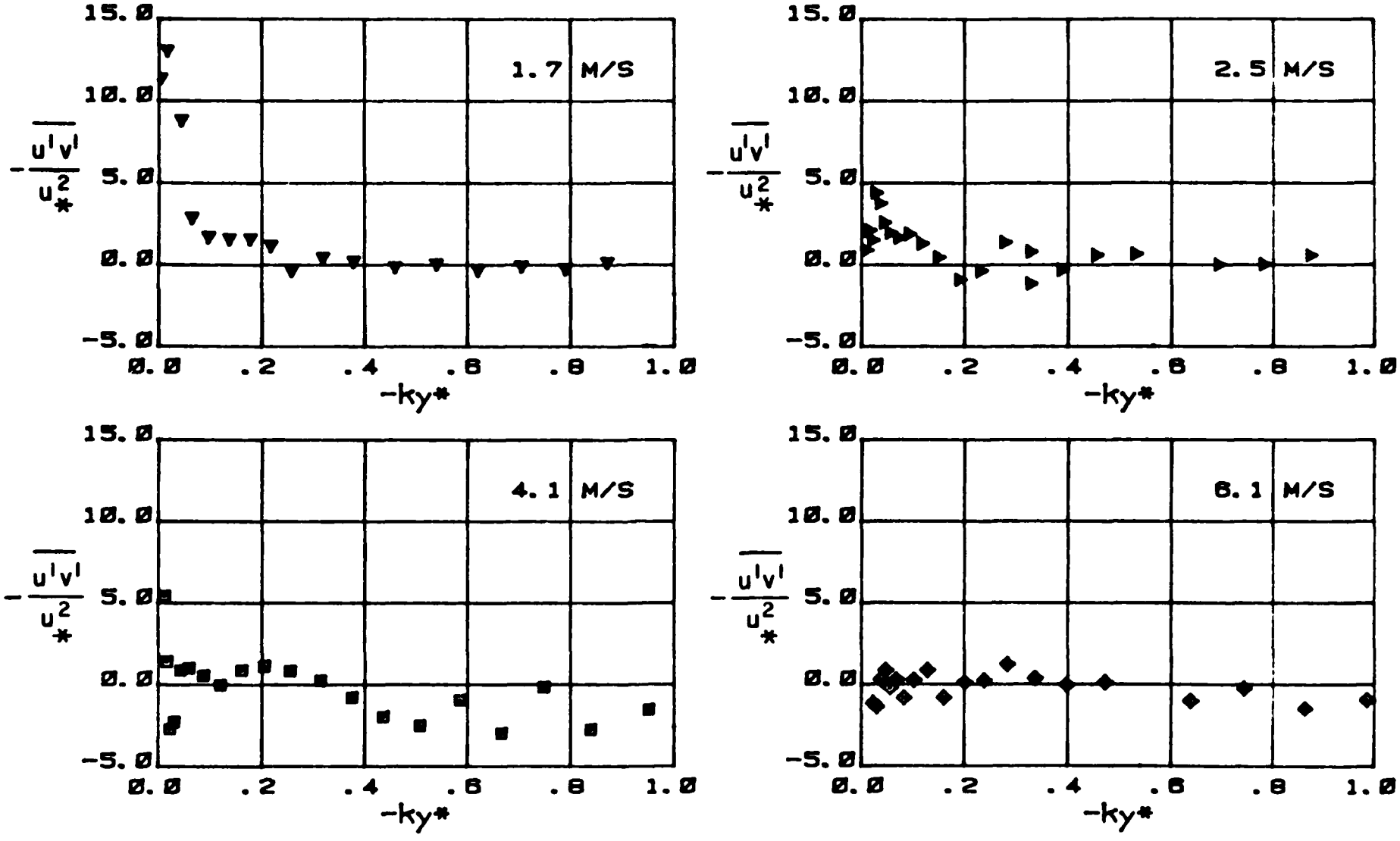

Figure 49. $-\overline{u'v'}/u_*$ versus -ky*.

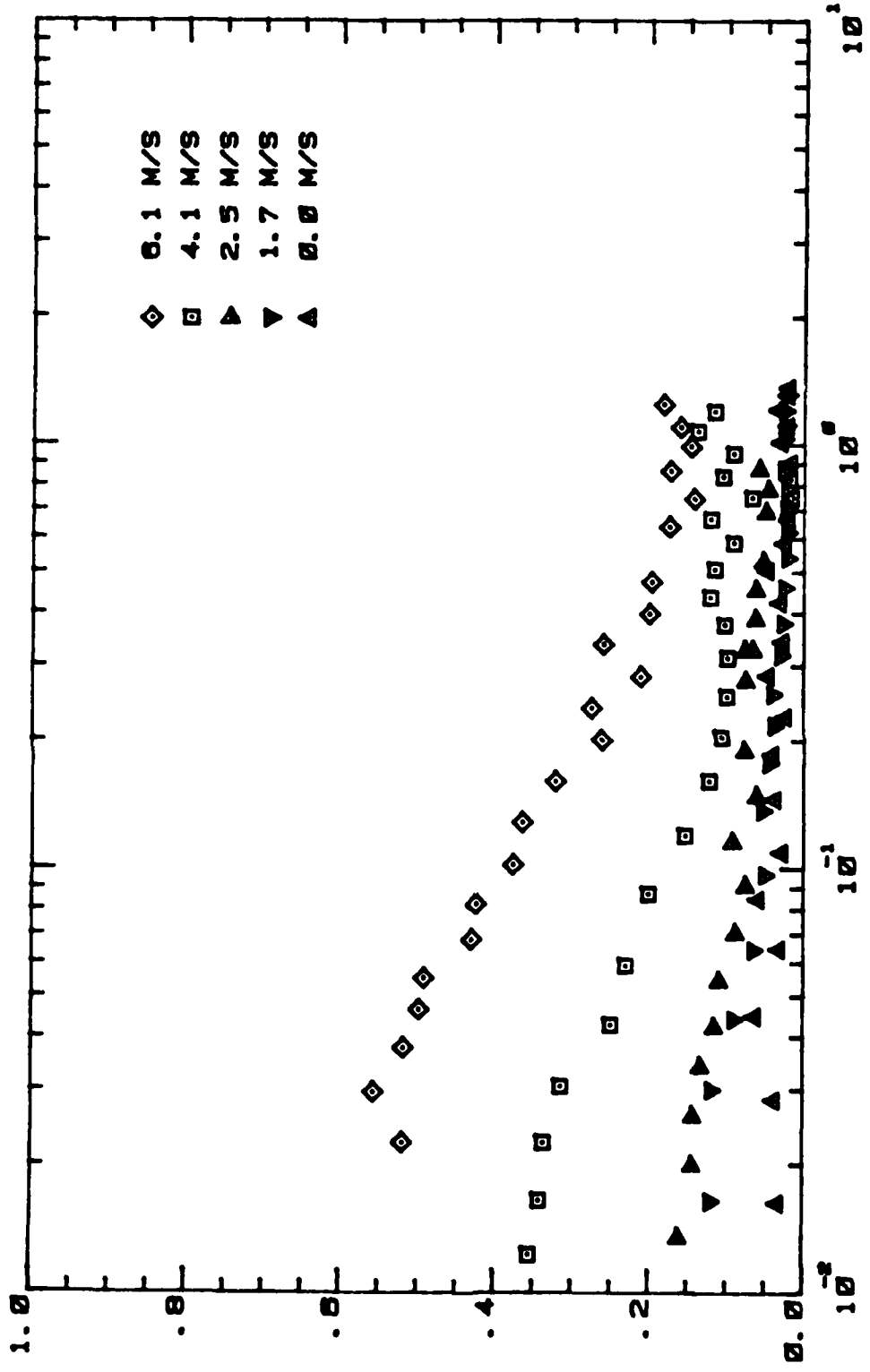

Figure 50. $\left(\overline{u'^2}\right)^{1/2}/(2\pi f_D \hat{\eta}_S/\sqrt{2})$ versus $-ky^*$.

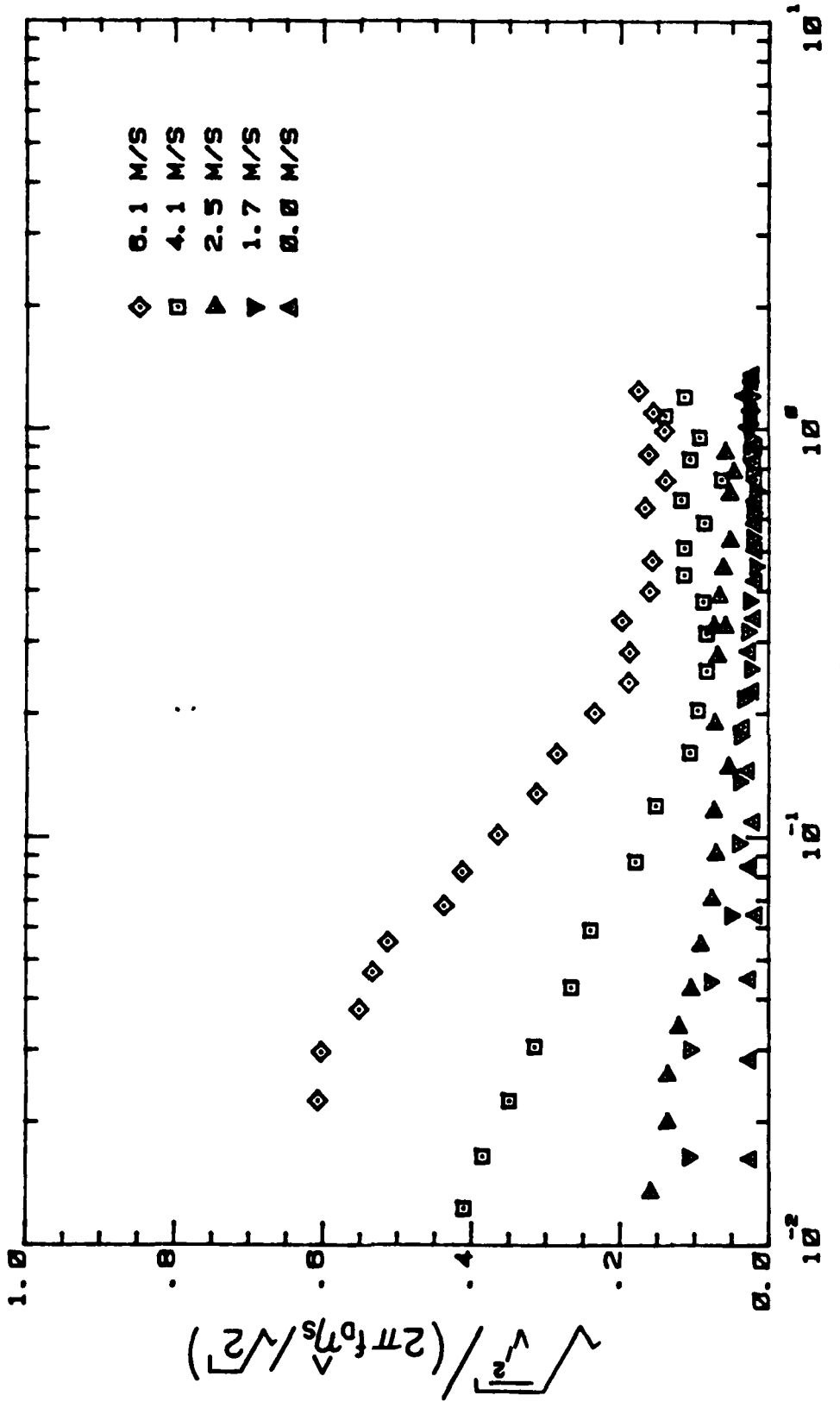

Figure 51. $\left(\overline{v'^2}\right)^{1/2}/(2\pi f_D \hat{\eta}_S/\sqrt{2})$ versus -ky*.

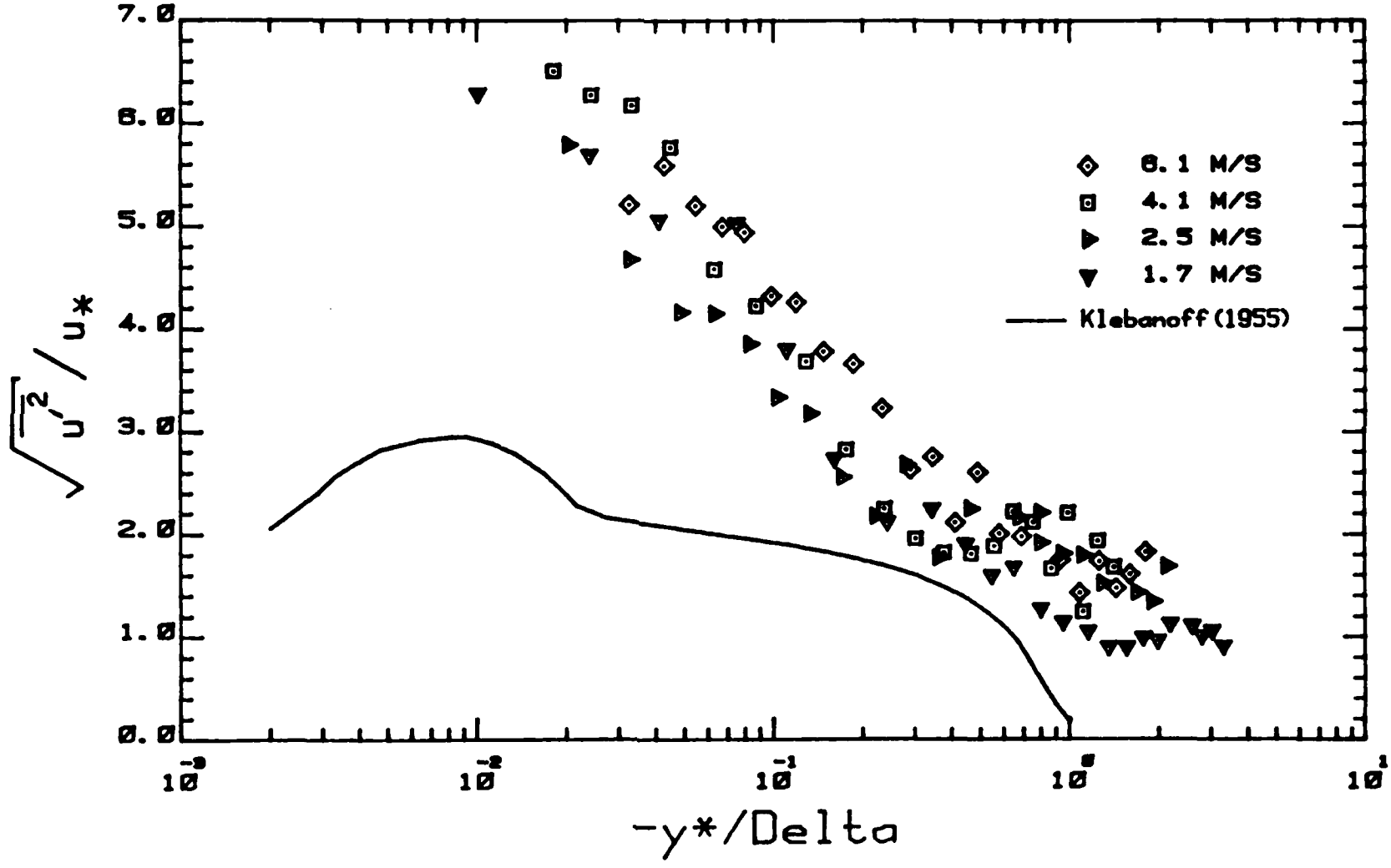

Figure 52. $(\overline{u'^2})^{1/2}/u_*$ versus $-y^*/\delta$.

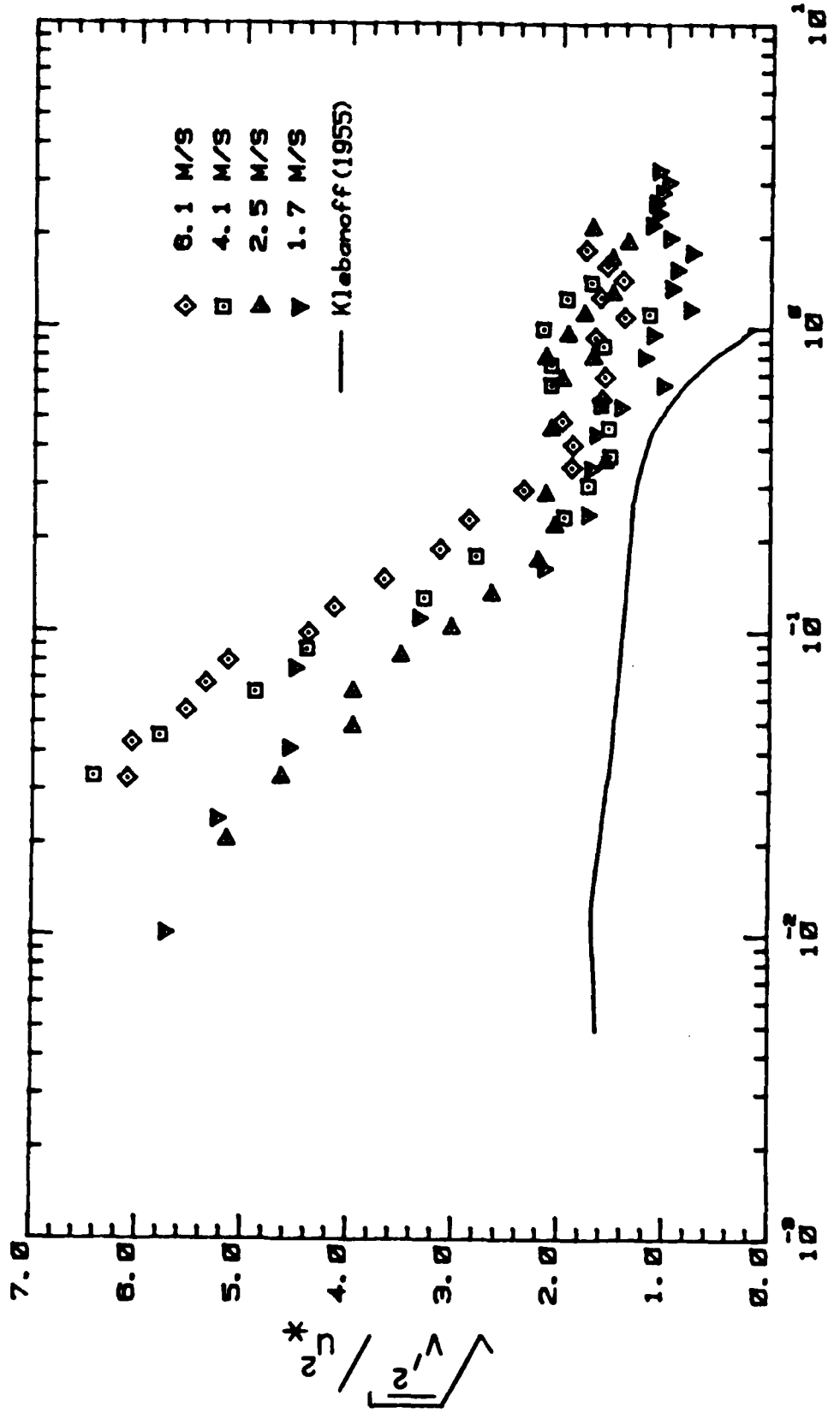

Figure 53. $\overline{(v'^2)}^{1/2}/u_*$ versus -y*/δ.

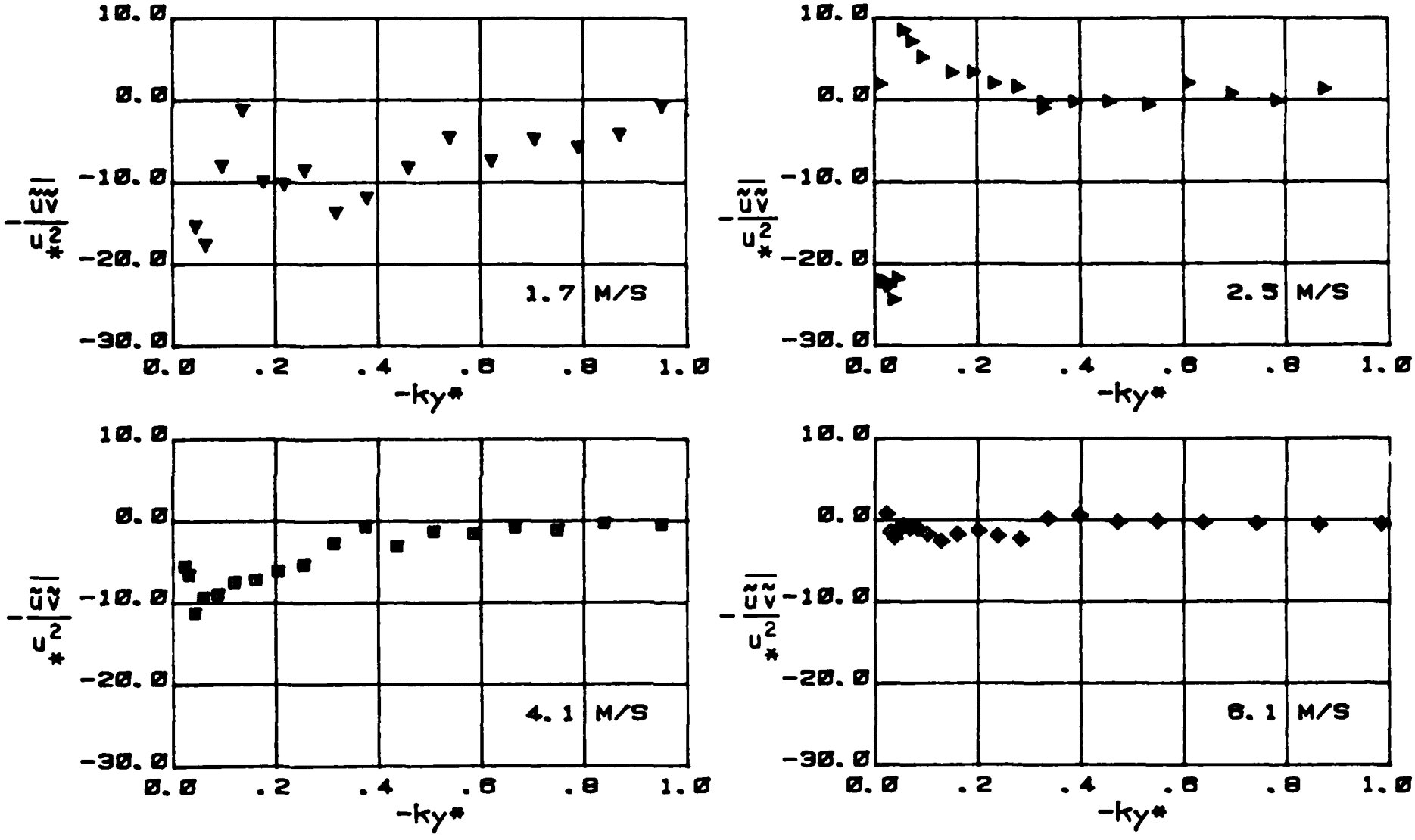

Figure 54. $-\overline{\tilde{u}\tilde{v}}/u_*^2$ versus -ky*.

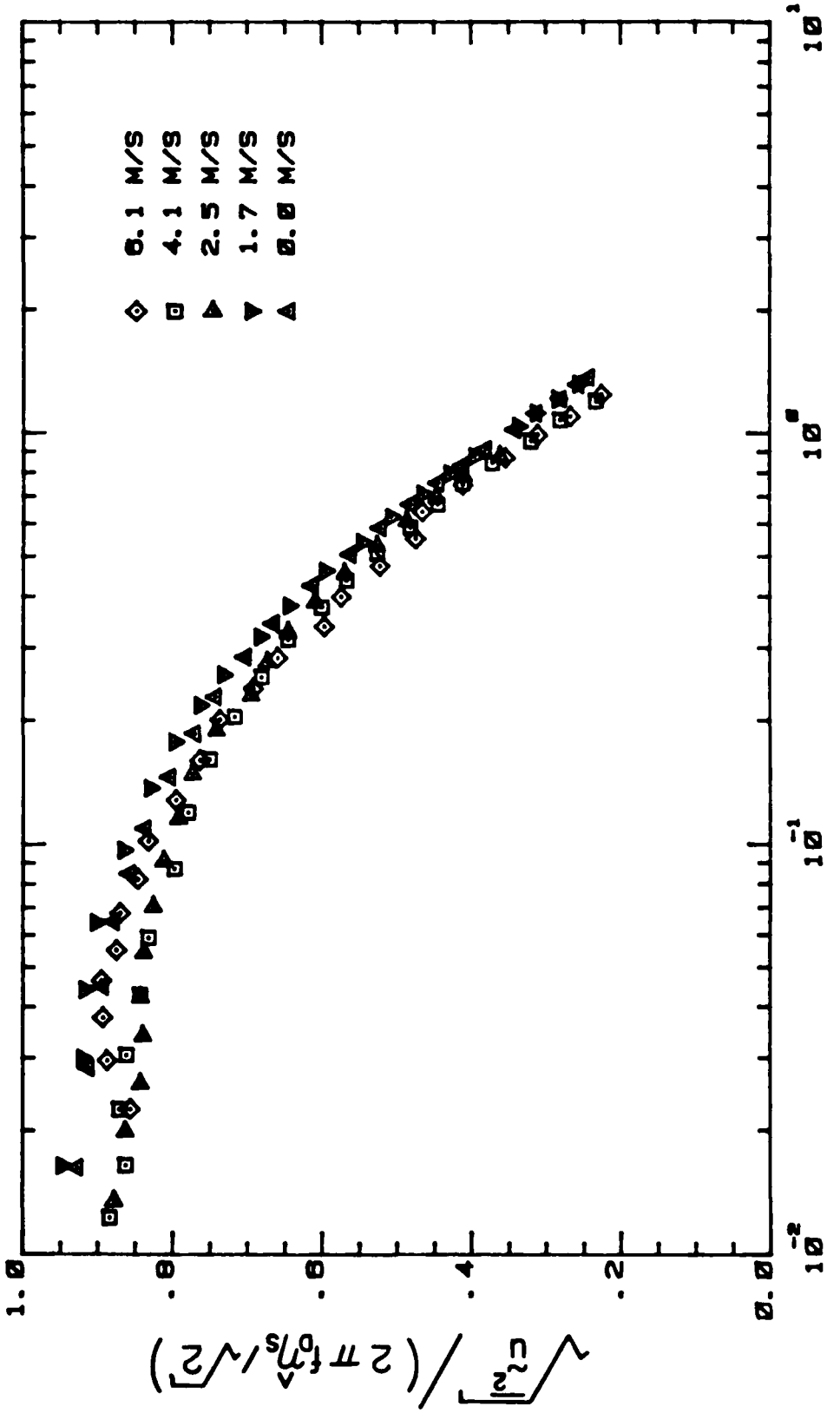

Figure 55. $(\overline{u^2})^{1/2}/(2\pi f_D \hat{\eta}_S/\sqrt{2})$ versus $-ky^*$.

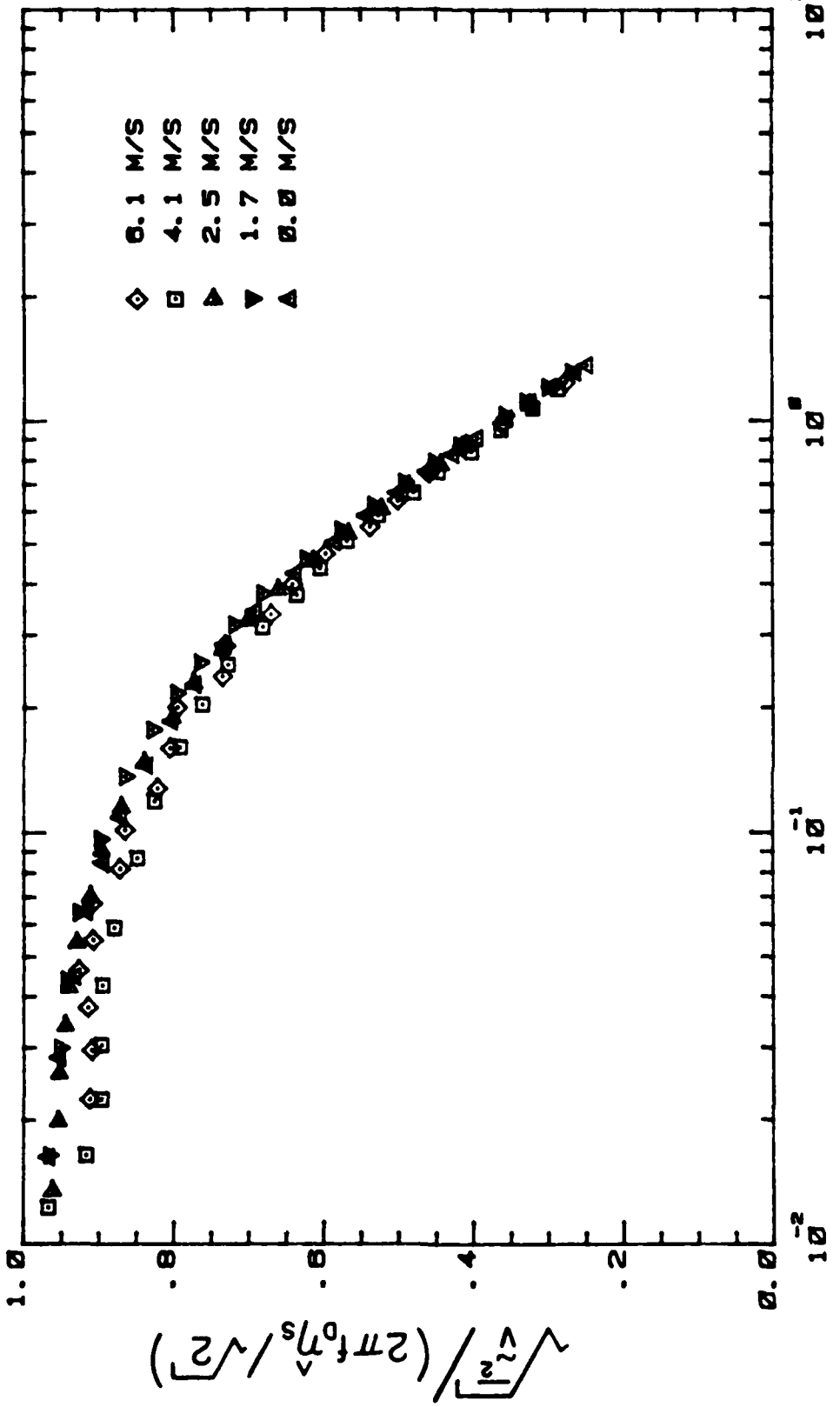

Figure 36. $(\overline{v^2})^{1/2}/(2\pi f_D \hat{\eta}_S/\sqrt{2})$ versus $-ky^*$.

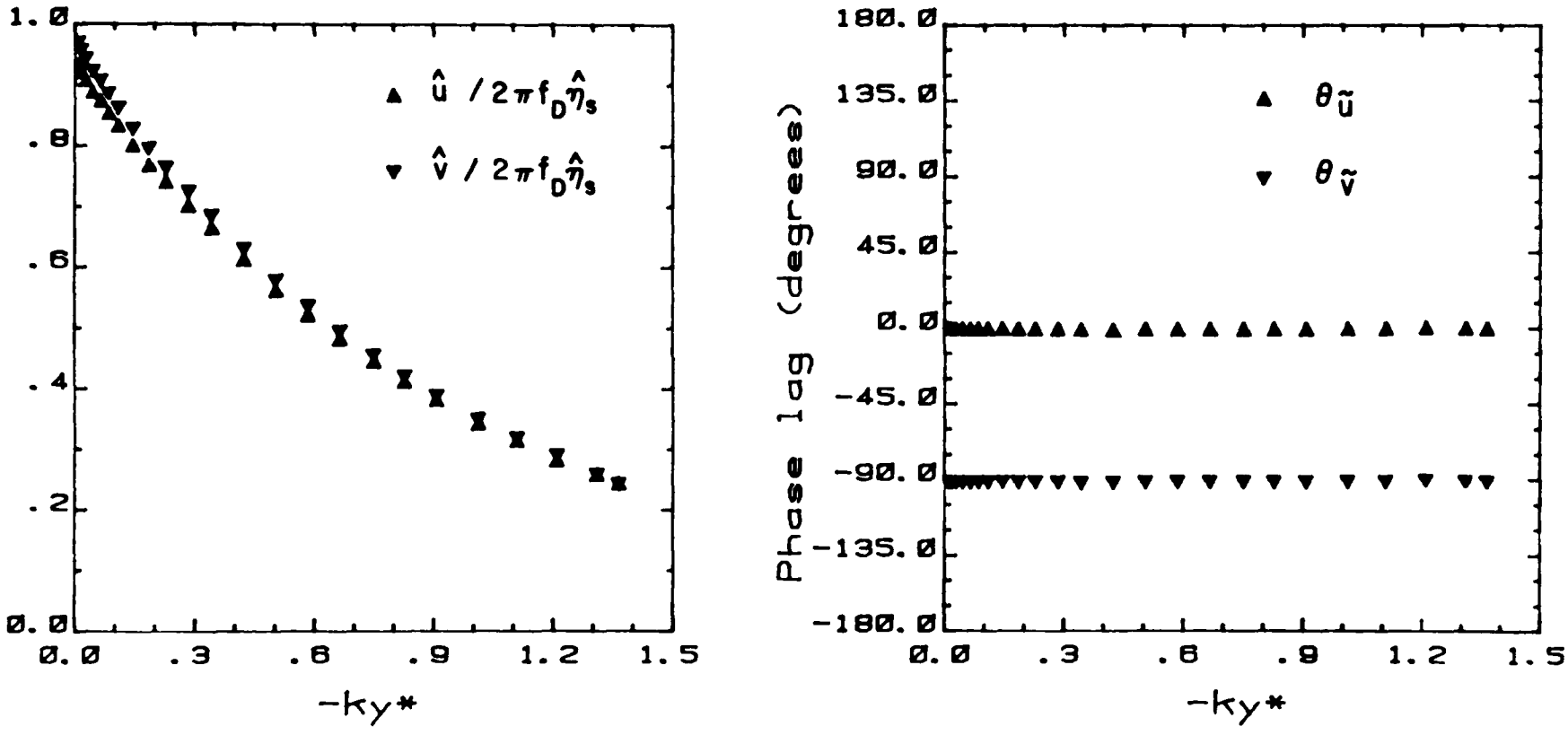

(a) u_∞ = 0.0 m/s

Figure 57. Amplitude and phase distributions of $\tilde{u}$ and $\tilde{v}$ with -ky* (MW-WF-EF).

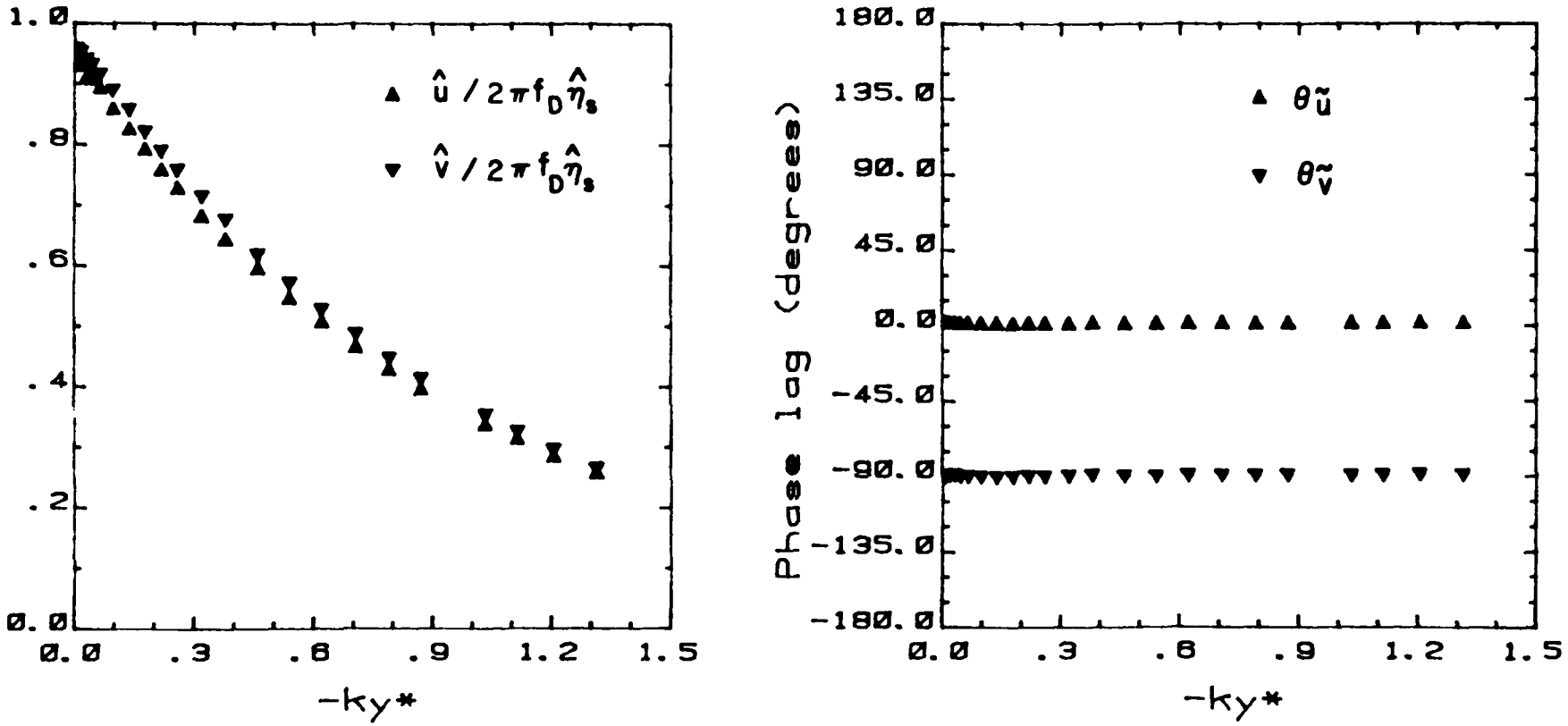

(b) u_∞ = 1.7 m/s

Figure 57. Amplitude and phase distributions of $\tilde{u}$ and $\tilde{v}$ with -ky* (MW-WF-EF).

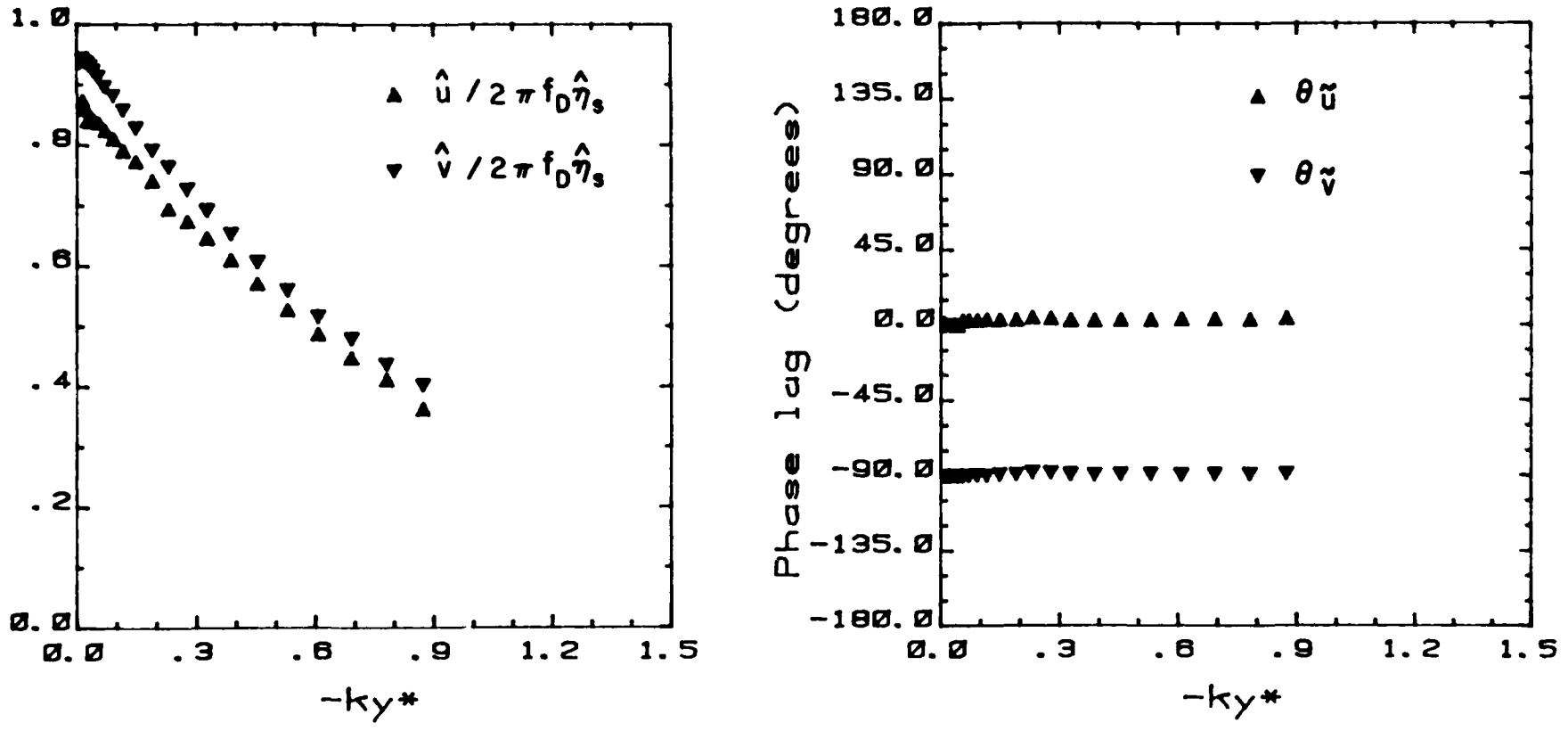

(c) u_∞ = 2.5 m/s

Figure 57. Amplitude and phase distributions of $\tilde{u}$ and $\tilde{v}$ with -ky* (MW-WF-EF).

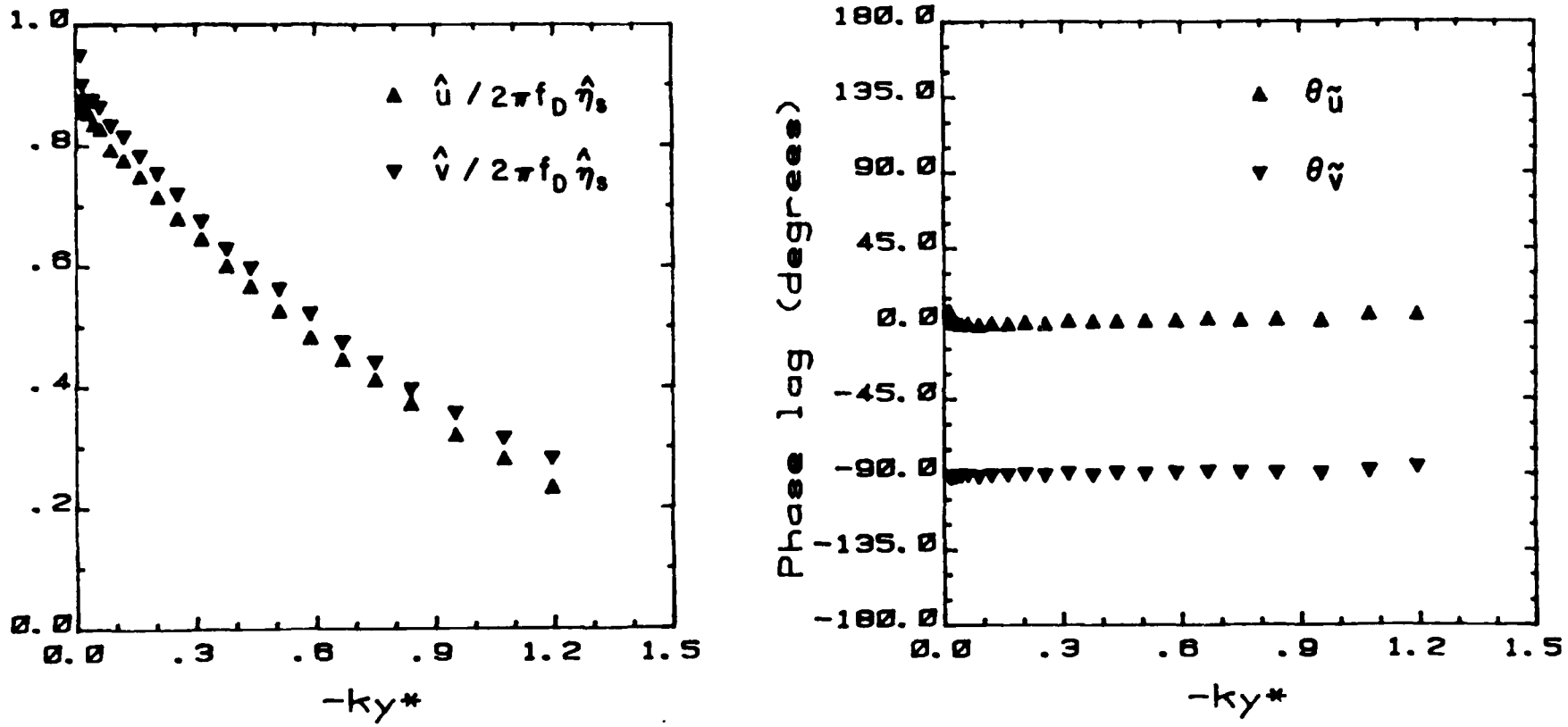

(d) u_∞ = 4.1 m/s

Figure 57. Amplitude and phase distributions of $\tilde{u}$ and $\tilde{v}$ with -ky* (MW-WF-EF).

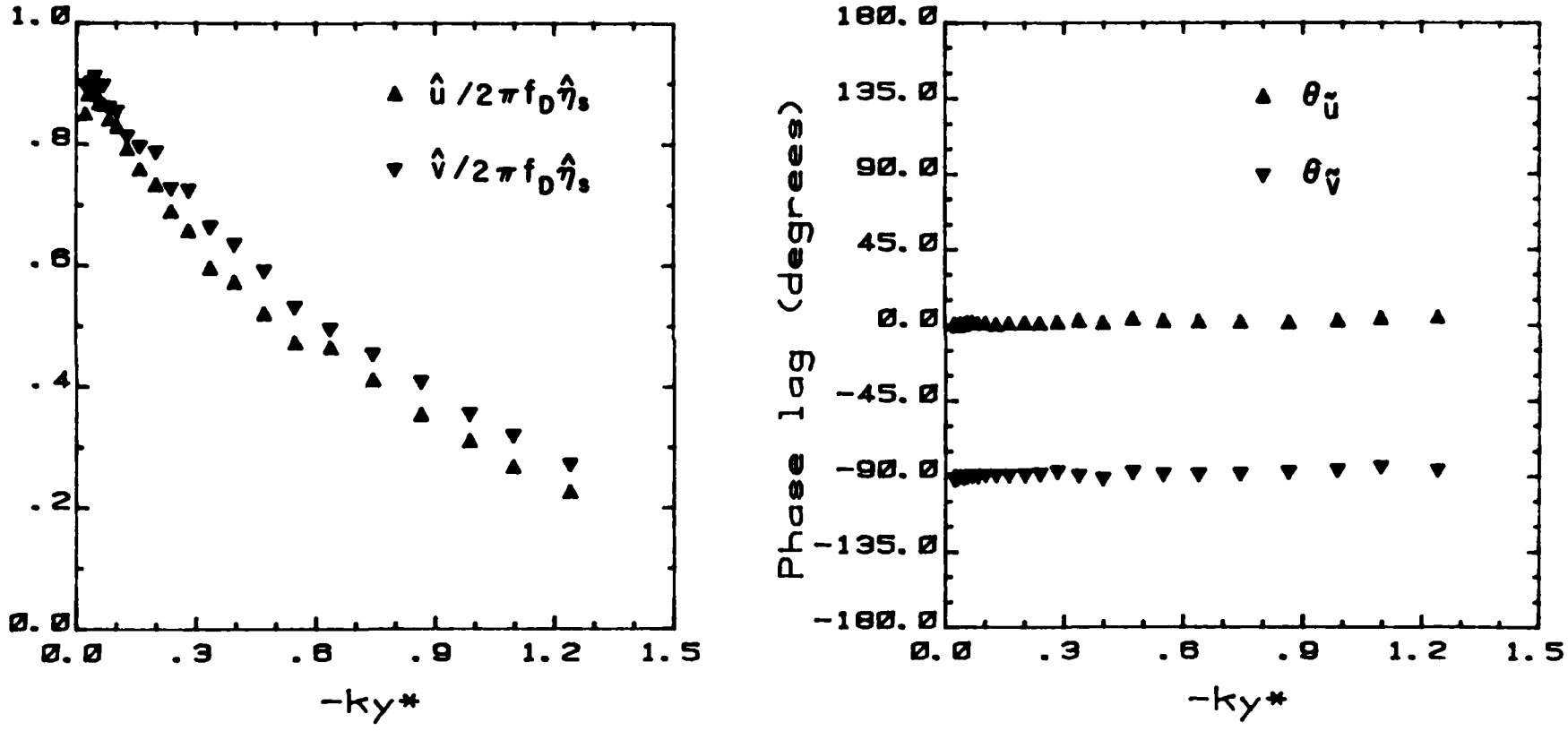

(e) u_∞ = 6.1 m/s

Figure 57. Amplitude and phase distributions of $\tilde{u}$ and $\tilde{v}$ with -ky* (MW-WF-EF).

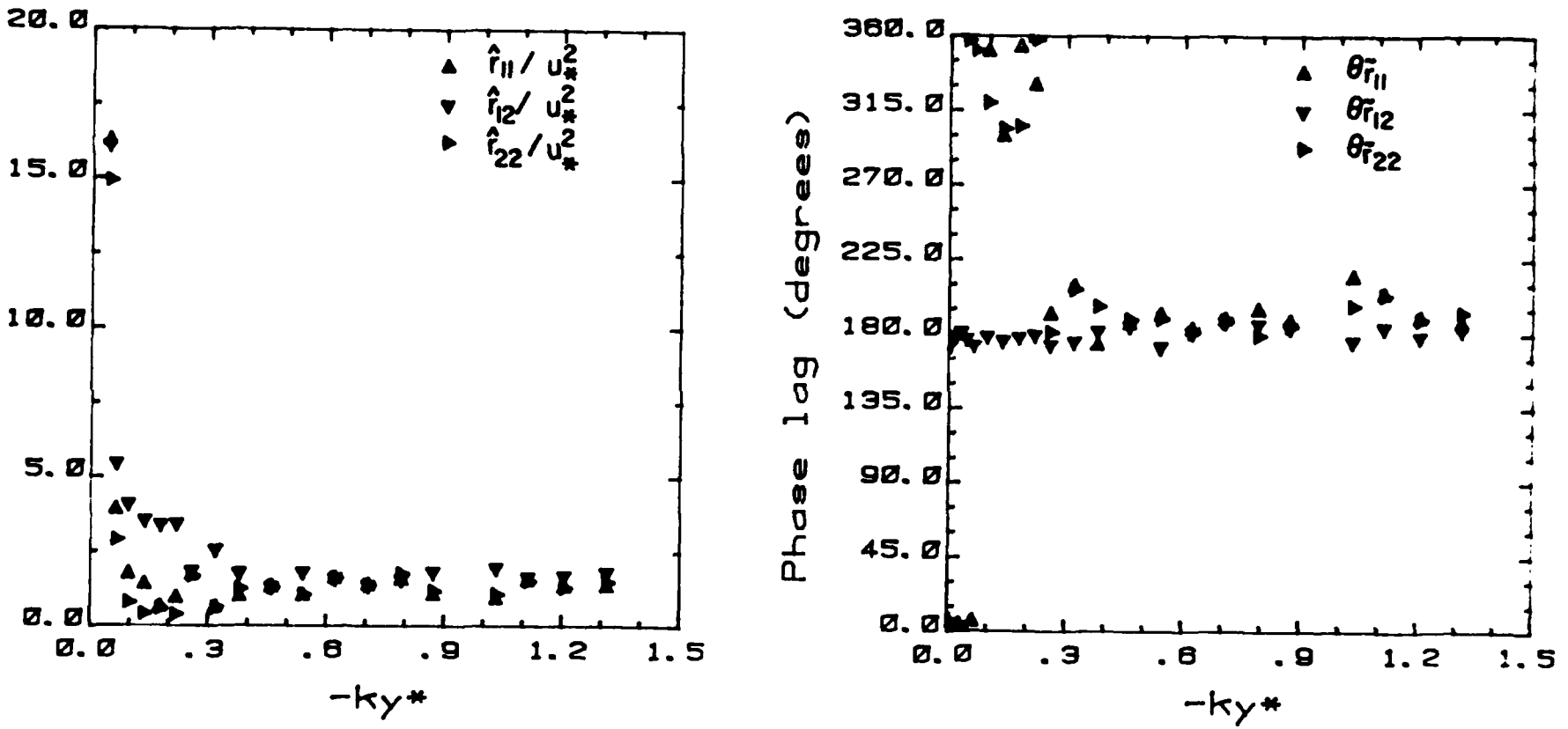

(a) u_∞ = 1.7 m/s

Figure 58. Amplitude and phase distributions of $\tilde{r}_{ij}$ with -ky* (MW-WF-EF).

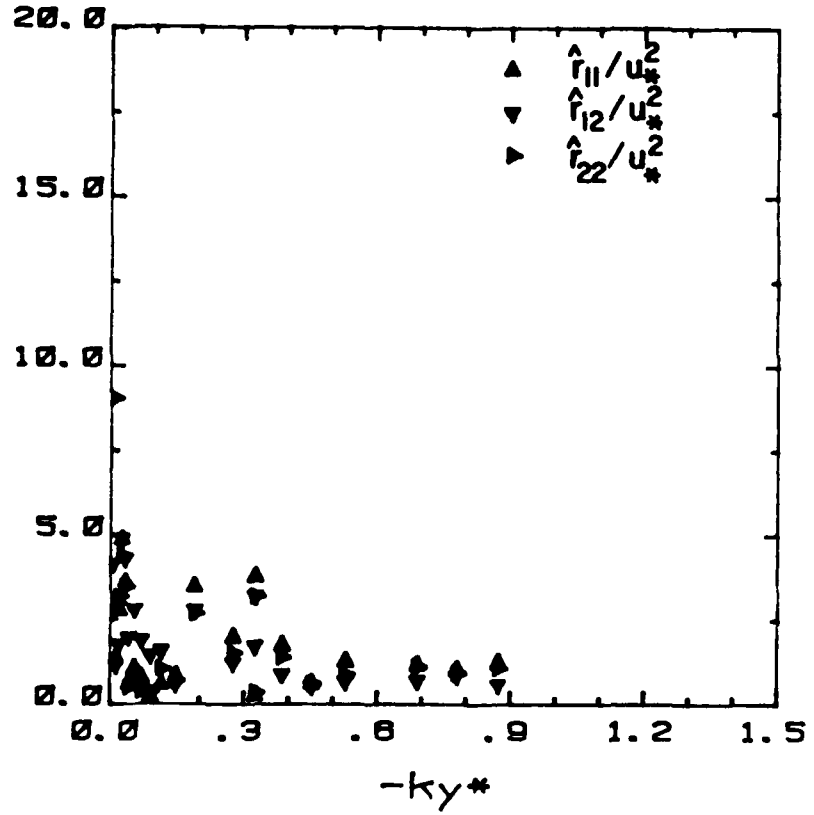

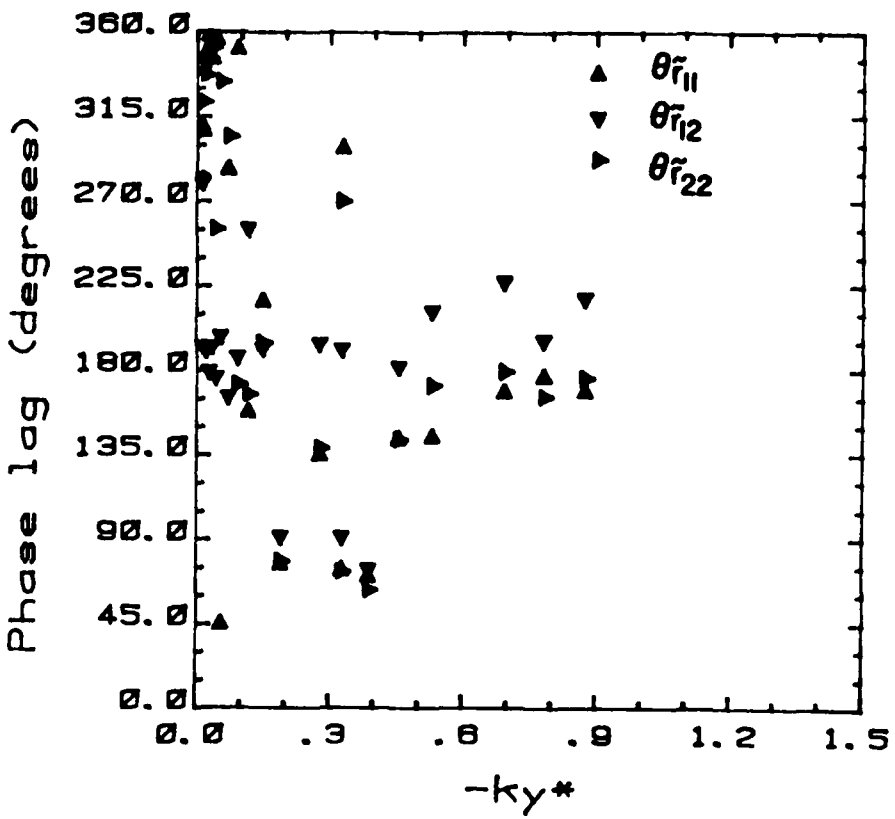

(b) u_∞ = 2.5 m/s

Figure 58. Amplitude and phase distributions of $\tilde{r}_{ij}$ with -ky* (MW-WF-EF).

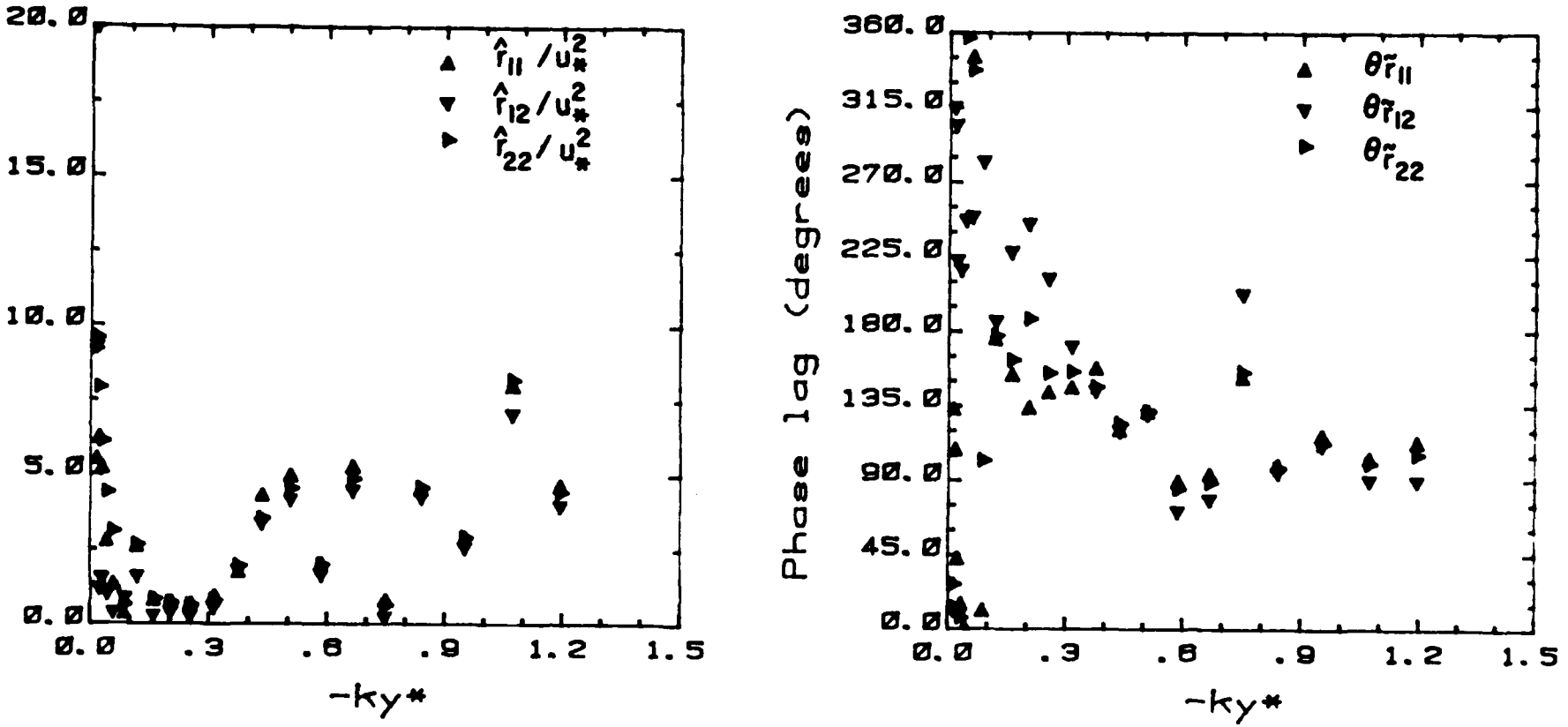

(c) u_∞ = 4.1 m/s

Figure 58. Amplitude and phase distributions of $\tilde{r}_{ij}$ with -ky* (MW-WF-EF).

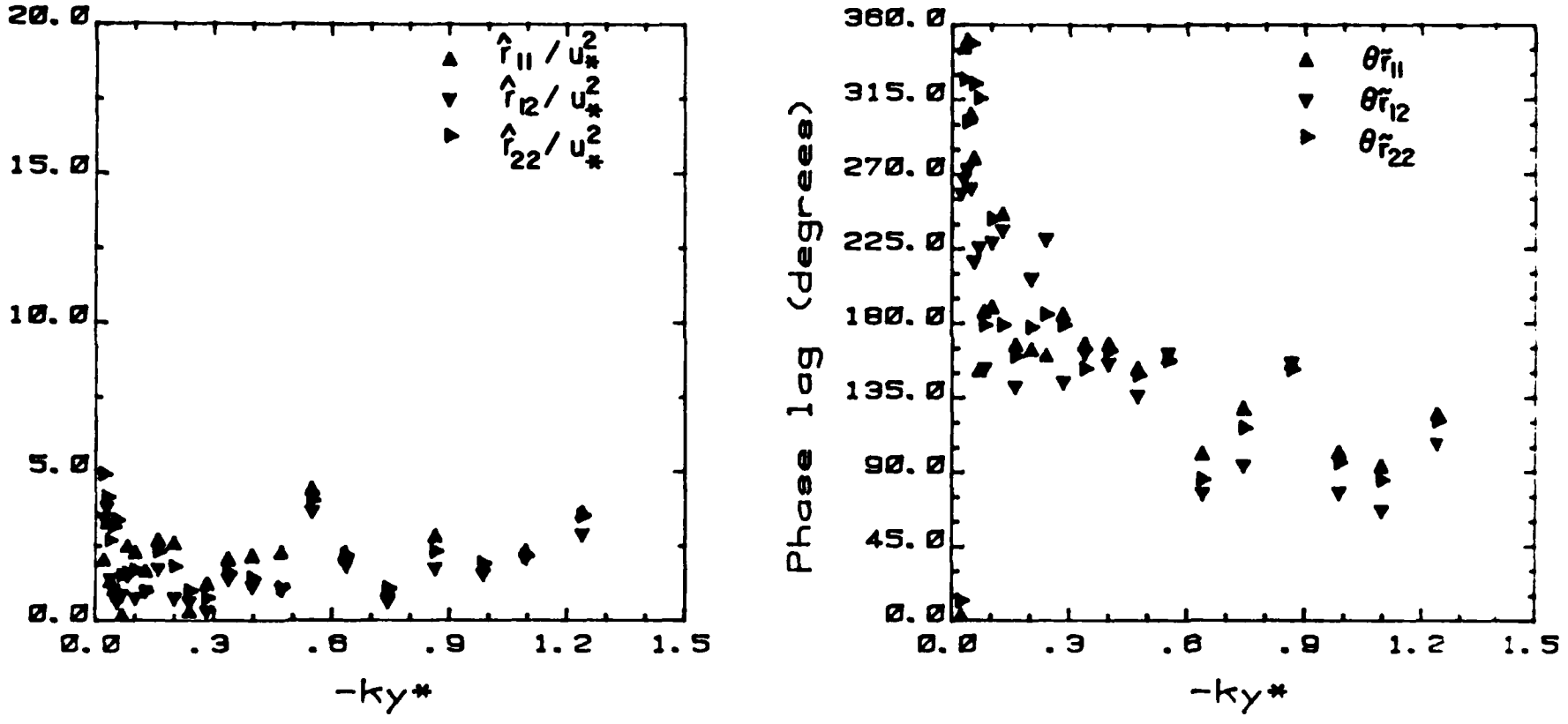

(d) u_∞ = 6.1 m/s

Figure 58. Amplitude and phase distributions of $\tilde{r}_{ij}$ with -ky* (MW-WF-EF).

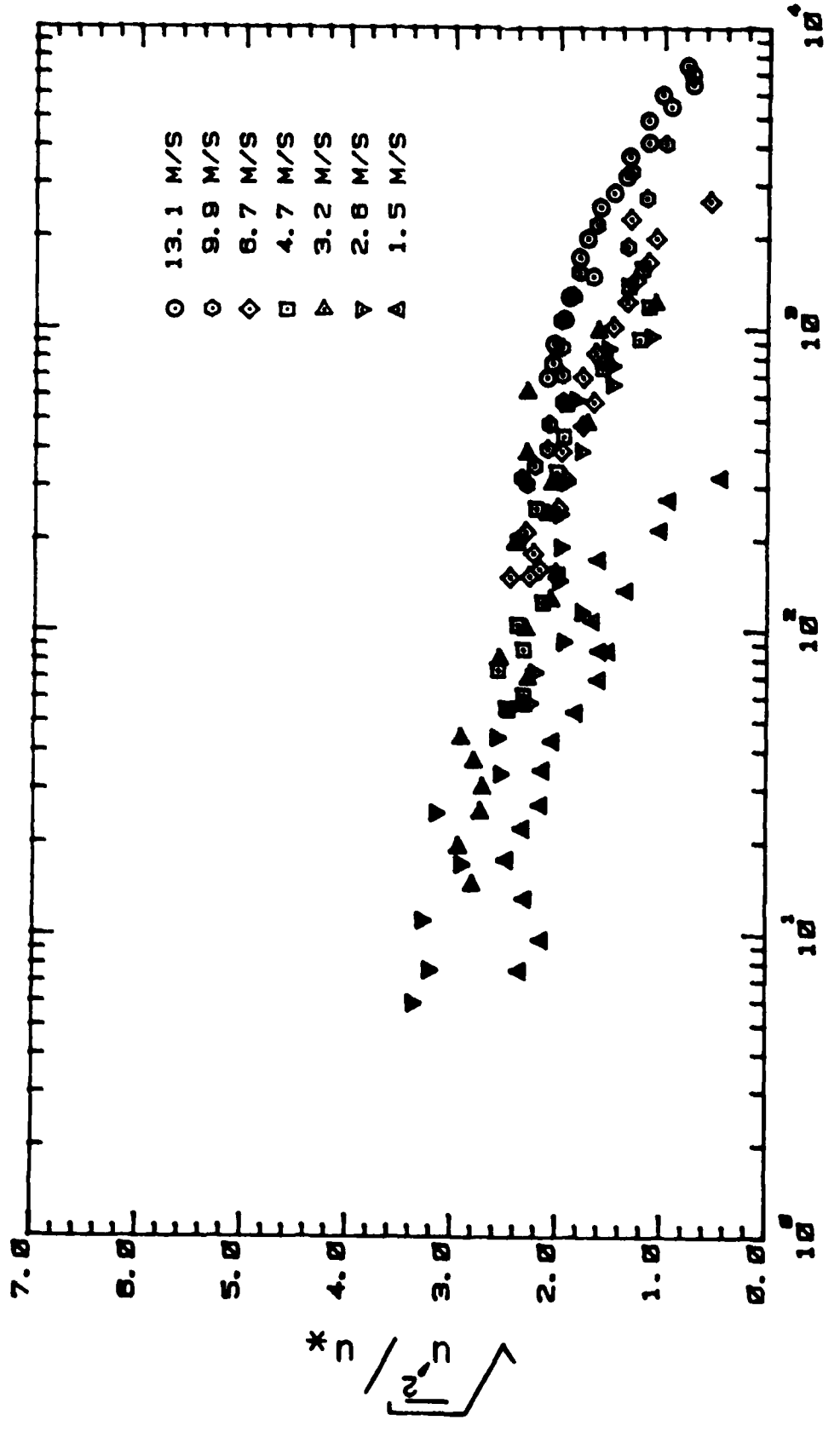

Figure 59. $\overline{(u'^2)}^{1/2}/u_*$ versus $-y^+$ (WW-EF).

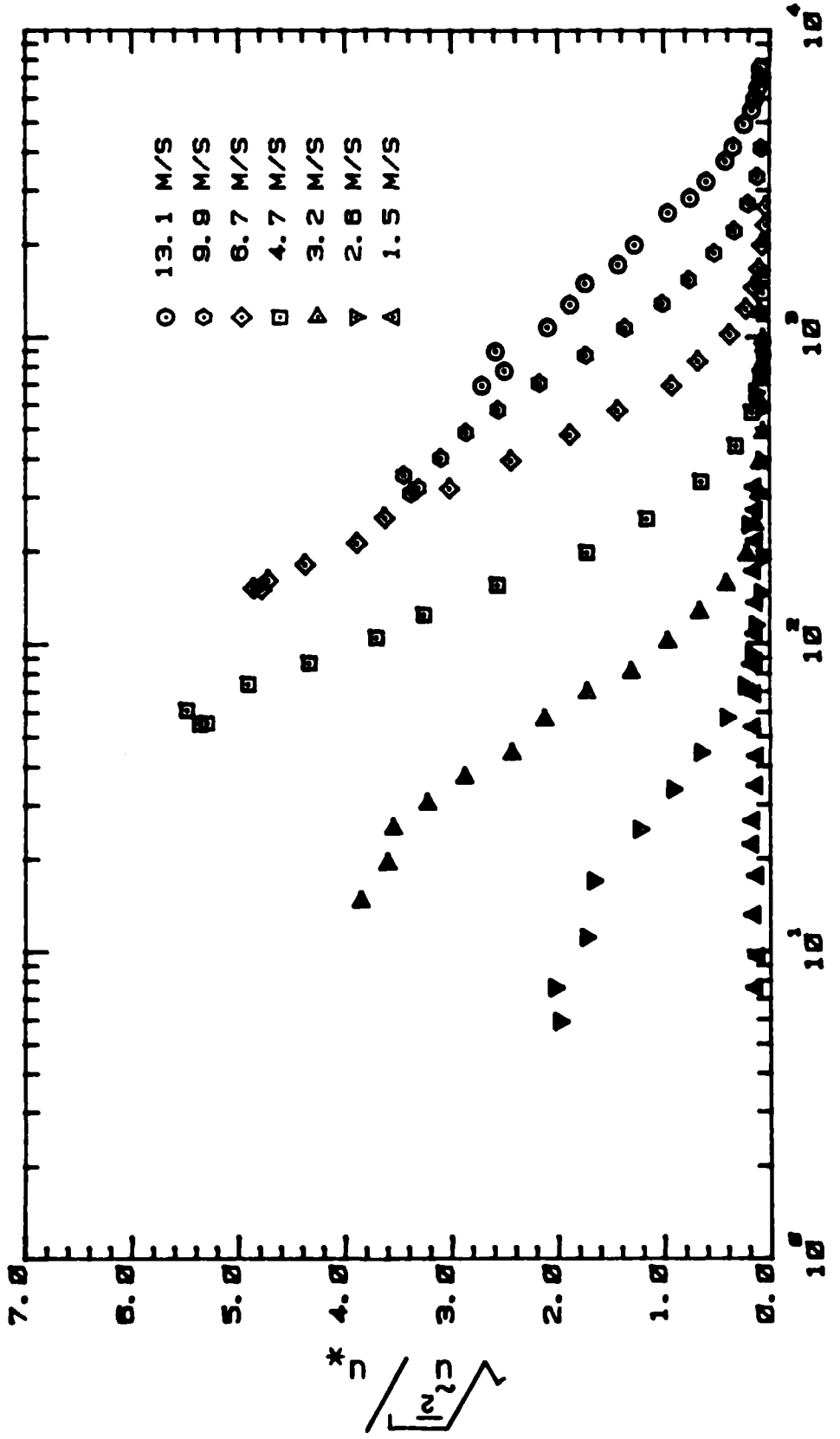

Figure 60. $(\overline{u^2})^{1/2}/u_*$ versus $-y^+$ (WW-EF).

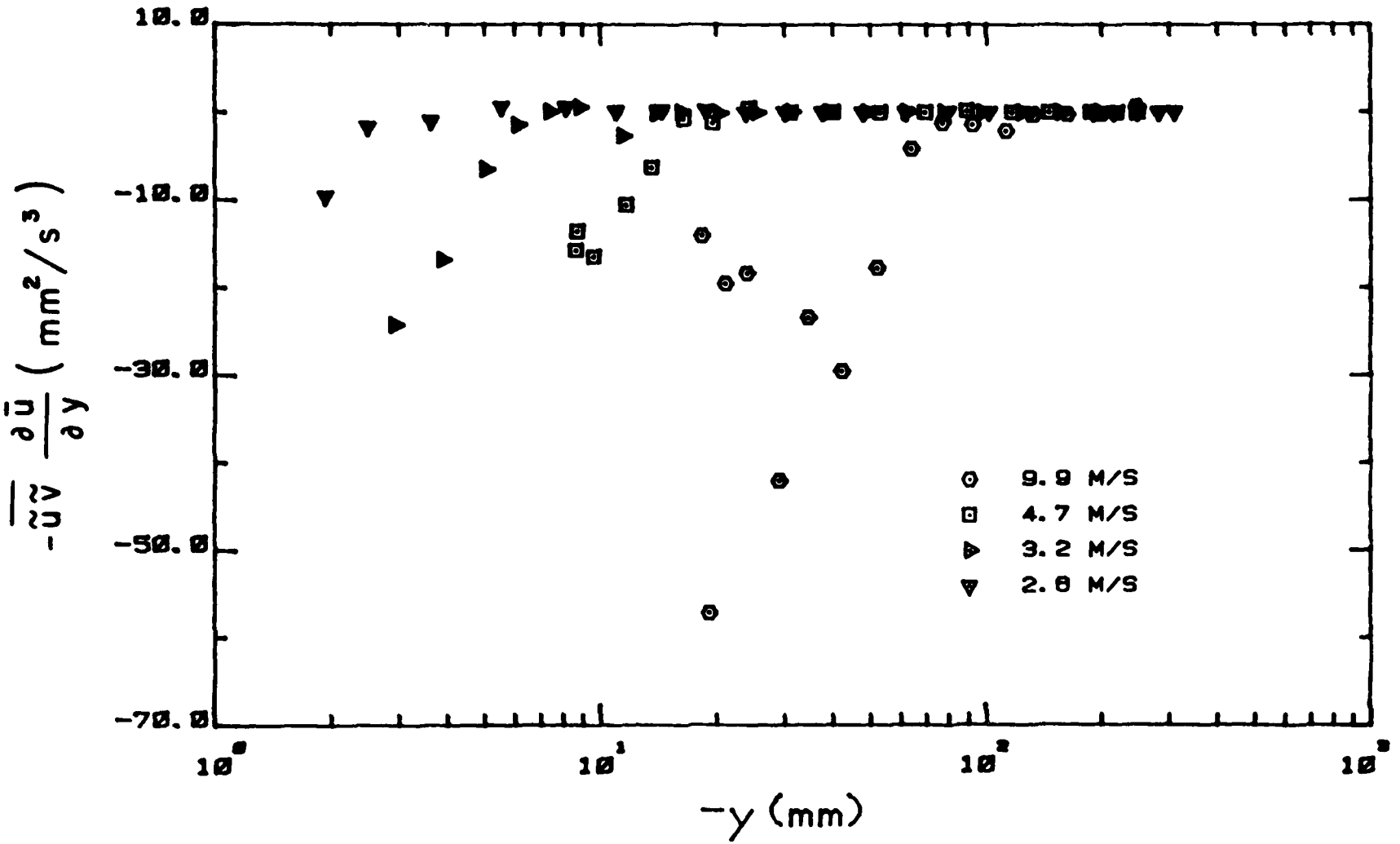

Figure 61. (a) $-\overline{\tilde{u}\tilde{v}}\ \partial\bar{u}/\partial y$ profiles in physical units (WW-EF).

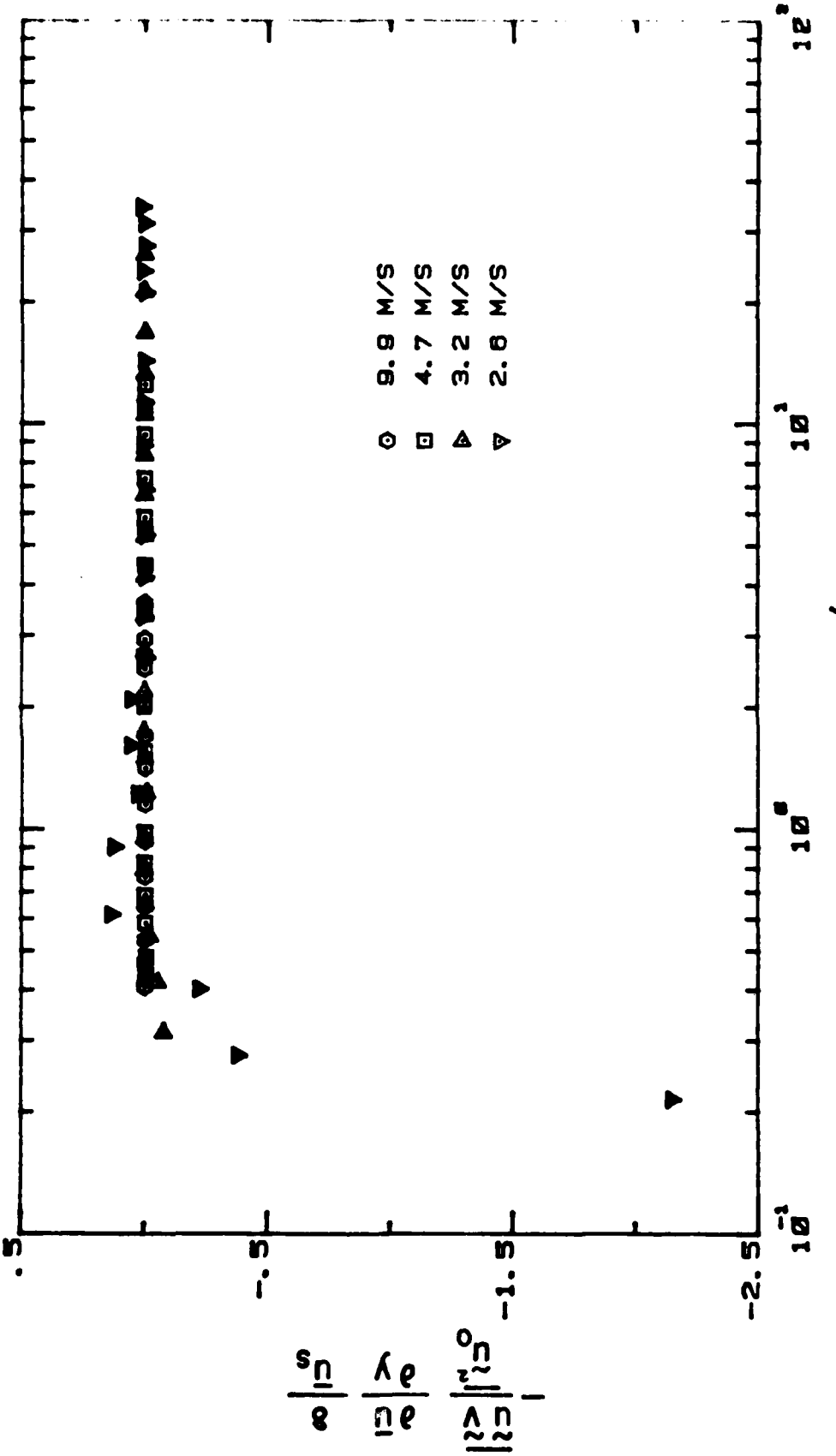

Figure 61. (b) $-\overline{uv}\ \partial\bar{u}/\partial y$ profiles in dimensionless units (WW-EF).

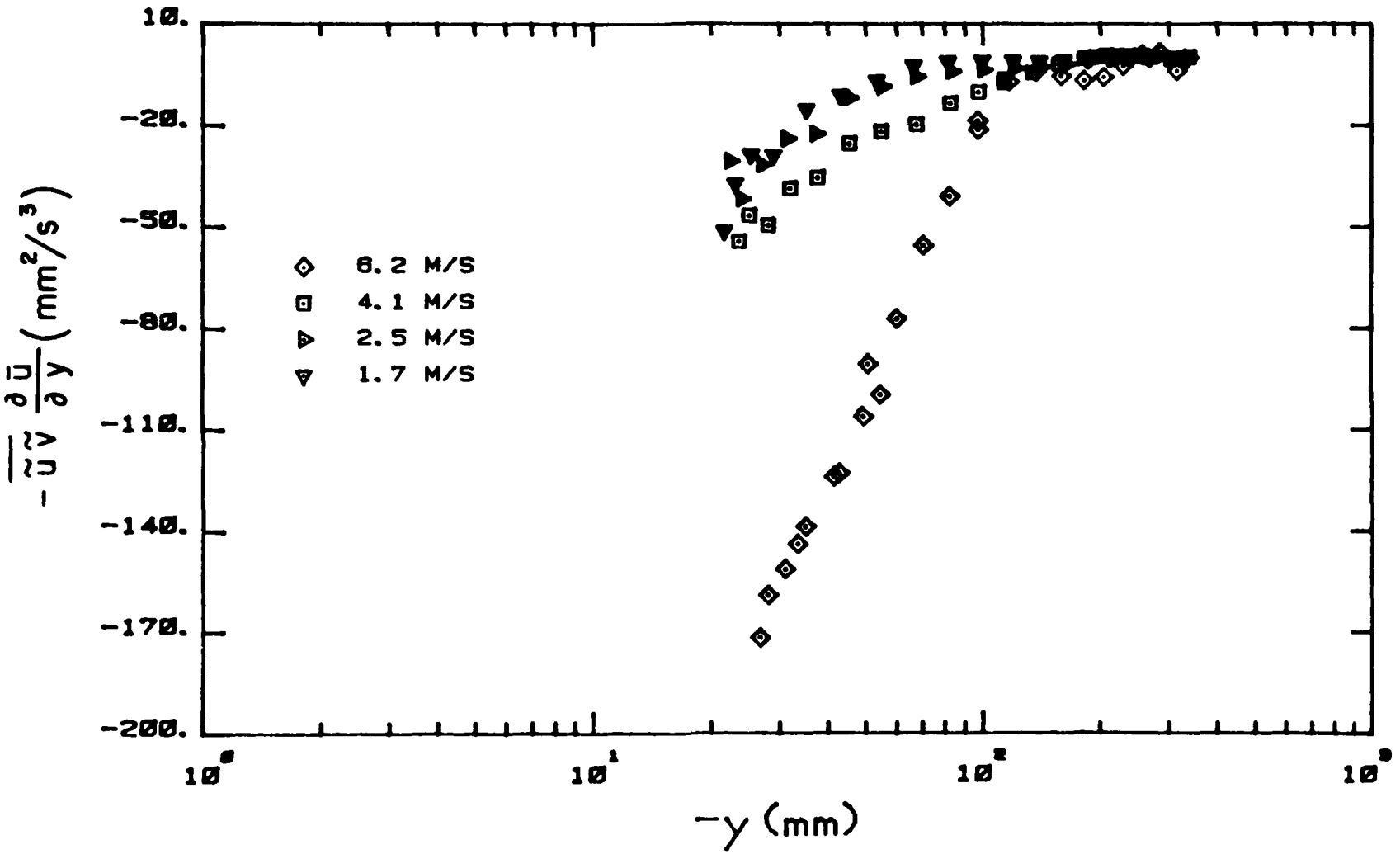

Figure 62. (a) $-\overline{\tilde{u}\tilde{v}}\ \partial\bar{u}/\partial y$ profiles in physical units (MW-EF).

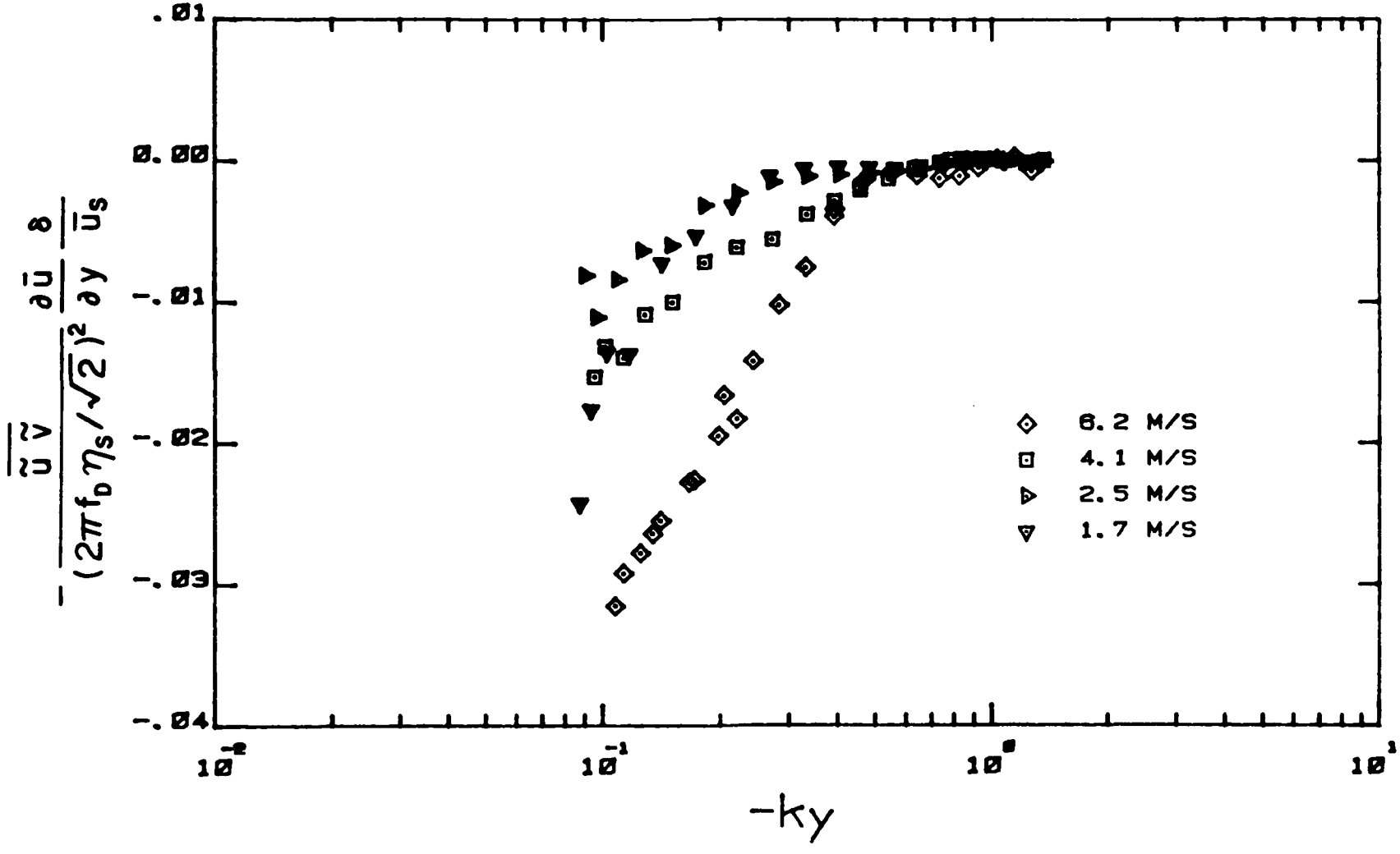

Figure 62. (b) $-\overline{\tilde{u}\tilde{v}}\ \partial\bar{u}/\partial y$ profiles in dimensionless units (MW-EF).

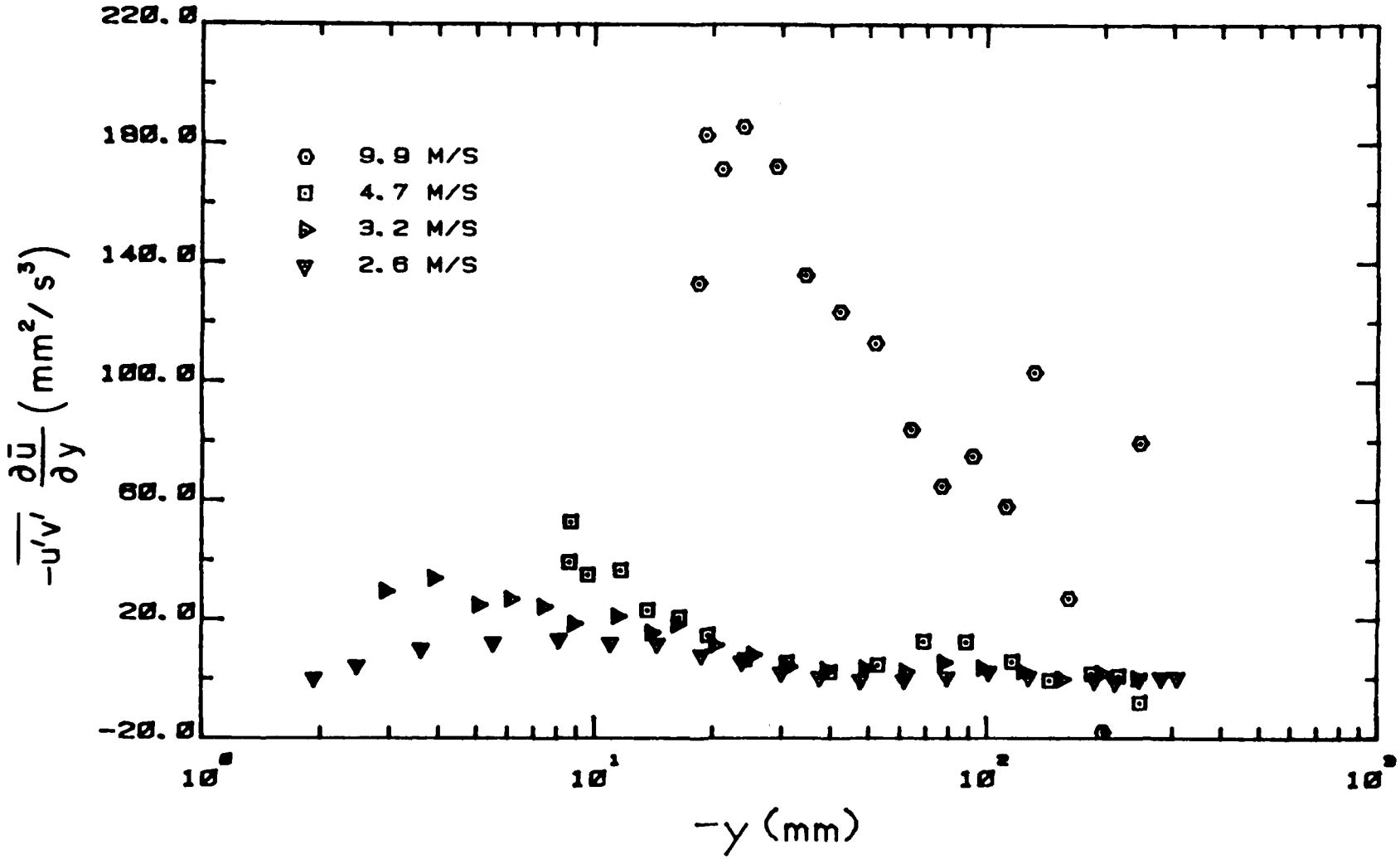

Figure 63. (a) $-\overline{u'v'}\ \partial\bar{u}/\partial y$ profiles in physical units (WW-EF).

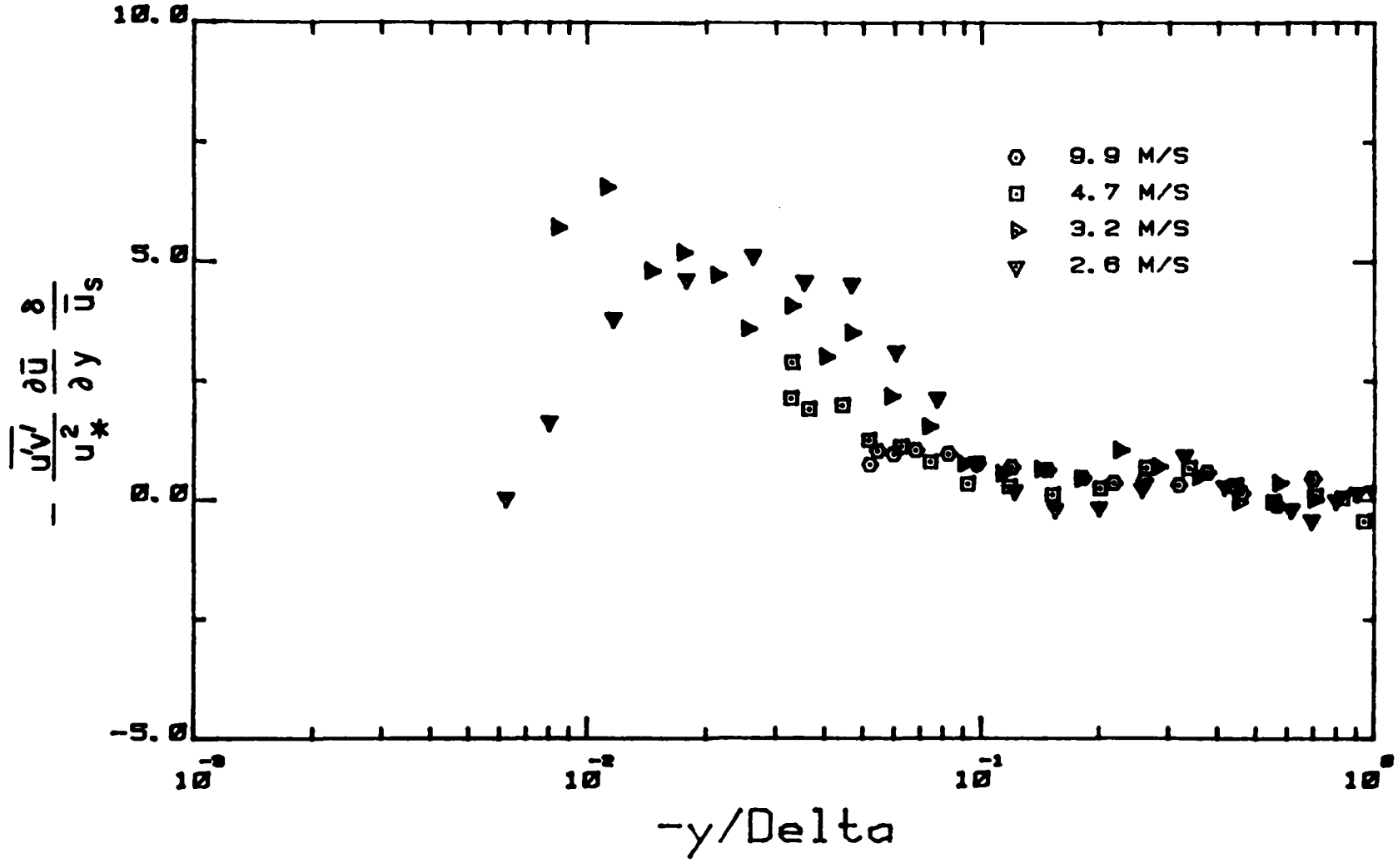

Figure 63. (b) $-\overline{u'v'}\,\partial\bar{u}/\partial y$ profiles in dimensionless units (WW-EF).

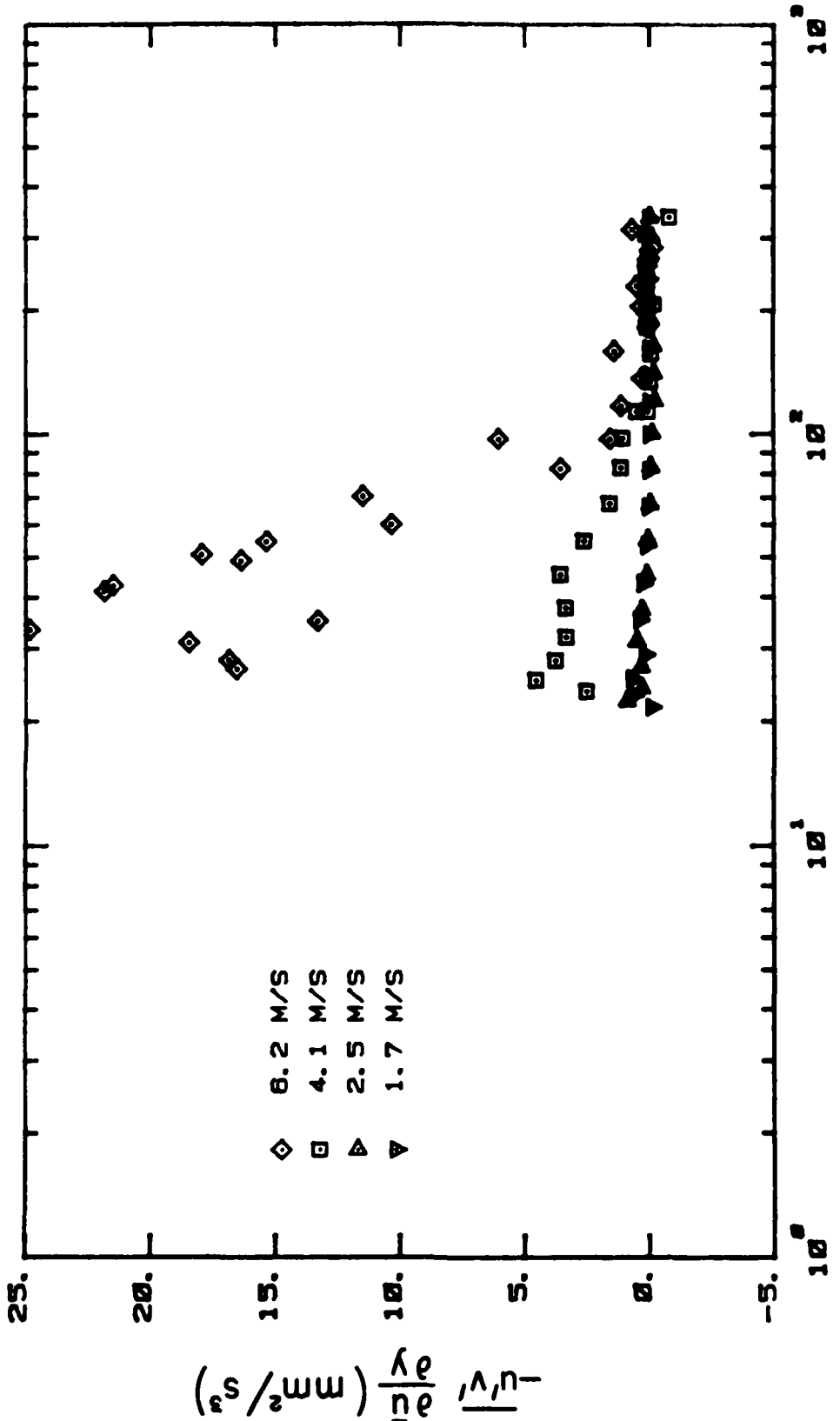

Figure 64. (a) $-\overline{u'v'}\ \partial\bar{u}/\partial y$ profiles in physical units (NW-EF).

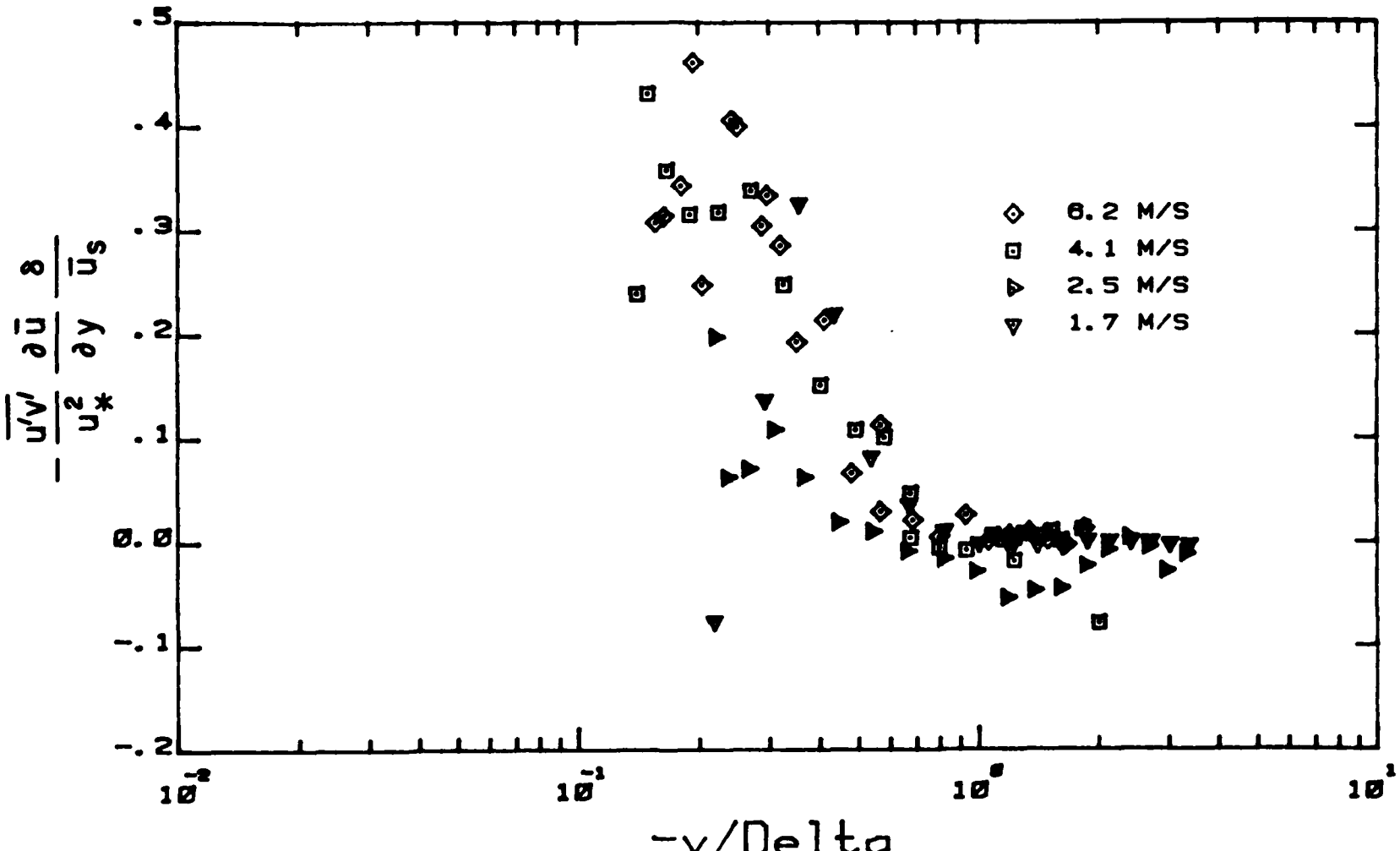

Figure 64. (b) $-\overline{u'v'}\ \partial\bar{u}/\partial y$ profiles in dimensionless units (MW-EF).

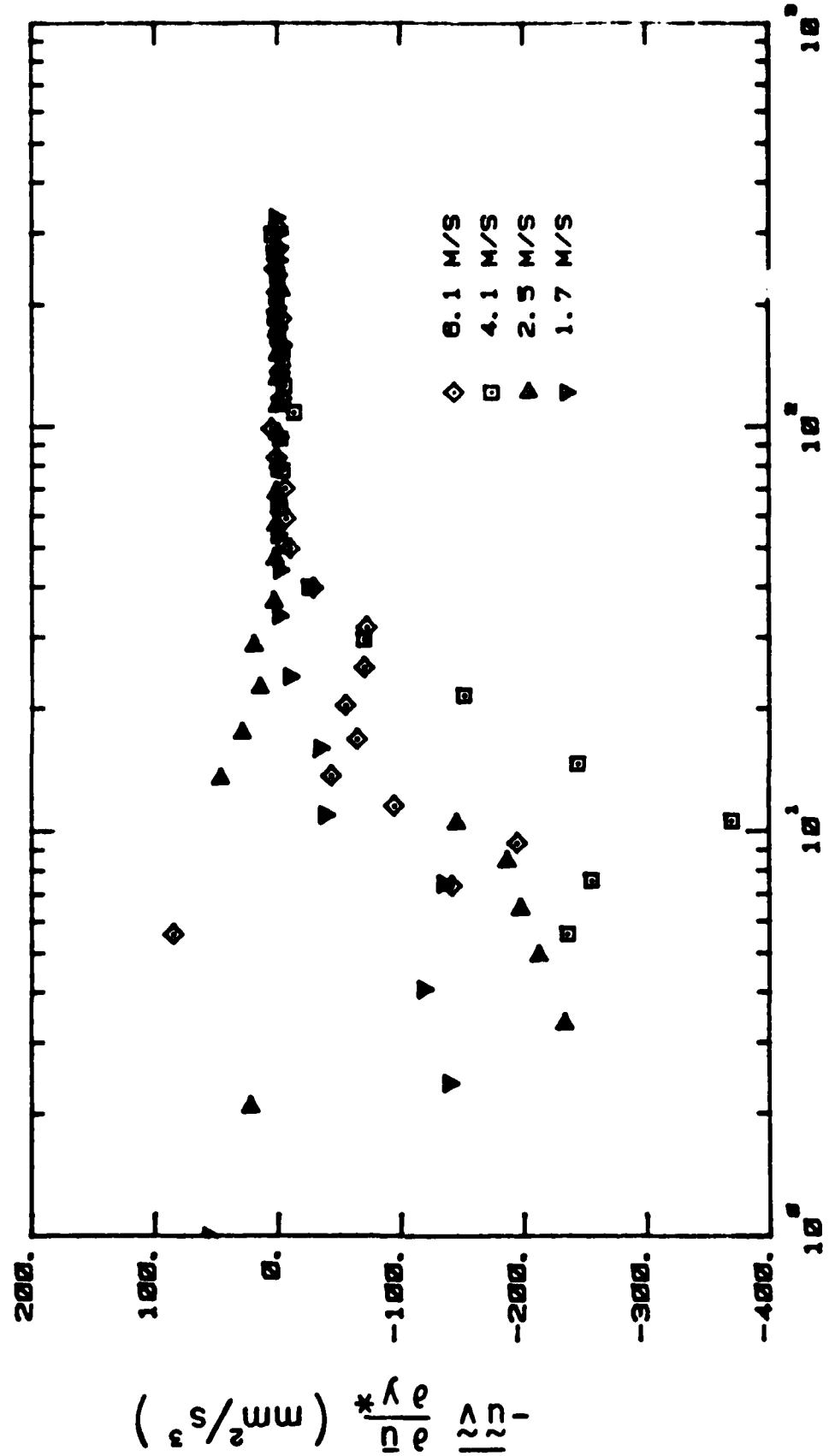

Figure 65. (a) $-\overline{\tilde{u}\tilde{v}}\ \partial\overline{u}/\partial y^*$ profiles in physical units (MW-WF-EF).

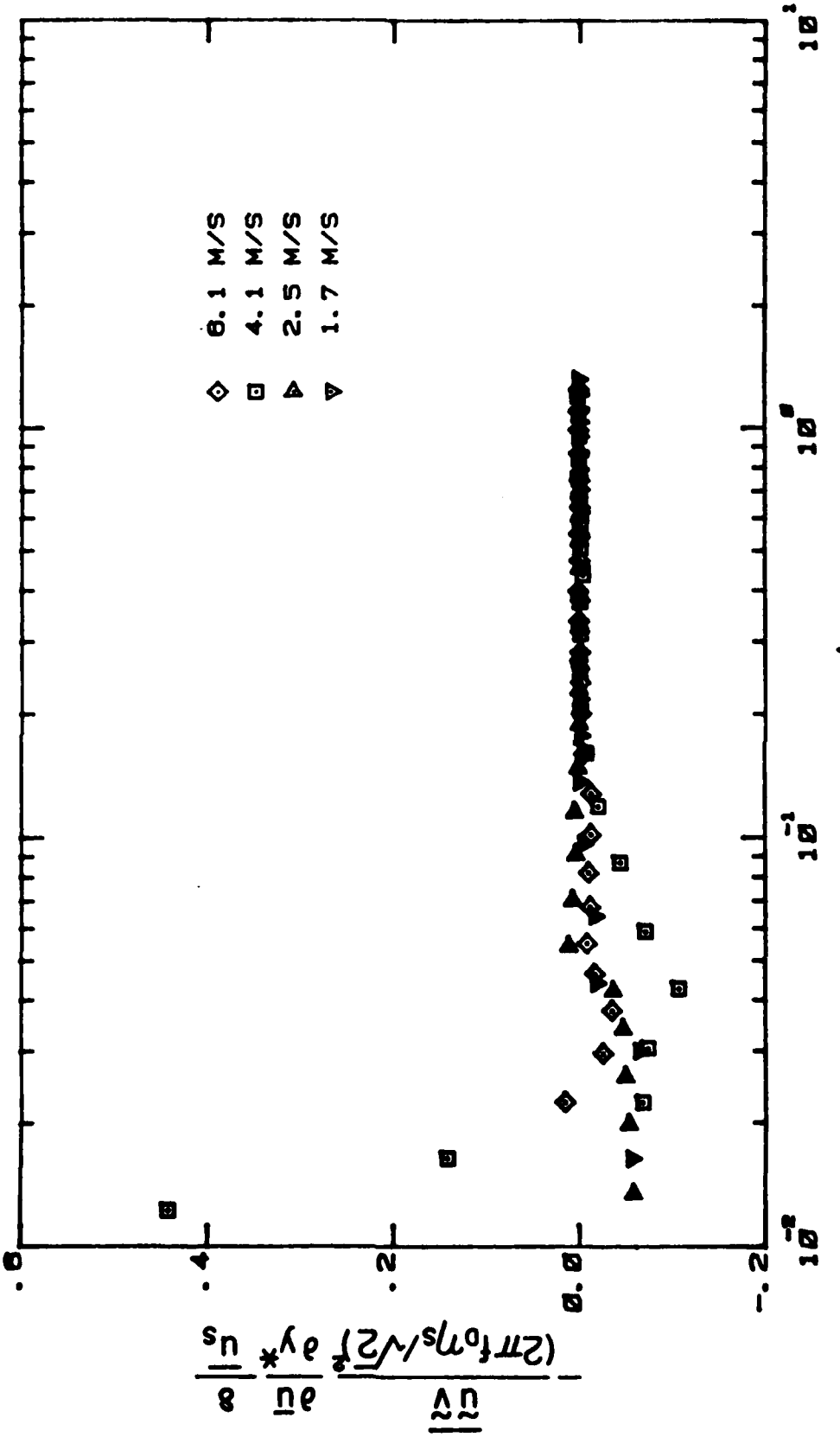

Figure 65. (b) $-\overline{\tilde{u}\tilde{v}}\ \partial\bar{u}/\partial y^*$ profiles in dimensionless units (MW-WF-EF).

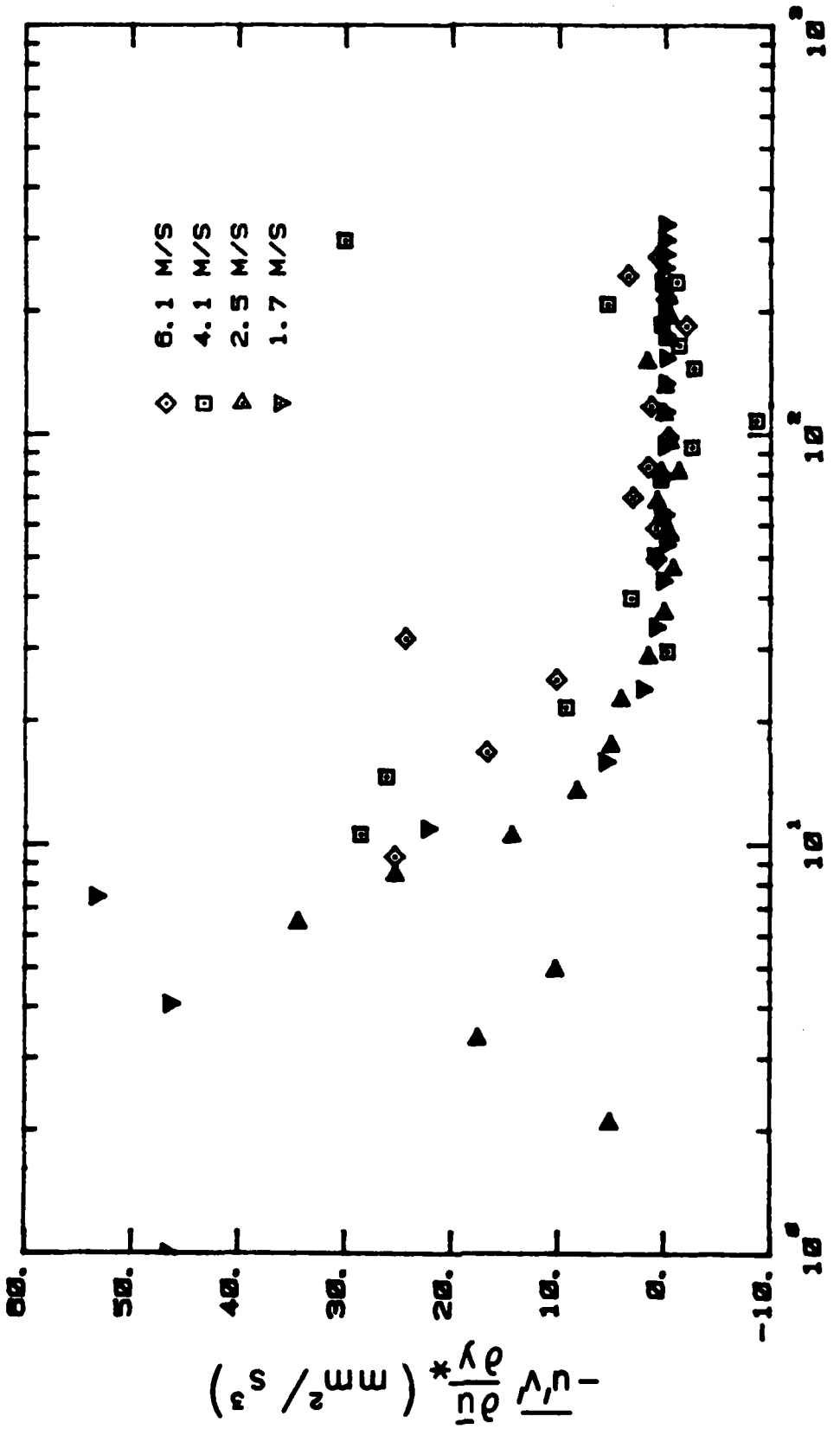

Figure 66. (a) $-\overline{u'v'}\ \partial\bar{u}/\partial y^*$ profiles in physical units (MW-WF-EF).

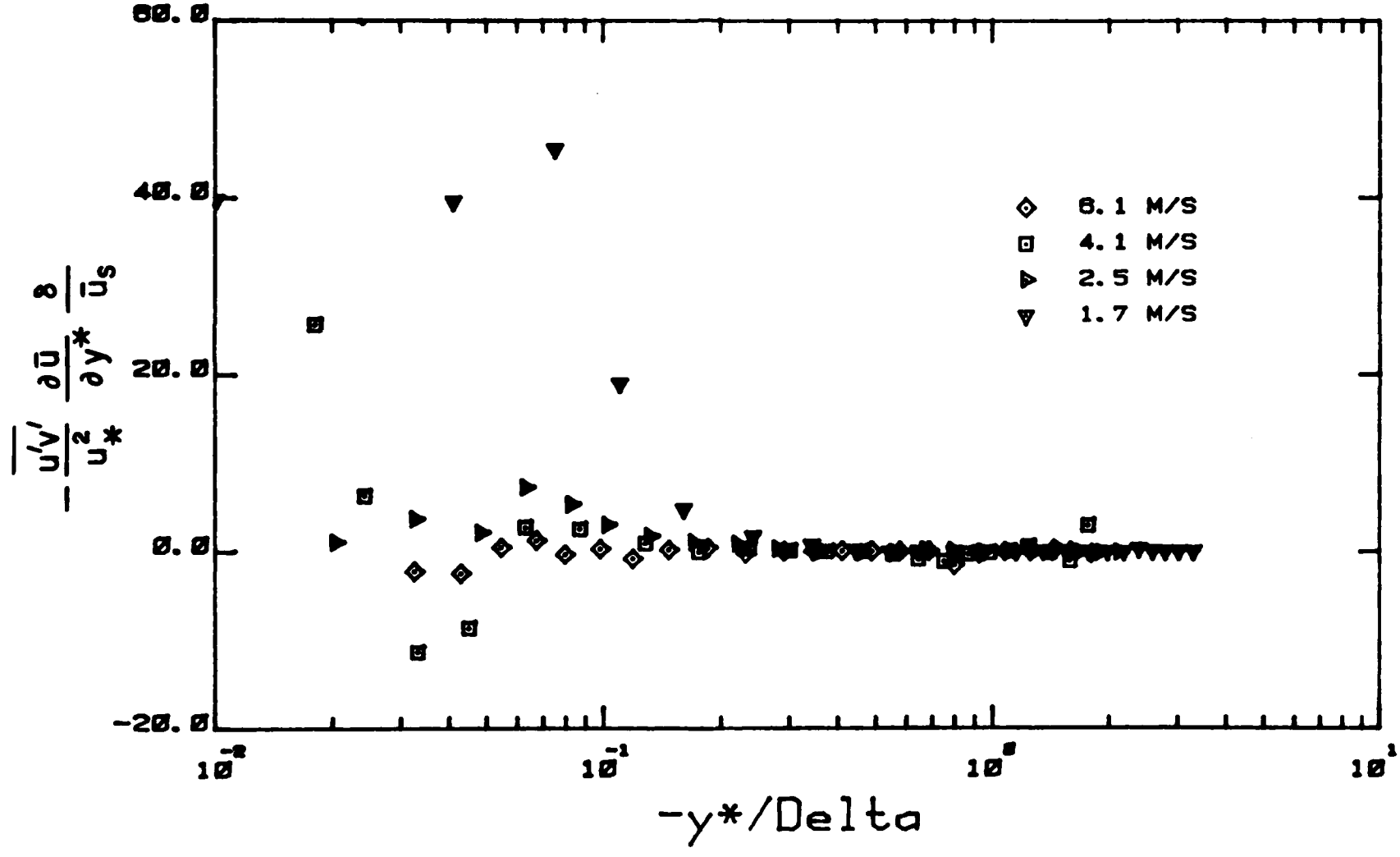

Figure 66. (b) $-\overline{u'v'}\ \partial\bar{u}/\partial y^*$ profiles in dimensionless units (MW-WF-EF).

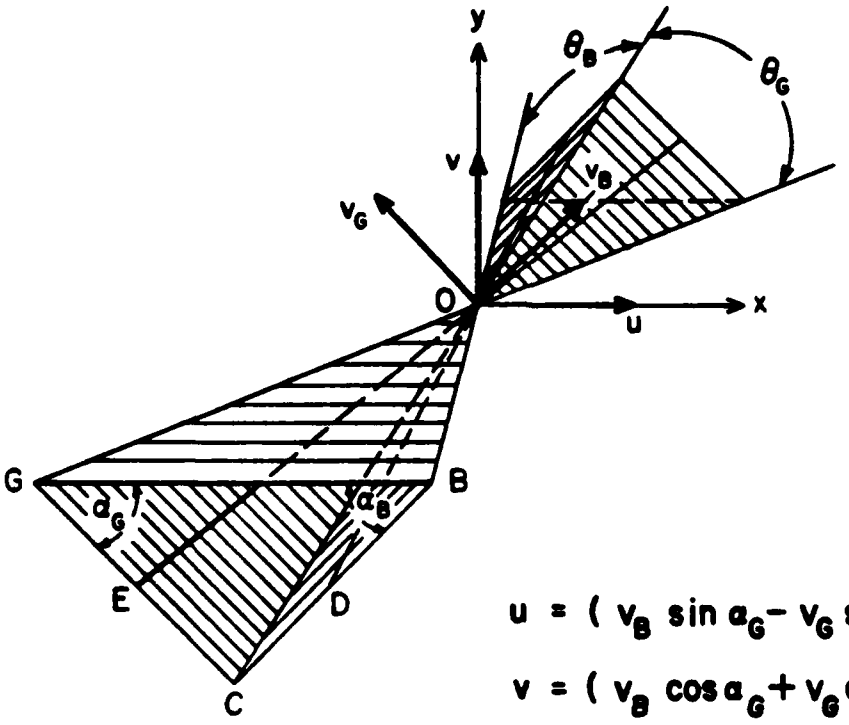

$$u = (v_B \sin \alpha_G - v_G \sin \alpha_B) / \sin (\alpha_B + \alpha_G)$$

$$v = (v_B \cos \alpha_G + v_G \cos \alpha_B) / \sin (\alpha_B + \alpha_G)$$

$v_B \perp$ DO in plane COB

$v_G \perp$ EO in plane COG

BO blue beam

GO green beam

CO cyan beam

Figure B.1. Laser Doppler anemometer (LDA) laser beam configuration.

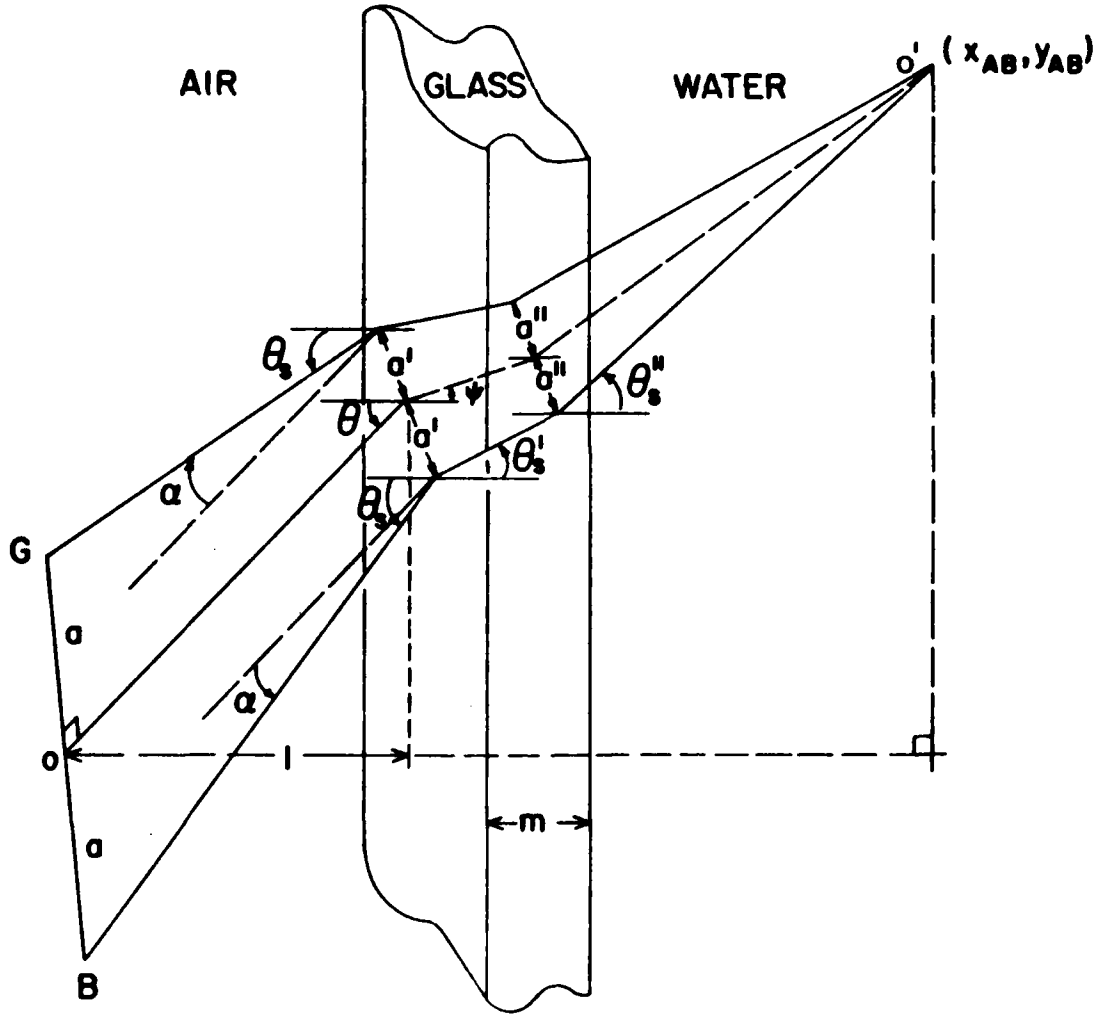

Figure B.2. LDA beam paths through the air-water-glass interfaces.

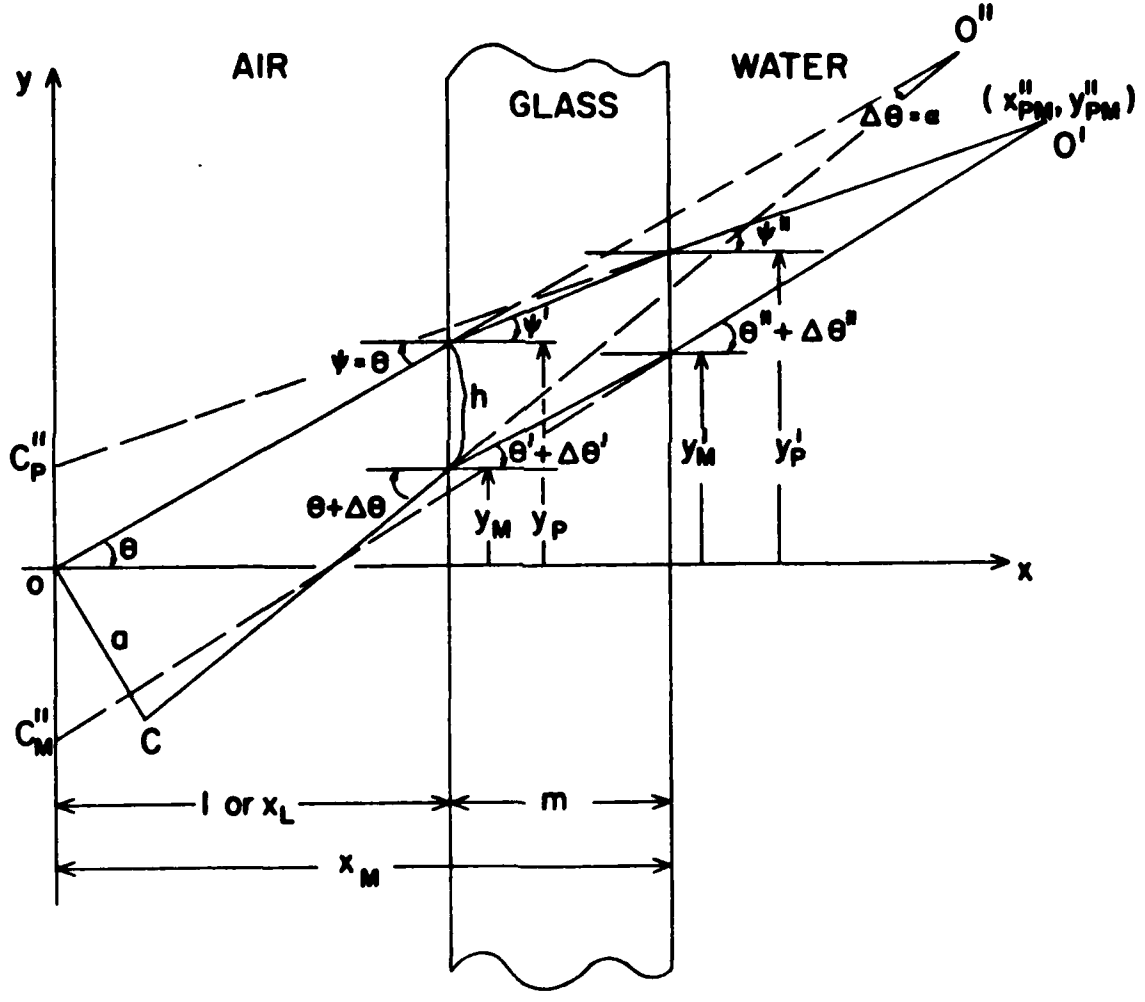

Figure B.3. LDA beam paths through the air-water-glass interfaces (side view).

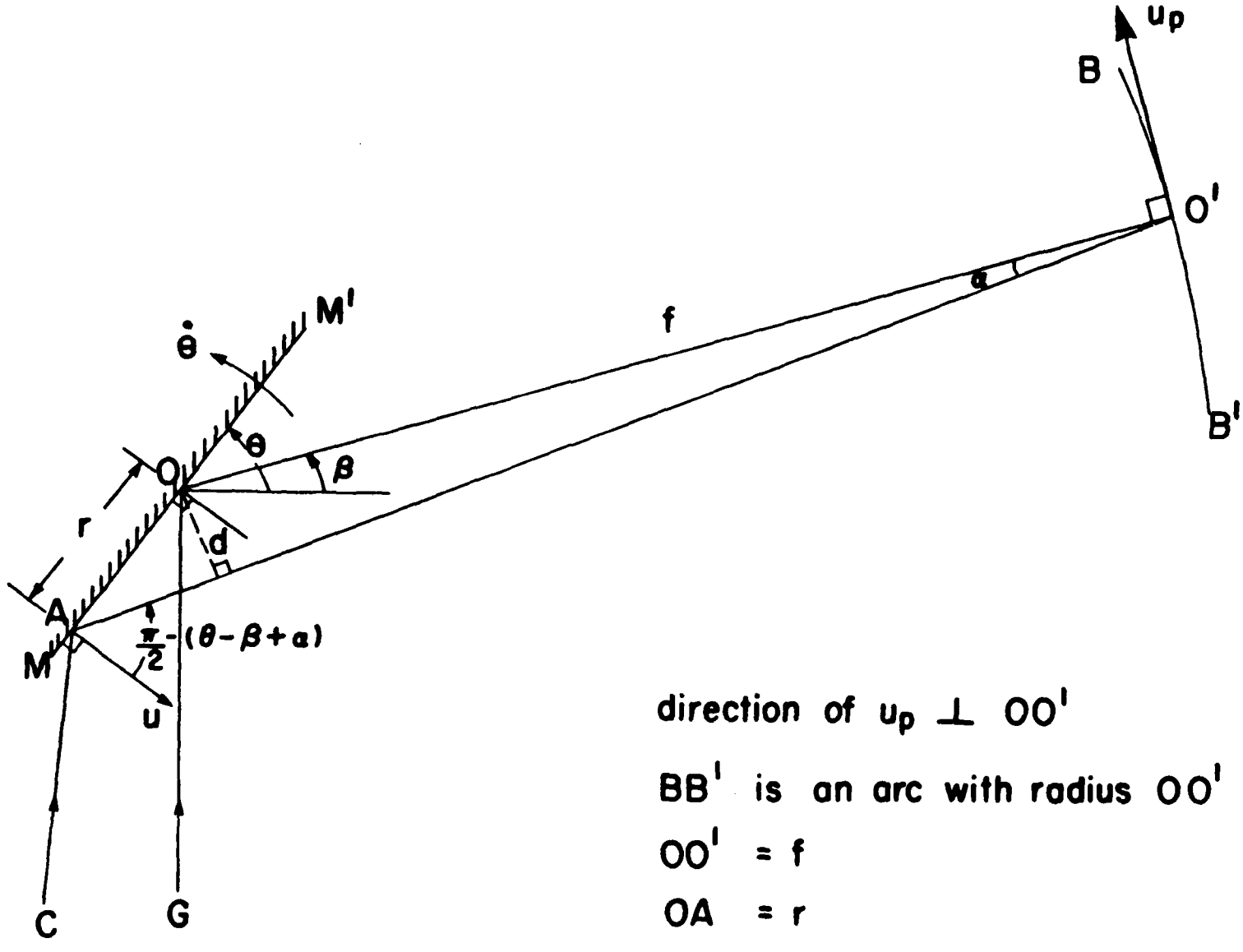

Figure B.4. Optical wave-follower in a homogeneous medium.

REFERENCES

Anisimova, YE.P., S.V. Debroklonskii, B.M. Lesnikov, and A.A. Speranskaya, "Transformation of wind velocity profiles and drift current along wind-generated wave profile," Bull. (Izv.) Acad. Sci. USSR, Atmospheric and Oceanic Physics, 14, 320-322, 1978.

Benilov, A.Yu, "Error of the method of linear filtration in the analysis of random field fluctuations of the near-water atmospheric layer and the upper ocean layer," Oceanography, 18, 17-20, 1978.

Benilov, A.Yu., O.A. Kouznetsov, and G.N. Panin, "On the analysis of wind wave-induced disturbances in the atmospheric turbulent surface layer," Boundary-Layer Meteorology, 6, 269-285, 1974.

Benilov, A.Yu and M.M. Zaslavskii, "Determination of wave and turbulent components of random hydrodynamic fields in the marine atmospheric surface layer," Bull. (Izv.) Acad. Sci. USSR, Atmospheric and Oceanic Physics, 10, 384-387, 1974.

Benjamin, T.B., "Shearing flow over a wave boundary," J. Fluid Mech., 6, 161-205, 1950.

Bliven, L.F., N.E. Huang, and S.R. Long, "A laboratory study of the velocity field below surface gravity waves," in Gas Transfer at Water Surfaces (W. Brutsaert and G.H. Jirka, Eds.), D. Reidel Publishing Company, 1984.

Bole, J.B. and E.Y. Hsu, "Response of gravity water waves to wind excitation," J. Fluid Mech., 35, 657-675, 1969.

Bowden, K.F. and R.A. White, "Measurements of the orbital velocities of sea waves and their use in determining the directional spectrum," Geophys. J. Roy. Astron. Soc., 12, 33-54, 1966.

Bradshaw, P., "Inactive motion pressure fluctuations in turbulent boundary layers," J. Fluid Mech., 30, 241-250, 1967.

Carr, L.W., "A review of unsteady turbulent boundary layer experiments," IUTAM Symposium on Unsteady Turbulent Shear Flows, Toulouse, France, May 1981, Springer-Verlag, 1981a.

Carr, L.W., "A compilation of unsteady turbulent boundary layer experimental data," AGARDograph No. 265, 1981b.

Cavaleri, L., J.A. Ewing, and N.D. Smith, "Measurement of the pressure and velocity field below surface waves," in Turbulent Fluxes Through the Sea Surface, Wave Dynamics, and Prediction (A. Favre and K. Hasselman, Eds.), Plenum Press, New York, 1978.

Chambers, A.J., P.A. Mangarella, R.L. Street, and E.Y. Hsu, "An experimental investigation of transfer of momentum at an air-water interface," Stanford Univ., Dept. Civil Eng., Tech. Report No. 133, 1970.

Chen, F.J., "Experimental approach to closure modeling of turbulent shear flow over a wavy surface," Ph.D. Dissertation, Stanford Univ., Dept. Civil Eng., 1981.

Cheung, T.K. and J.R. Koseff, "Simultaneous backward-scatter forward-scatter laser Doppler anemometer measurements in an open channel flow," DISA Information, 28, 3-9, 1983.

Colonell, J.M., "Laboratory simulation of sea waves," Stanford Univ., Dept. Civil Eng., Tech. Report No. 65, 1966.

Csanady, G.T., "Turbulent interface flow," J. Geophys. Res., 80, 2329-2342, 1978.

Dobroklonskii, S.V. and B.M. Lesnikov, "A laboratory study of the dynamic characteristics of drift currents in the presence of wind-driven waves," Bull. (Izv.) Acad. Sci. USSR, Atmospheric and Oceanic Physics, 11, 590-595, 1975.

Donelan, M.A., "Whitecaps and momentum transfer," in Turbulent Fluxes Through the Sea Surface, Wave Dynamics, and Prediction (A. Favre and K. Hasselmann, Eds.), Plenum Press, New York, 1978.

Gent, P.R. and P.A. Taylor, "A numerical model of the air flow above water waves," J. Fluid Mech., 77, 105-128, 1976.

Goossens, L.H.J., H.J.A. van Pagee, and P.J. Tessel, "Vertical turbulent diffusion in air-driven water flows," J. Hydraulics Div., Proc. ASCE, 108, September 1982.

Hanson, S., "Visualization of alignment errors and heterodyning constraints in laser Doppler velocimeters," Proc. LDA Symposium, Copenhagen, (Skovlunde, Denmark: DISA Elektronik A/S), 176-182, 1976.

Howe, B.M., A.J. Chambers, and R.L. Street, "Heat transfer at a mobile boundary," Adv. in Heat and Mass Transfer at Air-Water Interfaces, ASME, 1-10, 1978.

Howe, B.M., A.J. Chambers, S.P. Klotz, T.K. Cheung, and R.L. Street, A preliminary report on velocity and temperature measurements above and beneath an air-water interface: the data set," Stanford Univ., Dept Civil Eng., Tech. Report No. 261, 1981.

Howe, B.M., A.J. Chambers, S.P. Klotz, T.K. Cheung, and R.L. Street, "Comparison of profiles and fluxes of heat and momentum above and below an air-water interface," Trans. ASME, J. Heat Transfer, 104, 34-39, 1982.

Hsu, C.T. and E.Y. Hsu, "On the structure of turbulent flow over a progressive water wave: theory and experiment in a transformed wave-following coordinate system. Part 2," J. Fluid Mech., 131, 123-153, 1983.

Hsu, C.T., E.Y. Hsu, and R.L. Street, "The structure of modulated turbulent flow over progressive water waves," Stanford Univ., Dept. Civil Eng., Tech. Report No. 221, 1977.

Hsu, C.T., E.Y. Hsu, and R.L. Street, "On the structure of turbulent flows over a progressive water wave: theory and experiment in a transformed, wave-following coordinate system, J. Fluid Mech., 105, 87-117, 1981.

Hsu, C.T., H.Y. Wu, E.Y. Hsu, and R.L. Street, "Momentum and energy transfer in wind generation of waves," J. Phys. Ocean., 12, 929-951, 1982.

Hsu, E.Y., "A wind, water-wave research facility," Stanford Univ., Dept. Civil Eng., Tech. Report No. 57, 1965.

Hussian, A.K.M.F., "Coherent structures - reality and myth," Phys. Fluids, 26(10), 2816-2850, 1983.

Jayaraman, J., P. Parikh, and W.C. Reynolds, "An experimental study of the dynamics of an unsteady turbulent boundary layer," Stanford Univ., Dept. Mech. Eng., Thermoscience Division, Tech. Report No. TF-18, 1982.

Jones, I.S.F. and B.C. Kenney, "The scaling of velocity fluctuations in the surface mixed layer," J. Geophys. Res., 82, 1392-1396, 1977.

Katsaros, K.B., "Effects of precipitation on the eddy exchange in a wind-driven sea," Dynamics of Atmospheres and Oceans, 1, 99-126, 1976.

Kays, W.M. and M.E. Crawford, Convective Heat and Mass Transfer, McGraw-Hill Book Co., 1980.

Kitaigorodskii, S.A., The Physics of Air-Sea Interaction, Israel Program for Scientific Translation, Jerusalem (TT72-50062, U.S. Dept. of Commerce, Springfield, VA), 1973.

Kitaigorodskii, S.A. and Yu.Z. Miripolskii, "Turbulent-energy dissipation in the ocean surface layer," Bull. (Izv.) Acad. Sci. USSR, Atmospheric and Oceanic Physics, 4, 369-375, 1968.

Kitaigorodskii, S.A. and J.L. Lumley, "Wave-turbulence interactions in the upper ocean. Part 1. The energy balance of the interacting fields of surface wind waves and wind-induced three-dimensional turbulence," Sibley School of Mechanical and Aerospace Engineering, Report No. FDA-82-08, 1982.

Klebanoff, P.S., "Characteristics of turbulence in a boundary layer flow with zero pressure gradient," NACA Report No. 1247, 1955.

Kline, S.J. and F.A. McClintock, "Describing uncertainties in single-sample experiments," Mech. Engineering, 3-8, January 1953.

Klotz, S.P. and R.L. Street, "On the simulation of the coupled laminar boundary-layer at a smooth, phase-changing gas-liquid interface," in Numerical Methods in Laminar and Turbulent Flows, (C. Taylor and B.A. Schrefler, Eds.), Pineridge Press, Swansea, UK, 1981a.

Klotz, S.P. and R.L. Street, "The numerical simulation of the turbulent boundary-layers at a rough, air-water interface," in Numerical Methods in Laminar and Turbulent Flows (C. Taylor and B.A. Schrefler, Eds.), Pineridge Press, Swansea, UK, 1981b.

Kondo, J., "Parameterization of turbulent transport in the top meter of the ocean," J. Phys. Ocean., 6, 712-720, 1976.

Kondo, J., Y. Fujinawa, and G. Naito, "High frequency components of ocean waves and their relation to the aerodynamic roughness," J. Phys. Ocean., 3, 197-203, 1973.

Landau, L.D. and E.M. Lifshitz, Fluid Mechanics, Pergamon Press, 1959.

Lin, J. and M. Gad-el-Hak, "Turbulent current measurements in a wind-wave tank," J. Phys. Ocean., 89, 627-636, 1984.

Liu, W.T., K.B. Katsaros, and J.A. Businger, "Bulk parameterization of air-sea exchange of heat and water vapor including the molecular constraints at the interface," J. Atm. Sci., 36, 1722-1735, 1979.

Lumley, J.L. and E.A. Terray, "Kinematics of turbulence convected by a random wave field," Sibley School of Mechanical and Aerospace Engineering, Report No. FDA-82-02, 1982.

McLeish, W.L. and G.E. Putland, "Measurements of wind-driven flow profiles in the top millimeter of water," J. Phys. Ocean., 5, 516-518, 1975.

Miles, J.W., "On the generation of surface waves by shear flows. Part 2," J. Fluid Mech., 6, 568-582, 1959.

Moffat, R.J., "Contribution to the theory of uncertainty analysis for single-sample experiments," Vol. I, The 1980-81 AFOSR-HTTM-Stanford Conference on Complex Turbulent Flows, Stanford Univ., Dept. Mech. Eng., Thermoscience Div., 1981.

Navrotskii, V.V., "Waves and turbulence in the ocean surface layer," Oceanology, 7, 755-766, 1967.

Norris, H.L. and W.C. Reynolds, "Turbulent channel flow with a moving wavy boundary," Stanford Univ., Dept. Mech. Eng., Tech. Report No. TF-7, 1975.

Papadimitrakis, Y.A., "Velocity and pressure measurements in the turbulent boundary layer above mechanically generated water waves," Ph.D. dissertation, Stanford Univ., Dept. Civil Eng., 1982.

Phillips, O.M., The Dynamics of the Upper Ocean, Second Ed., Cambridge University Press, London, 1977.

Phillips, O.M. and M.L. Banner, "Wave breaking in the presence of wind drift and swell," J. Fluid Mech., 66, 625-640, 1974.

Plate, E.J., P.C. Chang, and G.M. Hidy, "Experiments on the generation of small waves by wind," J. Fluid Mech., 35, 625-656, 1969.

Reynolds, W.C. and A.K.M.F. Hussain, "The mechanics of an organized wave in turbulent shear flow. Part 3. Theoretical models and comparisons with experiments," J. Fluid Mech., 54, 263-288, 1972.

Schlichting, H., Boundary-Layer Theory, Seventh Ed., McGraw-Hill Book Co., 1979.

Shemdin, O.H., "Wind-generated current and phase speed of wind waves," J. Phys. Ocean., 2, 411-419, 1972.

Shonting, D.H., "A preliminary investigation of momentum flux in ocean waves," Pure and Appl. Geophys., 57, 149-152, 1964.

Shonting, D.H., "Measurements of particle motions in ocean waves," J. Marine Res., 25, 162-181, 1967.

Shonting, D.H., "Autospectra of observed particle motion in wind waves," J. Marine Res., 26, 411-419, 1968.

Shonting, D.H., "Observations of Reynolds stresses in wind waves," Pure and Appl. Geophys., 81, 202-210, 1970.

Simpson, J.H., "Observations of the directional characteristics of sea waves," Geophys. J. Roy. Astron. Soc., 17, 93-120, 1969.

Street, R.L., "Turbulent heat and mass transfers across a rough, air-water interface: a simple theory," Int. J. Heat Mass Transfer, 22, 885-899, 1979.

Sutherland, A.J., "Spectral measurements and growth rates of wind-generated water waves," J. Fluid Mech., 33, 545-560, 1968.

Taira, K., "Wave particle velocities measured with a Doppler current meter," J. Ocean. Soc. Japan, 27, 218-, 1971.

Takeuchi, K. and T.R. Mogel, "A performance of a mini-computer," Rev. Sci. Instrum., 46(6), 686-691, 1975.

Tennekes, H. and J.L. Lumley, A First Course in Turbulence, MIT Press, 1972.

Thornton, E.B. and R.F. Krapohl, "Water particle velocities measured under ocean waves," J. Geophys. Res., 79, 847-852, 1974.

Wehausen, J.V. and E.V. Laitone, "Surface waves," in Handbuch der Physik, Band IX, Springer, 1960.

White, F.M., Viscous Fluid Flow, McGraw-Hill Book Co., 1974.

Wu, J., "Laboratory studies of wind-wave interactions," J. Fluid Mech., 34, 91-111, 1968.

Wu, J., "Wind-induced drift currents," J. Fluid Mech., 68, 49-70, 1975.

Yefimov, V.V. and G.N. Khristoforov, "Some features of the velocity field in the layer of wind-driven swell," Bull. (Izv.) Acad. Sci. USSR, Atmospheric and Oceanic Physics, 5, 597-602, 1969.

Yefimov, V.V. and G.N. Khristoforov, "Spectra and statistical relations between the velocity fluctuations in the upper layer of the seas and surface waves," Bull. (Izv.) Acad. Sci. USSR, Atmospheric and Oceanic Physics, 7, 841-851, 1971.

Yefimov, V.V. and G.N. Khristoforov, "Dynamics of surface waves with allowance for the turbulent nature of the motion," Bull. (Izv.) Acad. Sci. USSR, Atmospheric and Oceanic Physics, 8, 28-35, 1972.

unclassified

SECURITY CLASSIFICATION OF PAGE (When Data Entered)

REPORT DOCUMENTATION PAGE		READ INSTRUCTIONS BEFORE COMPLETING FORM
1. REPORT NUMBER Technical Report No. 287	2. GOVT ACCESSION NO.	3. RECIPIENT'S CATALOG NUMBER
4. TITLE (and Subtitle) A STUDY OF THE TURBULENT LAYER IN THE WATER AT AN AIR-WATER INTERFACE		5. TYPE OF REPORT & PERIOD COVERED Technical Report 6. PERFORMING ORG. REPORT NUMBER 287
7. AUTHOR(s) Tak Kee Cheung		8. CONTRACT OR GRANT NUMBER(s) Contract N00014-84-K-0242
9. PERFORMING ORGANIZATION NAME AND ADDRESS Stanford University Stanford, CA 94305		10. PROGRAM ELEMENT, PROJECT, TASK AREA & WORK UNIT NUMBERS NR-661-003/11/18/83 (430)
11. CONTROLLING OFFICE NAME AND ADDRESS Fluid Mechanics Division Office of the Naval Research 800 North Quincy Street, Arlington, Virginia 22217		12. REPORT DATE January 1985 13. NUMBER OF PAGES 275 pages
14. MONITORING AGENCY NAME & ADDRESS(if different from Controlling Office)		15. SECURITY CLASS. (of this report) unclassified 15a. DECLASSIFICATION/DOWNGRADING SCHEDULE

16. DISTRIBUTION STATEMENT (of this Report)

This document is unclassified and its distribution is unlimited.

DISTRIBUTION STATEMENT A

Approved for public release;
Distribution Unlimited

17. DISTRIBUTION STATEMENT (of the abstract entered in Block 20, if different from Report)

18. SUPPLEMENTARY NOTES

19. KEY WORDS (Continue on reverse side if necessary and identify by block number)

water waves, turbulence, ocean-atmosphere interface, laboratory experiments, laser instrument

20. ABSTRACT (Continue on reverse side if necessary and identify by block number)

SEE REVERSE SIDE

DD FORM 1 JAN 73 1473 EDITION OF 1 NOV 65 IS OBSOLETE

unclassified

SECURITY CLASSIFICATION OF THIS PAGE (When Data Entered)

ABSTRACT

Because the global weather and ocean circulations are driven by transfers across the atmosphere-ocean interface, studies of it remain at the forefront of research efforts in atmospheric sciences and oceanography. Many questions concerning the momentum and energy transfers in the water surface layer beneath the air-water interface remain unanswered. The present experimental program was undertaken with the goal of learning how the energy, which is transferred from the wind, is distributed among the mean, wave, and turbulent flow fields in the water. The interactions between these three flow fields were also examined.

The experiments were performed in the Stanford Wind, Water Wave Research Facility. A two-component, frequency-shifted, laser Doppler anemometer system was used with frequency trackers to measure the water velocity. Three major sets of experiments were done: i) wind-generated waves in Eulerian coordinates with wind speeds ranging from 1.5 m/s to 13.1 m/s; ii) wind-ruffled mechanically generated waves (22 mm in amplitude and at a frequency of 1 Hz) in Eulerian coordinates with wind speeds ranging from 0.0 to 6.2 m/s, and iii) wind-ruffled mechanically generated waves in wave-following Eulerian coordinates with wind speeds ranging from 0.0 to 6.1 m/s. A novel optical wave-follower, which allowed velocity measurements very close to the mobile surface, was constructed and deployed in the wave-following measurements. The mean, wave, and turbulent fields were isolated, and from them, other quantities of interest were computed.

The results show that the waves affect the mean flow, but the mean velocity profiles show logarithmic behavior. The wave field generally agrees with the prediction of a linear water-wave theory. In the wind-wave experiments, the turbulent quantities behave similar to those in flows over flat plates. In the mechanical-wave experiments, the turbulent quantities have different trends from those of the wind-wave cases, which suggests possible weak wave-related turbulence. The mean wave-induced shear stress is negative, which implies that the waves augment the mean flow. Thus, the waves can also transfer energy indirectly to turbulence via the mean flow. The turbulent field draws its energy from the mean flow through the mean turbulent shear stress and from the wave field via the wave-induced turbulent stresses. Experimental observations agree with simple analysis of the momentum and energy equations. This study contributes to the basic understanding of the fundamental principles which govern transfers at an air-water interface.

END

FILMED

7-85

DTIC